

**DEVELOPMENT OF HIGHLY EFFICIENT g-C<sub>3</sub>N<sub>4</sub> BASED METAL  
OXIDE NANOCOMPOSITES FOR PHOTOCATALYTIC APPLICATIONS**

**THESIS**

**SUBMITTED IN PARTIAL FULFILMENT OF THE REQUIREMENTS  
FOR THE AWARD OF THE DEGREE OF**

***Doctor of Philosophy***

**IN**

**CHEMISTRY**

**BY**

**GANDAMALLA AMBEDKAR**

**(Roll No. 716058)**

**RESEARCH SUPERVISOR**

**DR. VISHNU SHANKER**



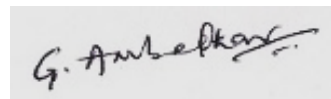
**DEPARTMENT OF CHEMISTRY  
NATIONAL INSTITUTE OF TECHNOLOGY WARANGAL  
WARANGAL – 506 004, TELANGANA, INDIA**

**AUGUST – 2021**

## **DECLARATION**

I hereby declare that the matter embodied in this thesis entitled “**Development of highly efficient g-C<sub>3</sub>N<sub>4</sub> based metal oxide nanocomposites for photocatalytic applications**” is based entirely on the results of the investigations and research work carried out by me under the supervision of **Dr. Vishnu Shanker**, Associate Professor, and Head, Department of Chemistry, National Institute of Technology, Warangal. I declare that this work is original and has not been submitted in part or full, for any degree or diploma to this or any other Institute/University.

I declare that this written submission represents my ideas in my own words and where others' ideas or words have been included, I have adequately cited and referenced the original sources. I also declare that I have adhered to all principles of academic honesty and integrity and have not misrepresented or fabricated or falsified any idea/data/fact/source in my submission. I understand that any violation of the above will be a cause for disciplinary action by the Institute and can also evoke penal action from the sources which have thus not been properly cited or from whom proper permission has not been taken when needed.



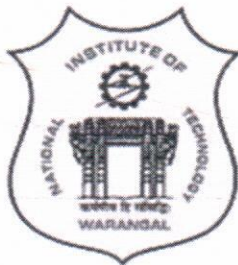
Date: 09.08.2021.

(Gandamalla Ambedkar)

Place: **NIT Warangal**

**Roll Number: 716058**

Dr. Vishnu Shanker  
Associate Professor  
Head of the Department



Department Chemistry  
National Institute of Technology  
Warangal - 506 004,  
Telangana, India.  
Tel: +91-870-2462675  
Fax: +91-870-2459547  
Email: vishnu@nitw.ac.in

## CERTIFICATE

This is to certify that the research work presented in this thesis entitled "**Development of Highly Efficient g-C<sub>3</sub>N<sub>4</sub> Based Metal Oxide Nanocomposites for Photocatalytic Applications**" submitted by **Mr. Gandamalla Ambedkar**, for the award of the degree of **Doctor of Philosophy in Chemistry**, National Institute of Technology, Warangal, carried out under my guidance and supervision. This work has not been submitted earlier either in part or in full, for any degree or diploma to this or any other Institute/University.

Date: 09.08.2021.

**(Dr. Vishnu Shanker)**

Place: **Warangal**



## ACKNOWLEDGEMENTS



---

## **ACKNOWLEDGEMENTS**

During the course of my Doctoral Research work, I have received the assistance and support from the following people:

First and foremost, I am truly indebted and I express my earnest gratitude for my Research Supervisor **Dr. Vishnu Shanker**, Associate Professor and Head, Department of Chemistry, National Institute of Technology Warangal, for his inestimable expertise and astute guidance. His unabated enthusiasm, which stems from his absolute command over the subject, has been a constant source of inspiration for me to work hard and the outcome is expressed in the form of this thesis. I will be forever thankful to him for all the time he has spent with me in innumerable discussions. The thesis would not have been completed without his support.

I express my sincere thanks to **Prof. N. V. Ramana Rao**, Director, NIT Warangal, for giving me the opportunity to carry out my research work and for providing instrumentation facilities. I greatly acknowledge **Ministry of Human Resource Development (MHRD)** for the financial support in the form of fellowship.

I wish to express my heart full thanks to **Prof. Yen-Pei Fu**, Mr. Atul Verma, Mr. Pandiyarajan Anand, and Mr. Sanath Kumar, Department of material science and engineering, National Dong Hwa University (**NDHU Taiwan**), for their continuous support, valuable suggestions and providing facilities to carry out a part of my research work during my doctoral research, and I greatly acknowledge **TEEP@Asian Plus** for selecting me to a **Short Term Research Internship Program (STRIP)** for a duration of six months.

I express my gratitude to the Doctoral Scrutiny Committee members: **Dr. Vishnu Shanker**, Chairman and Head, Department of Chemistry, **Prof. K. V. Gobi**, Department of Chemistry, **Dr. Raghu Chitta**, Department of Chemistry, and **Prof. N. Narsaiah**, Department of Metallurgical and Materials Engineering, NIT Warangal, for their detailed review, constructive suggestions and excellent advice during the progress of this research work.

My sincere thanks to Prof. V. Rajeshwar Rao, Prof. K. V. Gobi, and Prof. P.V. Srilakshmi, Former Heads of the Department of Chemistry during the period of my research work.

---

I would like to thank all the faculty members from Chemistry Department Prof. A. Ramachandraiah, Prof. K. Laxma Reddy, Prof. V. Rajeshwar Rao, Prof. K. V. Gobi, Prof. P. V. Srilakshmi, Dr. D. Kasinath, Dr. N. Venkatathri, Dr. Raghu Chitta, Dr. B. Srinivas, Dr. K. Hari Prasad, Dr. S. Nagarajan, Dr. M. Raghavendra, Dr. CH. Jugun Prakash, Dr. Ravinder Pawar, Dr. Mukul Pradhan Dr. Rajeshkhanna Gaddam Dr. V. Rajeshkumar for their cooperation and encouragement.

I convey my special thanks from the bottom of my heart to my seniors, Dr. Saikumar Manchala, Dr. T. Surendar, for their continuous support and encouragement in each and every step of my research work.

Many friends have helped me stay sane through these difficult years. With all happiness, I acknowledge the cheerful assistance rendered by all my research colleagues, Dr. B. Santosh Kumar, Dr. K. Chaitanya Kumar, Dr. K. Koteswar Reddy, Dr. G. Srinivasa Rao, Dr. M. Satyanarayana, Dr. V. Krishnaiah, Dr. R. Raj Kumar, Dr. P. Sagar Vijay Kumar, Dr. A. Ajay Kumar, Dr. K. Yugender, Dr. L. Suresh, Dr. E. Hari Mohan, Mr. Phani Kumar, Dr. Vikram Sagar, Dr. G. Ramesh, Dr. S. Nagaraju, Dr. B. Papalal, Dr. N.V. Bharath, Ms. R. Hithavani, Dr. A. Varun, Dr. K. Sujatha, Dr. K. Ramaiah, Dr. P. Vinay, Dr. S. Rangaswamy Reddy, Dr. T. Sanjeeva, Ms. P. Sowmya, Mr. N. Satyanarayana, Mr. J. Parameshwara Chary, Mr. P. Babji, Mr. M. Srikanth, Mr. K. Vijender Reddy, Mr. K. Satish, Mr. A. Ramesh, Mr. R. Venkatesh, Mr. Ch. Raju, Mr. A. Naveen Reddy, Mr. A. Bhargav sai, Mr. T. Dhanunjaya rao, Ms. G. Sivaparvathi, Ms. M. Sirisha, Ms. T. Shirisha, Ms. B. Sravanti, Mr. P. Venkatesham, Mr. B. Prashanth, Mr. R. Varaprasad, Mr. R. Arun, Ms. Akanksha, Mr. B. Anjaiah, Mr. Madhu, Mr. Naik, Mr. B. Srikanth, Ms. Tohira Banoo, Ms. Khushboo Agarwala and Mr. Vinay Raj Ganesh (CSE).

I express special thanks to my lab mates Dr. K. Vimal Kumar, Dr. Chirra Suman, Dr. V. Sunil Kumar, Mr. S. Suresh, Mr. K. Shekar, Mr. G. Srinath, Mr. G. Sripal Reddy, and Mr. Karingula Sampath.

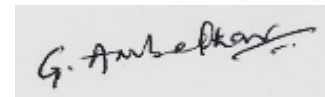
I sincerely acknowledge the assistance provided by all the supporting staff, Department of Chemistry, NIT-Warangal.

I wouldn't have come this far without the love, care, encouragement of some of the wonderful friends. I would like to thank each of them including Dr. P. Nagaiah, Mr. M. Vinay, Mr. A. Mahesh, Mr. D. Balakrishna, Mr. A. Srikanth, Mr. D. Ganesh, Mr. R. Shrikanth, Mr. Md. Sana, Mr. Md. Zameer Mr. B. Srinivas, Mr. B. Nagaraju, Mr. B. Vamshi, Mr. R. Brahmi, Dr. Md.

---

Anif Pasha. Mr. M. Ram, Mr. E. Kamal, and D. Rajesh for all lighting up my life with their friendship.

The most pleasant part of this acknowledge is that it gives me a unique opportunity to thank my parents, **Late Shri. Gandamalla Narsaiah** and **Smt. Laxmamma**, and my beloved brothers **Mr. Rambabu, Mr. Ramanaiah, Mr. Arjun, Mr. Manoj, Mr. Aravind Srinivas and Mr. Sai Charan (Rider)**, my beloved sisters **Ms. Padma, and Ms. Akshitha**. My deepest gratitude goes to my family members for their unflagging love and unconditional support throughout my life and my studies.



(Ambedkar Gandamalla)

**This Thesis is Dedicated to My Beloved  
Father Late. Shri. Gandamalla Narsaiah**

---

## CONTENTS

---

# Table of Contents

<b>Chapter I.....</b>	<b>1</b>
<b>Introduction.....</b>	<b>1</b>
1.1 Background .....	1
1.2 State of problem .....	1
1.3 Objectives of the present research work .....	2
1.4 Scope of the present research work.....	2
1.5 Photocatalysis.....	2
1.5.1 Semiconductor photocatalysis .....	3
1.5.2 Basic principle of the semiconductor photocatalysis .....	4
1.5.3 Mechanism of the semiconductor photocatalysis .....	5
1.5.4 Photocatalysts and selection .....	7
1.5.5 Applications of photocatalysis.....	9
1.5.6 Why visible light active photocatalysis? .....	9
1.5.7 Strategies to develop an efficient visible-active photocatalyst.....	10
1.5.7.1 Metal ion doping.....	10
1.5.7.2 Non–metal doping.....	11
1.5.7.3 Co-doping.....	12
1.5.7.4 Dye sensitization.....	12
1.5.7.5 Metal/semiconductor heterostructure.....	12
1.5.7.6 Semiconductor/semiconductor nanocomposites.....	13
1.6 Photocatalysis at ‘Nanoscale’ .....	14
1.7 References .....	14
<b>Chapter II .....</b>	<b>19</b>
<b>Materials and analytical techniques.....</b>	<b>19</b>
2.1 Synthesis of nanomaterials.....	19
2.2 Techniques for characterization of nanomaterials .....	20
2.2.1 Powder X-Ray diffraction (PXRD) .....	20
2.2.2 Fourier transform infrared spectroscopy (FT-IR).....	22
2.2.3 X-ray photoelectron spectroscopy (XPS) .....	23
2.2.4 UV–Visible diffuse reflectance spectroscopy (UV-Vis DRS) .....	24

2.2.5 Fluorescence spectroscopy (PL) .....	25
2.2.6 Scanning electron microscopy (SEM) .....	26
2.2.7 Field emission Scanning electron microscope (FE-SEM) .....	27
2.2.8 Transmission electron microscope (TEM) .....	27
2.2.9 Energy-dispersive X-ray spectroscopy (EDS).....	27
2.2.10 Surface Area Analysis (BET) .....	28
2.2.11 Thermo-gravimetric analysis (TGA) .....	28
2.3 Photocatalytic experiments .....	29
2.4 References .....	29
<b>Chapter III.....</b>	<b>31</b>
<b>Development of versatile CdMoO<sub>4</sub>/g-C<sub>3</sub>N<sub>4</sub> nanocomposite for enhanced photoelectrochemical oxygen evolution reaction and photocatalytic dye degradation applications.....</b>	<b>31</b>
3.1 Introduction .....	31
3.2 Experimental section .....	33
3.2.1 Materials and method .....	33
3.2.2 Synthesis of bulk CN .....	33
3.2.3 Synthesis of CMO/CN composite photocatalyst .....	33
3.2.4 Electrochemical measurements .....	34
3.2.5 Photocatalytic dye degradation experiments .....	35
3.3 Results and discussions .....	35
3.3.1 PXRD, FT-IR, and TGA studies .....	35
3.3.2 SEM, EDS, elemental mapping and TEM studies.....	38
3.3.3 UV-Vis DRS, PL, TRFL and BET studies .....	39
3.3.4 XPS studies.....	43
3.3.5 Electrochemical and Photo-assisted electrocatalytic OER activity .....	45
3.3.6 Photocatalytic dye degradation studies.....	48
3.3.7 Probable reaction mechanism for dye degradation.....	53
3.4 Conclusions .....	55
3.5 References .....	56

<b>Chapter IV .....</b>	<b>61</b>
<b>Facile Fabrication of Novel SrMoO<sub>4</sub>/g-C<sub>3</sub>N<sub>4</sub> Hybrid Composite for High-Performance Photocatalytic Degradation of Dye Pollutant under Sunlight .....</b>	<b>61</b>
4.1 Introduction .....	61
4.2 Experimental section .....	62
4.2.1 Materials .....	62
4.2.2 Synthesis of G-CN .....	62
4.2.3 Synthesis of SMO .....	63
4.2.4 Synthesis of SMO/G-CN composite photocatalysts .....	63
4.2.5 Electrochemical Impedance Spectroscopy (EIS) .....	64
4.2.6 Photocatalytic Dye degradation experiments .....	64
4.3 Results and discussions .....	65
4.3.1 PXRD and FT-IR studies .....	65
4.3.2. FE-SEM, EDS, and elemental mapping studies .....	66
4.3.3 XPS analysis .....	68
4.3.4 UV-Vis DRS, PL, and TGA studies .....	69
4.3.5 Photocatalytic degradation of RhB dye pollutant .....	71
4.3.6 Proposed mechanism .....	76
4.4 Conclusions .....	78
4.5 References .....	78
<b>Chapter V .....</b>	<b>84</b>
<b>Microwave-assisted synthesis of ZnAl-LDH/g-C<sub>3</sub>N<sub>4</sub> composite for degradation of antibiotic ciprofloxacin under visible-light illumination .....</b>	<b>84</b>
5.1 Introduction .....	84
5.2 Experimental section .....	86
5.2.1 Materials and method .....	86
5.2.2 Synthesis of g-C <sub>3</sub> N <sub>4</sub> .....	86
5.2.3 Synthesis of ZnAl-LDH .....	86
5.2.4 Synthesis of ZnAl-LDH/CN composite photocatalysts .....	86
5.2.5 LC-MS studies .....	87
5.2.6 Photocatalytic activity .....	87
5.3. Results and discussions .....	88
5.3.1. PXRD, FT-IR, and TRFL studies .....	88

5.3.2 FE-SEM, TEM, and EDS studies .....	91
5.3.3 UV-Vis DRS and BET studies .....	93
5.3.4 XPS Analysis .....	95
5.3.5 Photocatalytic activity studies .....	97
5.3.6 Proposed reaction mechanism .....	101
5.3.7 Photocatalytic CIP degradation pathway.....	104
5.4 Conclusions .....	108
5.5 References .....	108
<b>Chapter VI.....</b>	<b>114</b>
<b>Photo-thermal studies of stable and potential Ce(MoO<sub>4</sub>)<sub>2</sub>/g-C<sub>3</sub>N<sub>4</sub> binary composite towards degradation of ciprofloxacin and methylene blue under visible light.....</b>	<b>114</b>
6.1 Introduction .....	114
6.2 Experimental Section .....	115
6.2.1 Materials .....	115
6.2.2 Synthesis of pure g-C <sub>3</sub> N <sub>4</sub> .....	116
6.2.3 Synthesis of Ce(MoO <sub>4</sub> ) <sub>2</sub> .....	116
6.2.4 Synthesis of Ce(MoO <sub>4</sub> ) <sub>2</sub> /g-C <sub>3</sub> N <sub>4</sub> binary composites .....	116
6.2.5 Photocatalytic experiments.....	117
6.3 Results and discussions .....	118
6.3.1 PXRD, FT-IR, and UV-Vis DRS studies .....	118
6.3.2 FE-SEM, TEM, EDS, and elemental mapping analysis.....	120
6.3.3 XPS Studies .....	122
6.3.4 PL, TRFL, and BET studies .....	123
6.3.5 Photocatalytic activity studies .....	126
6.3.6 Effect of temperature on degradation studies .....	129
6.3.7 Photocatalytic mechanism for CeM/g-CN-20 binary composite photocatalyst .....	131
6.4 Conclusions .....	133
6.5 References .....	134

<b>Chapter VII .....</b>	<b>138</b>
<b>Summary and Conclusions .....</b>	<b>138</b>
7.1 Present thesis .....	138
7.2 Conclusions .....	138
7.3 Summary .....	140
7.4 Recommendations for future work.....	141
<b>List of Publications .....</b>	<b>142</b>
<b>Conferences and Seminars .....</b>	<b>144</b>
<b>Workshops and Courses.....</b>	<b>146</b>

## Symbols and Abbreviations

nm	:	Nanometre
cm	:	Centimetre
Å	:	Angstrom
$\theta$	:	Theta (Angle)
$\lambda$	:	Lambda (Wavelength)
$\beta$	:	Beta
eV	:	Electron volt
$\epsilon$	:	Epsilon
$\nu$	:	Nu
mL	:	milli Litre
$\mu$ L	:	micro Litre
M	:	Molarity
mM	:	milli Molar
$\mu$ mol	:	micro Mole
t	:	Time
h	:	Hours
min	:	Minutes
°C	:	Degree centigrade
K	:	Kelvin
k	:	Degradation rate constant
$\mu$ m	:	Micro metre
g	:	Grams
mg	:	milli Grams
W	:	Watts
R	:	Reflectance
NHE	:	Normal Hydrogen Electrode
VB	:	Valence Band
CB	:	Conduction Band
Ns	:	Nano Seconds

HOMO	:	Highest Occupied Molecular Orbital
LUMO	:	Lowest Unoccupied Molecular Orbital
$h^+$	:	Hole
$O_2^{\cdot-}$	:	Superoxide anion radical
$\cdot OH$	:	Hydroxyl radical
RT	:	Room Temperature
SEM	:	Scanning Electron Microscopy
FE-SEM	:	Field Emission-Scanning Electron Microscopy
TEM	:	Transmission Electron Microscopy
PL	:	Photoluminescence
TRFL	:	Time Resolved Florescence Lifetime
PXRD	:	Powder X-ray Diffraction
EIS	:	Electrochemical Impedance Spectroscopy
$R_{ct}$	:	Charge Transfer Resistance
XPS	:	X-Ray Photoelectron Spectroscopy
BET	:	Brunauer–Emmett–Teller
EDS	:	Energy Dispersive X-ray Spectroscopy
FT-IR	:	Fourier Transform Infra-Red
UV-Vis DRS	:	Ultra violet-Visible Diffuse Reflectance Spectroscopy
TGA	:	Thermogravimetric Analysis

---

## **THESIS ABSTRACT**

The development of an alternative clean energy resources and pollution free energy harvesting technologies for environmental remediation is in high demand for the sustainable growth of human society. Among the various types of strategies employed for utilizing the renewable energy resources, semiconductor photocatalysis has been emerged as one of the most promising technology owing to its visible light harvesting capability, eco-friendly, cost-effective, and easily availability. Recently, graphitic carbon nitride ( $g\text{-C}_3\text{N}_4$ ) which is a metal-free polymeric semiconducting material a suitable band gap to absorb enhanced radiation in visible light range. Further, its intriguing features such as tunable band gap, high chemical stability against oxidation and thermal stability up to 500 °C on contrary to many other organic semiconductors has made  $g\text{-C}_3\text{N}_4$  as a fascinating material for photocatalytic applications. The high recombination rate of photoinduced electron–hole pairs affect the efficiency of  $g\text{-C}_3\text{N}_4$  nanosheets and consequently limits its practical applications. Therefore, modifications of  $g\text{-C}_3\text{N}_4$  as to make it a valuable material for visible light driven photocatalysis is of great importance. A few efforts have been made to improve the photocatalytic activity of  $g\text{-C}_3\text{N}_4$  by employing different modifications such as loading co-catalyst, designing appropriate textural properties, doping and coupling with a metal or semiconductor material. However, the coupling is a feasible strategy to form a nano/heterojunction by  $g\text{-C}_3\text{N}_4$  nanosheet with a semiconductor to improve its photocatalytic performance. In this context, the present thesis work has been focused on the designing and development of highly efficient  $g\text{-C}_3\text{N}_4$  based hybrid nanocomposite, with visible light absorption, separation efficiency and suppressed recombination of the photoinduced excitons, thereby enhancing their photocatalytic efficiency.

Both bulk and surface properties of these materials are examined and characterized using PXRD, FT-IR, SEM, FE-SEM, EDS, TEM, TGA, UV-vis DRS, PL, TRFL, XPS and BET surface area analysis. Photocatalytic efficacies of the synthesized catalysts are tested for degradation of organic pollutants such as Rhodamine B, Methylene blue and colorless antibiotic pollutant Ciprofloxacin under visible light irradiation. Based on the experimental results, a plausible reaction pathway is proposed. Moreover, the synthesized hetero/nanojunctions possess high photostability and reusability. Hence, these nanostructured semiconductor photocatalysts could be of potential interest for other practical applications such as water splitting and  $\text{CO}_2$  reduction under visible light irradiation.



## Chapter I

### Introduction



# **Chapter I**

## **Introduction**

### **1.1 Background**

Clean and renewable energy production, as well as environmental problems, have emerged as the top issues and challenges for humanity over the last decade as global population growth and economic development continue to accelerate. Thus, the rapid growth of the human population and the intensification of industrial and agricultural activities led to a continuous increase in the demand for earth's limited supply of fresh water. In this context, protection of natural water resources and development of new technologies for water and wastewater treatment became key environmental issues of the 21<sup>st</sup> century.<sup>[1-4]</sup> Breakthrough by Honda and Fujishima in 1970 has opened up a great opportunity for the use of photocatalysis in the fields of sustainable energy utilization and environmental remediation.<sup>[5-7]</sup> In photocatalysis one can use visible light as energy sources and the possibility of introducing another pollutant is also ruled out.

The most important advantages of solar energy are its ecological purity and it offers the possibility of accomplishing energy cycles without pollution of the environment and additional heating of the earth. Hence, photocatalysis is emerging as one of the possible means that can provide viable solutions for the development of pollution free technologies for both environmental remediation and alternative clean energy supply. However, this technology is widely investigated for the water splitting and degradation of organic pollutants in the water/air body under UV light.<sup>[8,9]</sup> In the past decades, tremendous efforts have been made for improving photocatalytic efficiency under visible light irradiation.<sup>[10,11]</sup> Unfortunately, photocatalytic applications under visible light are still limited due to the low efficiency caused by a number of challenging issues such as narrow light-response range, bulk structure and surface structure, the high recombination rate of charge carriers, and poor material stability. Therefore, the development of highly efficient visible light active photocatalyst is today's demand.

### **1.2 State of problem**

The growth in population and industrialization has severe negative impact on the environment and the ecosystem, including organisms and plants. Because of modernization and to live a better lifestyle, we are exhausting non-renewable energy resources and also releasing harmful chemicals into the environment. However, technology is lacking where we may utilize

natural renewable and inexhaustible resources for the sustainable growth and development. In fact the earth is bleeding because of acid rain, CFC's, global warming, polluted drains etc.<sup>[12]</sup> The 21<sup>st</sup> century started with environmental protection as the most important task. Photocatalysis technology can mimic natural photosynthesis as it directly converts solar energy into chemical energy and represent an attractive strategy for renewable energy generation and environmental remediation. Unfortunately, the performance of present photocatalysts does not meet the needs of practical applications. Therefore, the development of a highly effective visible light active photocatalyst for environmental protection is still being sought.

### **1.3 Objectives of the present research work**

The objectives of the present research work are

- To design and develop visible light active nanocomposite photocatalysts by various synthetic strategies.
- To characterize the nanocomposites for structural, chemical and optical properties.
- To study the photocatalytic activity for degradation of organic pollutants Rhodamine B, Methylene Blue, Ciprofloxacin under visible light irradiation.

### **1.4 Scope of the present research work**

The successfully developed novel g-C<sub>3</sub>N<sub>4</sub> based metal oxide nanocomposite photocatalysts can be potentially applied for photocatalytic water splitting for hydrogen fuel, photocatalytic conversion of CO<sub>2</sub> to energy-rich hydrocarbon fuels and photodecomposition of other organic substances for environmental remediation. Furthermore, it would be interesting to work on the perovskite type materials and g-C<sub>3</sub>N<sub>4</sub> based photocatalysts with unique Nano-architectures in order to fulfill the needs of practical applications. Low cost, highly photo-stable, eco-friendly synthetic strategies and the possibility of using visible light as a radiation source for these photocatalysts can result in both economically and environmentally advantageous.

### **1.5 Photocatalysis**

The name “photocatalysis” is a collection of two words, “photo” and “catalysis”. Catalysis is the process by which a substance accelerates the rate of a chemical reaction (oxidation/reduction) without being altered or consumed in the end. This substance is referred to as a catalyst because it increases the rate of a reaction by lowering the activation energy.<sup>[13]</sup> Photocatalysis is a reaction

that uses light to activate a substance known as a photocatalyst in order to change the rate of a chemical reaction without involving the photocatalyst itself.

### 1.5.1 Semiconductor photocatalysis

Semiconductor photocatalysis is a promising technology that offers a simple way to harness solar energy for the advancement of a sustainable society.<sup>[14]</sup> Artificial photosynthesis can be described as photocatalytic degradation of organic pollutants and photocatalytic water splitting. Artificial photosynthesis based on semiconductor nanostructures mimics' natural photosynthesis. (Figure 1.1) demonstrates the similarities and differences between natural and artificial photosynthesis. In natural photosynthesis, plants uses chlorophyll and sunlight to generate glucose (organic matter) and oxygen from carbon dioxide and water.<sup>[15]</sup> While the photocatalyst in artificial photosynthesis generates strong oxidizing agents and electronic holes to break down the organic matter (dye) into carbon dioxide and water under the solar light and it can also decompose water into hydrogen and oxygen.<sup>[16,17]</sup> This has long inspired extensive research in various scientific disciplines to better understand and even imitate biological energy-transfer processes using artificial materials and technologies to achieve water splitting, photocatalytic CO<sub>2</sub> conversion to energy-rich hydrocarbon fuels, and environmental purification by visible light.

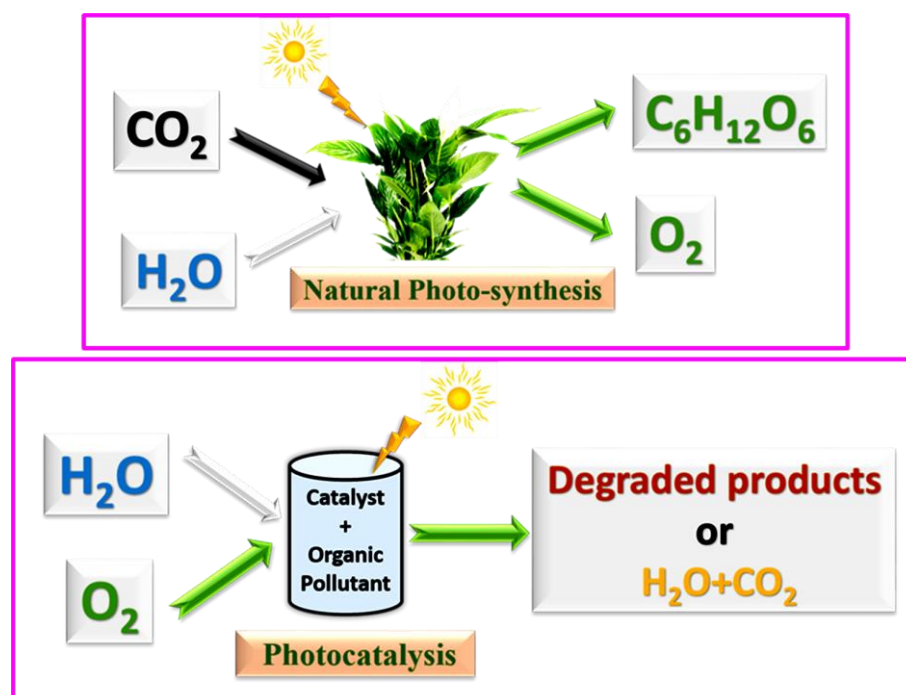


**Figure 1.1:** Schematic illustration for the process of natural photosynthesis and photocatalysis (photodegradation of organic pollutants).

### 1.5.2 Basic principle of the semiconductor photocatalysis

The key role of a semiconductor photocatalyst in a photocatalysis process is to induce or accelerate specific reduction and oxidation (redox) reactions in the presence of light. When the semiconductor photocatalyst is exposed to light ( $h\nu$ ) with equal or higher energy than the band gap, an electron is elevated from the valence band (VB) to the conduction band (CB), leaving a positive hole in the VB and an electron in the CB (Step-1) as depicted in (Figure 1.2). The photo-generated excitons (electrons and holes), once spatially separated, may migrate to the surface of the photocatalyst and eventually to the adsorbed acceptor molecules, thereby initiating the resultant reduction or oxidation process. The semiconductor can donate electrons to acceptors at the surface (Step-2), whereas holes can transfer to donor species at the surface (Step-3). At the same time, a large proportion of the photo-generated excitons recombine by dissipating the input energy as heat or emitted light (Step-4). The remaining part of photo-generated excitons trapped on the surface can recombine with their opposite-charge counterparts (Step-5). Both of these recombination processes (Steps-4 and-5) are disadvantageous to the photocatalytic reaction's efficiency.<sup>[18,19]</sup>

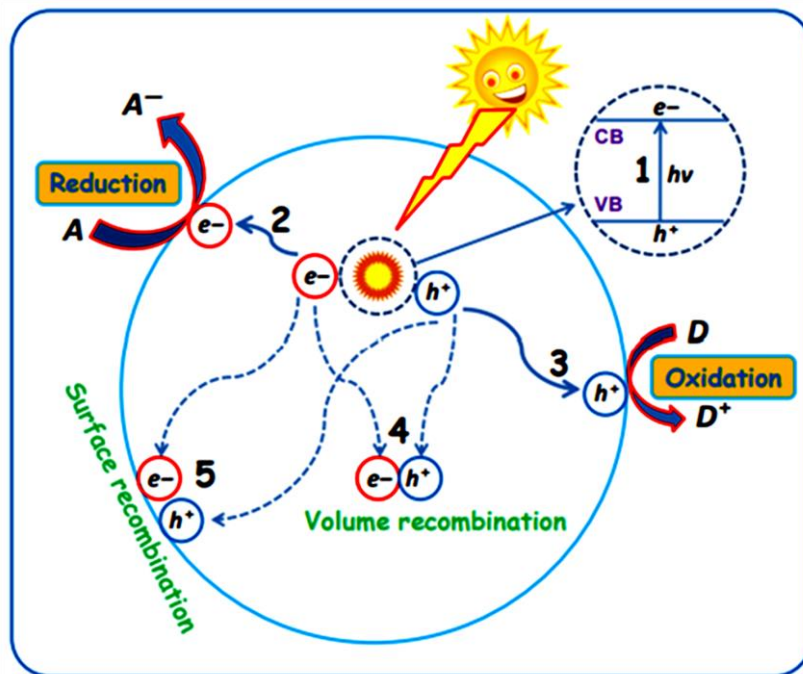
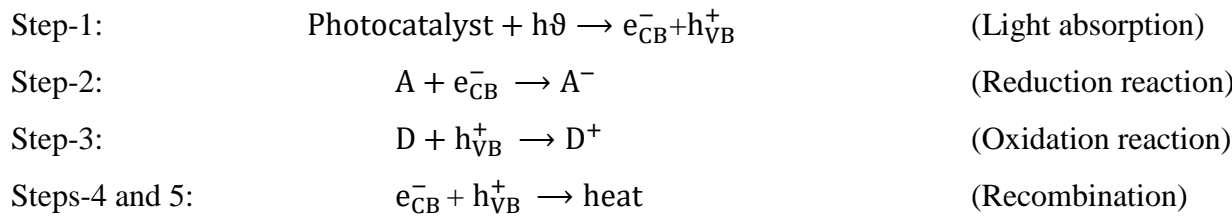


**Figure 1.2:** Schematic illustration of the major processes involved on a semiconductor photocatalyst under light irradiation.

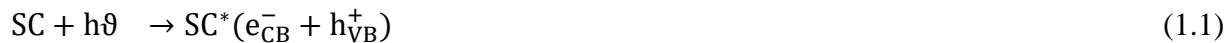
The process described above could be briefly expressed by the following equations



The charge transfer capacity and recombination rate is determined by the adsorbate species band edge position and redox potential.<sup>[20,21]</sup> For an affirmative electron transfer reaction, the edge potential of the electron acceptors should be positioned below the CB of the semiconductor (more positive), while the edge potential of the electron donors should be located above the VB of the semiconductor (more negative). High photocatalytic activity necessitates the efficient separation and rapid transport of photo-generated excitons to their adequate active sites for the desired redox reactions.

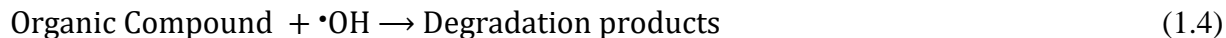
### 1.5.3 Mechanism of the semiconductor photocatalysis

It has been recommended that the superoxide anion radicals ( $O_2^-$ ) and hydroxyl radicals ( $\cdot OH$ ) are the primary reactive species in the photocatalytic pollutants degradation processes.<sup>[22,23]</sup> However, the VB and CB of a semiconductor photocatalyst should be located in such a way that the hydroxyl radicals oxidation potential ( $E^0_{(\text{H}_2\text{O}/\cdot\text{OH})} = +2.8 \text{ eV vs.NHE}$ ) and superoxide radicals reduction potential  $E^0_{(\text{O}_2/\text{O}_2^-)} = -0.3 \text{ eV vs.NHE}$  are well within the band gap for successful photocatalytic degradation. To put it another way, the holes redox potential must be sufficiently positive to produce  $\cdot OH$ , while the electrons must be sufficiently negative to produce  $O_2^-$ . For photocatalytic environmental remediation, valence band hole ( $h_{\text{VB}}^+$ ) are the important elements that involve the oxidative decomposition of environmental pollutants. These valence band hole ( $h_{\text{VB}}^+$ ) can oxidize pollutants directly and also will react with adsorbed water ( $H_2O$ ) or adsorbed hydroxyl groups ( $\cdot OH$ ) on semiconductor photocatalysts (SC). The formation of the  $\cdot OH$  radical can occur in two ways. As depicted in Equation (1.2) and (1.3).

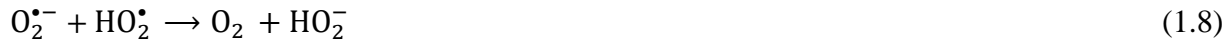




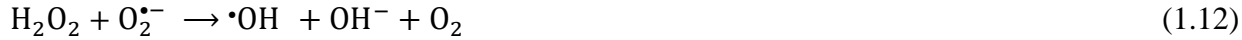
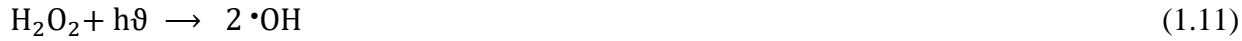
The formed  $\cdot\text{OH}$  rapidly attacks pollutants at the surface and in solution as well and can convert them into degraded products (carbon dioxide and water).



Since oxygen is the primary electron acceptor in these experiments, it is commonly believed that it plays an important role in photocatalysis. As shown in Equation. (1.5), Oxygen can trap conduction band electrons to form  $\text{O}_2^{\bullet-}$ , these superoxide ions can react with hydrogen ions forming  $\text{HO}_2^{\bullet}$ .



According to the equation below,  $\text{H}_2\text{O}_2$  can be generated from  $\text{HO}_2^{\bullet}$  species. The photogenerated hydrogen peroxide decomposes further to produce hydroxyl radicals.



The majority of reactive hydroxyl radicals are formed by photo-generated hole reactions. On the other hand, they could not be produced without the presence of water molecules, preventing the photodegradation of liquid phase organics. A few studies have shown that the photocatalytic reaction cannot take place without the presence of water molecules.<sup>[24]</sup> The reducing conduction band (CB) electrons are more significant when using a photocatalytic reaction to produce hydrogen from water splitting. In order to initiate hydrogen production, the conduction band level must be more negative than the hydrogen production level:



The redox potential for overall reaction at  $\text{pH} = 7$  is  $E_H = -1.23$  V (NHE), with the corresponding half-reactions of  $-0.41$  V (Eq. 1.16) and  $0.82$  V, which gives a  $\Delta G^\circ = +237$  kJ/mole.

#### 1.5.4 Photocatalysts and selection

The photocatalytic properties of semiconductors are strongly influenced by their electronic band structure. The semiconductors band edge position is one of the most important and useful parameters to consider while using it as a photocatalyst.<sup>[25]</sup> The ability of a semiconductor to undergo photogenerated excitons transfer to adsorbed species on its surface is governed by the band energy positions of the semiconductor and the redox potentials of the adsorbed species.<sup>[26]</sup> Since the first report of employing photocatalyst for decomposing cyanide.<sup>[27]</sup> The applications in environmental purification have been rapidly developed, and we may find various products and technologies around us to purify the environment by using photocatalysts. On the other hand, a large number of semiconductor materials, such as  $\text{TiO}_2$ ,  $\text{Fe}_2\text{O}_3$ ,  $\text{ZnO}$ ,  $\text{WO}_3$ ,  $\text{SrMoO}_4$ ,  $\text{CdMoO}_4$ ,  $\text{MoS}_2$ ,  $\text{CdS}$ ,  $\text{Ag}_3\text{PO}_4$ ,  $\text{BaBiO}_3$ , etc., are known to catalyze the photochemical reaction.<sup>[28–30]</sup> Generally, low bandgap materials have a more viable light harvesting capacity compared to more band gap materials. However, the practical utilization of a photocatalyst for water splitting to produce  $\text{H}_2$  fuel and degradation of organic pollutants to protect the environment is still a huge challenge due to its low efficiency. The photocatalytic material selection should be based on the characteristics shown in (Figure 1.3). An ideal photocatalyst should possess the following characteristics as shown in (Figure 1.4): (i) photoactive; (ii) have the ability to utilize visible and/or near-UV light; (iii) photostable (not prone to photo-anodic corrosion); (iv) biologically and chemically inert; (v) non-toxic and (vi) inexpensive.<sup>[7,31]</sup>

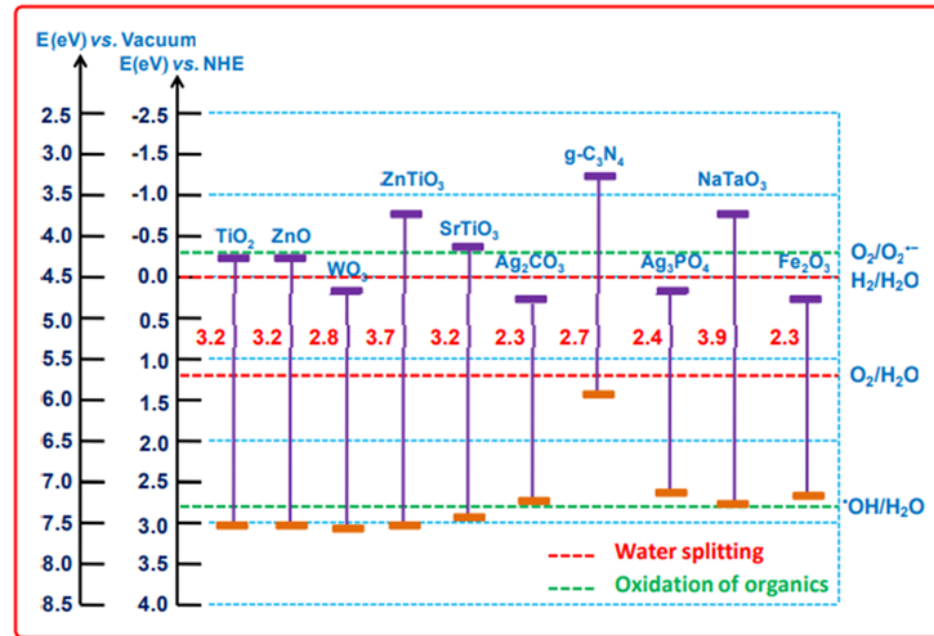


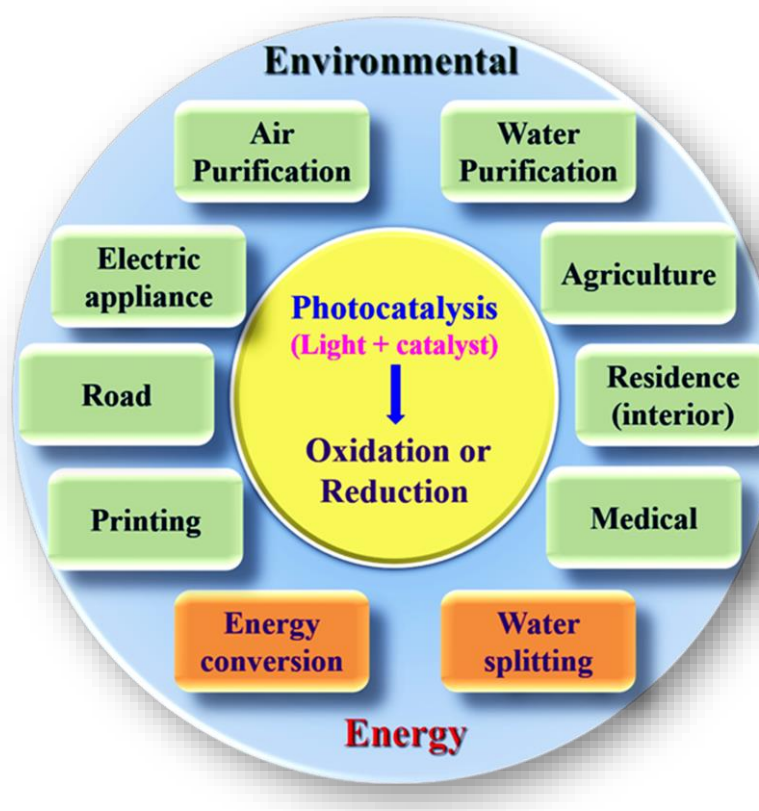
Figure 1.3: Band gap energy and band edge positions of different semiconductor materials.



Figure 1.4: Characteristics of an ideal photocatalyst.

### 1.5.5 Applications of photocatalysis

Both the technological and economical importance of photocatalysis has increased considerably over the past decade. However, there is a great challenge to use visible light as a source of energy in photoreaction to solve the environmental problem and energy crisis in the future. In the recent investigation, photocatalytic processes have been widely used in various applications as depicted in (Figure 1.5) such as disinfection of drinking water, antibacterial for textile industries, antimicrobe for plastic container, persistent toxic compounds treatment, organic degradation, self-cleaning, soil purifications, deodorization, sterilization, air purification, high efficiency/low cost solar cells, and even clean renewable hydrogen energy production from water splitting.<sup>[32-40]</sup>



*Figure 1.5: Potential applications of semiconductor photocatalysis.*

### 1.5.6 Why visible light active photocatalysis?

Visible light active photocatalysts are critical for efficient solar energy conversion because visible light accounts for approximately 45% of total solar energy, while UV light accounts for only 4% and the remaining part is IR light approximately 50%.<sup>[41,42]</sup> It means that the visible light

active photocatalysis is of great opportunity to utilize maximum compartment in the solar energy spectrum as shown in (Figure 1.6). To utilize solar energy efficiently, research for developing the high-performance visible light photocatalysts have never stopped, which can be clearly reflected from the increasing numbers of research papers and patents relating to photocatalysis.

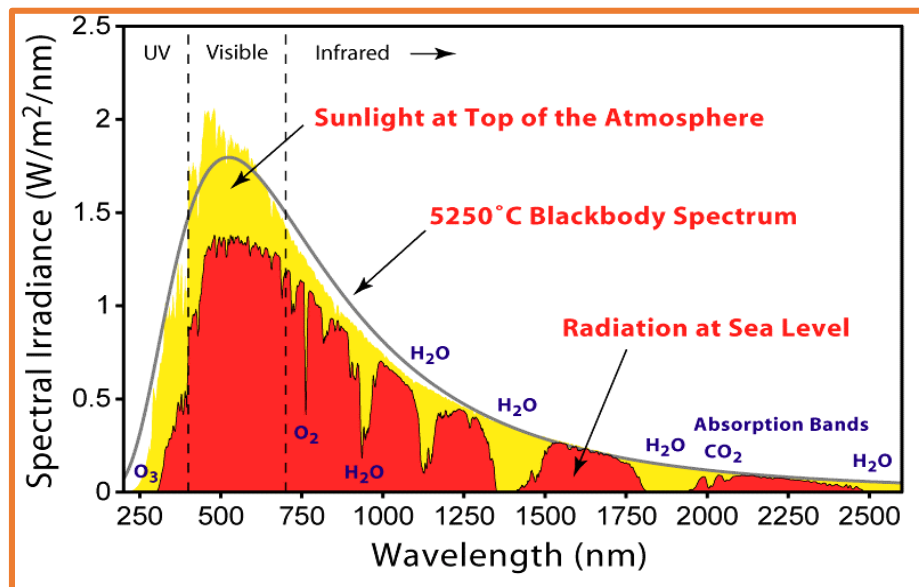


**Figure 1.6:** The wavelength distribution of solar light.

### 1.5.7 Strategies to develop an efficient visible-active photocatalyst

Various semiconductor photocatalysts, such as  $\text{TiO}_2$ ,  $\text{SnO}_2$ ,  $\text{ZnO}$ , and  $\text{ZnS}$ , have been studied and used in environmental applications over the last few decades.<sup>[43–45]</sup> Despite their high photocatalytic activity and good chemical stability, the practical applications of semiconductor catalysts are limited because of low absorption coefficient and mismatch with the solar spectrum. As a result, the current research in the field of photocatalysis primarily focuses on the search for active photocatalytic materials with band gap corresponding to the visible light energy. Recently, significant efforts have also been made to modify semiconductor photocatalysts that are capable of using visible light, including metal ion doping, non-metal doping, creating oxygen vacancies, dye sensitization and coupling with metal or another semiconductor.<sup>[46–50]</sup>

#### 1.5.7.1 Metal ion doping

Metal ion doping has been mainly studied to improve the photocatalytic performance under irradiation of UV light. Nowadays, visible light active photocatalysis using metal ion-doped semiconductors has been a topic of prime concern for many researchers. Subsequently, these have

revealed the extended absorption spectra into the visible light area. This property has been described by the electrons transfer from dopant ion to the semiconductor conduction band is called as metal to conduction band charge-migration. Various metal ions, including rare earth metal ions (such as Yb, La and Ce) and transition metal ions (such as V, Cr, Fe, Ni, Co, Pt, and Ru) have been explored as possible dopants for visible light photocatalysis. Depending on the dopant,<sup>[51,52]</sup> two different situations can be reached, as schematically represented in (Figure 1.7) (1) a p-type doping, by the introduction of cations which act as electron acceptor, (2) n-type doping, by incorporating electron donors.<sup>[53]</sup>

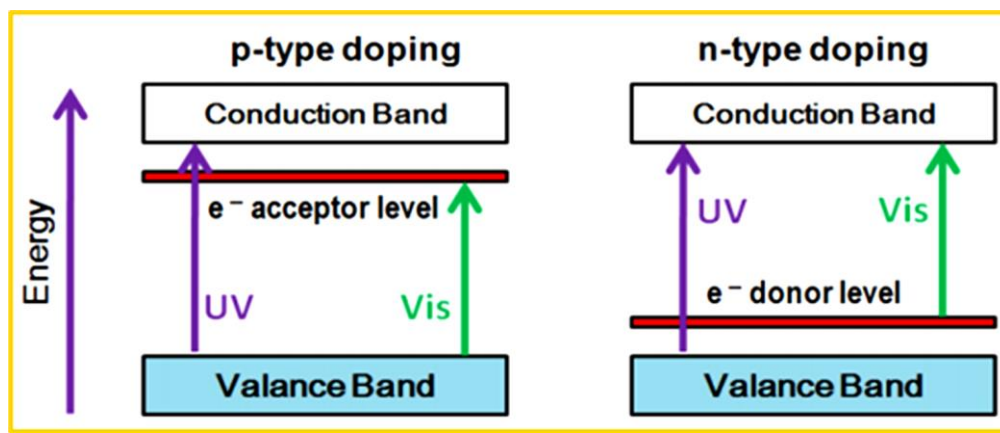


**Figure 1.7:** Schematic representation of the energy levels of doped semiconductors: p-type doping and n-type doping.

### 1.5.7.2 Non-metal doping

Non-metal doping is a versatile and effective strategy for band gap engineering of transition metal oxide semiconductors for materials design, light harvesting and doping stability. Doping with non-metallic elements such as C, N, F, P, and S have been studied extensively since the first report on N-doped TiO<sub>2</sub> in 2001.<sup>[54]</sup> It was initially proposed that nitrogen-doped titania is able to change its light response into the visible area by collaborating 2p orbitals of lattice O with 2p orbitals of N and increases the photocatalytic performance by the reducing bandgap of the TiO<sub>2</sub>. Among all non-metals, nitrogen has been the most widely investigated dopant for photocatalytic applications of TiO<sub>2</sub>. Still, current revisions have revealed both practically and theoretically, the localized nitrogen 2p orbitals above the VB and the excitations from N 2p orbital to the CB are made in TiO<sub>2</sub> under visible light irradiation.<sup>[55,56]</sup> Unlike metal and non-metal ion dopants, they exchange lattice oxygen and are less likely to form recombination centers.

### 1.5.7.3 Co-doping

In most cases, the metal-doped photocatalysts also do not reach the expected results. In recent times, the development of co-doping has also been widely reported. Few reports have revealed that N and F co-doping is beneficial for low energy cost and a decrease of defect formation for the incorporation of N due to the donor (F) and acceptor (N) charge compensation effect.<sup>[57,58]</sup> Ta-doped TiO<sub>2</sub> with co-doped nitrogen effectively changes the photo-absorption capability.<sup>[59]</sup> Although the successful results with the co-doping approach depend on the position, amount, and choice of the elements used, and thus, a large amount of experimental and theoretical research is underway.

### 1.5.7.4 Dye sensitization

Apart from structural modifications such as metal doping and co-doping, there is a possibility of modifying the photocatalyst surface with another substance that absorbs light energy and transfers to the photocatalyst. This substance is referred to as “photosensitizer”. Sensitization has been studied by several groups and to be one of the most effective ways to extend the photoresponse of wide bandgap semiconductors into the visible region.<sup>[60,61]</sup> Surface Dye sensitization has been studied in many areas, such as dye-sensitized solar cells and photovoltaic devices. However, to a lesser extent, sensitized visible light active photocatalytic degradation of pollutants and water splitting has been reported. The principle involved in the dye sensitized photocatalytic degradation of organic pollutants is based on the absorption of visible light for exciting an electron from the highest occupied molecular orbital (HOMO) to the lowest unoccupied molecular orbital (LUMO) of a dye.<sup>[62]</sup> The excited dye molecule subsequently transfers electrons into the conduction band of the semiconductor and these injected electrons reach quickly to the surface where O<sub>2</sub> to form superoxide radical O<sub>2</sub><sup>•-</sup> and 'OOH. These reactive species can also disproportionate to give 'OH. The subsequent radicals chain reactions can lead to the degradation of the dye.

### 1.5.7.5 Metal/semiconductor heterostructure

Another effective method for reducing the recombination rate of photo-generated excitons and hence increasing their lifetime is to make metal/semiconductor nanocomposites. Superficial deposition of noble metals (Ag, Au, and Pt) improves the photocatalytic performance under visible light irradiation. The advantages of metal in metal/semiconductor promotes the charge migration,

act as an electron trapping agent and then reducing electron-hole pair recombination effect.<sup>[63–65]</sup> The metallic elements in the metal/semiconductor photocatalyst could also improve the light absorption capacity of semiconductors through a plasmonic enhancement effect.

#### 1.5.7.6 Semiconductor/semiconductor nanocomposites

In relation to single-component photocatalysts, which generally have less flexibility in altering their electronic property by doping and low efficiency of photoinduced charge transporters. The integration of two different types of semiconductors to make a heterojunction nanocomposite is an effective strategy to promote exciton separation and minimize exciton recombination for enhanced photocatalytic activity.<sup>[66,67]</sup> Choosing the two photocatalysts of the composite system just by the relative band positions for composite photocatalysts may not assure the enhanced photocatalytic performances, the other factors like development of intimate solid-solid interface, morphologies of individual catalysts, synthesis methods, etc. will be taken into consideration for the fabrication of efficient composite photocatalyst systems.

According to the valence and conduction band edge potentials of the two semiconductors, the heterojunction nanocomposites can be classified into three types: straddling gap (Type-I), staggered gap (Type-II) and broken gap (Type-III), as depicted in (Figure 1.8). Especially, the type-II (staggered gap) heterojunction nanocomposite has the excellence of developing a constructive interface combination and the spatially isolated charge carrier on other sides of the hetero/nano junction in which holes can be regulated to one side and electrons to another side.<sup>[68]</sup> The spatially separated excitons in the type-II hetero/nanostructures could make them a more suitable candidate for enhanced photocatalytic degradation of organic pollutants and water splitting too. These semiconductor/semiconductor nanocomposites can also overcome the drawbacks of the individual components and induce a synergistic effect which further improves the photostability and charge separation.

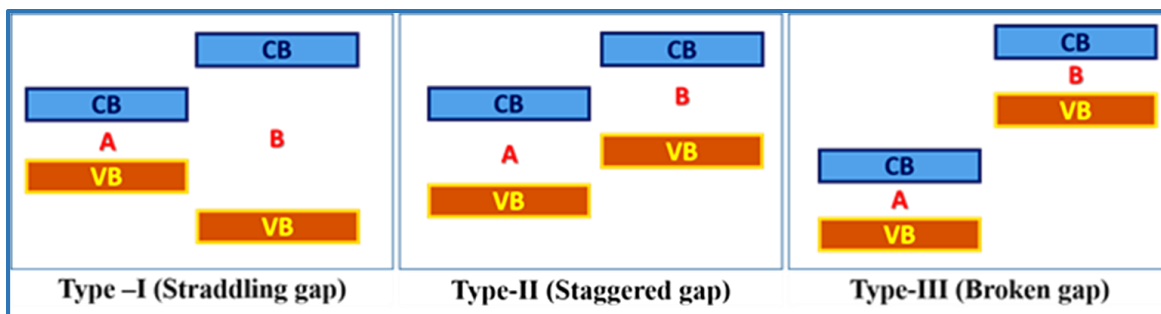


*Figure 1.8: Different types of semiconductor heterojunctions.*

## 1.6 Photocatalysis at ‘Nanoscale’

It is well understood that catalytic behavior is not only material-dependent, but also size-dependent because quantum confinement and surface phenomena based on particle size dominate material properties at the nanoscale.<sup>[69,70]</sup> The smaller a semiconductor particle becomes, more the number of atoms located at the surface and the surface area to volume ratio increases. This may enhance the available surface active sites and interfacial charge-carrier transfer rates, thus leading to the higher catalytic activities.<sup>[71,72]</sup> Therefore, nanoscale research allows scientists to alter and enhance the physical and chemical properties of a material by controlling electronic energy levels via quantum size and surface effects. Because of their distinct structural, optical, and chemical properties when compared to their bulk counterparts, nanostructured materials have emerged as novel photocatalysts for solar energy harvesting in recent years.<sup>[73,74]</sup> The well-known diverse nanostructures such as nanoparticles, porous nanospheres, nanotubes, nanorods, nanowires, nanosheets, nanoplates and other more complex structures have been demonstrated to show extraordinary unconventional properties, which can greatly enrich the material selection and open a new degree of freedom for the design of effective photocatalytic systems.<sup>[75–80]</sup> The availability of a diverse range of nanostructures can enable the flexible integration of multiple functional components to create heterogeneous structures with distinct properties or unprecedented performance. As a result, next-generation semiconductor nanoarchitectures with highly efficient and stable visible light responsive photocatalysts are still being developed for clean energy production and environmental remediation.

## 1.7 References

- [1] M. Balat, *Energy Exploration & Exploitation* **2005**, *23*, 141–167.
- [2] A. Chel, G. Kaushik, *Alexandria Engineering Journal* **2018**, *57*, 655–669.
- [3] S. Garrido, T. Sequeira, M. Santos, *Applied Sciences* **2020**, *10*, 5755.
- [4] M. Motoshita, S. Pfister, M. Finkbeiner, *Environmental Science & Technology* **2020**, *54*, 9083–9094.
- [5] A. FUJISHIMA, K. HONDA, *Nature* **1972**, *238*, 37–38.
- [6] A. Fujishima, T. N. Rao, D. A. Tryk, *Journal of Photochemistry and Photobiology C: Photochemistry Reviews* **2000**, *1*, 1–21.
- [7] A. Mills, S. Le Hunte, *Journal of Photochemistry and Photobiology A: Chemistry* **1997**,

108, 1–35.

[8] J. Zhao, X. Yang, *Building and Environment* **2003**, *38*, 645–654.

[9] S. Rehman, R. Ullah, A. M. Butt, N. D. Gohar, *Journal of Hazardous Materials* **2009**, *170*, 560–569.

[10] D. Bahnemann, *Solar Energy* **2004**, *77*, 445–459.

[11] R. M. Mohamed, D. L. McKinney, W. M. Sigmund, *Materials Science and Engineering: R: Reports* **2012**, *73*, 1–13.

[12] M. Nissan, *Population and Environment* **1996**, *17*, 459–489.

[13] X. Yang, D. Wang, *ACS Applied Energy Materials* **2018**, *1*, 6657–6693.

[14] N. Serpone, A. V. Emeline, *The Journal of Physical Chemistry Letters* **2012**, *3*, 673–677.

[15] J. A. Bassham, *Journal of Chemical Education* **1959**, *36*, 548.

[16] A. Gandamalla, S. Manchala, P. Anand, Y.-P. Fu, V. Shanker, *Materials Today Chemistry* **2021**, *19*, 100392.

[17] S. Manchala, A. Gandamalla, N. R. Vempuluru, S. Muthukonda Venkatakrishnan, V. Shanker, *Journal of Colloid and Interface Science* **2021**, *583*, 255–266.

[18] S. Zhu, D. Wang, *Advanced Energy Materials* **2017**, *7*, 1700841.

[19] H. Hennig, *Angewandte Chemie International Edition* **2015**, *54*, 4429–4429.

[20] P. V Kamat, *The Journal of Physical Chemistry Letters* **2012**, *3*, 663–672.

[21] E. Maggio, N. Martsinovich, A. Troisi, *The Journal of Chemical Physics* **2012**, *137*, 22A508.

[22] F. Parrino, S. Livraghi, E. Giamello, R. Ceccato, L. Palmisano, *ACS Catalysis* **2020**, *10*, 7922–7931.

[23] Y. Nosaka, A. Y. Nosaka, *Chemical Reviews* **2017**, *117*, 11302–11336.

[24] M. Pawar, S. Topcu Sendoğdular, P. Gouma, *Journal of Nanomaterials* **2018**, *2018*, 1–13.

[25] H. Yan, X. Wang, M. Yao, X. Yao, *Progress in Natural Science: Materials International* **2013**, *23*, 402–407.

[26] M. C. Toroker, D. K. Kanan, N. Alidoust, L. Y. Isseroff, P. Liao, E. A. Carter, *Physical Chemistry Chemical Physics* **2011**, *13*, 16644.

[27] S. N. Frank, A. J. Bard, *Journal of the American Chemical Society* **1977**, *99*, 303–304.

[28] W.-K. Jo, S. Kumar, S. Eslava, S. Tonda, *Applied Catalysis B: Environmental* **2018**, *239*, 586–598.

[29] S. Tonda, S. Kumar, V. Shanker, *Journal of Environmental Chemical Engineering* **2015**, *3*, 852–861.

[30] O. M. Ishchenko, V. Rogé, G. Lamblin, D. Lenoble, *Semiconductor Photocatalysis - Materials, Mechanisms and Applications* **2016**, *3*–30.

[31] H. Kisch, D. Bahnemann, *The Journal of Physical Chemistry Letters* **2015**, *6*, 1907–1910.

[32] Y. K. Mishra, G. Modi, V. Cretu, V. Postica, O. Lupan, T. Reimer, I. Paulowicz, V. Hrkac, W. Benecke, L. Kienle, R. Adelung, *ACS Applied Materials & Interfaces* **2015**, *7*, 14303–14316.

[33] Z. Zhou, Y. Zhang, Y. Shen, S. Liu, Y. Zhang, *Chemical Society Reviews* **2018**, *47*, 2298–2321.

[34] J. M. Coronado, F. Fresno, M. D. Hernández-Alonso, R. Portela, *Design of Advanced Photocatalytic Materials for Energy and Environmental Applications*, Springer London, London, **2013**.

[35] A. Ibadon, P. Fitzpatrick, *Catalysts* **2013**, *3*, 189–218.

[36] J. Gamage, Z. Zhang, *International Journal of Photoenergy* **2010**, *2010*, 1–11.

[37] S. Lacombe, N. Keller, *Environmental Science and Pollution Research* **2012**, *19*, 3651–3654.

[38] S. Chaturvedi, P. N. Dave, *Materials Science Forum* **2012**, *734*, 273–294.

[39] J. Liu, H. Wang, M. Antonietti, *Chemical Society Reviews* **2016**, *45*, 2308–2326.

[40] R. Wang, K.-Q. Lu, Z.-R. Tang, Y.-J. Xu, *Journal of Materials Chemistry A* **2017**, *5*, 3717–3734.

[41] S. T. Henderson, D. Hodgkiss, *British Journal of Applied Physics* **1964**, *15*, 947–952.

[42] C. Stanley, A. Mojiri, G. Rosengarten, *Nanophotonics* **2016**, *5*, 161–179.

[43] K. Hashimoto, H. Irie, A. Fujishima, *Japanese Journal of Applied Physics* **2005**, *44*, 8269–8285.

[44] Y. Li, Q. Yang, Z. Wang, G. Wang, B. Zhang, Q. Zhang, D. Yang, *Inorganic Chemistry Frontiers* **2018**, *5*, 3005–3014.

[45] X. Chen, Z. Wu, D. Liu, Z. Gao, *Nanoscale Research Letters* **2017**, *12*, 143.

[46] H. R. Rajabi, M. Farsi, *Journal of Molecular Catalysis A: Chemical* **2015**, *399*, 53–61.

[47] L. Zhou, H. Zhang, H. Sun, S. Liu, M. O. Tade, S. Wang, W. Jin, *Catalysis Science & Technology* **2016**, *6*, 7002–7023.

[48] P. Wang, J. Wang, T. Ming, X. Wang, H. Yu, J. Yu, Y. Wang, M. Lei, *ACS Applied Materials and Interfaces* **2013**, *5*, 2924–2929.

[49] S. G. Kumar, L. G. Devi, *The Journal of Physical Chemistry A* **2011**, *115*, 13211–13241.

[50] B. Shao, Z. Liu, G. Zeng, Z. Wu, Y. Liu, M. Cheng, M. Chen, Y. Liu, W. Zhang, H. Feng, *ACS Sustainable Chemistry & Engineering* **2018**, *6*, 16424–16436.

[51] J. Choi, H. Park, M. R. Hoffmann, *The Journal of Physical Chemistry C* **2010**, *114*, 783–792.

[52] E. Finazzi, C. Di Valentin, G. Pacchioni, *The Journal of Physical Chemistry C* **2009**, *113*, 220–228.

[53] Y. Gao, X. Liu, W. Hu, J. Yang, *Physical Chemistry Chemical Physics* **2020**, *22*, 12973–12979.

[54] R. Asahi, *Science* **2001**, *293*, 269–271.

[55] M. Batzill, E. H. Morales, U. Diebold, *Physical Review Letters* **2006**, *96*, 026103.

[56] S. Livraghi, M. C. Paganini, E. Giamello, A. Selloni, C. Di Valentin, G. Pacchioni, *Journal of the American Chemical Society* **2006**, *128*, 15666–15671.

[57] M. Li, J. Zhang, W. Dang, S. K. Cushing, D. Guo, N. Wu, P. Yin, *Physical Chemistry Chemical Physics* **2013**, *15*, 16220.

[58] M. Jia, Z. Yang, H. Xu, P. Song, W. Xiong, J. Cao, Y. Zhang, Y. Xiang, J. Hu, C. Zhou, Y. Yang, W. Wang, *Chemical Engineering Journal* **2020**, *388*, 124388.

[59] Y. F. Zhao, C. Li, J. Y. Hu, Y. Y. Gong, L. Y. Niu, X. J. Liu, *Physics Letters A* **2016**, *380*, 910–916.

[60] M. Grätzel, *Journal of Photochemistry and Photobiology C: Photochemistry Reviews* **2003**, *4*, 145–153.

[61] P. Chowdhury, J. Moreira, H. Gomaa, A. K. Ray, *Industrial & Engineering Chemistry Research* **2012**, *51*, 4523–4532.

[62] D. Chatterjee, S. Dasgupta, *Journal of Photochemistry and Photobiology C: Photochemistry Reviews* **2005**, *6*, 186–205.

[63] T. S. Atabaev, *Frontiers of Materials Science* **2018**, *12*, 207–213.

[64] L. Wang, Z. Liu, J. Han, R. Li, M. Huang, *Nanoscale Research Letters* **2019**, *14*, 148.

[65] M. An, L. Li, Y. Cao, F. Ma, D. Liu, F. Gu, *Molecular Catalysis* **2019**, *475*, 110482.

[66] L. Zhang, M. Jaroniec, *Applied Surface Science* **2018**, *430*, 2–17.

[67] S.-M. Lam, J.-C. Sin, A. R. Mohamed, *Materials Science in Semiconductor Processing* **2016**, *47*, 62–84.

[68] Y. Wang, Q. Wang, X. Zhan, F. Wang, M. Safdar, J. He, *Nanoscale* **2013**, *5*, 8326–8339.

[69] T. Edvinsson, *Royal Society Open Science* **2018**, *5*, 180387.

[70] C. Q. Sun, *ChemInform* **2006**, *37*, 1–120.

[71] M. Kumar Sahu, *International Journal of Applied Engineering Research* **2019**, *14*, 491–494.

[72] S. Suresh, *Nanoscience and Nanotechnology* **2013**, *3*, 62–74.

[73] T. Tatarchuk, M. Bououdina, W. Macyk, O. Shyichuk, N. Paliychuk, I. Yaremiy, B. Al-Najar, M. Pacia, *Nanoscale Research Letters* **2017**, *12*, 141.

[74] M. M. Hasan Farooqi, R. K. Srivastava, *Journal of Alloys and Compounds* **2017**, *691*, 275–286.

[75] Z. Liu, D. Qin, J. Zhao, Q. Feng, Z. Li, H. Bai, D. D. Sun, *Polymers* **2019**, *11*, 974.

[76] H. Bai, Z. Liu, D. D. Sun, S. H. Chan, *Energy* **2014**, *76*, 607–613.

[77] Y. Aoyama, Y. Oaki, R. Ise, H. Imai, *CrystEngComm* **2012**, *14*, 1405–1411.

[78] K. Nakata, B. Liu, Y. Ishikawa, M. Sakai, H. Saito, T. Ochiai, H. Sakai, T. Murakami, M. Abe, K. Takagi, A. Fujishima, *Chemistry Letters* **2011**, *40*, 1107–1109.

[79] J. Sarkar, G. G. Khan, A. Basumallick, *Bulletin of Materials Science* **2007**, *30*, 271–290.

[80] M. B. Gawande, A. Goswami, T. Asefa, H. Guo, A. V. Biradar, D.-L. Peng, R. Zboril, R. S. Varma, *Chemical Society Reviews* **2015**, *44*, 7540–7590.



## Chapter II

# Materials and analytical techniques



## Chapter II

### Materials and analytical techniques

#### 2.1 Synthesis of nanomaterials

There are two methods usually followed for the synthesis of nanomaterials: “top-down” and “bottom-up”. Both approaches have been developed with a focus on control over the particle size, size distribution, morphology, and homogeneity. As the name suggests, “top-down” is essentially the breaking of the system till the nano size is reached (e.g. ball milling and liquid exfoliation). While “bottom-up” means we understand building up from the atomic or molecular precursor to form clusters and subsequently nanoparticles. However, nanomaterials synthesis has been a challenging job for material scientists who have developed several new methods for obtaining mono-dispersed nanoparticles. The technique used for the preparation of nanomaterials depends on the interested material and size of the material. The great demand for fine particles of semiconductor materials has stimulated a lot of activity towards their synthesis by soft chemical techniques. There are some well-known soft chemical techniques, which are used for the synthesis of semiconductor nanomaterials as shown in (Figure 2.1). Among them, sol-gel, microwave, polymeric-precursor, hydrothermal, solvothermal, ion-exchange, solid-state chemical and sonochemical approaches are some of the frequently used methods.<sup>[1-4]</sup>

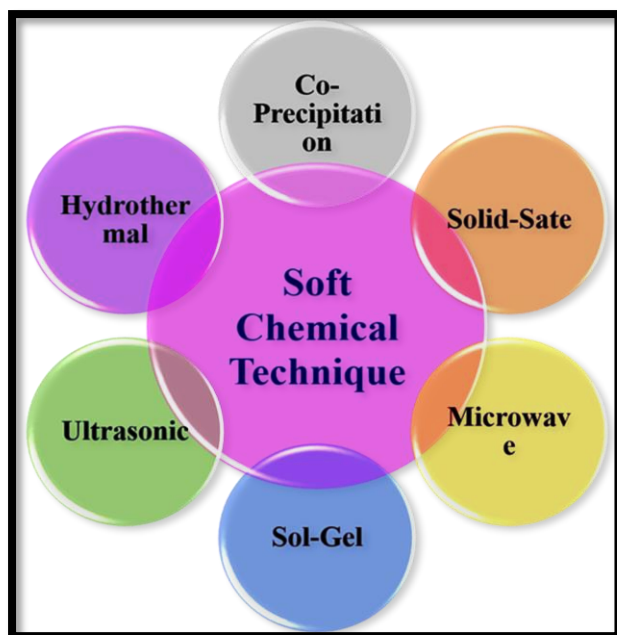


**Figure 2.1:** Synthesis methods of semiconductor photocatalysis.

Several things have to be appraised for the utility of a particular synthetic methodology: (i) the homogeneity of product phase, (ii) the range of applicability for different class of materials, (iii) the control over the average particle size and range of sizes obtainable, and (iv) the reproducibility of average size and shape of particles. The main principle for the synthesis of nanomaterials is to generate a large number of nuclei and to control the growth and aggregation of grains.

For a facile and effective control of crystalline phase and particle size, *in-situ* precipitation and hydrothermal strategies, which favor the formation of nanoparticles, were used in this research. Comparing with sol-gel, solid-state and other methods, the elimination of subsequent steps greatly simplifies the hydrothermal synthesis method.<sup>[5]</sup> Moreover, for the synthesis of pristine g-C<sub>3</sub>N<sub>4</sub> we followed well known thermal condensation method and for the synthesis of SrMoO<sub>4</sub>, a simple modified hydrothermal method was followed, and for the SrMoO<sub>4</sub>/g-C<sub>3</sub>N<sub>4</sub> composite photocatalysts, a simple mixing and heating methodology was followed. The ZnAl-LDH was synthesized by a simple hydrothermal method, and a facile, cost-effective, and simple one-step microwave irradiation method was employed for the synthesis of ZnAl-LDH/g-C<sub>3</sub>N<sub>4</sub> composites. In addition, a one-step simple hydrothermal method was used for the synthesis of pristine Ce(MoO<sub>4</sub>)<sub>2</sub> and Ce(MoO<sub>4</sub>)<sub>2</sub>/g-C<sub>3</sub>N<sub>4</sub> composites. The pristine CdMoO<sub>4</sub> was synthesized by a simple hydrothermal method, and for the fabrication of CdMoO<sub>4</sub>/g-C<sub>3</sub>N<sub>4</sub> composite photocatalysts, a facile *in-situ* hydrothermal method was adopted. The detailed synthesis procedures are discussed in the following chapters.

## **2.2 Techniques for characterization of nanomaterials**

The morphology, structure, chemical composition and surface area of the synthesized materials and their composites are determined by different characterization techniques, which are described hereafter. The detailed explanation and interpretation of the results obtained by different characterization techniques are discussed in the respective chapters.

### **2.2.1 Powder X-ray diffraction (PXRD)**

PXRD technique is one of the most versatile techniques used to determine the crystal structure of the materials. It is also employed to know the qualitative and quantitative analysis of solid phases and provides information on the crystallite size of specific components. Besides, to know the lattice constants and presence of foreign atoms in the crystal lattice of an active

component of the catalyst. The PXRD spectrum is obtained by the interaction of a high energy X-ray beam with the crystalline materials as depicted in (Figure 2.2), which satisfies the Braggs law. Braggs Law is expressed by as following (equation 2.1).<sup>[6]</sup>

$$n\lambda = 2ds\sin\theta \quad (2.1)$$

Where  $n$  = order of reflection

$\lambda$  = Wavelength of incident x-rays

$d$  = Distance between planes

$\theta$  = Incident angle

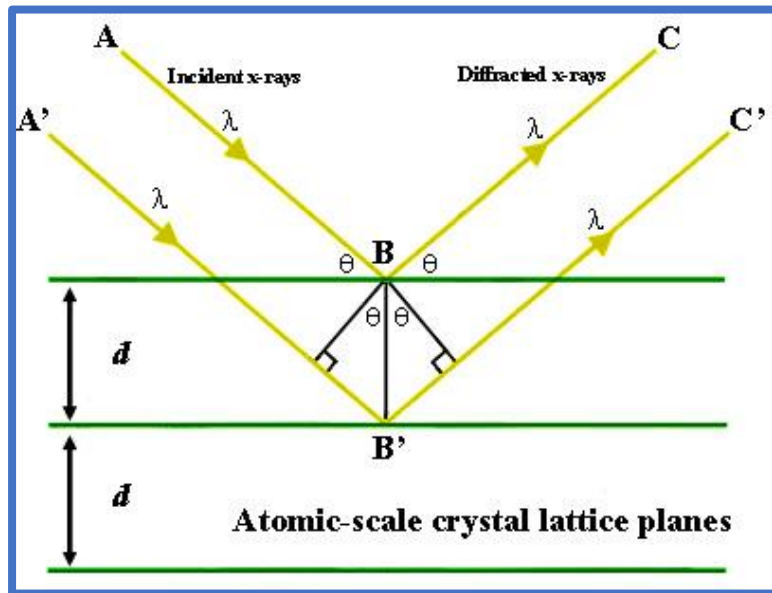


**Figure 2.2: Bragg's Law for X-ray diffraction.**

The universal database is also known as the Joint Committee on Powder Diffraction Standards (JCPDS), is used to identify the crystal structures of the materials.<sup>[7]</sup> The JCPDS is a collection of standard PXRD patterns, which corresponds to the inter-planar distances of specific crystallographic properties of the materials. In the present study, the powder X-ray diffraction patterns of synthesized materials were recorded by the PXRD instruments, PANalytical Advance, and Rigaku X-ray diffractometer. Corresponding data was collected in the scanning range of  $2\theta = 10^\circ$  to  $80^\circ$  by using  $\text{Cu-}\kappa\alpha$  radiation of ( $\lambda=1.54 \text{ \AA}^\circ$ ). The grain size can be determined from the broadening of the diffracted beam using the Scherer's formula (equation 2.2).<sup>[8]</sup>

$$t = \frac{0.9\lambda}{B\cos\theta} \quad (2.2)$$

Where t = Diameter of the grain

$\lambda$  = Wavelength of x-rays

$\theta$  = Diffraction angle

B = Full width half maximum (FWHM) of the diffraction peak.

The B is measured from the broaden peak at FWHM and obtained from Warren's formula (equation 2.3):

$$B^2 = B_M^2 - B_S^2 \quad (2.3)$$

Where,  $B_M$  = FWHM of the sample.

$B_S$  = FWHM of a standard sample of grain size of around 2  $\mu\text{m}$ .

### 2.2.2 Fourier transform infrared spectroscopy (FT-IR)

The infrared area of the electromagnetic spectrum includes radiation with wavelengths ranging from 1-1000 microns. This range is allocated to 3 regions; Far IR (200 - 10  $\text{cm}^{-1}$ ), Mid IR (4000 - 200  $\text{cm}^{-1}$ ) and Near IR (12500 - 4000  $\text{cm}^{-1}$ ). The common and majority of analytical applications are limited to a portion of the middle region extending from 4000 to 400  $\text{cm}^{-1}$ . The absorption spectra in the infrared region originate from the transitions between vibrational (along with rotational) levels of a molecule present in its ground electronic state upon irradiation with infrared radiation.

The atoms in a molecule are never stationary and a good approximation is to treat them as a combination of point masses held together by Hooke's law of forces. By classical mechanics, it can be shown that the displacements of the masses from their mean positions are always the sum of the displacements due to a particular set of vibrations.<sup>[9]</sup> If in these sets of vibrations the masses are in phase and the motion of all the nuclei involved are such that the center of gravity of the molecule remains unaltered, then such vibrations are known as the fundamental modes of vibration of the molecule. Mostly, a normal mode is localized largely to a group within the molecule and hence corresponds to stretching or bending of one or few bonds only and hence associated with that particular functional group. Whether for the functional group or the entire molecule, the vibrations are universally classified either as stretching or as bending types. Stretching vibrations, which correspond to the oscillations leading to a change in the bond lengths, can be further subdivided into symmetric or asymmetric stretching vibrations. Bending vibrations are characterized

by continuously changing the angle between the bonds and is further sub-classified as wagging, rocking, twisting, or scissoring.

One of the primary requirements for vibrating molecules to interact with the oscillating electric field of the incident radiation and to undergo a transition between two vibrational energy levels is that the molecular dipole moment must change during the vibration. The intensity of the absorption is determined by the magnitude of this dipole moment change. Owing to symmetry, some of the vibrations in a molecule may not induce a change in dipole moment and hence are transparent to infrared radiations *i.e.*, IR inactive. In the present study, the FT-IR spectra of synthesized materials were recorded by the Perkin Elmer (Spectrum 100) FT-IR spectrophotometer with the KBr pellet method.

### 2.2.3 X-ray photoelectron spectroscopy (XPS)

XPS is a surface analytical technique; sometimes calls it an Electron Spectroscopy for Chemical Analysis (ESCA), used to determine the elemental composition at the parts per thousand ranges, chemical and electronic state of the elements that exist in the samples. When a beam of X-ray is irradiated on the sample, the electrons are ejected from the surface and the kinetic energy of the ejected electrons is calculated by using (equation 2.4).<sup>[10]</sup>

$$\text{Kinetic energy} = h\nu - BE - \varphi_s \quad (2.4)$$

Where  $h\nu$  = Energy of photons

$BE$  = Binding energy of an electron

Atoms of a higher positive oxidation state show a higher binding energy due to the extra coulombic interaction between the photo-emitted electron and the core ion. This ability to distinguish between different oxidation states and chemical environments is one of the major strengths of the XPS technique. The positions of the XPS peaks in the spectrum plotted as emission intensity *vs.* the electron binding energy gives the information about the surface chemical composition of the sample. Furthermore, the intensity of the peaks are related to the concentration of the element within the sampled region. Thus, the technique offers a quantitative analysis of the surface composition. In the present study, the XPS spectra of synthesized materials were recorded on the VGS Thermo K-Alpha, and PHI 5000 Versa Probe III instruments with monochromatic Al K $\alpha$  X-ray radiation and all the obtained XPS peaks were fitted with Gaussian function.

## 2.2.4 UV–Visible diffuse reflectance spectroscopy (UV-Vis DRS)

In UV–Vis DRS technique, when a powdered sample irradiates with UV or visible light, the light can be reflected in all directions. Some portion of the light is scattered within a solid sample and reverted to the surface is considered to be a diffuse reflection. Barium sulphate ( $\text{BaSO}_4$ ) is used as a reference standard and it must be recorded prior to that of any other powder sample.<sup>[11]</sup> In the present study, UV-Vis-DRS studies of the as-synthesized materials were evaluated by using Thermo Scientific Evolution 600 UV-Vis-NIR, and JASCO V-650 spectrophotometer where  $\text{BaSO}_4$  was used as a reference.

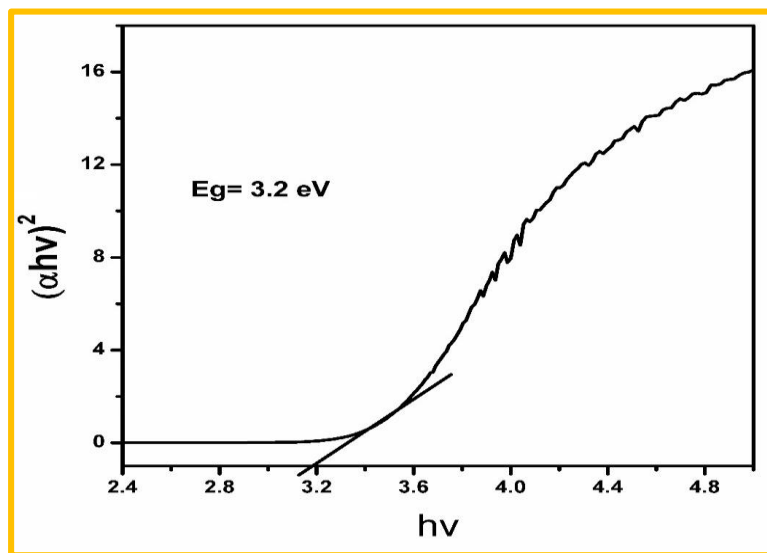


**Figure 2.3:** Determination of bandgap energy using Kubelka–Munk function.

The semiconductor bandgap energy can be determined by the following formula (equation 2.5) and it has shown in (Figure 2.3):

$$\alpha h\nu = A(h\nu - E_g)^\eta \quad (2.5)$$

Where  $A$ = Constant

$h$  = Planck's constant

$E_g$  = Band gap energy

$\alpha$  = Absorption coefficient

$\nu$  = Light frequency

The variable  $\eta$  depends on the type of optical transition caused by photon absorption.  $E_g$  (bandgap) can be expected according to a plot of  $(\alpha h\nu)^2$  Vs energy ( $h\nu$ ). The 'α' was determined from the Kubelka–Munk function (equation 2.6).<sup>[12]</sup>

$$\alpha = \frac{(1-R)^2}{2R} \quad (2.6)$$

Where 'α' is the reflection coefficient of the sample.

'R' is the reflectance.

### 2.2.5 Fluorescence spectroscopy (PL)

Fluorescence is the best technique to study the luminescent properties of the materials, where the molecules of the sample are excited by a certain wavelength of the light irradiation and emit different wavelength radiation. The emission spectrum thus gives evidence for both quantitative and qualitative analysis. Fluorescence spectroscopy is mainly concerned with the electronic and vibrational states. The procedures which happen among the emission and absorption of light are regularly verified by a Jablonski diagram named after Prof Alexander Jablonski, regarded as the father of fluorescence.<sup>[13]</sup> At each of these electronic energy levels, the fluorophores can occur in a number of vibrational energy levels, depicted by 0, 1, 2, etc. The first electronic excited state is generally depicted as,  $S_1$  as shown in (Figure 2.4). Once, the molecule reaches this  $S_1$  state, relaxation can occur via several pathways. Fluorescence is one of these methods which results in the emission of light. Essential pathways are:

1. Collisional deactivation leading to non-radiative relaxation.
2. Intersystem crossing
3. Phosphorescence
4. Internal Conversion
5. Fluorescence

Relaxation of the molecules from the  $S_1$  state to the  $S_0$  state with the emission of light is called fluorescence and it has a short lifetime ( $\sim 10^{-10}$  to  $10^{-7}$  sec). The wavelength of the emitted light is dependent on the bandgap between the  $S_0$  and the  $S_1$  states. An overall energy balance for the fluorescence process could be written as following (equation 2.7).

$$E_{flour} = E_{abs} - E_{vib} - E_{solv.relax} \quad (2.7)$$

Where,  $E_{flour}$  = Emitted light energy.

$E_{abs}$  = Absorbed light energy by the molecule during excitation.

$E_{vib}$  = molecule energy is lost from vibrational relaxation  $E_{solv.relax}$  = the difference in the energy of various bands always corresponds to that between the lowest vibrational level of the first excited state, and the ground state. For a given molecule, absorption energy is always greater than the

fluorescence energy. Thus the emitted light is observed at longer wavelengths than the excitation. This is known as Stokes shift.

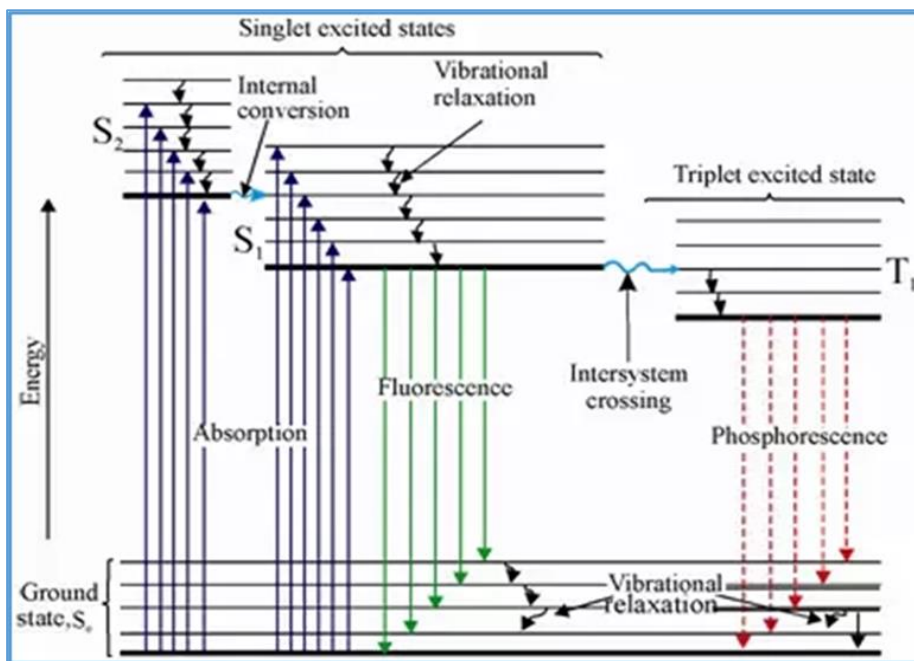


**Figure 2.4:** Electronic transition energy level diagram: Jablonski diagram was adapted from the website (<https://www.quora.com/What-is-the-Jablonski-diagram>).

In the present study, Photoluminescence (PL) spectra were measured on (PerkinElmer LS45; Xe lamp; U.S.A.) instrument and the life of the photogenerated carrier was predicted with the assistance of the time-resolved fluorescence lifetime (TRFL; FL920 Edinburgh Instruments; U.K.).

## 2.2.6 Scanning electron microscopy (SEM)

SEM is a powerful technique that is classified under scanning probe microscopy (SPM); it uses a focused beam of high energy electrons to give the morphological structure of the compound by scanning.<sup>[14]</sup> The electrons collision with atoms in the compound surface gives several signals that can be observed. It gives information about the orientation of materials making up the sample, sample external morphology, and elemental composition. Finally, data is collected over a particular area of the compound, 2D image is generated. SEM facilitates the analysis of samples with a resolution down to the nanometer scale.

In the present study, the morphological characteristics and chemical composition were recorded on a scanning electron microscope (SEM), VEGA3, Tescon, USA integrated with an energy dispersive X-ray spectrometer (EDS).

### **2.2.7 Field emission Scanning electron microscope (FE-SEM)**

FE-SEM is a magnifying instrument equipped with field emitter and emission source. The electron source produces the negative electrons with a large and stable current in the small beam and, these electrons are freed on the sample in a zig-zag pattern to obtain surface morphological properties of the sample.<sup>[15]</sup> There are two classes of emission source: thermionic emitter and field emitter. Field emitter type is the main difference between the SEM and the FE-SEM. In the present study, the morphological characteristics and chemical composition are investigated by field emission scanning electron microscope (FE-SEM; JEOL JSM-7000F instrument) integrated with an energy dispersive X-ray spectrometer (EDS).

### **2.2.8 Transmission electron microscope (TEM)**

TEM is an SPM technique in which electrons beam having the energy of the order of hundreds of KeV is transmitted over an ultra-thin sample, interacting with the sample as it passes through to provide morphological, topographical, compositional and crystallographic information of the sample. An image is obtained from the interaction between electrons and sample; the image is magnified and captured by a sensor. High-resolution TEM allows the researchers to outlook samples on a molecular level in the order of a few angstroms ( $10^{-10}$  m), making it possible to analyze structure and texture at a significantly high resolution. The TEM operates nearly on the equal basic principles as SEM as both use electrons. In the present study, the morphology of the as-synthesized materials was examined by using TEM; JEOL JEM-3010 instrument operated at 100 kV.

### **2.2.9 Energy-dispersive X-ray spectroscopy (EDS)**

EDS is a quantitative and qualitative X-ray micro-analytical technique that can determine the chemical composition of a sample. A beam of the electron is directed on the compound in either SEM or TEM. The primary beam of electrons penetrates the compound and interrelates with the compositional atoms. Bremsstrahlung X-rays, which means “braking radiation”, is denoted as

characteristic and background X-rays. The X-rays are recorded by an Energy Dispersive detector which shows the signal as a spectrum.<sup>[16]</sup>

### 2.2.10 Surface Area Analysis (BET)

Nitrogen adsorption-desorption (BET) measurements of the synthesized materials were carried out on (Quantachrome Autosorb 1; U.S.A.) instrument at 77 K and the specific surface areas of the samples were determined by using the (Brunauer-Emmett-Teller) BET analysis. This technique involves the adsorption and desorption of N<sub>2</sub> gas onto the surface of the materials at its boiling point. The number of gas molecules required to form a monolayer on the surface can be calculated by using (equation 2.8).<sup>[17]</sup>

$$\frac{1}{V(\frac{P_0}{P}-1)} = \frac{1}{V_m C} + \frac{C-1}{V_m C} * \frac{P}{P_0} \quad (2.8)$$

Where “P” and “P<sub>0</sub>” are the equilibrium pressure and the saturation pressure of N<sub>2</sub> gas, “V” is the volume of the gas adsorbed, “V<sub>m</sub>” is the amount of monolayer of N<sub>2</sub> adsorbed, and “C” is BET constant. A monolayer of N<sub>2</sub> molecules adsorbed and the BET constant are calculated from the

intercept and slope plot between “ $\frac{1}{V(\frac{P_0}{P}-1)}$ ” against “P/P<sub>0</sub>”. The specific surface area of these porous samples can be calculated by using the following (equation 2.9).

$$\text{Specific surface area (m}^2\text{g}^{-1}\text{)} = \frac{V_m A_m N}{22414 * W} \quad (2.9)$$

Where “A<sub>m</sub>” is the cross-sectional area of N<sub>2</sub> (16.2 x 10<sup>-20</sup> m<sup>2</sup> for N<sub>2</sub>), “N” is the Avogadro number, and “W” is the weight of the sample (g).

### 2.2.11 Thermo-gravimetric analysis (TGA)

TGA is a continuous procedure to contemplate the thermal degradation of materials. The analysis includes the estimation of sample weight with respect to the reaction temperature based on the programmed rate of heating. Along these lines, the mass of the sample reduces rapidly in a narrow temperature range and ultimately levels off as the reactant becomes spent, which is shown as residual mass. This estimation gives data about physical and chemical phenomena like phase transitions, adsorption, and desorption, thermal decomposition, chemisorptions.<sup>[18]</sup> In the present study, TGA was carried out on a NETZSCH, STA-2500 Regulus thermo analyzer with a heating rate of 10 °C/min (from RT-800 °C) under N<sub>2</sub> atmosphere.

## 2.3 Photocatalytic experiments

Photocatalytic technology attracts much attention due to the application on completely removing environmental pollutants in wastewater and effluents. Unlike the conventional biodegradable and activated carbon adsorption method, photocatalysis offers a powerful platform for oxidation processes in the treatment of bio-resistant organic contaminants such as dye wastewater by converting them into water and carbon dioxide.

To expand the application of photocatalysts, Rhodamine B (RhB), Methylene blue (MB), and Ciprofloxacin (CIP) were chosen as model pollutants for the study of photocatalytic activity. The photocatalytic activities of all the synthesized samples were evaluated by monitoring the photocatalytic degradation of RhB, MB, and CIP in an aqueous solution under direct sunlight and 35W Xe Arc Lamp. In each experiment, 100/50/30 mg of photocatalyst was added to 100 mL or 50 mL respective pollutant solution with a concentration of 5/10/20 mg L<sup>-1</sup>. Prior to irradiation, the suspensions were magnetically stirred in the dark for 30 min to achieve adsorption equilibrium between the pollutant/dye molecules and the photocatalyst. At given irradiation time intervals, the suspensions were periodically withdrawn and centrifuged to separate the photocatalyst particulates for analysis. The filtrates were analyzed by recording variations at the wavelength of maximal absorption in the UV-Vis spectrophotometer.

## 2.4 References

- [1] M. Navarrete-Magaña, A. Estrella-González, L. May-Ix, S. Cipagauta-Díaz, R. Gómez, *Journal of Environmental Management* **2021**, 282, 111602.
- [2] T. Debnath, A. Bandyopadhyay, T. Chakraborty, S. Das, S. Sutradhar, *Materials Research Bulletin* **2019**, 118, 110480.
- [3] M. V. Morales-Gallardo, J. E. Pascoe-Sussoni, C. Delesma, X. Mathew, F. Paraguay-Delgado, J. Muñiz, N. R. Mathews, *Journal of Alloys and Compounds* **2021**, 866, 158447.
- [4] S. Kundu, L. Ma, Y. Chen, H. Liang, *Journal of Photochemistry and Photobiology A: Chemistry* **2017**, 346, 249–264.
- [5] Y. X. Gan, A. H. Jayatissa, Z. Yu, X. Chen, M. Li, *Journal of Nanomaterials* **2020**, 2020, 1–3.
- [6] L. S. Birks, H. Friedman, *Journal of Applied Physics* **1946**, 17, 687–692.
- [7] T. N. Blanton, T. C. Huang, H. Toraya, C. R. Hubbard, S. B. Robie, D. Louër, H. E. Göbel,

G. Will, R. Gilles, T. Raftery, *Powder Diffraction* **1995**, *10*, 91–95.

[8] A. L. Patterson, *Physical Review* **1939**, *56*, 978–982.

[9] Z. Bacsik, J. Mink, G. Keresztury, *Applied Spectroscopy Reviews* **2004**, *39*, 295–363.

[10] A. Levasseur, P. Vinatier, D. Gonbeau, *Bulletin of Materials Science* **1999**, *22*, 607–614.

[11] P. George, P. Chowdhury, *The Analyst* **2019**, *144*, 3005–3012.

[12] D. G. Barton, M. Shtein, R. D. Wilson, S. L. Soled, E. Iglesia, *The Journal of Physical Chemistry B* **1999**, *103*, 630–640.

[13] D. Frackowiak, *Journal of Photochemistry and Photobiology B: Biology* **1988**, *2*, 399.

[14] D. McMullan, *Scanning* **2006**, *17*, 175–185.

[15] A. Mayeen, L. K. Shaji, A. K. Nair, N. Kalarikkal, in *Characterization of Nanomaterials*, Elsevier, **2018**, pp. 335–364.

[16] M. Scimeca, S. Bischetti, H. K. Lamsira, R. Bonfiglio, E. Bonanno, *European Journal of Histochemistry* **2018**, *62*, 89–99.

[17] F. Ambroz, T. J. Macdonald, V. Martis, I. P. Parkin, *Small Methods* **2018**, *2*, 1800173.

[18] J. P. Harmon, *Journal of the American Chemical Society* **2005**, *127*, 14952–14952.

◆-----◆

## Chapter III

# Development of versatile CdMoO<sub>4</sub>/g-C<sub>3</sub>N<sub>4</sub> nanocomposite for enhanced photoelectrochemical oxygen evolution reaction and photocatalytic dye degradation applications

◆-----◆

## Chapter III

# Development of versatile CdMoO<sub>4</sub>/g-C<sub>3</sub>N<sub>4</sub> nanocomposite for enhanced photoelectrochemical oxygen evolution reaction and photocatalytic dye degradation applications

### 3.1 Introduction

Nonrenewable energy sources depletion and scarcity of energy for future needs are the big issues to the humankind. Several technologies like photocatalysis (PC), electrocatalysis (EC), and photoelectrocatalysis (PEC) are widely developed in recent years to address the above issues. Among the developed technologies PEC water splitting and CO<sub>2</sub> reduction are the best ways to generate clean and sustainable energy with more efficiency.<sup>[1,2]</sup> PEC water oxidation and reduction reactions are widely accepted and most promising routes to fulfill the future energy demands because it can utilize solar energy to generate clean, sustainable and environment-friendly hydrogen at the cathode and oxygen at the anode (OER) of an electrolytic cell.<sup>[3,4]</sup> Though being one of the half-reaction, OER becomes the key step to limit the overall efficiency of water electrolysis and PEC is critically essential to diminish the energy barrier and it requires more kinetic energy for four electron transfer reaction.<sup>[5,6]</sup> Tremendous efforts have been put recently to develop the highly efficient PEC with reduced overpotential having a small Tafel slope. In this aspect noble metal oxide based EC such as Ru<sub>2</sub>O, IrO<sub>2</sub> are widely used for water oxidation reactions in both acidic as well as alkaline medium.<sup>[7,8]</sup>

Due to less abundance and more expensive nature, the use of these noble metal oxides are limited. Recently scientists are focused on various types of non-noble metal oxides for high-performance PEC-OER which are cheaply available and more efficient also.<sup>[9-11]</sup> On the other hand, water reservoirs such as lakes and rivers are being contaminated with an assortment of microbial, inorganic and organic impurities. For example, the presence of personal care products, pharmaceuticals, textiles, dyes and pesticides.<sup>[12]</sup> It is a very big challenge for the complete elimination of these contaminants by conventional water treatment approaches. However, in recent years heterogeneous photocatalysts has gained more attention as a prospective approach to deal with the environmental pollution and global energy crisis because of it is green, economic, and efficient approach towards pollutant removal and clean energy production by the utilization of solar energy.<sup>[13-15]</sup>

Several heterogeneous photocatalytic materials such as d-block metal oxides, oxynitrides, and sulfides have been developed to address the above issues. Even though, there are serious shortcomings in heterogeneous photocatalysts because of their high fabrication costs, fast charge recombination, photo corrosion, poor reusability, and less selectivity to the target pollutants. To solve above disadvantages, the current trend to improve the selectivity, efficiency, and stability of heterogeneous photocatalysts.<sup>[16,17]</sup> In recent years, metal free, two-dimensional (2D) polymeric graphitic carbon nitride (CN) recognized as a notable heterogeneous photocatalyst, because of its attractive intrinsic properties, such as suitable bandgap (2.7 eV) for harvesting more light energy, tunable electronic structure, more elemental abundance, superior chemical and thermal stabilities, cost effective synthesis and ecofriendly nature.<sup>[18,19]</sup> Having these amazing properties, it has been used in numerous photocatalytic applications, including degradation of environmentally hazardous pollutants, solar water splitting to produce O<sub>2</sub> and H<sub>2</sub>, reduction of CO<sub>2</sub>, sensors, and catalysts for selective organic transformations.<sup>[20,21]</sup> Even though, there are some limitations for its practical applications because of the more recombination of photo-induced excitons and less charge transfer capacity towards the catalyst surface. Hence, modification of CN towards the formation of composites with other semiconductors, doping, loading with metals and changing the morphology are developed for the enhancement of the photocatalytic activity of CN.<sup>[22–27]</sup>

In metal molybdates family (MMoO<sub>4</sub>, M = Pb, Cd, Ba, Na), cadmium molybdate (CMO) has gained significant attention recently, because of its excellent chemical, optical, electronic, and structural properties gives an advantage for its potential applications towards heterogeneous photocatalysis for environmental remediation and clean energy production.<sup>[28–31]</sup> Unfortunately, CMO is active under UV light illumination because of its wide bandgap range (3-4 eV). In this regard, lot of strategies have been employed to enhance the absorbance capacity towards visible light active photocatalyst for CMO.<sup>[32–34]</sup> Among the developed methods, the construction of Z-scheme heterojunction with CMO and visible light active and well-matched band energy levels of CN is one of the better ways to inhibit the recombination of photo-induced excitons, increase the light absorption capacity, and enhance the photocatalytic activity. Besides, the valance band (VB) and conduction band (CB) edge potentials of CMO are lower than those of CN, which supports the well matched energy band structure that is advantageous for the construction of a Z-scheme heterostructure. Bo Chai et al. reported recently a fabrication of CdMoO<sub>4</sub>/g-C<sub>3</sub>N<sub>4</sub> heterostructure composite photocatalyst via a precipitation-calcination process for the photocatalytic dye

degradation. Zhao et al. also reported the synthesis of CdMO<sub>4</sub>/g-C<sub>3</sub>N<sub>4</sub> composite via simple mixing and calcination method for CO<sub>2</sub> reduction as well as dye degradation.<sup>[27,35–38]</sup>

In the present work, we have successfully fabricated CMO microspheres on the CN sheets through a simple one-pot *in-situ* hydrothermal method. The optimized CMO/CN composite photocatalyst show remarkable performance in the PEC-OER and photocatalytic degradation of MB under light illumination, compared with those of pure CMO and CN. Moreover, we have studied the effect of CMO loading on the photocatalytic and PEC properties. Based on our experimental results we have proposed a possible photocatalytic degradation mechanism and role of the photogenerated reactive species analyzed by the trapping experiments. To the best of our knowledge, this is the first report for the fabrication of CMO/CN heterojunction composites by a simple one-pot *in-situ* hydrothermal approach for the potential PEC-OER and photocatalytic degradation of MB dye under light illumination.

## 3.2 Experimental section

### 3.2.1 Materials and method

Melamine (Otto Kemi, 98.0%), cadmium nitrate tetrahydrate (Aldrich, 98.0%), ammonium molybdate tetrahydrate (Finar, AR grade), polyethylene glycol 600 (Merck, for synthesis), silver nitrate (Aencore 99.8%), isopropyl alcohol (Choneye, extra pure 99.9%), EDTA-2Na (Panreac, 90.0%), benzoquinone (Aencore 99.8%) and methylene blue (Aldrich, 85.0%). All reagents used in this work were analytically pure and no need for further purification. Double distilled water was used for making all aqua solutions.

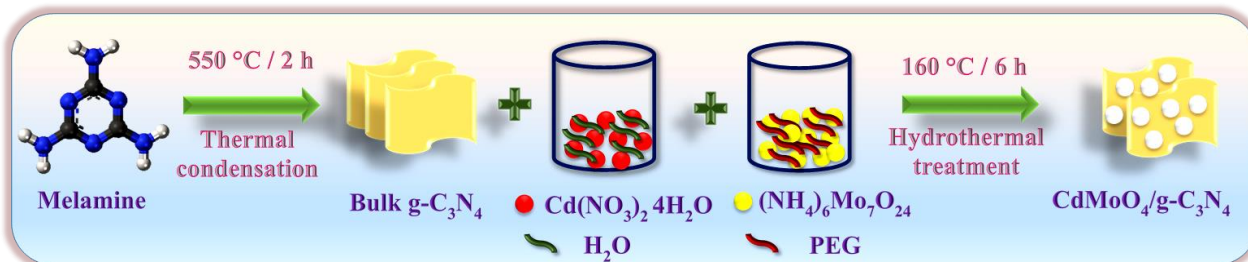
### 3.2.2 Synthesis of bulk CN

The bulk CN was prepared by a thermal condensation method using melamine as a precursor for carbon and nitrogen source. Concisely, in an alumina boat, 5 g of melamine was placed and calcinated at 550 °C for 2 h in a programmable tubular furnace with a heating rate of 5 °C/min at room temperature. Subsequently, the obtained light yellow-colored product was ground into a fine powder and collected for further use.

### 3.2.3 Synthesis of CMO/CN composite photocatalyst

A simple *in-situ* hydrothermal method was adopted for the fabrication of CMO/CN composite PC. Briefly, taken 30 mL of double distilled water with the calculated amount of CN was dissolved, and kept stirring at room temperature for 30 min. Subsequently, 1 mmol of

cadmium nitrate tetrahydrate ( $\text{Cd}(\text{NO}_3)_2 \cdot 4\text{H}_2\text{O}$ ) was added and continued stirring for another 30 min and mark as solution A. Simultaneously, to the 30 mL of polyethylene glycol and 1 mmol of ammonium molybdate tetrahydrate ( $(\text{NH}_4)_6\text{Mo}_7\text{O}_{24} \cdot 4\text{H}_2\text{O}$ ) was added and stirred for 30 min at room temperature, and mark as solution B. Then, solution B was added drop by drop to the solution A while stirring and continue for 1 h, at room temperature. Afterward, the total reaction mixture was transferred to pre-cleaned Teflon lined autoclave and kept in a microprocessor-controlled programmable oven and maintain the temperature for 6 h at 160 °C with a heating rate of 3 °C/min. After cooling to room temperature, the product was washed with ethanol several times and kept for drying in a hot air oven. Based on the above method we have synthesized successfully a series of CMO/CN composite PC with the different CMO to CN ratio of 5, 10, 15 wt% and named as CMO/CN-5, CMO/CN-10, CMO/CN-15. For the synthesis of pure CMO, the same method was followed in the absence of CN. A detailed schematic representation of the synthesis methodology is exemplified in Scheme 3.1.



**Scheme 3.1:** Schematic representation of fabrication of CMO/CN composite.

### 3.2.4 Electrochemical measurements

The EC and PEC measurements were performed in a three-electrode system controlled by potentiostat/galvanostat CHI, 6273D workstation. The electrodes are immersed in 1M  $\text{H}_2\text{SO}_4$  electrolyte, synthesized catalyst coated over glassy carbon electrode with active surface area of 0.071  $\text{cm}^2$  as working electrode (WE),  $\text{Ag}/\text{AgCl}$  (in sat KCl) as reference electrode (RE), and platinum (Pt) as counter electrode (CE). The PEC characterization was performed using 35 W Xe arc lamp illuminating backwards. Before, electrochemical characterization the electrolyte solution was saturated by purging  $\text{N}_2$  gas for 20 minutes. Cyclic voltammetry (CV) was performed at scan speed of 50  $\text{mV s}^{-1}$  followed by Linear sweep voltammetry (LSV) was recorded at a scan speed of 5  $\text{mV s}^{-1}$  without iR-correction. Based on Nernst equation the potentials were converted to Reversible Hydrogen Energy (RHE) ( $E_{\text{RHE}} = E_{\text{Ag/AgCl}} + 0.0591\text{pH} + 0.198$ ). Electrocatalyst ink was

prepared by dissolving 10 mg of catalyst in 150  $\mu$ l of DI water with 20  $\mu$ l of 5% Nafion were added and ultrasonicated for 30 min. A known amount of catalyst was drop casted over the glassy carbon electrode and dried in room temperature.

### **3.2.5 Photocatalytic dye degradation experiments**

The photocatalytic activity of the fabricated pure CN, CMO, and CMO/CN composite photocatalysts were evaluated by their degradation efficiency of an organic pollutant (MB) in aqueous media by using 35 W Xe arc lamp as a light source. Maintaining the temperature 30 °C for the photocatalytic reaction system, a jacketed beaker with external water circulating system was used. For every test, 50 mL of MB 10 ppm (10 mg/L) solution was taken and 50 mg of photocatalyst powder was added. To establish the adsorption/desorption equilibrium between the fabricated photocatalyst and dye solution, the above mixture solution was stirred under the dark condition for 30 min before the light irradiation. At every 20 min irradiation time intervals, 2-3 mL of solution was withdrawn from the reaction mixture and centrifuge to separate the catalyst and dye solution for the determination of the concentration of the MB after the degradation process by measuring its absorbance at 663 nm using UV-vis spectrophotometer (Evolution 220). With the increasing of photocatalytic degradation reaction time, the concentration of the dye solution was an inversely proportional way. Besides, to understand the photodegradation reaction pathway of fabricated composite photocatalysts, trapping experiments were performed under similar experimental conditions as mentioned above, but the addition of different quenchers such as disodium ethylene diamine tetraacetate (EDTA-2Na) for  $h^+$ , isopropyl alcohol (IPA) for hydroxyl radicals ( $\cdot OH$ ), benzoquinone (BQ) for superoxide anion radicals ( $O_2^{\cdot -}$ ), and silver nitrate ( $AgNO_3$ ) for electrons ( $e^-$ ) respectively was added to the reaction mixture before starting the photocatalytic degradation process.

## **3.3 Results and discussions**

### **3.3.1 PXRD, FT-IR, and TGA studies**

To know the crystal structures of synthesized photocatalysts, PXRD studies are carried out for the pure CN, CMO, and CMO/CN composite photocatalysts and the results are depicted in Figure 3.1(a). For the CMO, all major diffraction peaks are observed strong and sharp which are in tetragonal phase and well agree with the standard JCPDS card number (07-0209) because of the distinctive diffraction peaks of (112), (004), (200), (211), (204), (220), (116), (312), (224), (008),

(400), and (316) crystal planes correspond to  $2\theta$  at  $29.23^\circ$ ,  $31.95^\circ$ ,  $34.79^\circ$ ,  $39.92^\circ$ ,  $47.94^\circ$ ,  $50.01^\circ$ ,  $55.23^\circ$ ,  $58.96^\circ$ ,  $60.56^\circ$ ,  $66.76^\circ$ ,  $73.41^\circ$ , and  $77.67^\circ$  respectively. From the diffraction data, any extra impurity peaks are not recognized, which suggests the formation of the pure tetragonal phase of CMO.<sup>[39]</sup> For the CN, the major peak observed at  $27.6^\circ$  which is (002) plane responsible for the interplanar stacking of CN and small diffraction peak which is appeared at  $13.2^\circ$  corresponds to the in-plane motifs of (001) plane.<sup>[40]</sup> In composite materials both the phases of CMO and CN are observed which confirms to the successful formation of CMO/CN composite photocatalyst. Moreover, in Figure 3.1(b), it is noticed that with the increasing CMO amount on CN the diffraction peak at  $29.23^\circ$  intensity increases in CMO/CN composite photocatalysts. Besides the CN major peak which is appeared at  $27.6^\circ$  intensity was decreased with the decreasing amount of CN in CMO/CN composite photocatalysts which tells that the co-existence of CMO and CN in the synthesized CMO/CN composite photocatalysts. Also, it was observed that all the crystalline diffraction peaks of CMO are shifted to higher diffraction angles after adding CMO into CN which suggests that the formation of heterojunction between CMO and CN.

To distinguish the structural vibrations, composition and functional groups present in the fabricated photocatalyst materials FT-IR studies were carried out and depicted in Figure 3.1(c). For FT-IR absorption spectra of CN, the sharp and major characteristic peak at  $807\text{ cm}^{-1}$  corresponds to s-triazine ring stretching vibrations and the peaks at 1570, 1416, 1325, and 1247  $\text{cm}^{-1}$  are attributed to the aromatic C-N stretching vibrations, the peak at  $1638\text{ cm}^{-1}$  belongs to CN stretching vibrations. Besides, the broadband which appeared at  $3100\text{-}3300\text{ cm}^{-1}$  can be assigned to stretching vibrational modes of residual amino (N-H) fragments.<sup>[41,42]</sup> For CMO, the sharp band at  $438\text{ cm}^{-1}$  and broadband at  $790\text{ cm}^{-1}$  correspond to the bending and asymmetric stretching vibrational modes of Mo-O-Mo and Mo-O in the  $\text{MoO}_4^{2-}$  tetrahedron group respectively. Meanwhile, the strong absorption band appears at  $3430\text{ cm}^{-1}$  which is ascribed to the O-H stretching vibrations and peaks at 1426 and  $1621\text{ cm}^{-1}$  assigned to H-O-H bending vibrations respectively due to the surface adsorption of water molecules.<sup>[43-45]</sup> In the FT-IR spectra of CMO/CN composite photocatalysts, the characteristic band of CMO at  $790\text{ cm}^{-1}$  and characteristic peak at  $807\text{ cm}^{-1}$  of CN are mixed, we can clearly observe that with the increase in the CMO amount those peaks are expanded. The absorption bands of CMO are mixed with those of CN, which further confirm the formation of CMO/CN composite photocatalysts.

TG analysis was carried out under the  $N_2$  atmosphere to further confirm the amount of CMO loaded in the fabricated CMO/CN composite photocatalysts, and results depicted in Figure 3.1(d). For the CN, the mass loss region identified in the range of 530  $^{\circ}C$  to 750  $^{\circ}C$  which is 100 % due to the burning of pure CN.<sup>[46]</sup> There is no mass loss identified for the CMO and stable up to 800  $^{\circ}C$ . TGA plot for the CMO/CN composite photocatalysts are giving clear information about the loaded composition of CMO into CN moiety. The amount of CMO in the CMO/CN composite photocatalysts can be easily estimated from the residual weight after heating to 800  $^{\circ}C$ .<sup>[47]</sup> Therefore, the weight loss regions of CMO in CMO/CN-5, CMO/CN-10, and CMO/CN-15 composite photocatalysts are detected as 6.2, 11.4, and 17.8% respectively. From the TGA studies, the formation of CMO/CN composite is further confirmed.

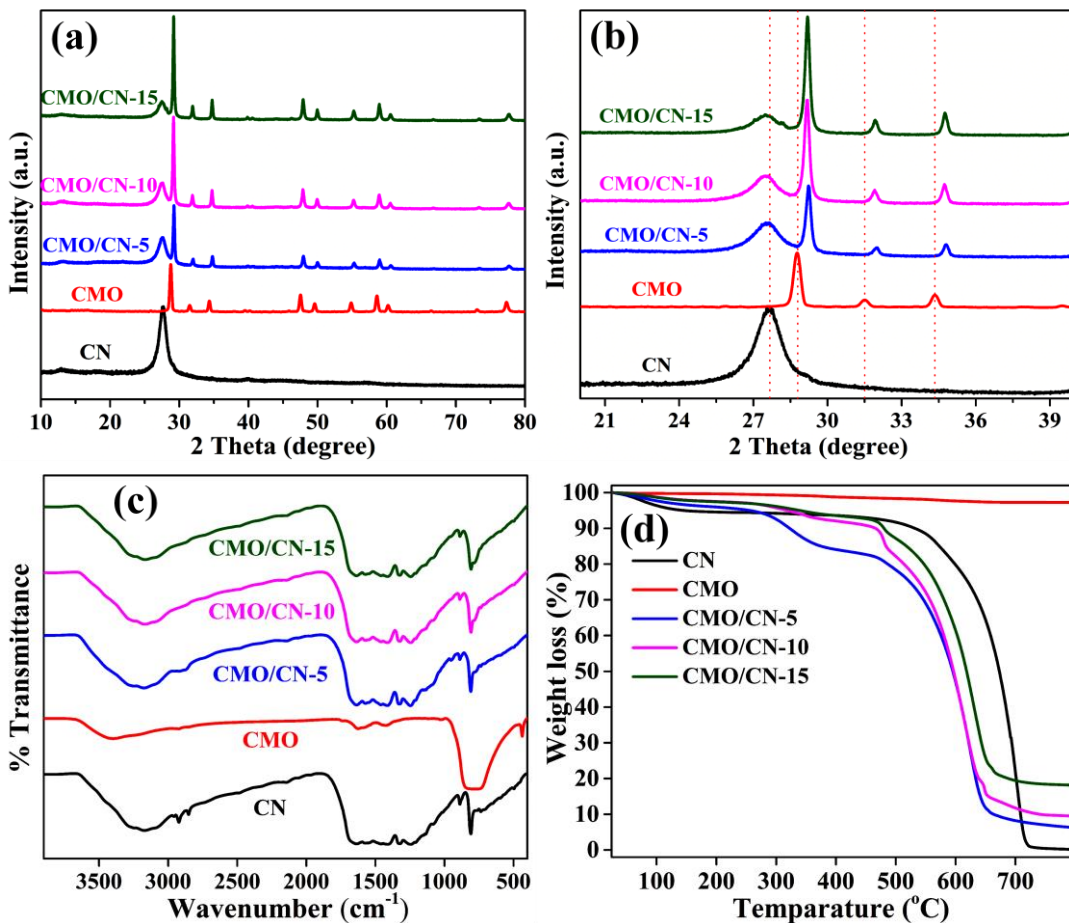


**Figure 3.1:** (a) PXRD patterns of synthesized CN, CMO, and CMO/CN composite photocatalysts, (b) respective expanded PXRD patterns in the range of  $2\theta=20^{\circ}$ - $40^{\circ}$ , (c) FT-IR analysis of CN, CMO, CMO/CN composites photocatalysts, and (d) TGA analysis of CN, CMO and CMO/CN composite photocatalysts.

### 3.3.2 SEM, EDS, elemental mapping and TEM studies

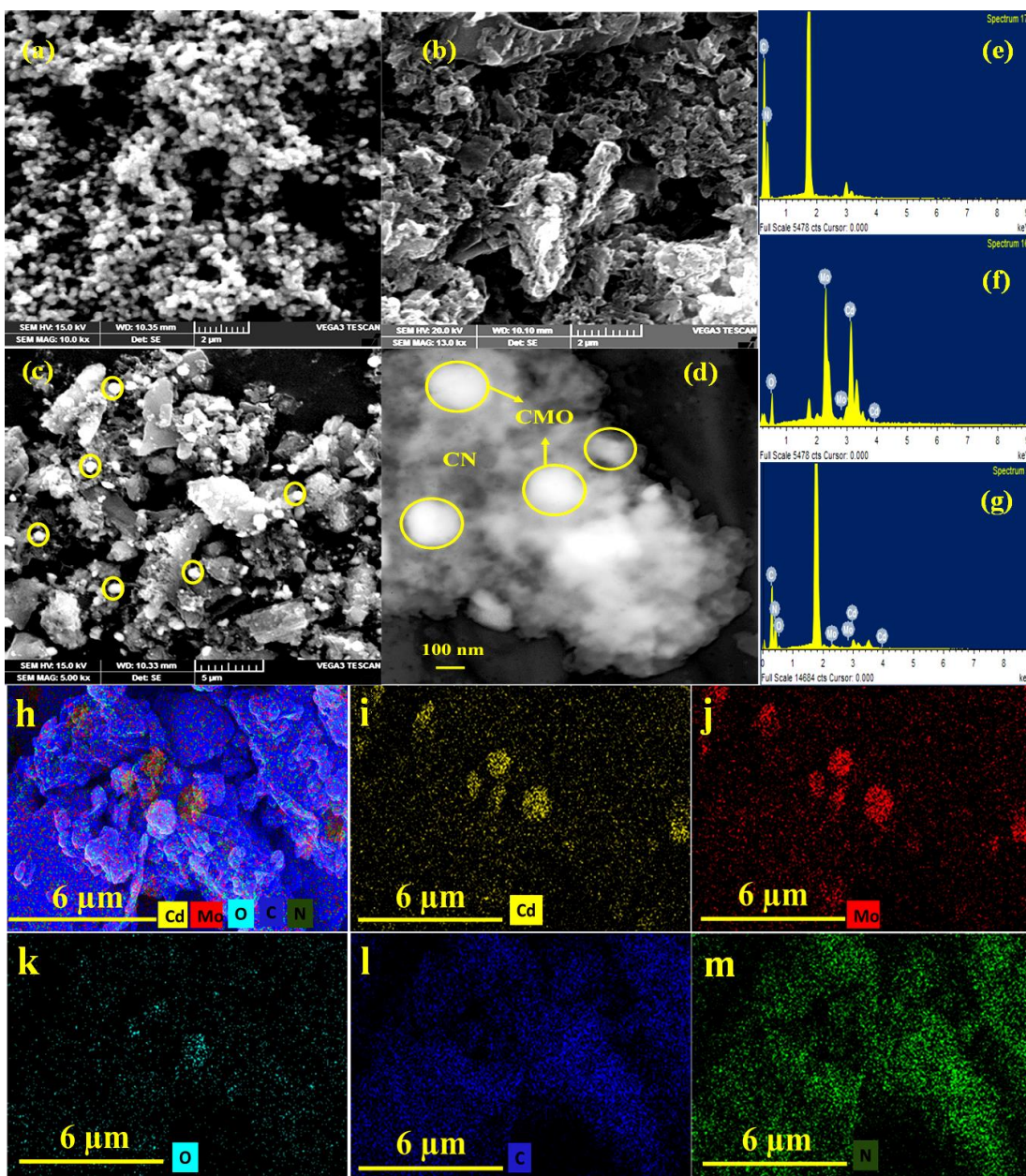


**Figure 3.2:** SEM images of (a) CMO, (b) CN, (c) CMO/CN-10 composite photocatalyst, TEM image of (d) CMO/CN-10 composite photocatalyst, EDS elemental analysis of (e) CN, (f) CMO, (g) CMO/CN-10 composite photocatalysts, and EDS elemental mapping images of (h-m) CMO/CN-10 composite photocatalysts.

To understand the surface morphology and elemental composition of the synthesized CN, CMO, and CMO/CN composite photocatalysts, SEM analysis was performed as shown in Figure

3.2, Figure 3.2(a) represents the SEM image of CMO with small spherical like morphology. Similarly, Figure 3.2(b) depicts the SEM image of CN having identical sheets like morphology. While, there is no crash of morphology being observed in CMO/CN-10 composite photocatalyst, and it represent the both of parent morphologies of CMO and CN, respectively. In Figure 3.2(c) the yellow circles indicate the spherical form of CMO and rest of the part corresponds to CN. The transmission electron microscope (TEM) analysis were carried out to analyze the formation of CMO/CN-10 heterojunction and shown in the Figure 3.2(d). From the EDS elemental analysis, it was noted that all the elements of CN and CMO are present in the CMO/CN-10 composite photocatalyst as depicted in Figure 3.2(e-g). From the EDS elemental mapping analysis of CMO/CN-10 confirms the presence of constituent elements in the composite as shown in Figure 3.2(h-m).

### **3.3.3 UV-Vis DRS, PL, TRFL, and BET studies**

To describe the optical properties of fabricated CN, CMO, and CMO/CN composite photocatalysts, UV-Vis DRS analysis was performed and shown in Figure 3.3(a-b). As depicted in Figure 3.3(a), for the CN absorption edge at 467 nm, although, optical absorption for CMO displayed at the UV region around 369 nm, which is well coordinated with PL spectra values. After CMO hybridizing with CN, the absorption edge values lie between those of CMO and CN. A little blue shift in the absorption edge was observed after adding CMO to CN, demonstrating that CMO has a strong interface with CN. Moreover, compared to CMO the absorption edge shifts towards higher wavelength region after hybridizing with CN. Although, with the increase in the amount of CMO on CN the absorption edge was gradually shifted toward the lower wavelength region which further confirms the formation of heterojunction between two semiconductors. The more absorption capacity of the CMO/CN composite photocatalysts can, therefore be responsible for the more photogenerated charge carriers need for the photocatalytic degradation of MB solution as well as OER performance. Furthermore, the bandgap energies of CN, CMO and CMO/CN-10 composite photocatalyst are shown in Figure 3.3(b). From the Tauc plot, the calculated bandgap energies are 2.68, 3.31, and 2.71 eV respectively and tabulated in Table 3.1.

**Table 3.1:** Calculated Band gap energy, pore volume and surface area values of fabricated photocatalysts.

Photocatalyst	Band gap (eV)	Pore volume (cc/g)	Surface area (m <sup>2</sup> /g)
CN	2.68	0.0084	19.23
CMO	3.31	0.009	2.48
CMO/CN-10	2.71	0.0032	7.68

The PL and TRFL studies were carried to examine the electron-hole pair recombination rate as well as the average lifetime of the photogenerated electrons at room temperature for the synthesized CN, CMO, and CMO/CN-10 composite photocatalysts and shown in Figure 3.3(c-d). Generally accepted and well known that the intensity of the PL emission peak is directly proportional to the recombination probability of the photogenerated excitons. As depicted in Figure 3.3(c), the excitation and emission wavelengths of as-prepared CMO are 310 and 370 nm respectively. This is because of the charge- transfer transition between ligand orbital of (O<sub>2</sub>) to the metal orbital of (Mo 4d) within the MoO<sub>4</sub><sup>2-</sup> complex, which is known as ligand to metal charge transfer process (LMCT) in the CMO structure.<sup>[48]</sup> For the CN, excitation and emission values are 365 and 465 nm respectively.

High emission peak intensity of CN indicates the more recombination of photogenerated excitons.<sup>[49]</sup> However, it was noticed that the PL intensity was suppressed remarkably after the addition of CMO on CN owing to the formation of interfacial charge transfer between the two photocatalysts through Z-scheme which facilitates suppressing the photogenerated excitons recombination.<sup>[36]</sup> Moreover, the TRFL studies were used to understand the role of the interface on the dynamics of the photogenerated excitons. As shown in Figure 3.3(d), the decay curves of CN, CMO, and CMO/CN-10 composite photocatalysts are fitted with a 'bi-exponential' function as following (equation 3.1).<sup>[50]</sup>

$$\text{Fit} = B + A_1 \exp\left(\frac{-x}{t_1}\right) + A_2 \exp\left(\frac{-x}{t_2}\right) \quad (3.1)$$

Where B is the exponential constant, A<sub>1</sub> and A<sub>2</sub> are the constants related to non-radiative and radiative processes respectively, and t<sub>1</sub> and t<sub>2</sub> are the shorter and longer decay lifetimes for non-radiative and radiative relaxation process. The average lifetime of the excitons was estimated from the following (equation 3.2).<sup>[51]</sup>

$$t_{av} = \frac{A_1 t_1 + A_2 t_2}{A_1 + A_2} \quad (3.2)$$

List of fitted parameters like shorter and long lifetime components ‘ $t_1$ ’ and ‘ $t_2$ ’ along with average lifetime ‘ $t_{av}$ ’ of CMO, CN, and CMO/CN-10 are depicted in Table 3.2.

**Table 3.2:** Calculated relative contribution percentages of lifetimes  $t_1$  and  $t_2$  and  $t_{av}$

Photocatalysts	A <sub>1</sub> (rel. %)	t <sub>1</sub> (ns)	A <sub>2</sub> (rel. %)	t <sub>2</sub> (ns)	t <sub>av</sub> (ns)
CN	3.05	3.36	0.16	13.04	3.85
CMO	9.56	1.23	9.56	1.23	1.23
CMO/CN-10	0.09	21.21	2.77	3.96	4.50

The calculated average lifetime of CMO/CN-10 is 4.50 ns, which is more than CN 3.85 ns, and much higher than CMO 1.23 ns. Owing the improvement of an average lifetime of photogenerated excitons are supports the formation of strong heterojunction between the CMO and CN in CMO/CN-10 composite photocatalyst. Moreover, having less PL emission intensity and more lifetime of photogenerated excitons leads to enhance the photocatalytic activity of CMO/CN-10.

The surface area, pore diameter and pore volume of the synthesized CN, CMO and CMO/CN-10 composite photocatalysts were analyzed using nitrogen adsorption measurements. Before the measurements the sample was degassed for 12 h at 150 °C and depicted in Figure 3.3(e-f). As shown in Figure 3.3(e), nitrogen adsorption isotherms of CN, CMO and CMO/CN-10 along with pore size distribution as shown in Figure 3.3(f). Compared to CN and CMO, the CMO/CN-10 composite surface area was decreased and CN is responsible for surface area enhancement and CMO is responsible for surface area decline. The surface area and pore volumes of CN, CMO, and CMO/CN-10 are determined to be 19.23, 2.48, and 7.68 m<sup>2</sup>/g and 0.0084, 0.009, and, 0.0032 cc/g respectively. Besides, the complete list of surface area and pore volume are depicted in Table 3.1. However, the surface area of CMO/CN-10 was found to be lesser than the CN and CMO. The CMO is responsible for the surface area decreases in CMO/CN-10 composite. Many other factors are responsible for the better photocatalytic activity of composite photocatalyst rather than surface area and more importantly CMO and CN plays a key role in enhancing the photocatalytic activity by suppressing the recombination of photogenerated excitons. The same type of results are reported by earlier researchers as well.<sup>[52,53]</sup>

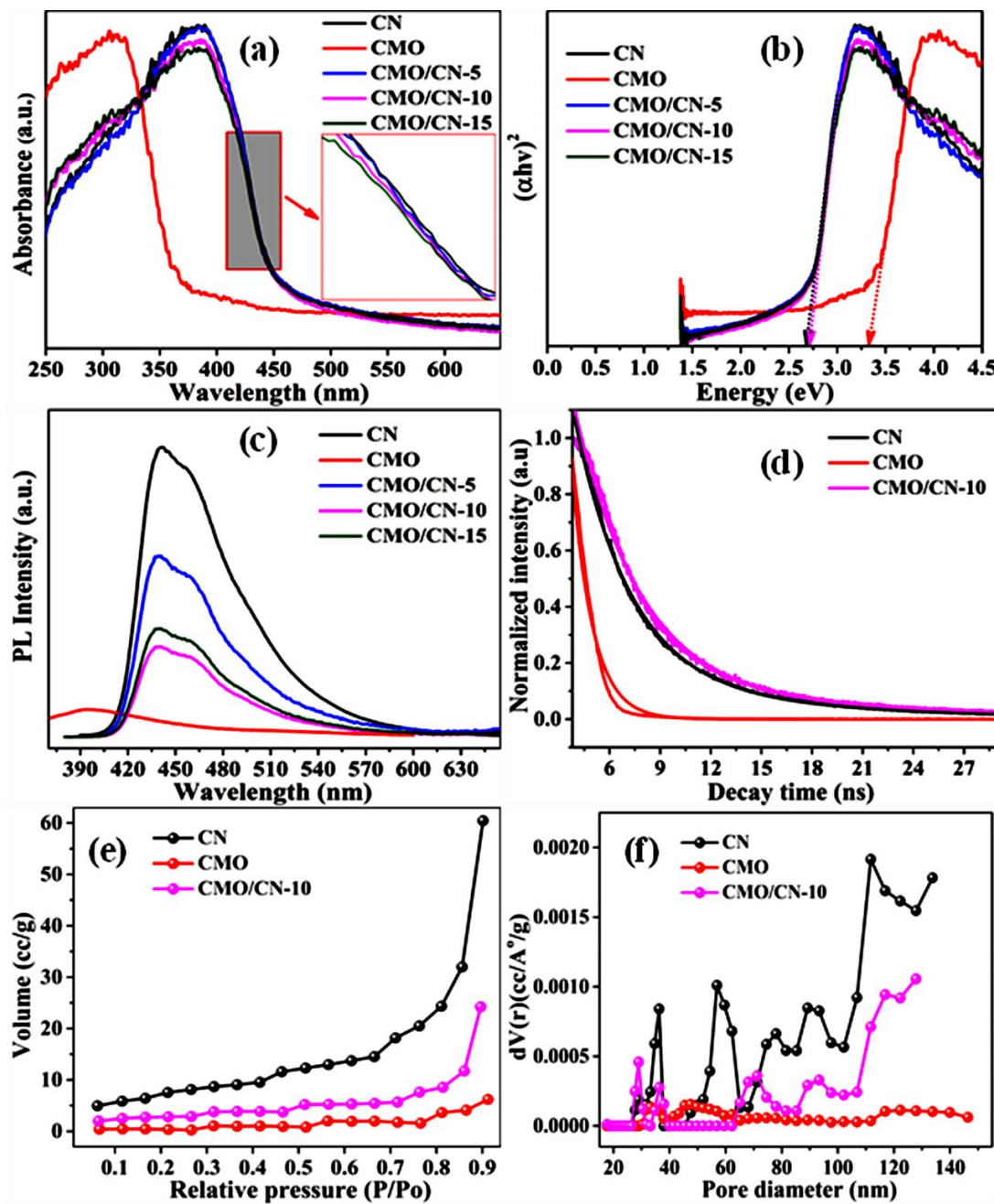


**Figure 3.3:** (a) UV-Vis DRS spectra of CN, CMO, and CMO/CN composite photocatalysts, (b) Tauc plots of CN, CMO, and CMO/CN composite photocatalysts, (c) PL spectra of CN, CMO, and CMO/CN composite photocatalysts, (d) time resolved fluorescent lifetime of CN, CMO, CMO/CN-10 composite photocatalysts, (e) nitrogen adsorption isotherms of CN, CMO, CMO/CN-10 composite photocatalysts, and (f) respective pore size distribution.

### 3.3.4 XPS studies

To further confirm the valance states and elemental composition of the fabricated CN, CMO and CMO/CN-10 composite photocatalysts are analyzed by assisting with XPS and results are depicted in Figure 3.4(a-f). As shown in Figure 3.4(a), the survey spectrum of CN, CMO, and CMO/CN-10 composite photocatalysts display the existence of corresponding elements Cd, Mo, N, C, and O with sharp photoelectron peaks appearing at binding energies of 404.86 eV (Cd 3d), 232.76 eV (Mo 3d), 396.87 eV (N 1s), 285.80 eV (C 1s), and 529.82 eV (O 1s) respectively, which evidences the CMO and CN are existing in the fabricated CMO/CN-10 composite photocatalysts.<sup>[35,54]</sup> The high resolution C 1s XPS spectra of CN and CMO/CN-10 composite are depicted in Figure 3.4(b), and further deconvoluted into three peaks with binding energies of 284.73 eV, 288.15 eV, 289.27eV and 285.18 eV, 287.76 eV, 289.54 eV corresponds to surface adventitious carbon,  $sp^2$  hybridized aromatic ring carbon (N-C=N), and  $sp^3$  carbon of C-N-C groups, which indicates the existence of CN in the CMO/CN-10 composite respectively.<sup>[40]</sup> High resolution N 1s XPS spectra of CN and CMO/CN-10 composite are shown in Figure 3.4(c), which is deconvoluted into three peaks with binding energies of 398.59 eV, 399.60 eV, 404.74 eV, and 398.03 eV, 399.50 eV, 405.58 eV corresponds to the triazine rings which are having  $sp^2$  hybridized N, tertiary N bonded to C (N-(C)<sub>3</sub>), and amino groups (C-N-H), are in the CMO/CN-10 composite respectively. Figure 3.4(d), depicts the high resolution XPS spectra of Cd 3d in the CMO and CMO/CN-10 composite photocatalyst, which are further deconvoluted into two doublets with two different oxidation states of Cd<sup>3+</sup> and Cd<sup>2+</sup>. The peak appears with binding energies at 406.43 eV, 414.77 eV corresponds to Cd 3d<sub>3/2</sub> of Cd<sup>3+</sup> and the peaks appears with binding energies at 405.10 eV, 411.99 eV corresponds to Cd 3d<sub>5/2</sub> of Cd<sup>2+</sup> valance ions in CMO. While, for the CMO/CN-10 composite photocatalyst, the peaks displayed at binding energies of 406.28 eV, 413.00 eV corresponds to Cd 3d<sub>3/2</sub> of Cd<sup>3+</sup> and the peaks displayed at binding energies of 404.88 eV, 411.54 eV corresponds to Cd 3d<sub>5/2</sub> of Cd<sup>2+</sup> in the Cd valance ions. Here Cd<sup>3+</sup> peak is the dominating. Compared to CMO, in CMO/CN-10 composite the binding energies are shifted towards less energy region, due to the formation of composite.<sup>[55-57]</sup>

Figure 3.4(e), shows the high resolution XPS spectra of Mo 3d in CMO and CMO/CN-10 composite, which are deconvoluted into two doublet peaks which are having two specific oxidation states Mo<sup>6+</sup> and Mo<sup>5+</sup>. The peaks appear at 232.63 eV, 236.68 eV are assigned to the Mo 3d<sub>3/2</sub> which are characteristic of Mo valance ions in the Mo<sup>6+</sup> and the peaks appear at 231.98 eV, 235.23

eV are assigned to Mo 3d<sub>5/2</sub>, which are characteristic of Mo valance ions in the Mo<sup>5+</sup> of CMO. Whereas, the peaks at the binding energies of 232.57 eV, 236.65 eV corresponds to the Mo 3d<sub>3/2</sub> of Mo<sup>6+</sup> and the peaks at the binding energies of 231.58 eV, 243.30 eV corresponds to the Mo 3d<sub>5/2</sub> of Mo<sup>5+</sup> oxidation states of CMO/CN-10 composite photocatalyst.

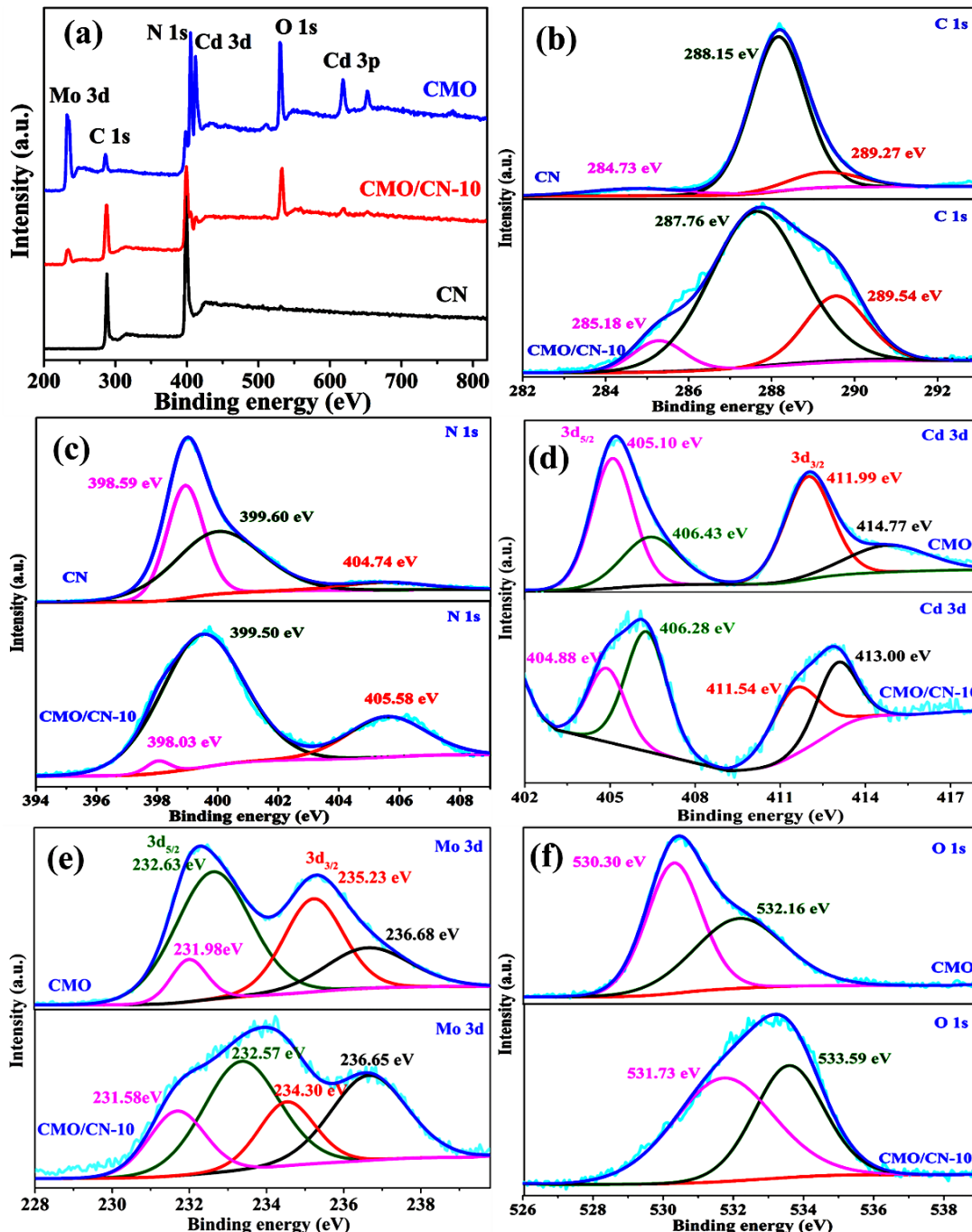


**Figure 3.4:** (a) XPS survey scan of CN, CMO and CMO/CN-10. (b) Cd 3d, (c) Mo 3d, (d) N 1s (e) C 1s, and (f) O 1s spectra of CMO/CN-10 composite photocatalyst.

From the above findings concludes that after the formation of composite the binding energies are shifted to low energy region.<sup>[58–60]</sup> High resolution O 1s XPS spectra of CMO and CMO/CN-10 are shown in Figure 3.4(f), for the CMO and CMO/CN-10 two deconvoluted peaks which appears at binding energies of 530.30 eV, 532.16 eV and 531.73 eV and 533.59 eV correspond to the O anions, chemisorbed O species, and C-O bonds, respectively. Compared to CMO, the CMO/CN-10 composite the binding energies are shifted to higher energy. The above XPS results further confirms the formation of CMO/CN composites with intimate interfacial contact between CMO and CN respectively. Moreover, these XPS results are corelates with the PXRD and TEM results and supports the formation of CMO/CN composites.

### 3.3.5 Electrochemical and Photo-assisted electrocatalytic OER activity

Figure 3.5(a) shows the redox couples (oxidation-reduction peaks) of CN, CMO, and CMO/CN-10 by performing CV in the potential range of -1.0 to 2.0 V using three-electrode system. The oxidation and reduction peaks are assigned to reversible electrochemical reactions related to Cd-O/Cd-O-O-OH. According to standard redox potential, potential at 0.37 V the CN dissociate to  $(CN)_2 + 2 H^+ + 2 e \rightleftharpoons 2 HCN$  and Potential at -0.658 V denotes the reduction of Cd  $(OH)^{2-} + 2e \rightleftharpoons Cd + 4 OH^-$  for CMO and CMO/CN-10 electrocatalyst, were as transition metal Mo does not directly involve in redox reaction but enhances the conductivity of the electrochemical performance of the electrodes.<sup>[61]</sup> Potential at 1.49 V denotes water oxidation  $2H_2O + 2 e \rightleftharpoons H_2 + 2OH^-$ . Figure 6b shows the LSV of the electrocatalyst series recorded at 5mV s<sup>-1</sup> under dark condition showing higher onset potential of 2.01 V vs RHE for CN and CMO samples, for composite series the onset potential slightly reduced to 1.95 V for CMO/CN-10 with maximum current density of 9.76 mA cm<sup>-2</sup> and the results were tabulated in Table 3.3.

**Table 3.3:** Calculated values of current density, onset potential under dark and light conditions, and over potentials of the fabricated pure as well as composite photocatalysts.

Material	Current density in dark (mA/cm <sup>2</sup> )	Current density in Light (mA/cm <sup>2</sup> )	Onset Potential in dark	Onset Potential in Light	Over Potential (η <sub>10</sub> )
CN	8.56	28.1147	2.01	1.88	0.8016
CMO	9.13	41.3850	2.01	1.84	0.7642
CMO/CN-5	8.28	43.3465	1.96	1.76	0.7223
CMO/CN-10	9.76	52.7450	1.95	1.77	0.7097
CMO/CN-15	8.52	52.8778	1.96	1.79	0.7132

Under dark condition, the catalyst series struggles to attain the current density of 10 mA/cm<sup>2</sup> as shown in Figure 3.5(b). In order to enhance the performance of the electrocatalyst, photo-assisted electrocatalytic OER activity was performed by illuminating 35 W Xe arc lamp over the electrocatalyst, and similar studies are published by our group.<sup>[62,63]</sup> Figure 3.5(c) shows the LSV of electrocatalyst series upon light illumination, the onset potential of CN and CMO samples reduced to 1.88 V and 1.84 V vs RHE with overpotential ( $\eta$ ) at current density 10 mA/cm<sup>2</sup> shows 0.80 V and 0.76 V and for composite series the onset potential reduced to 1.76, 1.77, and 1.79 V vs RHE with overpotential ( $\eta$ ) of 0.72, 0.70, 0.71 V for CMO/CN-5, CMO/CN-10, CMO/CN-15 samples.<sup>[64,65]</sup> On comparing the performance of the electrocatalyst under light condition, CMO/CN-10 catalyst shows least onset and overpotential with the maximum current density of 52.74 mA/cm<sup>2</sup> and the results are tabulated in Table 3.3. As shown in Figure 3.5(d) the Tafel plots of CN, CMO, and CMO/CN series of samples and the results were extracted from polarization LSV curves given by  $\eta = b \log(j/j_0)$  where “ $\eta$ ” denotes the overpotential “ $b$ ” is the Tafel slope and “ $j/j_0$ ” denotes the current density and exchange current density.<sup>[66]</sup> Smaller Tafel value indicates the fastest OER reaction rate here CMO/CN-10 shows the least Tafel value of 283 mV dec<sup>-1</sup>, whereas CMO/CN-15 (313 mV dec<sup>-1</sup>), CMO/CN-5 (337 mV dec<sup>-1</sup>), CMO (380 mV dec<sup>-1</sup>) and CN (386 mV dec<sup>-1</sup>) it's clear from the plot that CMO/CN-10 shows better performs than other catalyst series.

Electrochemical impedance spectra (EIS) was performed in dark and light condition to investigate the charge transfer properties, performed in high frequency range of 100 kHz to low frequency of 100 Hz in 0.01 V amplitude. The spectra were fitted with equivalent circuit model and provided in the graph, the smaller semicircle diameter is directly reflecting charge transfer resistance  $R_{ct}$  between the photoanode and electrolyte. Figure 3.5(e) shows EIS in dark for CN and CMO catalyst shows large charge transfer resistance  $R_{ct}$  of 15  $\Omega$  and 11.81  $\Omega$ , were as in light condition shown in Figure 3.5(f) the  $R_{ct}$  values are reduced to 12.56  $\Omega$  for CN and 10.04  $\Omega$  for CMO this clearly denotes that under the light condition the charge transfer properties are improved greatly. For the composite catalyst series, the resistance of 10.92  $\Omega$ , 7.59  $\Omega$ , and 9.76  $\Omega$ , for CMO/CN-5, CMO/CN-10, and CMO/CN-15 in dark condition, were as under light the resistance of 5.91  $\Omega$ , 5.72  $\Omega$ , and 5.78  $\Omega$  for CMO/CN-5, CMO/CN-10, and CMO/CN-15 respectively.

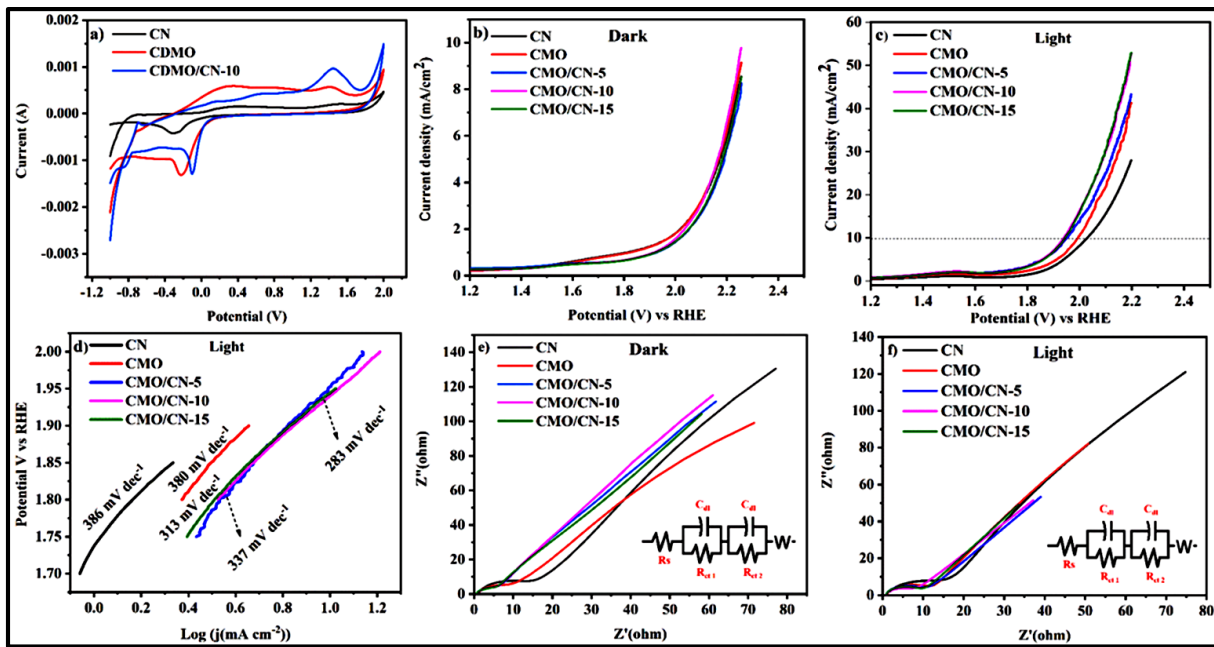


**Figure 3.5:** (a) Redox pairs of CN, CMO, and CMO/CN-10 composite electrocatalysts, (b, c) LSV of CN, CMO, CMO/CN-5, CMO/CN-10, and CMO/CN-15 composite electrocatalyst series performed under dark and light condition, (d) Tafel plot extracted from LSV of light, and (e, f) EIS of CN, CMO, CMO/CN-5, CMO/CN-10, and CMO/CN-15 composite electrocatalyst series performed under dark and light condition.

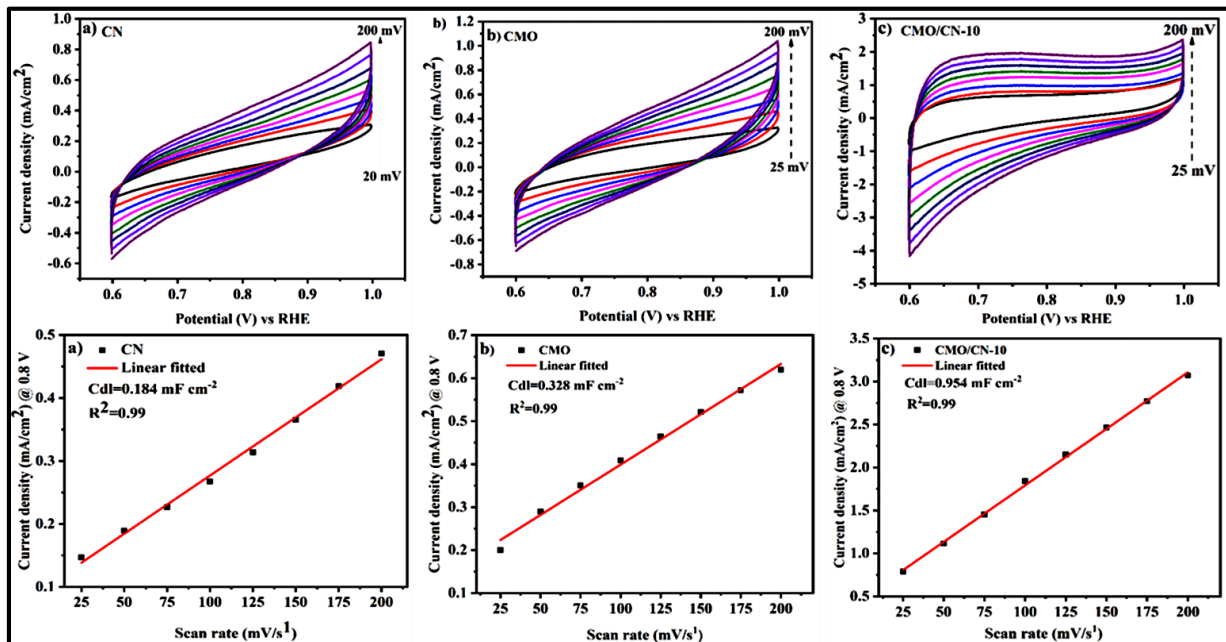


**Figure 3.6:** (a) ECSA of CN, (b) CMO, and (c) CMO/CN-10 composite electrocatalysts performed under light and their corresponding linear fitted curves at 0.8V vs RHE.

The Electrochemical active surface area (ECSA) of electrocatalyst were estimated from the double layer capacitance (Cdl), the Cdl were performed in light condition running CV in non-faradaic region, in the potential range of 0.6 V to 1.0 V vs RHE in increased scan rate of 25 mV s<sup>-1</sup> to 200 mV s<sup>-1</sup> for CN, CMO and CMO/CN-10 samples. The double layer charging current response of the electrocatalyst increase as of the scan rate increases from 25 mV s<sup>-1</sup> to 200 mV s<sup>-1</sup> and it is given by formula  $I=V \text{ cdl}$ . The current density vs voltage curves were shown in Figure 3.6(a) and the double layer capacitance values were estimated by plotting the  $\Delta j(j_a-j_c)$  at 0.8 V vs RHE against the scan rate, where the slope is twice  $C_{dl}$ .<sup>[67]</sup> The best electrocatalyst CMO/CN-10 shows the value of 0.954 mF cm<sup>-2</sup> with the high active surface area. The Figure 3.6(b-c) shows less activity with the values of 0.328 mF cm<sup>-2</sup> for CMO and 0.184 mF cm<sup>-2</sup> for CN.

### 3.3.6 Photocatalytic dye degradation studies

The photocatalytic activities of fabricated CN, CMO, and CMO/CN composite photocatalysts were investigated for the degradation efficiency of MB, a generally used dye, in water under light irradiation. The results are depicted in Figure 3.7. We conducted a photolysis reaction under light in the absence of catalysts which indicates that the photo-stability of MB. Although the catalytic reaction under dark condition (without light source) further confirms that the MB photocatalytic degradation occurs with the combination of light and catalyst are the major priorities. As shown in Figure 3.7(a), time dependent UV-Visible absorption spectrum for photocatalytic degradation of MB over the CMO/CN-10 under dark as well as light, in that MB shows characteristic absorption peak at 663 nm for the photocatalytic degradation curves of CN, CMO and CMO/CN composite photocatalysts with MB following trend was observed as shown in Figure 3.7(b). CMO/CN- 10 > CMO/CN-15 > CMO/CN-5 > CN > CMO respectively. Figure 3.7(c) clearly indicates the degradation of MB follows pseudo-first-order reaction kinetics model as shown in (equation 3.3).

$$-\ln (C_t/C_0) = k_t \quad (3.3)$$

Where  $C_t$  and  $C_0$  are the concentrations of MB at time  $t$  and initial concentration,  $k$  is the rate constant. The kinetic plots against  $-\ln (C_t/C_0)$  vs irradiation time, the slope of the linear fit curve gives information about the rate of degradation reaction. The degradation reaction rate constant of CMO/CN-10 is  $2.0 \times 10^{-2} \text{ min}^{-1}$  whereas for the CN, CMO, CMO/CN-5, and CMO/CN-15 is  $1.2 \times 10^{-2} \text{ min}^{-1}$ ,  $5.7 \times 10^{-3} \text{ min}^{-1}$ ,  $1.7 \times 10^{-2}$  and  $1.8 \times 10^{-2}$  respectively. From the kinetic plots the

degradation rate of CMO/CN-10 is almost 12.7 and 17.5 times more than the rate observed for CN, and CMO respectively.

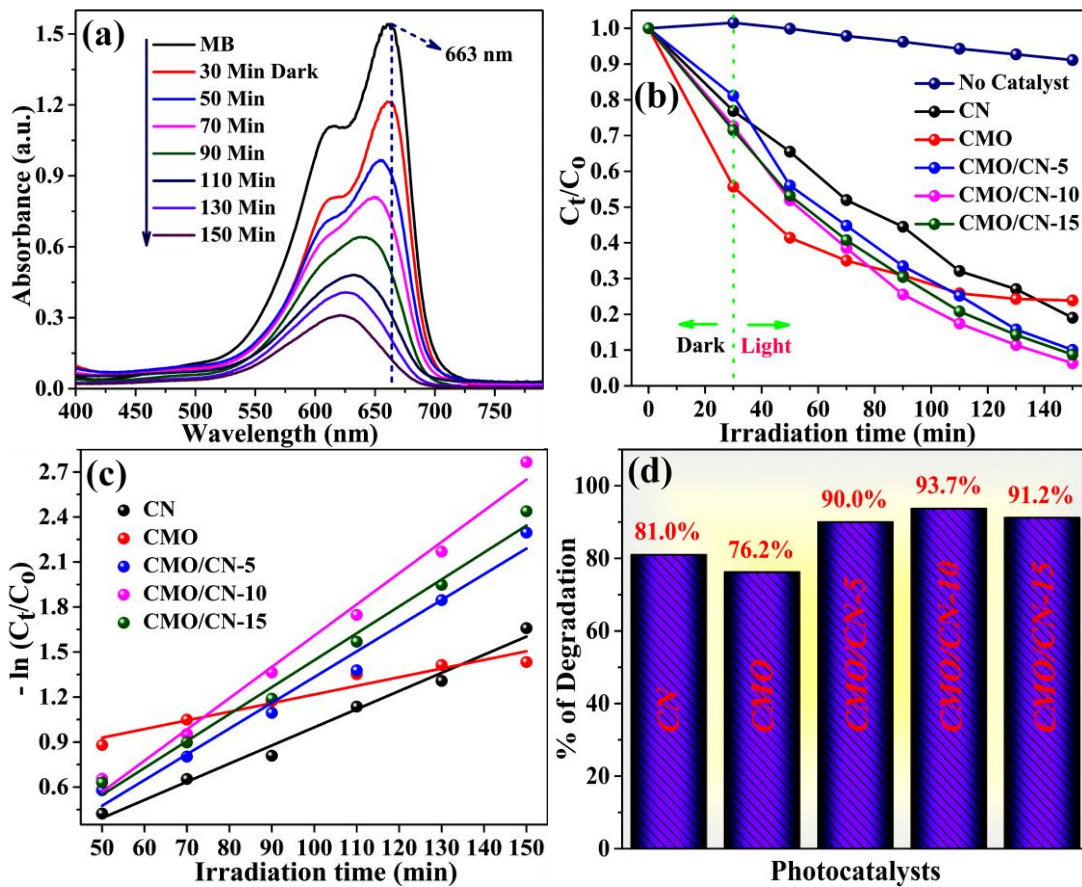


**Figure 3.7:** (a) Time dependent UV-Visible absorption spectra for photocatalytic degradation of MB over the CMO/CN-10 composite photocatalyst, (b) comparison of photocatalytic activity of synthesized CN, CMO, and CMO/CN composite photocatalysts in the terms of degradation curves, (c) first order kinetics graphs of CN, CMO and CMO/CN composite photocatalysts, and (d) percentage of MB degradation of CN, CMO and CMO/CN composite photocatalysts..

The percentage of degradation of MB for the CN, CMO, and CMO/CN composite photocatalysts are shown in Figure 3.7(d). Amongst the analyzed samples, the CMO/CN-10 has showed the highest MB degradation performance of 93.7 % which is higher than the CN (81.0%), CMO (76.2%), and remaining composites of CMO/CN. Interestingly, CMO has shown better photocatalytic activity even though bandgap is more than 3 eV. This is because we have used 35 W Xe arc lamp, which is the source for a small amount of UV light, and more amount of visible light. We have not used any cut off filters for exact wavelength (420 nm for visible light source)

for photocatalytic dye degradation studies. Moreover, with the increasing amount of CMO in CMO/CN composites, the photocatalytic activity was increased for CMO/CN-10 then decreased gradually. This may be explained by the following reasons. With the increasing amount of CMO in composites of CMO/CN, the photoactive sites on the CN may be blocked by CMO and self-agglomeration by the addition of an excess amount of CMO to CN causes the reduction in degradation activity. These findings clearly show that the formation of strong interactions between CN and CMO in the CMO/CN composite photocatalyst and their enhanced photocatalytic activities.

To study the effect of temperature on MB dye degradation efficiency for CMO/CN-10 composite photocatalyst, we conducted degradation experiments under same light source (35 W Xe arc lamp), with the help of jacketed beaker having water circulation arrangement to maintain the higher temperatures (40 °C and 50 °C). The temperature dependent photodegradation curves of MB over CMO/CN-10 was shown in Figure 3.8(a). At the higher temperatures degradation efficiency was increasing dramatically. At 30 °C the photodegradation was 97.3% while at 40 °C and 50 °C the degradation was 98.5 % and 99.09% respectively. Figure 3.8(b) depicts the rate constant for the degradation of MB dye at different temperatures, the rate constant was obtained from the slope of  $-\ln(C_t/C_0)$  vs irradiation time. The obtained linear fitted lines show that the MB degradation follows the pseudo first order kinetics. The rate constant values are increased significantly with increasing the temperature as follows,  $2.08 \times 10^{-2} \text{ min}^{-1}$  at 30 °C,  $2.25 \times 10^{-2} \text{ min}^{-1}$  at 40 °C, and  $2.45 \times 10^{-2} \text{ min}^{-1}$  at 50 °C. This rapid enhancement in the degradation process and rate constant values of MB can be ascribed to the effect of applied thermal energy to the reaction system leads to enhancement in the collisions between the reacting molecules. But temperature do not show more effect on the photodegradation efficiency as well as the rate of the reaction of MB dye. The most important parameter is the activation energy. In general, all the molecules are having energy, which should be more than activation energy then only fruitful collisions will happen between the two molecules. If an increase in the temperature of the reaction system, which leads to more amount of MB molecules adsorbed on the surface of the catalyst. In other terms, more active sites on the surface of the catalyst to further enhancement in the degradation of MB. Therefore, more photodegradation performance were observed for MB with the increasing in temperature. With the help of rate constant values at different temperatures, the activation parameters were calculated.

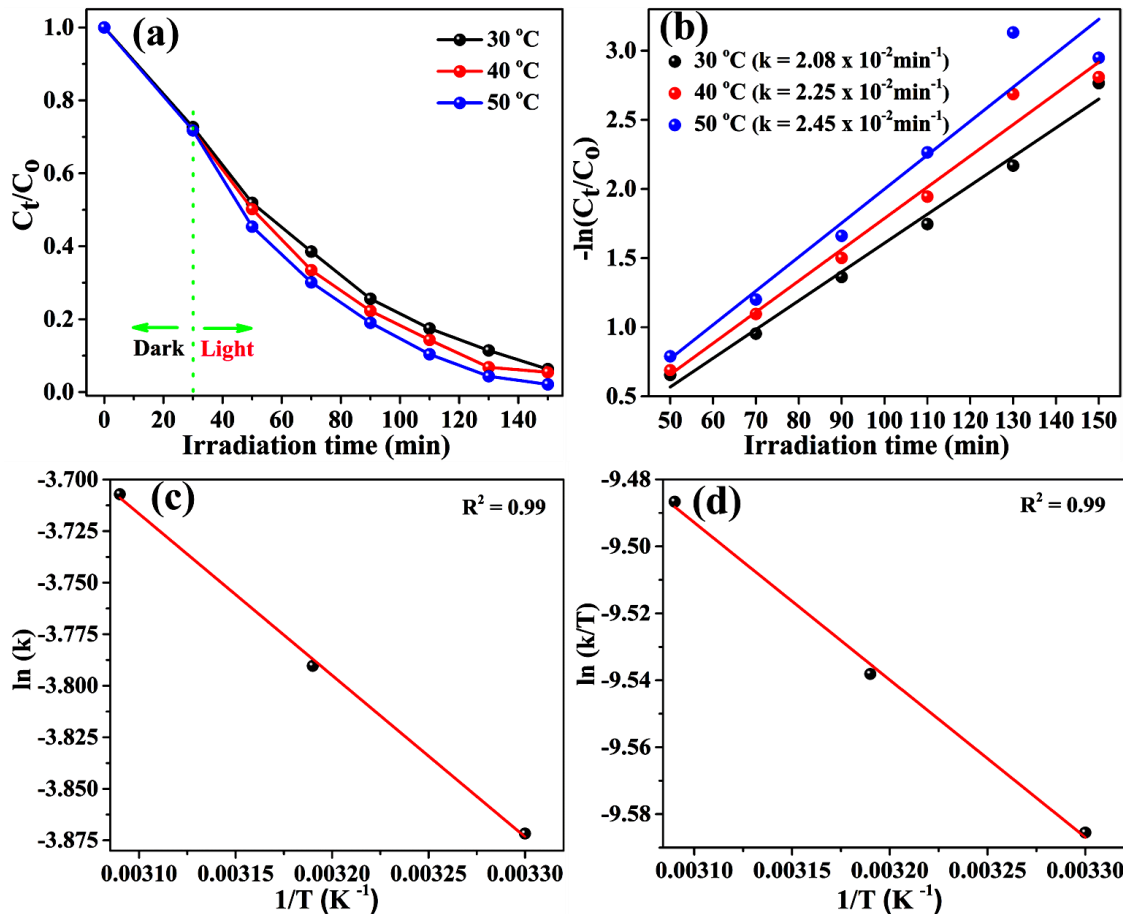


**Figure 3.8:** Curves of  $C_t/C_0$  (a), and  $-\ln(C_t/C_0)$  (b), as a function of time at different temperatures, the plot between  $\ln(k)$  vs  $1/T$  (c), and the plot between  $\ln(k/T)$  vs  $1/T$  (d).

As shown in Figure 3.8(c), the Activation energy were determined from the Arrhenius equation. The plot of  $\ln k$  vs  $(1/T)$  gives a linear slope. This slope value is substituted in the Arrhenius equation as shown below (equations 3.4 and 3.5).

$$\ln k = \ln A - E_a/RT \quad (3.4)$$

$$\ln \left( \frac{k}{T} \right) = \ln \left( \frac{K}{h} \right) - \frac{\Delta H}{RT} + \frac{\Delta S}{R} \quad (3.5)$$

Where 'k' is the rate constant of photodegradation reaction, 'A' is Arrhenius factor, 'R' is the universal gas constant, ' $E_a$ ' is the activation energy, 'h' is Plank's constant, 'K' is the Boltzmann constant, 'T' is the temperature in (Kelvin).  $\Delta S$  and  $\Delta H$  are the entropy and enthalpy of activation respectively. As depicted in Figure 3.8(d), entropy and enthalpy were calculated from the slope and intercepts of  $(\ln k/T)$  vs  $1/T$  plot respectively. Gibbs free energy of activation was calculated using the following (equation 3.6).

$$\Delta G = \Delta H - T\Delta S \quad (3.6)$$

The values of thermodynamic parameters  $\Delta S$  were negative and for  $\Delta H$ , and  $\Delta G$  were positive which indicates the photodegradation process follows non-spontaneous, endothermic and endergonic respectively. The detailed thermodynamic parameters are shown in the Table 3.4.

**Table 3.4:** Calculated values of activation energy, enthalpy, entropy and Gibbs free energy by Photodegradation at different temperatures of fabricated CMO/CN composite photocatalyst.

Temperature (°C)	$E_a$ (kJ mole <sup>-1</sup> )	$\Delta H$ (kJ mole <sup>-1</sup> )	$\Delta S$ (kJ mole <sup>-1</sup> K <sup>-1</sup> )	$\Delta G$ (kJ mole <sup>-1</sup> )
30	6.510	3.908	-0.043	16.937
40				17.367
50				17.797

To further investigate the role of reactive species, which are responsible for the photodegradation process of MB were studied by the scavenger test, with the addition of different quenchers to the reaction mixture, such as EDTA-2Na for  $h^+$ , isopropyl alcohol for hydroxyl radicals ( $\cdot OH$ ), benzoquinone for superoxide anion radicals ( $O_2^{\cdot-}$ ), and silver nitrate for electrons ( $e^-$ ) respectively.<sup>[68-70]</sup> As shown in Figure 3.9(a), for the CMO/CN-10, the degradation performance was less effected after the addition of benzoquinone, which means that  $O_2^{\cdot-}$  plays a minor role in the degradation process. After the addition of silver nitrate more degradation was observed indicating that  $e^-$  s are not responsible for the degradation process. With the addition of isopropyl alcohol, the degradation efficiency of CMO/CN-10 was suppressed dramatically and suggesting that  $\cdot OH$  are the main reactive species in MB degradation.<sup>[71]</sup> However, the slight decrease in the degradation of MB was observed by the addition of EDTA-2Na to the reaction which tells that  $h^+$  also act as one of the main reactive species. More interestingly, synthesized composite photocatalyst CMO/CN-10 was more stable as shown in Figure 3.9(b).

To estimate the stability of CMO/CN-10 composite photocatalyst was used up to four successive cycles, the same photocatalyst was washed thoroughly with water and ethanol several times and dry it overnight at 60 °C in hot air oven prior to run each cycle. The degradation percentage of the first cycle to fourth cycle as follows 93.71 % > 90.04 % > 89.86 % > 87.78 %. Figure 3.9(c) depicts the PXRD patterns of before and after photodegradation of CMO/CN-10 composite photocatalyst and Figure 3.9(d) shows the SEM image of after photodegradation of

CMO/CN-10 composite photocatalyst. It indicates that there is no change in crystal structure and morphology after the four successive runs.

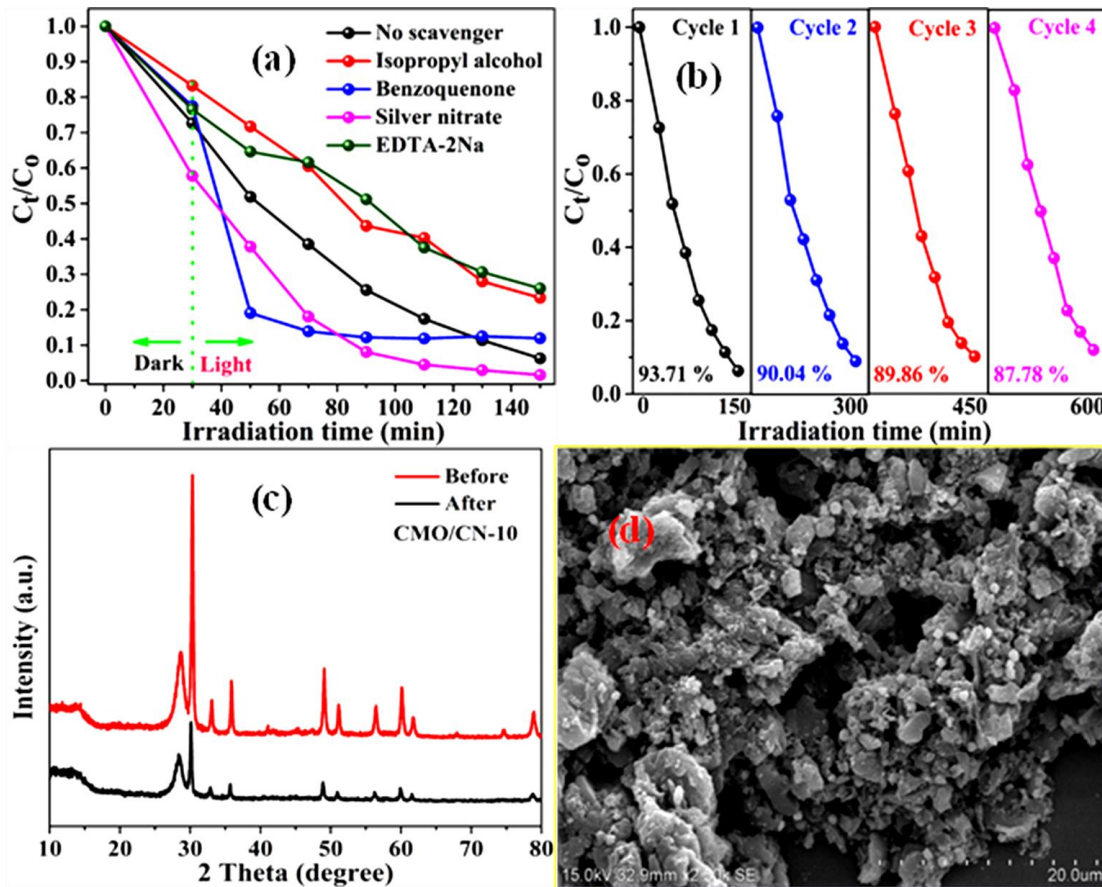


**Figure 3.9:** (a) Trapping experiments, (b) stability of CMO/CN-10 composite photocatalyst up to 4 cycles, (c) PXRD pattern of CMO/CN-10 composite photocatalyst before and after photodegradation of MB, and (d) SEM image of CMO/CN-10 composite photocatalyst after photodegradation of MB.

### 3.3.7 Probable reaction mechanism for dye degradation

In general, the mobility of photogenerated electrons and holes in the hybrid composite photocatalysts mainly based on the respective band edge positions of their constituents. In the present study, for the CN and CMO, VB and CB, edge potentials are determined from the following (equations 3.7 and 3.8).

$$E_{vb} = \chi - E^0 + 0.5 (E_g) \quad (3.7)$$

$$E_{cb} = E_{vb} - E_g \quad (3.8)$$

Where  $\chi$  is the electronegativity of CMO or CN,  $E^o$  is the energy of free electrons on the hydrogen scale (4.5 eV), and  $E_g$  is the bandgap of CMO or CN calculated from UV-Vis DRS data. The calculated VB and CB of CN and CMO are (+1.46 and -1.22 eV) and (+0.04 and +3.35 eV) respectively.<sup>[72]</sup>

Based on their VB edge potentials and bandgap energies we proposed two possible charge transfer mechanisms at the interface, one is a conventional double transfer mechanism and another is the Z-scheme transfer mechanism. If the CMO/CN-10 composite photocatalyst follows a double-transfer mechanism the photoreduction reaction would take place at CB of CMO, and the photooxidation process at the VB of CN. But these expected processes might be not possible. Because photogenerated electrons in the CB of CN could easily transfer to the CB of CMO, and the holes remain at VB of CN and resulting photoreduction to be done at CB of CMO. But, as the CB of CMO (+0.04 eV) is less negative than the reduction potentials of the  $O_2/O_2^-$  (-0.33 eV).

Subsequently, photogenerated electrons on the CB of CMO will not reduce  $O_2$  to yield  $O_2^-$  besides VB of CN (+1.46 eV) is less positive than the oxidation potential of  $^-\text{OH}/\text{H}_2\text{O}$  (+2.72 eV). Consequential, holes which are present at VB of CN cannot oxidize  $^-\text{OH}/\text{H}_2\text{O}$  to  $^-\text{OH}$ . From the above, all findings and photo generated electron trapping experiment results support the Z-scheme mechanism rather than the conventional double charge transfer mechanism in the CMO/CN-10 composite photocatalyst.<sup>[73-76]</sup> Due to their suitable bandgap as well as light absorption capacities of both CMO and CN are excited together under the light illumination to generate holes in the VB and electrons in the CB, as shown in Figure 3.10. The photoexcited electrons in the CB of CMO can easily transfer to VB of CN through Z-scheme, due to the formation of heterojunction between the well matched band edges potentials of both CMO and CN. As result recombination of electron on CB of CMO suppressed by the formation of heterojunction via Z-scheme.<sup>[77,78]</sup> Besides, the formation of more electron cloud at CB of CN can easily participate in the photooxidation reaction by using dissolved  $O_2$  to yield  $O_2^-$  and accumulated holes at VB of CMO can directly generate  $^-\text{OH}$  from  $^-\text{OH}/\text{H}_2\text{O}$  by participating photoreduction reactions respectively. Because the CB potential of CN (-1.22 eV) is more negative than that of  $O_2/O_2^-$  (-0.33 eV), and VB potential of CMO (+3.35 eV) is more positive than the oxidation potential of  $^-\text{OH}/\text{H}_2\text{O}$  (+2.72 eV). Moreover, the energy gap between CB of CMO to CB of CN, and VB of CMO to VB of CN is more than that of CB of CMO to VB of CN. Because of this Z-Scheme mechanism is more facilitative than

conventional mechanism. In this way ‘ $h^+$ ’ and ‘ $\cdot OH$ ’ plays the foremost role and ‘ $O_2^-$ ’ relatively negligible role in the photodegradation of pollutant dye MB.

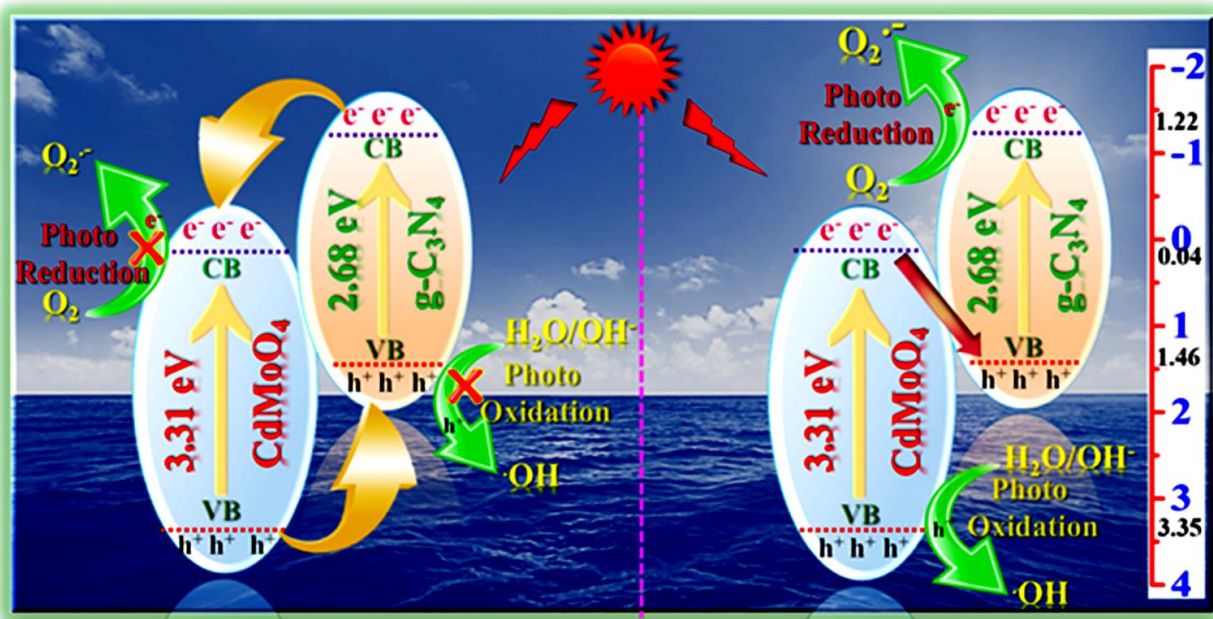


**Figure 3.10:** Tentative photocatalytic dye degradation mechanism of CMO/CN-10 composite photocatalyst.

### 3.4 Conclusions

In summary, we have successfully fabricated a versatile CMO/CN composite photocatalysts via a facile *in-situ* hydrothermal method. The optimized CMO/CN composite photocatalysts displayed remarkable photoelectrocatalytic OER and photocatalytic degradation of MB dye pollutant. CMO/CN-10 composite photocatalyst have shown less Tofel value and small charge transfer resistance ( $R_{ct}$ ) behavior with highest OER performance. Due to the formation of strong heterojunction between the components in CMO/CN composite that facilitate the interfacial charge transfer to suppress the direct recombination of photogenerated electron hole pairs, together with enhanced light absorption capacity. The trapping experiments supported that ( $\cdot OH$ ) and ( $h^+$ ) played a major role, whereas ( $O_2^-$ ) played minor roles in the degradation process. Notably, CMO/CN composites exhibited high recyclability and stability during successive recycles. Hence, the results provided in this work offer valuable insights into the improvement of photocatalysts for environmental remediation and sustainable energy generation applications.

### 3.5 References

- [1] H. Wang, T. Sun, L. Chang, P. Nie, X. Zhang, C. Zhao, X. Xue, *Electrochimica Acta* **2019**, *303*, 110–117.
- [2] S. Manchala, A. Gandomalla, N. R. Vempuluru, S. Muthukonda Venkatakrishnan, V. Shanker, *Journal of Colloid and Interface Science* **2021**, *583*, 255–266.
- [3] B. Zhang, S.-Y. Zhao, H.-H. Wang, T.-J. Zhao, Y.-X. Liu, L.-B. Lv, X. Wei, X.-H. Li, J.-S. Chen, *Chemical Communications* **2017**, *53*, 10544–10547.
- [4] M. Karimi-Nazarabad, E. K. Goharshadi, *Solar Energy Materials and Solar Cells* **2017**, *160*, 484–493.
- [5] C. Ho Lee, S. Uck Lee, in *Electrocatalysts for Fuel Cells and Hydrogen Evolution - Theory to Design*, IntechOpen, **2018**, p. 13.
- [6] M. Arif, G. Yasin, M. Shakeel, M. A. Mushtaq, W. Ye, X. Fang, S. Ji, D. Yan, *Materials Chemistry Frontiers* **2019**, *3*, 520–531.
- [7] J. Yang, D. Wang, H. Han, C. Li, *Accounts of Chemical Research* **2013**, *46*, 1900–1909.
- [8] B. Zhang, F. Li, F. Yu, X. Wang, X. Zhou, H. Li, Y. Jiang, L. Sun, *ACS Catalysis* **2014**, *4*, 804–809.
- [9] M. Shakeel, M. Arif, G. Yasin, B. Li, H. D. Khan, *Applied Catalysis B: Environmental* **2019**, *242*, 485–498.
- [10] K. Mamtani, D. Jain, D. Dogu, V. Gustin, S. Gunduz, A. C. Co, U. S. Ozkan, *Applied Catalysis B: Environmental* **2018**, *220*, 88–97.
- [11] A. Mishra, A. Mehta, S. Basu, N. P. Shetti, K. R. Reddy, T. M. Aminabhavi, *Carbon* **2019**, *149*, 693–721.
- [12] B. Petrie, R. Barden, B. Kasprzyk-Hordern, *Water Research* **2015**, *72*, 3–27.
- [13] S. Ouyang, Y. Bi, N. Umezawa, J. Ye, H. Tong, M. Oshikiri, *Advanced Materials* **2011**, *24*, 229–251.
- [14] T. P. Yoon, M. A. Ischay, J. Du, *Nature Chemistry* **2010**, *2*, 527–532.
- [15] S. Chu, A. Majumdar, *Nature* **2012**, *488*, 294–303.
- [16] P. D. Tran, L. H. Wong, J. Barber, J. S. C. Loo, *Energy & Environmental Science* **2012**, *5*, 5902.
- [17] A. Kubacka, M. Fernández-García, G. Colón, *Chemical Reviews* **2012**, *112*, 1555–1614.
- [18] W.-J. Ong, L.-L. Tan, Y. H. Ng, S.-T. Yong, S.-P. Chai, *Chemical Reviews* **2016**, *116*,

7159–7329.

- [19] X. Wang, K. Maeda, A. Thomas, K. Takanabe, G. Xin, J. M. Carlsson, K. Domen, M. Antonietti, *Nature Materials* **2009**, *8*, 76–80.
- [20] S. Cao, J. Low, J. Yu, M. Jaroniec, *Advanced Materials* **2015**, *27*, 2150–2176.
- [21] J. Fu, J. Yu, C. Jiang, B. Cheng, *Advanced Energy Materials* **2018**, *8*, 1701503.
- [22] W.-J. Ong, L.-L. Tan, S.-P. Chai, S.-T. Yong, A. R. Mohamed, *Nano Energy* **2015**, *13*, 757–770.
- [23] H. Huang, K. Xiao, N. Tian, F. Dong, T. Zhang, X. Du, Y. Zhang, *Journal of Materials Chemistry A* **2017**, *5*, 17452–17463.
- [24] J. Xue, S. Ma, Y. Zhou, Z. Zhang, M. He, *ACS Applied Materials & Interfaces* **2015**, *7*, 9630–9637.
- [25] S. Tonda, S. Kumar, S. Kandula, V. Shanker, *Journal of Materials Chemistry A* **2014**, *2*, 6772.
- [26] J. Ran, T. Y. Ma, G. Gao, X.-W. Du, S. Z. Qiao, *Energy & Environmental Science* **2015**, *8*, 3708–3717.
- [27] J. Liu, B. Cheng, J. Yu, *Phys. Chem. Chem. Phys.* **2016**, *18*, 31175–31183.
- [28] W.-S. Wang, L. Zhen, C.-Y. Xu, W.-Z. Shao, *Crystal Growth & Design* **2009**, *9*, 1558–1568.
- [29] L. Zhen, W. S. Wang, C. Y. Xu, W. Z. Shao, M. M. Ye, Z. L. Chen, *Scripta Materialia* **2008**, *58*, 461–464.
- [30] H. Liu, J. Huang, J. Chen, J. Zhong, J. Li, Q. Yang, D. Ma, *Materials Letters* **2018**, *228*, 421–423.
- [31] P. Madhusudan, J. Zhang, J. Yu, B. Cheng, D. Xu, J. Zhang, *Applied Surface Science* **2016**, *387*, 202–213.
- [32] J. Huang, H. Liu, J. Zhong, Q. Yang, J. Chen, J. Li, D. Ma, R. Duan, *Solid State Sciences* **2018**, *80*, 147–154.
- [33] H. Zhang, C.-G. Niu, X.-J. Wen, Y. Wang, G.-M. Zeng, *Catalysis Communications* **2016**, *86*, 124–128.
- [34] P. Madhusudan, J. Zhang, B. Cheng, J. Yu, *Physical Chemistry Chemical Physics* **2015**, *17*, 15339–15347.
- [35] B. Chai, J. Yan, G. Fan, G. Song, C. Wang, *Chinese Journal of Catalysis* **2020**, *41*, 170–

179.

- [36] L. Zhao, L. Zhang, H. Lin, Q. Nong, M. Cui, Y. Wu, Y. He, *Journal of Hazardous Materials* **2015**, *299*, 333–342.
- [37] J. Li, M. Zhang, Q. Li, J. Yang, *Applied Surface Science* **2017**, *391*, 184–193.
- [38] S. Kumar, S. Tonda, A. Baruah, B. Kumar, V. Shanker, *Dalton Trans.* **2014**, *43*, 16105–16114.
- [39] W. S. Wang, L. Zhen, C. Y. Xu, W. Z. Shao, Z. L. Chen, *Journal of Alloys and Compounds* **2012**, *529*, 17–20.
- [40] M. Groenewolt, M. Antonietti, *Advanced Materials* **2005**, *17*, 1789–1792.
- [41] S. Manchala, V. S. R. K. Tandava, L. R. Nagappagari, S. Muthukonda Venkatakrishnan, D. Jampaiah, Y. M. Sabri, S. K. Bhargava, V. Shanker, *Photochemical & Photobiological Sciences* **2019**, *18*, 2952–2964.
- [42] W.-K. Jo, S. Kumar, S. Eslava, S. Tonda, *Applied Catalysis B: Environmental* **2018**, *239*, 586–598.
- [43] S. Mostafa Hosseinpour-Mashkani, M. Maddahfar, A. Sobhani-Nasab, *Journal of Materials Science: Materials in Electronics* **2016**, *27*, 474–480.
- [44] J. Lin, Z. Zeng, Q. Wang, *Inorganica Chimica Acta* **2013**, *408*, 59–63.
- [45] N. P. Singh, N. R. Singh, N. M. Singh, *Optik* **2018**, *156*, 365–373.
- [46] S. Tonda, S. Kumar, M. Bhardwaj, P. Yadav, S. Ogale, *ACS Applied Materials & Interfaces* **2018**, *10*, 2667–2678.
- [47] L. Zhao, L. Zhang, H. Lin, Q. Nong, M. Cui, Y. Wu, Y. He, *Journal of Hazardous Materials* **2015**, *299*, 333–342.
- [48] Y. Liu, L. Ren, X. Qi, Y. Wang, X. Liu, J. Zhong, *RSC Advances* **2014**, *4*, 8772.
- [49] S. Tonda, W.-K. Jo, *Catalysis Today* **2018**, *315*, 213–222.
- [50] A. Verma, D. P. Jaihindh, Y.-P. Fu, *Dalton Transactions* **2019**, *48*, 8594–8610.
- [51] L. Lin, C. Hou, X. Zhang, Y. Wang, Y. Chen, T. He, *Applied Catalysis B: Environmental* **2018**, *221*, 312–319.
- [52] D. Li, S. Zuo, H. Xu, J. Zan, L. Sun, D. Han, W. Liao, B. Zhang, D. Xia, *Journal of Colloid and Interface Science* **2018**, *531*, 28–36.
- [53] A. Verma, S. Kumar, W.-K. Chang, Y.-P. Fu, *Dalton Transactions* **2020**, *49*, 625–637.
- [54] L. Zhao, L. Zhang, H. Lin, Q. Nong, M. Cui, Y. Wu, Y. He, *Journal of Hazardous Materials*

2015, 299, 333–342.

[55] B. D. Adams, C. K. Ostrom, A. Chen, *Langmuir* **2010**, 26, 7632–7637.

[56] C. Zeng, A. Ramos-Ruiz, J. A. Field, R. Sierra-Alvarez, *Journal of Environmental Management* **2015**, 154, 78–85.

[57] S. Richards, M. A. Baker, M. D. Wilson, A. Lohstroh, P. Seller, *Optics and Lasers in Engineering* **2016**, 83, 116–125.

[58] M. Morales-Luna, S. A. Tomás, M. A. Arvizu, M. Pérez-González, E. Campos-Gonzalez, *Journal of Alloys and Compounds* **2017**, 722, 938–945.

[59] R. Adhikari, S. Malla, G. Gyawali, T. Sekino, S. W. Lee, *Materials Research Bulletin* **2013**, 48, 3367–3373.

[60] J. Bi, Z. Zhou, M. Chen, S. Liang, Y. He, Z. Zhang, L. Wu, *Applied Surface Science* **2015**, 349, 292–298.

[61] T. Anitha, A. E. Reddy, Y. Anil Kumar, Y.-R. Cho, H.-J. Kim, *Dalton Transactions* **2019**, 48, 10652–10660.

[62] D. P. Jaihindh, A. Manikandan, Y. Chueh, Y. Fu, *ChemSusChem* **2020**, 13, 2726–2738.

[63] A. Verma, D. P. Jaihindh, Y.-P. Fu, *Dalton Transactions* **2019**, 48, 8594–8610.

[64] L. Wang, Y. Tong, J. Feng, J. Hou, J. Li, X. Hou, J. Liang, *Sustainable Materials and Technologies* **2019**, 19, e00089.

[65] L. Wang, W. Si, Y. Tong, F. Hou, D. Pergolesi, J. Hou, T. Lippert, S. X. Dou, J. Liang, *Carbon Energy* **2020**, 2, 223–250.

[66] J. Jiang, A. Zhang, L. Li, L. Ai, *Journal of Power Sources* **2015**, 278, 445–451.

[67] Q. Zhou, Y. Chen, G. Zhao, Y. Lin, Z. Yu, X. Xu, X. Wang, H. K. Liu, W. Sun, S. X. Dou, *ACS Catalysis* **2018**, 8, 5382–5390.

[68] R. He, K. Cheng, Z. Wei, S. Zhang, D. Xu, *Applied Surface Science* **2019**, 465, 964–972.

[69] X. Li, J. Xiong, Y. Xu, Z. Feng, J. Huang, *Chinese Journal of Catalysis* **2019**, 40, 424–433.

[70] R. He, J. Zhou, H. Fu, S. Zhang, C. Jiang, *Applied Surface Science* **2018**, 430, 273–282.

[71] Y. He, J. Cai, T. Li, Y. Wu, H. Lin, L. Zhao, M. Luo, *Chemical Engineering Journal* **2013**, 215–216, 721–730.

[72] R. Dhanabal, S. Velmathi, A. C. Bose, *Catalysis Science & Technology* **2016**, 6, 8449–8463.

[73] H. Yang, P. Wang, D. Wang, Y. Zhu, K. Xie, X. Zhao, J. Yang, X. Wang, *ACS Omega*

2017, 2, 3766–3773.

- [74] F. Paquin, J. Rivnay, A. Salleo, N. Stingelin, C. Silva, *J. Mater. Chem. C* **2015**, 3, 10715–10722.
- [75] J. Aliaga, N. Cifuentes, G. González, C. Sotomayor-Torres, E. Benavente, *Catalysts* **2018**, 8, 374.
- [76] H. Lin, Y. Liu, J. Deng, K. Zhang, X. Zhang, S. Xie, X. Zhao, J. Yang, Z. Han, H. Dai, *Journal of Environmental Sciences* **2018**, 70, 74–86.
- [77] C. Li, S. Yu, H. Che, X. Zhang, J. Han, Y. Mao, Y. Wang, C. Liu, H. Dong, *ACS Sustainable Chemistry & Engineering* **2018**, 6, 16437–16447.
- [78] M. Amiri, K. Dashtian, M. Ghaedi, S. Mosleh, R. Jannesar, *New Journal of Chemistry* **2019**, 43, 1275–1284.



## Chapter IV

# Facile fabrication of novel $\text{SrMoO}_4/\text{g-C}_3\text{N}_4$ hybrid composite for high-performance photocatalytic degradation of dye pollutant under sunlight



## Chapter IV

# Facile Fabrication of Novel SrMoO<sub>4</sub>/g-C<sub>3</sub>N<sub>4</sub> Hybrid Composite for High-Performance Photocatalytic Degradation of Dye Pollutant under Sunlight

### 4.1 Introduction

Due to the globalization and industrialization, the present world is facing the severe environmental and energy issues.<sup>[1-3]</sup> The industries like textile, leather, printing, and paper were generating pollutants and these are the major sources which are responsible for water and air contamination. These pollutants are hazardous to human and animal health even at their extreme trace concentration.<sup>[4-6]</sup> Hitherto, several methods such as photocatalytic degradation, membrane filtration, adsorption, flocculent precipitation, biological treatment, and so on were adopted for removal of water pollutants.<sup>[7-11]</sup> In comparison to these methods, the photocatalytic degradation method is widely preferred in the recent years, This is because, it is cost effective method as it employs the utilization of inexhaustible solar radiation as energy source and is found to be efficient, simple and convenient method.<sup>[12]</sup> Even though, numerous photocatalysts have been developed so far, nevertheless, designing of new photocatalyst is still on going and focused area of research with an objective to achieve more affordable photocatalyst with improved performance.

Amongst the numerous kinds of photocatalysts reported, SMO is a unique scheelite type material with the tetragonal phase is reported recently. SMO is widely used material in photoluminescence, magnetic materials, and photocatalytic applications owing to its intriguing crystal structure and optical properties.<sup>[13-17]</sup> However, the major limitation which restricts its exploration as a better photocatalyst is its energy bandgap of ~3.1 eV and therefore responses only to UV light in the solar spectrum.<sup>[18-20]</sup>

On contrary, G-CN with a graphene-like skeleton where three nitrogen atoms are alternatively arranged in a six-membered carbon ring with  $sp^2$  hybridization and the major advantage in utilizing G-CN is its adequate bandgap of ~2.7 eV, showing response to visible light.<sup>[21]</sup> In addition, abundance, non-toxicity, 2D layered structures, easy fabrication, high chemical, and thermal stability and distinctive optical properties are indeed reasons for recognizing g-CN as an excellent material for its numerous applications in various fields.<sup>[22-24]</sup> like

photocatalytic hydrogen fuel generation from water splitting, photodegradation of water/air pollutants, CO<sub>2</sub> reduction to useful hydrocarbons, antibiotic, organic transformations, and fuel cells.<sup>[25–31]</sup> As reported G-CN is a nonmetallic photocatalyst and the photocatalytic performance of G-CN is very limited for practical applications, as a result of low visible light absorption capacity and fast charge carriers recombination.<sup>[22]</sup> To enhance the photocatalytic efficiency of G-CN, several approaches have been developed including composite photocatalysts fabrication with another semiconductor, doping with metal ions, and co-catalyst loading. Among all these approaches, the most frequently used method for preparing composite photocatalysts is with energetically identical two semiconductors, where the developed composite photocatalysts allows faster separation and transfer of photo-induced excitons, further resulting in improvement of photocatalytic performance under visible light.<sup>[32–40]</sup>

In the present investigation, by employing the visible-light active G-CN and UV light-active SMO semiconductors, SMO/G-CN organic-inorganic hybrid composites were prepared for the first time with varying weight percentages of SMO and G-CN. The synthesized SMO/G-CN hybrid composite photocatalysts offer an excellent photocatalytic performance under sunlight due to low recombination and high photo-induced excitons separation efficiency between G-CN and SMO. Moreover, a most plausible photocatalytic dye degradation mechanism has been illustrated.

## 4.2 Experimental section

### 4.2.1 Materials

Strontium nitrate (Merck, 99.0%), ammonium molybdate tetrahydrate (Finar, AR grade), ethylene glycol, (SDFCL, 99.0%). Rhodamine B (Sigma, 95.0%), ammonium oxalate (Merck 99.0%), tertiary butyl alcohol (Merck, Emsure, ACS, Reagent for analysis) melamine (Otto Khemi, 98.0%), All the chemicals used in this work are no need for further purification which are analytically pure. All the aqua solutions were prepared by using double distilled (DD) water.

### 4.2.2 Synthesis of G-CN

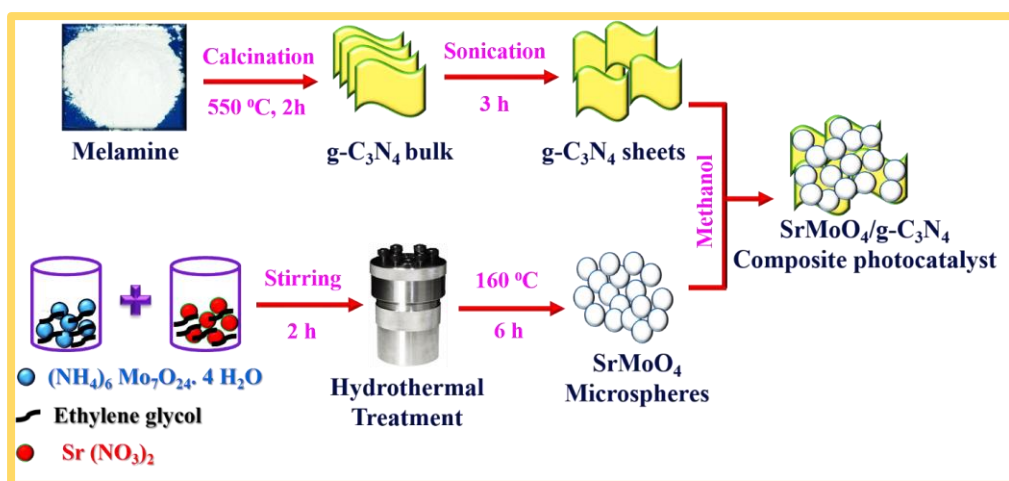
By well-known thermal condensation method G-CN was synthesized. Briefly, in an alumina boat, required amount of melamine was taken and kept in a tubular furnace with a heating rate of 5 °C per min, and subjected to calcinated at 550 °C for 2 h under a static air environment. At the end of the reaction, the light yellow-colored powder was obtained.

#### 4.2.3 Synthesis of SMO

By a simple hydrothermal method the pure SMO was synthesized. In brief, taken 2 mmol of  $\text{Sr}(\text{NO}_3)_2$  in a beaker containing 30 mL of ethylene glycol and meanwhile excess amount of  $(\text{NH}_4)_6\text{Mo}_7\text{O}_{24} \cdot 4\text{H}_2\text{O}$  was added in another beaker contains 30 mL ethylene glycol and stirred separately for 30 min. Further, the ammonium molybdate solution was transferred to the strontium nitrate solution drop by drop and continue stirring for 2 h at R.T. a white color jelly type solution was formed. The total mixture of solution was transferred into an autoclave hydrothermal bomb and kept in a microprocessor oven with the temperature of 160 °C for 6 h. After completion of the reaction, the attained product was centrifuged with ethanol thrice and dried overnight in a hot air oven.

#### 4.2.4 Synthesis of SMO/G-CN composite photocatalysts

For the synthesis of SMO/G-CN composite photocatalysts, a simple mixing and heating methodology was followed. Concisely, the calculated amount of G-CN was added into the beaker with 100 mL methanol, then sonicated for 3 h to disperse the bulk G-CN to G-CN nanosheets. To the above solution, the required amount of synthesized SMO spherical microcrystals was added and stirred for 6 h at 80 °C. After evaporation of the methanol completely, the powder was collected. A series of SMO/G-CN composite with varied ratios of SMO to G-CN (5, 10, and 15 wt. % of SMO) were synthesized and denoted as SMO/G-CN-5, SMO/G-CN-10, and SMO/G-CN-15 respectively. The procedure for the synthesis of pure as well as composite photocatalysts is represented in the below scheme (4.1).



**Scheme 4.1:** Schematic illustration for the synthesis of pure G-CN, pure SMO, and SMO/G-CN composite photocatalysts.

#### **4.2.5 Electrochemical Impedance Spectroscopy (EIS)**

The Electrochemical measurements were performed in a three-electrode system controlled by potentiostat/galvanostat (CH Instrument USA) workstation. The electrodes are immersed in 2 mM  $K_3[Fe(CN)_6]$  + 0.1 molar KCl electrolyte, synthesized catalyst coated over glassy carbon electrode (CHI, USA; 3 mm diameter) with active surface area of  $0.071\text{ cm}^2$  as working electrode (WE), Ag/AgCl (in sat KCl) as reference electrode (RE), and platinum (Pt) as counter electrode (CE). Electrocatalyst ink was prepared by dissolving 10 mg of catalyst in 150  $\mu\text{l}$  of DI water with 20  $\mu\text{l}$  of 5% Nafion were added and ultrasonicated for 30 min. A known amount of catalyst was drop cast over the glassy carbon electrode and dried in room temperature.

#### **4.2.6 Photocatalytic Dye degradation experiments**

In order to examine the photocatalytic activities of synthesized pure G-CN, pure SMO, and SMO/G-CN composite photocatalysts under the sunlight RhB selected as a model organic pollutant. Photocatalytic experiments on the samples were carried out under similar conditions in April 2019 at NIT Warangal during 11 am to 2 pm, where the fluctuation of the sunlight intensity is minimal during this month. The concentration of dye used in the photocatalytic experiments is 5 ppm (5 mg/lit) solution and the amount of catalyst used is 0.1 g. Before starting the photocatalytic experiment, the dye solution containing catalyst was stirred under the dark condition for 30 min to instituting absorption and desorption between the catalyst and dye solution.

Afterward, the resultant solution was irradiated to the sunlight. During the photocatalytic experiment, every 3 min the test samples were collected and centrifuged to separate the catalyst from the dye solution for the analysis of degradation rate of dye pollutant by using UV Visible spectroscopy Analytic Jena (Specord 205). We performed the blank experiments without catalyst and in the absence of sunlight and conclude that there is no considerable degradation of RhB in both, which indicates that, for the photocatalytic studies both catalyst and solar light are the primary elements.

It is necessary to study the role of photo-reactive species to explain the possible reaction mechanism in the photocatalytic dye degradation process. To established the photo-reactive species, scavenger test was conducted in the presence of ammonium oxalate (AO, 10 mmol), tertiary butyl alcohol (TBA, 10 mmol), and  $N_2$  purging in a similar fashion. Here, AO act as a quencher for holes, TBA act as a quencher for hydroxyl radical, and  $N_2$  act as a quencher for superoxide radical anion.

## 4.3 Results and discussions

### 4.3.1 PXRD and FT-IR studies

PXRD patterns of the synthesized materials of pure G-CN, pure SMO, and SMO/G-CN composite photocatalysts were shown in Figure 4.1(a). The results reveals that, all the peaks corresponding to SMO observed in the spectrum which are in agreement with reported data of JCPDS card number '08-0482'.<sup>[41-43]</sup> From these results it can be concluded that SMO crystallizes in the tetragonal phase with  $a = b = 5.3940 \text{ \AA}$  and  $c = 12.0200 \text{ \AA}$  crystallographic parameters, and there were no other additional peaks which means no impurities were observed. For pure G-CN, the peaks appeared at  $13.25^\circ$  and  $27.54^\circ$  corresponds to (100) and (002) planes, respectively.<sup>[44]</sup>

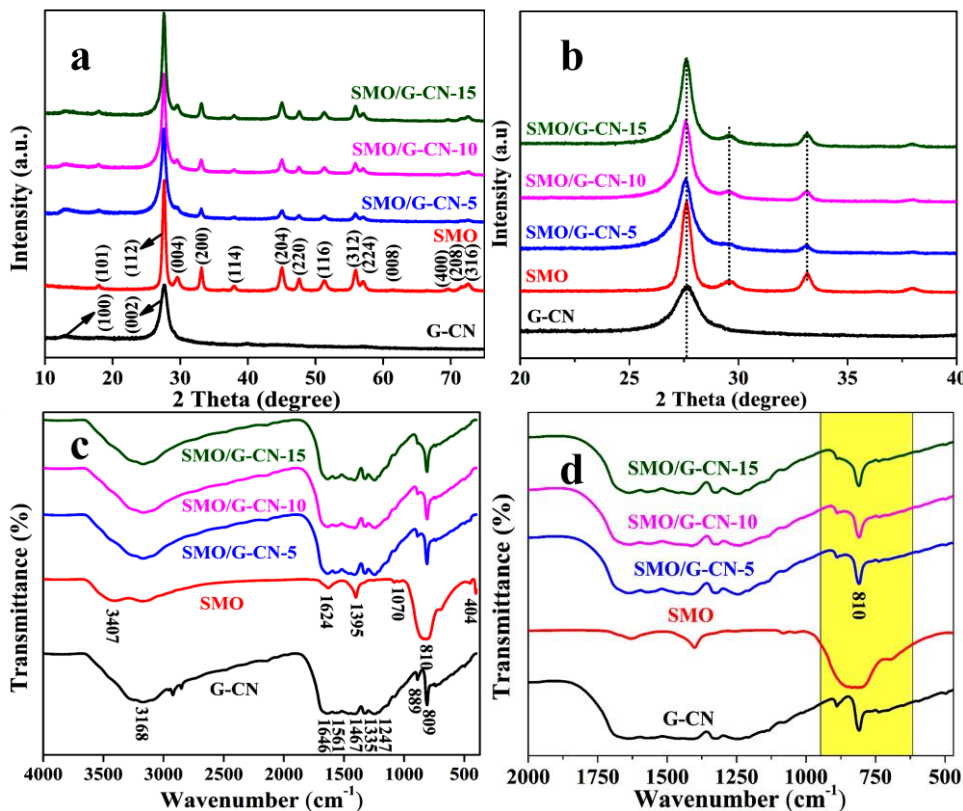


**Figure 4.1:** (a) PXRD, and (b) expanded PXRD patterns in the range of  $2\theta = 20^\circ - 40^\circ$  of pure G-CN, SMO and SMO/G-CN composite photocatalysts, (c) FT-IR analysis, and (d) expanded FT-IR patterns in the wavelength range of 2000 to  $570 \text{ cm}^{-1}$  of pure G-CN, SMO and SMO/G-CN composite photocatalysts.

Finally, in the case of SMO/G-CN nanocomposites, with an increase in the content of SMO to G-CN, a significant broadening of a diffraction peak at  $27.32^\circ$  of CN was observed and shown

in Figure 4.1(b). Further, the characteristic peak of G-CN at  $13.25^\circ$  corresponding to (100) was also observed in SMO/G-CN nanocomposites which clearly advocates the formation of SMO/G-CN composite photocatalysts.

Figure 4.1(c), depicts the FT-IR data of pure G-CN and SMO along with the series of composite photocatalysts respectively. The appearance of band at  $810\text{ cm}^{-1}$  for pure SMO is due to the asymmetric stretching vibrations of Mo-O in  $\text{MoO}_4^{2-}$  group. Also, the bending vibrational peak of the Mo-O-Mo bond has been observed at a wavenumber  $404\text{ cm}^{-1}$ . Further, two bands appeared at  $3407$  and  $1624\text{ cm}^{-1}$  owing to the stretching and bending vibrations of the hydroxide ( $\text{-OH}$ ) group of atmospheric  $\text{H}_2\text{O}$  molecules adsorbed on the surface of SMO particles.<sup>[45-47]</sup> The broad band observed at  $3168\text{ cm}^{-1}$  due to the stretching vibrations of N-H bond in G-CN. The strong vibrational band appearing in the range of  $1247$  to  $1637\text{ cm}^{-1}$  is mainly owing to the stretching vibrations of C-N and C=N bonds present in the  $\text{g-C}_3\text{N}_4$  molecule. Along with these peaks, a strong peak at  $809\text{ cm}^{-1}$  has also been observed in the spectrum, this peak is attributed to vibrations originated from the S-triazine ring present in the G-CN molecule<sup>[48-51]</sup>. It is obvious that all the characteristic peaks of G-CN, as well as SMO, are also present in the FT-IR spectrum of the SMO/G-CN composite photocatalysts synthesized in the present study. It is worth to mention that, the peak appearing at  $810\text{ cm}^{-1}$  in composites broaden upon increasing the amount of G-CN in the composites as shown in Figure 4.1(d). This clearly emphasizes the successful formation of SMO/G-CN composite photocatalysts.

#### **4.3.2. FE-SEM, EDS, and elemental mapping studies**

The morphology and elemental analysis of pure G-CN, pure SMO, and SMO/G-CN-10 composite photocatalysts were studied by FE-SEM, and the corresponding images were depicted in Figure 4.2(a-f). The FE-SEM images for pure G-CN in Figure 4.2(a-b) are the clear indication of its sheet-like morphology. Pure SMO in Figure 4.2(c-d), display their spherical shapes. These SMO microspheres are composed of numerous small and spherical nanoparticles with a rough surface. The FE-SEM images of SMO/G-CN-10 composite catalyst were shown in Figure 4.2(e-f). It can be seen from these images that the SMO microspheres are well dispersed on G-CN sheets, which indicates that the preparation methodology does not influence the morphology of SMO microspheres.

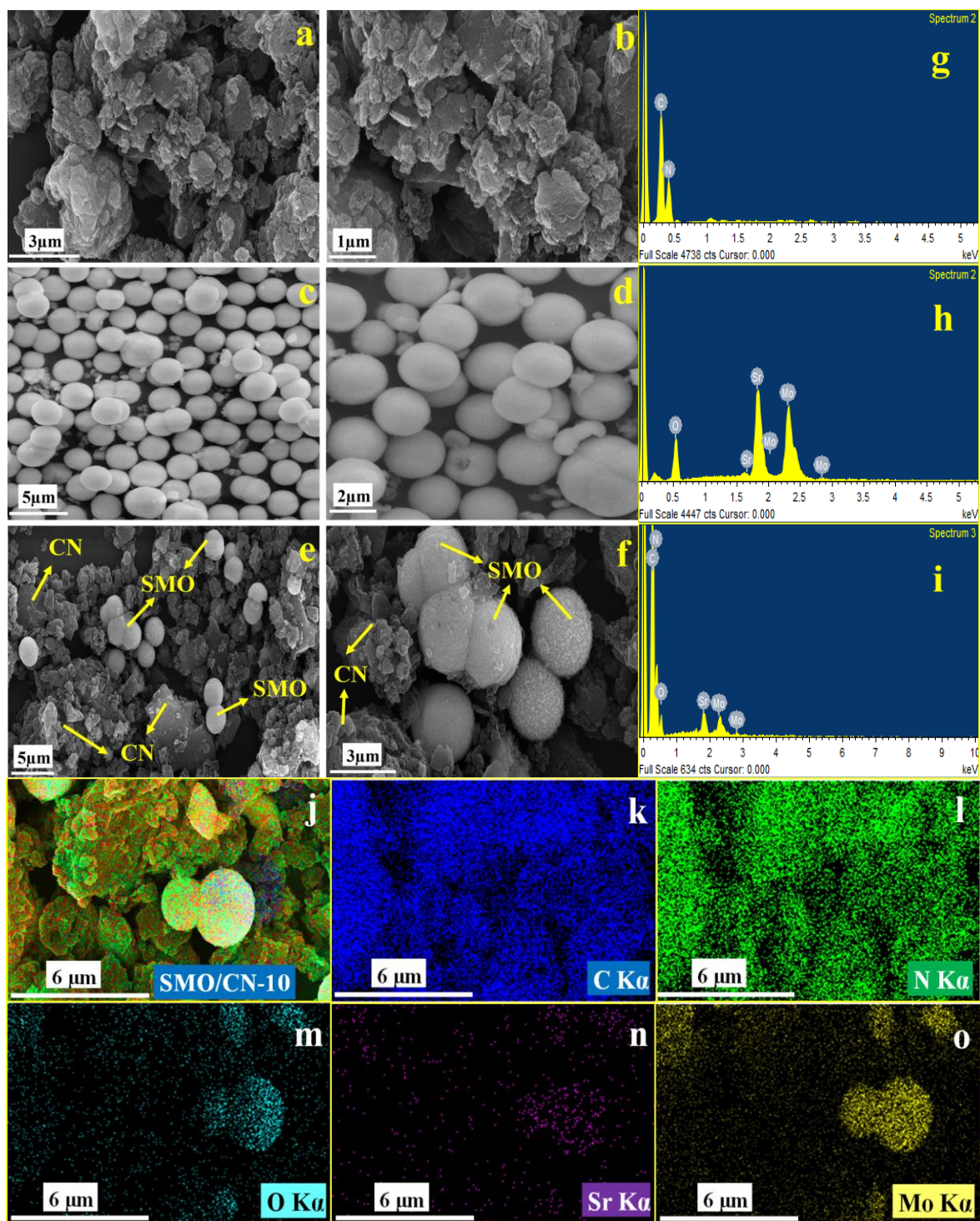


**Figure 4.2:** (a-b) FE-SEM images of pure G-CN sheets, (c-d) pure SMO, (e-f) SMO/G-CN-10 composite photocatalyst, (g) EDS elemental analysis of pure G-CN, (h) pure SMO, (i) SMO/G-CN-10 composite photocatalyst, and (j-o) EDS elemental mapping images of SMO/G-CN-10 composite photocatalyst.

EDS elemental analysis of the synthesized composite photocatalysts are shown in Figure 4.2(g-i), reveal that the respective elements which are present in pure G-CN and pure SMO remain in the SMO/G-CN-10 composite photocatalysts. As displayed in Figure 4.2(j-o), the EDS elemental mapping images of SMO/G-CN-10 composite photocatalyst indicates the presence of all corresponding elements like C, N, O, Sr, and Mo in the SMO/G-CN composite photocatalysts that are found in their ancestral materials i.e. SMO and G-CN.

### 4.3.3 XPS analysis

The chemical composition and oxidation states of the respective elements present in the synthesized SMO/G-CN-10 composite photocatalyst was estimated with an aid of XPS analysis. The XPS survey spectrum of SMO/G-CN-10 composite photocatalyst as depicted in Figure 4.3(a), confirms the presence of Sr, Mo, O, C, and N elements. The high-resolution C 1s spectra as can be seen in Figure 4.3(b), reveals the presence of two dissimilar peaks at a binding energy of 289.03 eV and 284.73 eV. These peaks can be ascribed to the nitrogen-containing aromatic ring which is having  $sp^2$  hybridized carbon (N-C=N) and  $sp^2$  C-C bonds, which denotes the main carbon environment in G-CN. The high-resolution N 1s spectrum demonstrated in Figure 4.3(c) can be divided into three peaks at 395.95 eV, 398.44 eV, and 400.91 eV. The major peak at 395.95 eV can be attributed to  $sp^2$  hybridized nitrogen in triazine rings of G-CN (C-N=C), the peaks at 398.44 eV and 400.91 eV are attributed to bridged ternary nitrogen in N-(C)<sub>3</sub> and amino functional groups (N-H), respectively.

Moreover, the C 1s  $sp^2$  hybridized (N-C=N, 289.03 eV) and two N 1s species in (C-N=C, 395.95 eV) and N-(C)<sub>3</sub> (398.44 eV), are structural conformational building blocks for G-CN.<sup>[52-54]</sup> Figure 4.3(d), represents the high-resolution XPS spectra of Sr 3d which can be resolved further into 3d<sub>3/2</sub> (131.41 eV) and 3d<sub>5/2</sub> (129.68 eV) which represents Sr ion in the '2+' oxidation state. The high-resolution XPS spectra of Mo 3d shown in the Figure 4.3(e), unveils that Mo is in the '6+' oxidation state with Mo 3d<sub>3/2</sub> (232.11 eV) and Mo 3d<sub>5/2</sub> (229.07 eV) binding energy values.<sup>[55]</sup> Figure 4.3(f), shows the high-resolution XPS spectrum of O 1s, 528.70 eV, and 536.07 eV corresponds to the O-Sr and O-H groups that appears because of the absorbed H<sub>2</sub>O on the surface of the catalyst.<sup>[56]</sup> All the above XPS results are correlated with the FE-SEM and EDX elemental analysis which further confirms the co-existence of respective elements of SMO and G-CN in SMO/G-CN-10 composite photocatalyst.

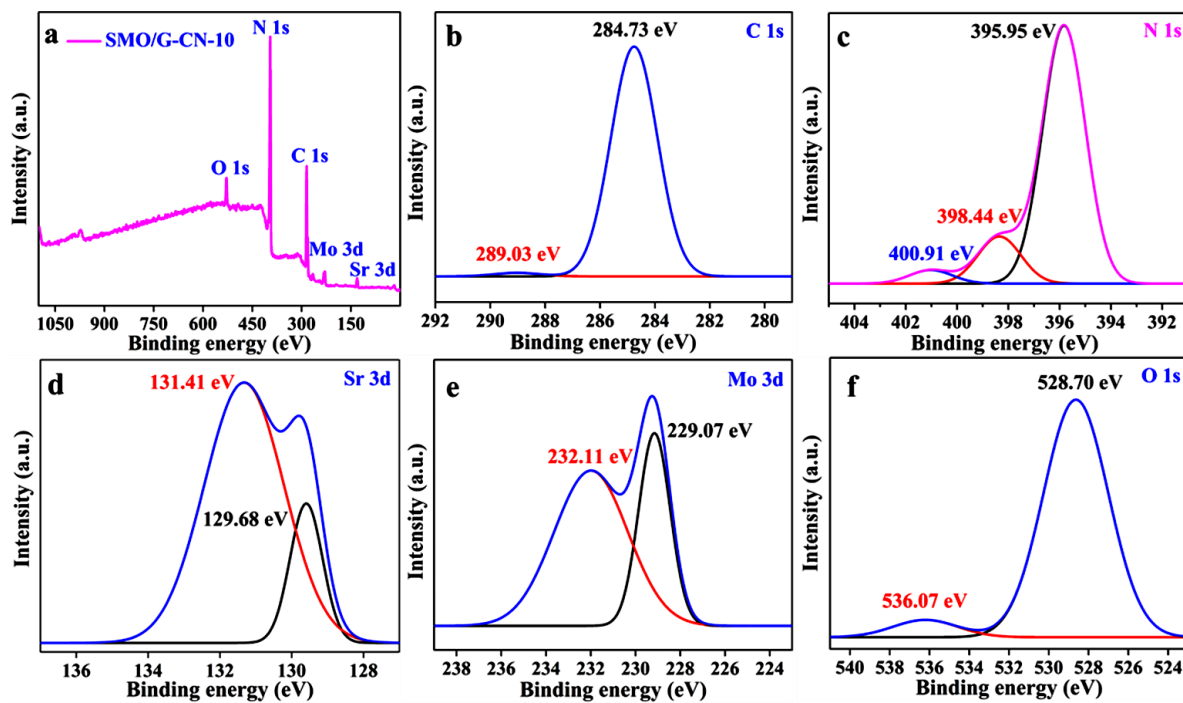


**Figure 4.3:** (a) XPS survey scan, (b) C 1s, (c) N 1s, (d) Sr 3d, (e) Mo 3d, and (f) O 1s spectra of SMO/G-CN-10 composite photocatalyst.

#### 4.3.4 UV-Vis DRS, PL, and TGA studies

Optical absorption of pure G-CN, pure SMO, and SMO/G-CN composite photocatalysts were investigated by UV-Vis DRS and the absorbance of the materials were shown in Figure 4.4(a). The pure SMO absorbs light in the UV range  $\sim 400$  nm, while pure G-CN absorbs the light with the wavelength of 450 nm under visible range. It is interesting to note that, the composites shows the absorption edge shifting towards the visible region from the UV region. This is due to the formation of SMO/G-CN composite photocatalysts with visible active G-CN sheets the absorption edge of composites are close to 450 nm. Therefore, from this optical property it can be predicted that the mentioned composite would certainly be a promising candidate for the enhanced photocatalytic activity of SMO/G-CN composite photocatalysts under sunlight, compared to pure SMO and G-CN, respectively. As shown in Figure 4.4(b), the respective optical band gaps of pure G-CN and SMO were calculated by Tauc equation (4.1).<sup>[57-60]</sup>

$$(\alpha h\vartheta)^{1/2} = B(h\vartheta - E_g) \quad (4.1)$$

Where ‘ $\alpha$ ’ is the absorption coefficient, ‘ $E_g$ ’ is the bandgap of the semiconductor, ‘ $B$ ’ is band tailing parameter and ‘ $h\vartheta$ ’ is the energy of the photons from Einstein’s equation.<sup>[61]</sup>

According to Tauc equation, the calculated bandgap of pure G-CN and SMO was found to be 2.71 and 3.10 eV, respectively.<sup>[42]</sup>

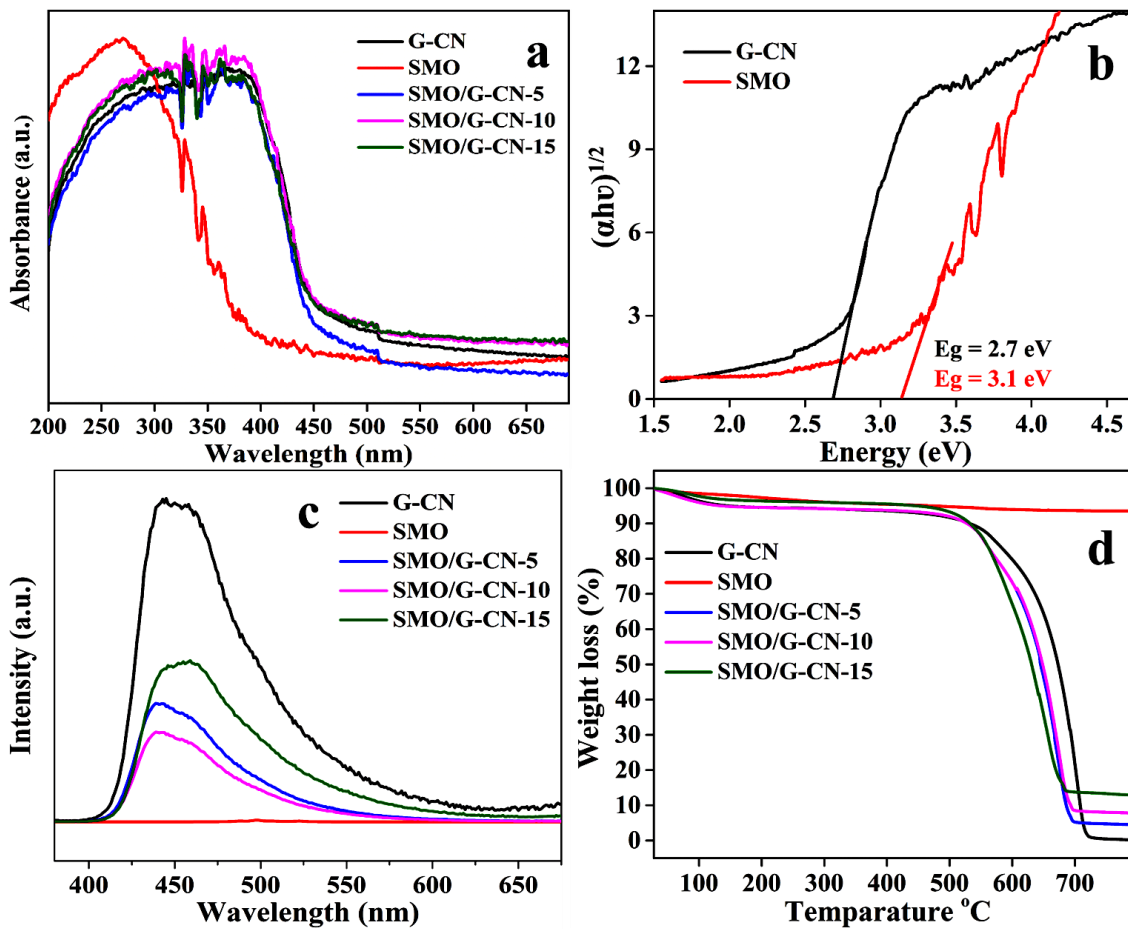


**Figure 4.4:** (a) UV-Visible DRS spectra of pure G-CN, pure SMO, and SMO/G-CN composite photocatalysts, (b) Tauc plots of pure G-CN and SMO, (c) PL spectra, and (d) TGA analysis of pure G-CN, SMO and SMO/G-CN composite photocatalysts.

In order to describe the photogenerated excitons separation and migration efficiency in the G-CN and SMO/G-CN composite photocatalyst, we performed PL spectra at R.T. and the results are shown in Figure 4.4(c) it is well known that with high PL emission intensity responsible for high recombination of photogenerated excitons, which leads to its reduced performance in photocatalysis. The PL spectra of pure G-CN the excitation wavelength at 365 nm, and the emission peak at 460 nm wavelength. The PL spectra of pure SMO the excitation and emission wavelength are 380 and 420 nm these results give agreement with the absorption spectra of G-CN and SMO.<sup>[62]</sup> The high PL emission peak intensity of G-CN shows high recombination of photogenerated

excitons, while the addition of SMO microcrystals to G-CN sheets, the recombination rate of excitons was suppressed remarkably since the formation of composite photocatalysts between two semiconductors. The low recombination rate of photogenerated excitons on SMO/G-CN-10 composite photocatalyst is responsible for the enhancement in the RhB dye degradation efficiency of the photocatalyst under sunlight.

TGA analysis were performed for pure G-CN, pure SMO, and SMO/G-CN composite photocatalysts to calculate the amount of SMO loaded on G-CN and the results are shown in Figure 4.4(d). TGA analysis of pure G-CN shows the burning starts at 550 °C and ends at ~730 °C which confirms the decomposition of G-CN.<sup>[63]</sup> And pure SMO gives a straight TGA curve, indicating the pure SMO to be stable up to 800 °C. However, the addition of SMO microcrystals on the G-CN sheets decreases the thermal stability of SMO/G-CN composite photocatalysts, because of the ability of SMO to activate oxygen and oxidize G-CN to produce gaseous products.<sup>[64]</sup> This is the reason for the reduced decomposition temperature of SMO/G-CN composite photocatalysts in comparison to pure G-CN. The appropriate weight loss of the series of composite photocatalysts (SMO/G-CN-5, SMO/G-CN-10, and SMO/G-CN-15) was found to be 4.4, 7.9, and 13.7 %, which is approximately close to the amount of loaded SMO, respectively.

#### **4.3.5 Photocatalytic degradation of RhB dye pollutant**

In this section, the synthesized materials photocatalytic activity was investigated by its ability to degrade organic dye RhB in water under sunlight. Figure 4.5(a) depicts the plots between the concentration of RhB ( $C/C_0$ ) and irradiation time ( $t$ ) over pure G-CN, pure SMO, and SMO/G-CN composite photocatalysts, where ' $C_0$ ' is the primary concentration of RhB and ' $C$ ' is the concentration at a particular time ( $t$ ). As shown in Figure 4.5(a) the photocatalytic degradation efficiency of pure SMO is very less, because its absorption spectra range lies in UV region which is limited in the solar spectrum. Whereas the pure G-CN also shows limited photocatalytic activity even though it is in the visible region of the solar spectrum, because of photogenerated excitons have a more recombination and low redox ability. Among all composites, SMO/G-CN-10 displayed the highest photo-degradation of Rh B under sunlight because of the formation of a strong heterojunction between semiconductors of G-CN and SMO. The plots of  $-\ln (C/C_0)$  against irradiation time ( $t$ ), gives linear curves and includes error bars as shown in Figure 4.5(b), which clearly indicates that photo-degradation rate of the RhB dye follows the first-order kinetic equation model as shown in below equation (4.2).

$$\ln(C/C_0) = kt \quad (4.2)$$

Where 'k' is the rate constant ( $\text{min}^{-1}$ ). From the above results, it can be concluded that SMO/G-CN-10 composite photocatalyst shows the enhanced photo-degradation rate ( $0.0976 \text{ min}^{-1}$ ) of dye pollutants under sunlight, which has been 4 and 40 times higher than those of pure G-CN ( $0.0245 \text{ min}^{-1}$ ), pure SMO ( $0.0024 \text{ min}^{-1}$ ), and other composites also. This is attributed to the synergistic effect between the interface of G-CN and SMO. A complete table of the rates of the reaction are shown in Table 4.1.

**Table 4.1:** Calculated rate constant values of the synthesized photocatalysts.

S. No.	Photocatalysts	Rate constant k ( $\text{min}^{-1}$ )
1	SMO	0.0024
2	G-CN	0.0245
3	SMO/G-CN-5	0.0552
4	SMO/G-CN-10	0.0976
5	SMO/G-CN-15	0.0737

These results indicate that the synthesized SMO/G-CN composite photocatalysts show remarkable photocatalytic activity compared to pure SMO and G-CN. Although the loaded G-CN sheets amount with SMO microcrystals is increased from 5 wt% to 15 wt%, the photocatalytic activity trend was firstly increased up to 10 wt% then decreased. But it was significantly high photocatalytic activity compared to pure G-CN, and SMO. The decrease in the photocatalytic activity might be explained by the following causes (1) the optimum G-CN amount is responsible for good dispersion with the SMO microcrystals which esteem the separation and migration efficiency of photogenerated excitons and (2) more G-CN amount leads to the formation of agglomeration due to these active sites on G-CN blocked resulting there are no photogenerated excitons, subsequently decrease the photocatalytic activity.

To understand the reusability and photo-stability of the synthesized SMO/G-CN-10 composite photocatalyst, we have performed four successive runs after the photocatalytic activity of the SMO/G-CN-10 composite under sunlight with same experimental conditions as mentioned above. Prior to each run the sample were collected and washed with DD water several times and dried in a hot air over and use for further cycle, in every cycle we used freshly prepared RhB solution with used photocatalyst and the corresponding results are depicted in the Figure 4.5(c).

Percentage of degradation plots of of pure G-CN, pure SMO and SMO/G-CN composite photocatalysts with error bars is shown in Figure 4.5(d). Comparison of some organic pollutants degradation performances of SrMoO<sub>4</sub> based photocatalysts with previous reports are showed in Table 4.2.

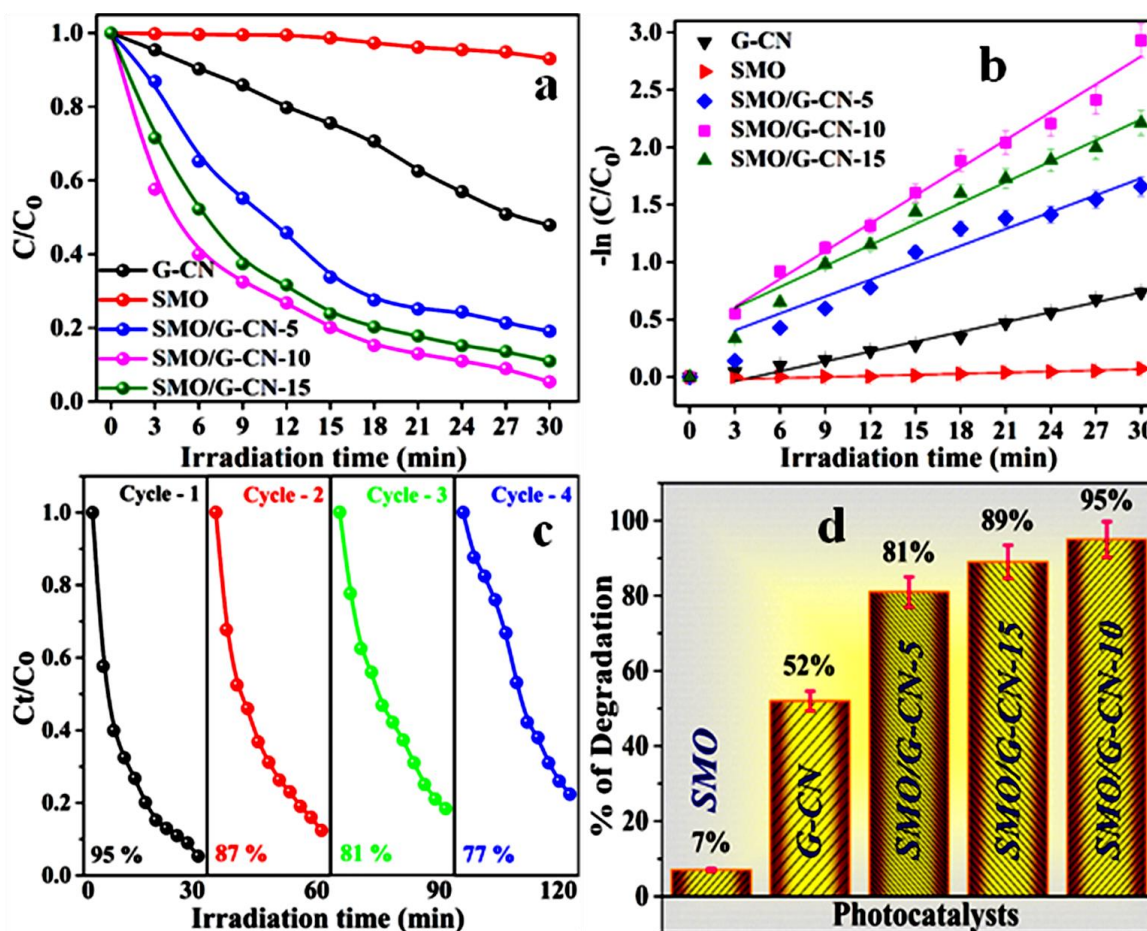


**Figure 4.5:** (a) Photocatalytic activity comparison curves of synthesized pure G-CN, pure SMO, and SMO/G-CN composite photocatalysts, (b) respective first-order kinetic plots of pure G-CN, pure SMO and SMO/G-CN composite photocatalysts with error bars, (c) stability studies of the SMO/G-CN-10 composite photocatalyst for degradation of RhB during four successive experimental runs, and (d) percentage of degradation plots of of pure G-CN, pure SMO and SMO/G-CN composite photocatalysts with error bars.

**Table 4.2:** Comparison of pollutants degradation performances of  $\text{SrMoO}_4$  based photocatalysts with previous reports.

Photocatalyst	Catalyst amount (mg)	Pollutant name & concentration (ppm)	Light source	Degradation % and time	Reference
Mn doped $\text{SrMoO}_4$	20	Methylene blue & 10	350 W Xe lamp	85% & 140 min	[65]
$\text{SrMoO}_4/\text{Bi}^{+3}$	150	Methylene blue & 10	UV light irradiation	40% & 180 min	[66]
$\text{SrMoO}_4/0.1\text{Eu/SiO}_2$	200	Methylene blue & 10	Xe lamp	97.74 & 120 min	[67]
$\text{AMoO}_4$ (A = Ca, Sr, Ba)	100	Tetracycline & 10	Uv light	79 % & 3 h	[68]
$\text{SrMoO}_4$ nanocrystals	200	Methyl blue solution & 10	350 W Xe lamp	98 % & 120 min	[17]
$\text{SrMoO}_4$ nanostructures	100	Methyl orange & 5	Uv light	73 % & 60 min	[69]
$\text{SrMoO}_4/\text{g-C}_3\text{N}_4$	100	Rhodamine B & 5	Sunlight	95% & 30 min	Present work

In the photocatalytic dye degradation process, the role of photo reactive species could be studied by holes and radicals trapping experiments. However, TBA,  $\text{N}_2$ , and AO were used for hydroxyl radicals ( $\cdot\text{OH}$ ), superoxide anion ( $\text{O}_2^{\cdot-}$ ), and holes ( $\text{h}^+$ ) scavengers,<sup>[70]</sup> respectively. Figure 4.6(a), shows the photocatalytic activity of RhB rapidly decreases after  $\text{N}_2$  treatment. This indicates that dissolved  $\text{O}_2$  plays a major role with the formation of  $\text{O}_2^{\cdot-}$  for the degradation of RhB over SMO/G-CN-10 composite photocatalyst under sunlight illumination. After the addition of TBA, a significant change in the degradation of RhB was observed. Whereas with the addition of AO, the rate of photocatalytic degradation of RhB is considerably decreased compared with no scavenger under the same experimental conditions.<sup>[71]</sup> These results indicate the photo-induced  $\text{O}_2^{\cdot-}$ ,  $\cdot\text{OH}$ , and  $\text{h}^+$  plays important role in the RhB degradation over SMO/G-CN-10 composite photocatalyst under sunlight and the order of the reactive species for the degradation of RhB as following  $\text{O}_2^{\cdot-} > \text{h}^+ > \cdot\text{OH}$ .

The  $\cdot\text{OH}$  radical generation during the photocatalytic reaction can be easily detected by a photoluminescence (PL) technique using terephthalic acid (TA) as a probe molecule, which readily reacts with  $\cdot\text{OH}$  to produce the highly Fluorescent product, 2-hydroxyterephthalic acid. The details of the experimental procedures have been reported in earlier report<sup>[72]</sup>. From Figure 4.6(b), it can

be seen that the maximum intensity peaks in the PL spectra were observed at approximately 435 nm, signifies the formation of 2-hydroxy terephthalic acid, concludes that  $\cdot\text{OH}$  is formed in the photocatalytic oxidation process, which is in agreement with the results of TBA quenching. From Figure 4.6(b), it is also observed that the PL intensity increases gradually with increasing irradiation time, which demonstrates that  $\cdot\text{OH}$  is indeed generated on the sunlight irradiated surface of SMO/G-CN-10 composite photocatalyst.

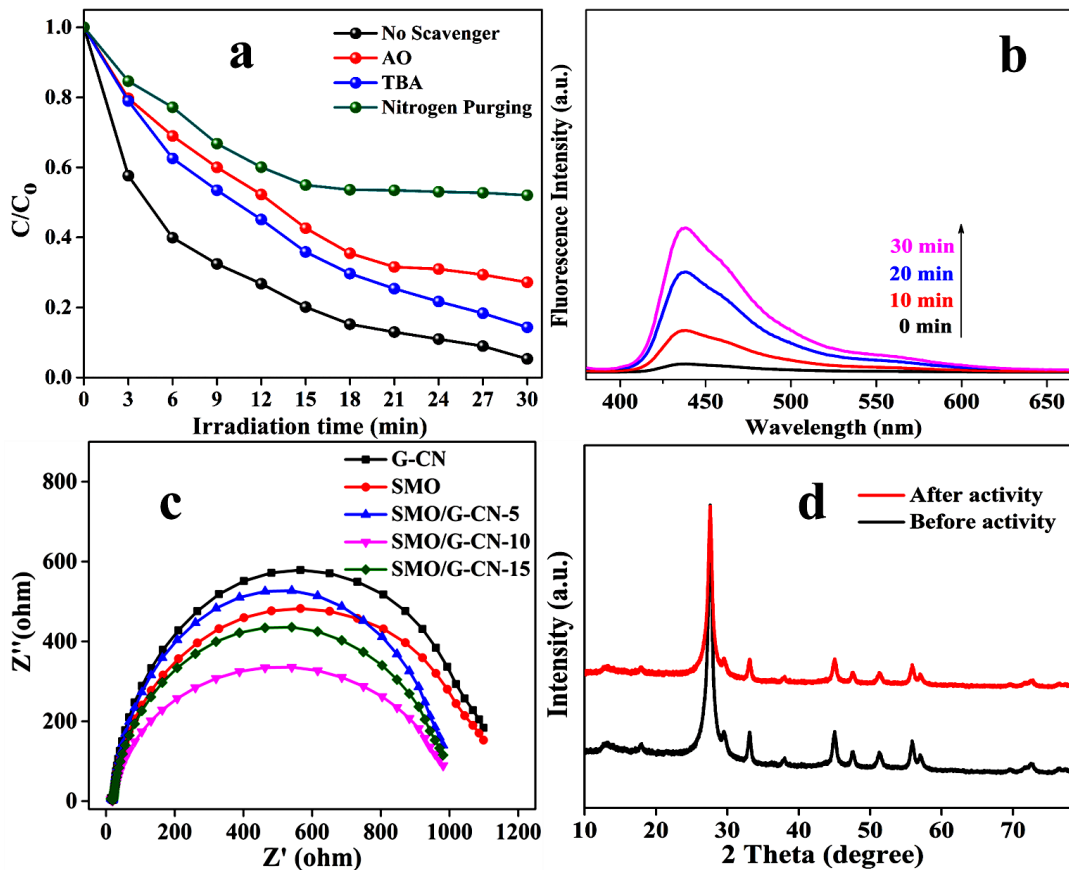


**Figure 4.6:** (a) Different scavenger's effect on performance over the SMO/G-CN-10, (b)  $\cdot\text{OH}$  trapping PL spectra of the SMO/G-CN-10 composite photocatalyst with TA solution under sunlight light irradiation, (c) EIS of G-CN, SMO, and SMO/G-CN composite photocatalysts, and (d) PXRD pattern of SMO/G-CN-10 composite before and after photocatalytic degradation of RhB.

As shown in Figure 4.6(c) electrochemical impedance spectroscopy (EIS) for G-CN and SMO photocatalyst shows large charge transfer resistance ( $R_{ct}$ ) of  $1191\ \Omega$  and  $1174\ \Omega$ . For the composites of SMO/G-CN photocatalyst series, the resistance was  $1074\ \Omega$ ,  $1036\ \Omega$ , and  $1066\ \Omega$ , for SMO/G-CN-5, SMO/G-CN-10, and SMO/G-CN-15. From the  $R_{ct}$  values we conclude that SMO/G-CN-10 composite shows less resistance compared with all other composites and bare

materials also, this results also supports the enhancement in the rate of photocatalytic degradation of RhB under sunlight. As shown in Figure 4.6(d), the PXRD of SMO/G-CN-10 composite photocatalyst before and after the photocatalytic dye degradation study, from the PXRD plots we conclude that there is no change in the crystal structure that indicates the stability of SMO/G-CN-10 composite. These results are important from a practical application point of view.

#### 4.3.6 Proposed mechanism

Based on our experimental results, the synthesized SMO/G-CN-10 composite photocatalyst can improve the photocatalytic performance under sunlight. To describe the photo-degradation process, we have proposed the plausible reaction mechanism for SMO/G-CN-10 composite photocatalyst over the degradation of RhB dye under sunlight and shown in Figure 4.7. The conduction band (CB) and valence band (VB) energy potentials of the synthesized photocatalysts can be calculated from the following equations (4.3 and 4.4).

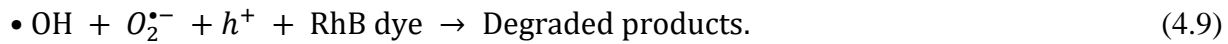
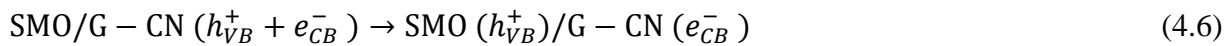
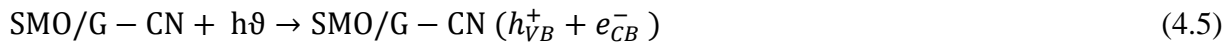
$$E_{VB} = X - E_0 + 0.5 E_g \quad (4.3)$$

$$E_{CB} = E_{VB} + E_g \quad (4.4)$$

Where  $E_{CB}$  and  $E_{VB}$  are the energy potentials of the corresponding valence band and conduction band respectively, ' $E_g$ ' is the bandgap energy which is calculated from the UV-Vis DRS, 'X' is the absolute electronegativity of the semiconductor, which is determined by the geometric mean of the electronegativity of all the atoms present in the material, and ' $E_0$ ' is the energy of free electrons on the hydrogen scale (4.5 eV). The CB and VB edge potentials of SMO (-0.30 eV and +2.80 eV vs. NHE)<sup>[38]</sup>, whereas the CB and VB edge potentials of G-CN (-1.30 eV and +1.41 eV vs. NHE).<sup>[73]</sup> CB and VB redox potentials of G-CN are more negative than those of SMO. It is well known that for the generation of  $O_2^{\cdot-}$ , CB potential is more negative than (-0.33 eV vs. NHE), and for 'OH formation, VB potential more positive than (+2.68 eV vs. NHE).<sup>[74]</sup> Based on VB and CB edge potentials and bandgap energies of SMO and G-CN, two charge transfer mechanisms are possible. One is a conventional double transfer mechanism and another is the Z-scheme transfer mechanism. If the SMO/G-CN-10 composite photocatalyst follows a double-transfer mechanism the photo-reduction reaction would take place at CB of SMO, and the photo-oxidation would takes place at the VB of G-CN as shown in Figure 4.7(a). But these expected processes might be not possible. Since CB potential of SMO (-0.30) is less negative than the reduction potentials of the  $O_2/O_2^{\cdot-}$  (-0.33 eV vs. NHE). Besides, VB of G-CN (+1.41 eV) is less

positive than the oxidation potential of  $\text{^{\circ}OH/H}_2\text{O}$  (+2.68 eV vs. NHE). Above discussions support the Z-scheme mechanism rather than the conventional double charge transfer mechanism for the SMO/G-CN-10 composite photocatalyst.<sup>[75,76]</sup> Due to their suitable bandgap of both SMO and G-CN are excited together under the sunlight illumination to generate holes in the VB and electrons in the CB, as shown in Figure 4.7(b). The photo-excited electrons in CB of SMO can easily transfer to VB of CN through Z-scheme. Besides, the formation of more electron cloud in CB of G-CN can easily participate in the photo-reduction reaction by using dissolved  $\text{O}_2$  to yield  $\text{O}_2^{\bullet-}$ . Since CB potential of G-CN (-1.30 eV) is more negative than that of  $\text{O}_2/\text{O}_2^{\bullet-}$  (-0.33 eV vs. NHE). Meanwhile, the accumulated holes at VB of SMO can directly generate  $\bullet\text{OH}$  from  $\text{^{\circ}OH/H}_2\text{O}$  by participating photo-oxidation reactions. Since VB potential of SMO (+2.80 eV) is more positive than the oxidation potential of  $\text{^{\circ}OH/H}_2\text{O}$  (+2.68 eV vs. NHE). Moreover, the energy gap between CB of SMO to CB of G-CN, is approximately equal to CB of SMO to VB of G-CN and the energy gap between VB of SMO to VB of G-CN is more than the CB of SMO to VB of G-CN. Because of this Z-Scheme mechanism is more facilitative than conventional mechanism.<sup>[40]</sup> From the above discussion photo-generated superoxide anion and hydroxyl radicals are the major reactive species for the degradation of RhB dye under sunlight and supported by the electro n-hole pair trapping experiment results.

Because of well-matched, coinciding band-structures, photogenerated excitons effectively separated and migration towards the surface of SMO/G-CN-10 composite photocatalyst leads to the enhancement in photocatalytic activity. Plausible photocatalytic degradation mechanism of RhB dye pollutants under sunlight for SMO/G-CN-10 composite photocatalyst is represented by the following equations (4.5 to 4.9).



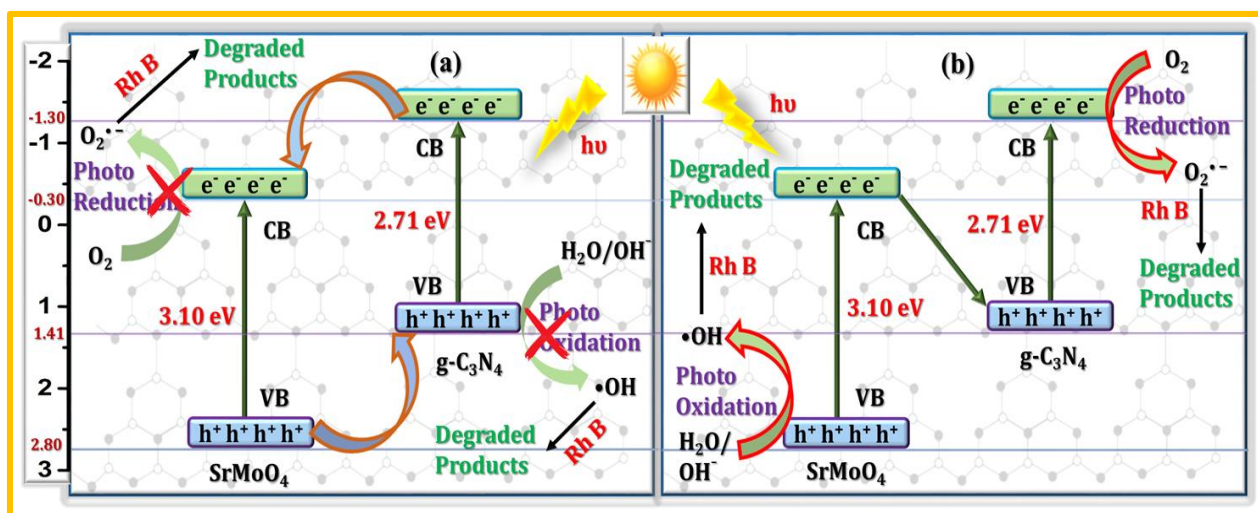


**Figure 4.7:** (a) Proposed double transfer mechanism, and (b) Z-Scheme mechanism for SMO/G-CN-10 composite photocatalyst for degradation of RhB dye under sunlight illumination.

#### 4.4 Conclusions

In brief we have successfully fabricated SMO/G-CN composite photocatalysts with intimate interaction by a simple, facile mixed heating methodology, the binary composite shows much higher photocatalytic degradation efficiency of Rh-B under sunlight. The UV-Vis spectroscopy studies reveal that the photo-degradation was achieved 95% within 30 min under sunlight illumination. The enhancement in photocatalytic dye degradation of RhB for SMO/G-CN-10 composite supports the PL and EIS results. Photo-generated  $O_2^-$  and  $\cdot OH$  are the primary active species for the photocatalytic RhB dye degradation process. The optimized SMO/G-CN-10 composite photocatalyst shows the highest degradation rate ( $0.0976 \text{ min}^{-1}$ ) which is 4 and 40 times higher than those of G-CN ( $0.0245 \text{ min}^{-1}$ ) and SMO ( $0.0024 \text{ min}^{-1}$ ). The enhanced performance in the new synthesized nanocomposite is ascribed to the interfacial interactions among those of G-CN and SMO. This interfacial contact leads to the better-suppressed recombination, and transfer efficiency of photogenerated excitons. Present investigation might be useful for dye degradation as well as water splitting applications in a future perspective.

#### 4.5 References

- [1] R. Kelishadi, *Journal of Environmental and Public Health* **2012**, 2012, 1–2.
- [2] G. Lofrano, S. Meriç, G. E. Zengin, D. Orhon, *Science of the Total Environment* **2013**, 461–462, 265–281.

[3] S. Manchala, L. R. Nagappagari, S. Muthukonda Venkatakrishnan, V. Shanker, *International Journal of Hydrogen Energy* **2018**, *43*, 13145–13157.

[4] S. D. Richardson, T. A. Ternes, *Analytical Chemistry* **2014**, *86*, 2813–2848.

[5] N. Bolong, A. F. Ismail, M. R. Salim, T. Matsuura, *Desalination* **2009**, *239*, 229–246.

[6] S. Siliveri, S. Chirra, C. Tyagi, A. Gandamalla, A. K. Adepu, S. Goskula, S. R. Gujjula, N. Venkatathri, *ChemistrySelect* **2019**, *4*, 9135–9142.

[7] R. R. S. Coronado-Castañeda, M. L. Maya-Treviño, E. Garza-González, J. Peral, M. Villanueva-Rodríguez, A. Hernández-Ramírez, *Catalysis Today* **2019**, 0–1.

[8] A. Ejraei, M. A. Aroon, A. Ziarati Saravani, *Journal of Water Process Engineering* **2019**, *28*, 45–53.

[9] W. Li, B. Mu, Y. Yang, *Bioresource Technology* **2019**, *277*, 157–170.

[10] S. Ni, C. Wu, Y. Wang, X. Guo, Z. Zhao, X. Sun, *Hydrometallurgy* **2019**, *187*, 63–70.

[11] R. Changotra, H. Rajput, J. Paul Guin, L. Varshney, A. Dhir, *Chemical Engineering Journal* **2019**, *370*, 595–605.

[12] D. Huang, Z. Li, G. Zeng, C. Zhou, W. Xue, X. Gong, X. Yan, S. Chen, W. Wang, M. Cheng, *Applied Catalysis B: Environmental* **2019**, *240*, 153–173.

[13] E. Gürmen, E. Daniels, J. S. King, *The Journal of Chemical Physics* **1971**, *55*, 1093–1097.

[14] J. C. Sczancoski, L. S. Cavalcante, N. L. Marana, R. O. da Silva, R. L. Tranquilin, M. R. Joya, P. S. Pizani, J. A. Varela, J. R. Sambrano, M. Siu Li, E. Longo, J. Andrés, *Current Applied Physics* **2010**, *10*, 614–624.

[15] T. Thongtem, S. Kungwankunakorn, B. Kuntalue, A. Phuruangrat, S. Thongtem, *Journal of Alloys and Compounds* **2010**, *506*, 475–481.

[16] S. M. Hosseinpour-mashkani, A. Sobhani-Nasab, M. Mehrzad, *Journal of Materials Science: Materials in Electronics* **2016**, *27*, 5758–5763.

[17] Y. Zhu, G. Zheng, Z. Dai, J. Mu, Z. Yao, *Journal of Materials Science & Technology* **2017**, *33*, 834–842.

[18] Z.-F. Yao, G.-H. Zheng, Z.-X. Dai, L.-Y. Zhang, *Applied Organometallic Chemistry* **2018**, *32*, e4412.

[19] A. K. Soni, R. Joshi, K. Jangid, R. Tewari, R. S. Ningthoujam, *Materials Research Bulletin* **2018**, *103*, 1–12.

[20] E. Çiftyürek, K. Sabolsky, E. M. Sabolsky, *Sensors and Actuators B: Chemical* **2017**, *249*,

296–310.

- [21] A. Thomas, A. Fischer, F. Goettmann, M. Antonietti, J.-O. Müller, R. Schlögl, J. M. Carlsson, *Journal of Materials Chemistry* **2008**, *18*, 4893.
- [22] X. Ma, J. Zhang, B. Wang, Q. Li, S. Chu, *Applied Surface Science* **2018**, *427*, 907–916.
- [23] J. Zhang, Y. Chen, X. Wang, *Energy & Environmental Science* **2015**, *8*, 3092–3108.
- [24] D. Zheng, C. Pang, Y. Liu, X. Wang, *Chemical Communications* **2015**, *51*, 9706–9709.
- [25] J. Yu, M. Jaroniec, *Applied Surface Science* **2015**, *358*, 1.
- [26] Q. Han, B. Wang, J. Gao, Z. Cheng, Y. Zhao, Z. Zhang, L. Qu, *ACS Nano* **2016**, *10*, 2745–2751.
- [27] S. C. Yan, Z. S. Li, Z. G. Zou, *Langmuir* **2009**, *25*, 10397–10401.
- [28] Z. Sun, H. Wang, Z. Wu, L. Wang, *Catalysis Today* **2018**, *300*, 160–172.
- [29] R. Li, Y. Ren, P. Zhao, J. Wang, J. Liu, Y. Zhang, *Journal of Hazardous Materials* **2019**, *365*, 606–614.
- [30] M. Bellardita, E. I. García-López, G. Marcì, I. Krivtsov, J. R. García, L. Palmisano, *Applied Catalysis B: Environmental* **2018**, *220*, 222–233.
- [31] K. Rabé, L. Liu, N. A. Nahyoon, Y. Zhang, A. M. Idris, J. Sun, L. Yuan, *Journal of the Taiwan Institute of Chemical Engineers* **2019**, *96*, 463–472.
- [32] J. Li, H. Hao, J. Zhou, Z. Zhu, *New Journal of Chemistry* **2016**, *40*, 9638–9647.
- [33] G. Li, B. Wang, J. Zhang, R. Wang, H. Liu, *Applied Surface Science* **2019**, *478*, 1056–1064.
- [34] F. Guo, W. Shi, M. Li, Y. Shi, H. Wen, *Separation and Purification Technology* **2019**, *210*, 608–615.
- [35] Y. Shen, Z. Zhu, X. Wang, A. Khan, J. Gong, Y. Zhang, *Materials Research Bulletin* **2018**, *107*, 407–415.
- [36] L. Zhao, L. Zhang, H. Lin, Q. Nong, M. Cui, Y. Wu, Y. He, *Journal of Hazardous Materials* **2015**, *299*, 333–342.
- [37] L. Sun, J. Li, X. Li, C. Liu, H. Wang, P. Huo, Y. sheng Yan, *Journal of Colloid and Interface Science* **2019**, *552*, 271–286.
- [38] S. Tonda, S. Kumar, V. Shanker, *Journal of Environmental Chemical Engineering* **2015**, *3*, 852–861.
- [39] J. Guo, P. Li, Z. Yang, *Catalysis Communications* **2019**, *122*, 63–67.
- [40] A. Gandamalla, S. Manchala, P. Anand, Y.-P. Fu, V. Shanker, *Materials Today Chemistry*

2021, 19, 100392.

- [41] D. Chen, K. Tang, F. Li, H. Zheng, *Crystal Growth & Design* **2006**, *6*, 247–252.
- [42] R. Karthik, N. Karikalan, S.-M. Chen, J. Vinoth Kumar, C. Karuppiah, V. Muthuraj, *Journal of Catalysis* **2017**, *352*, 606–616.
- [43] T. Defence, W. B. Demore, O. F. Raper, T. P. J. Izod, P. Wayne, M. Gauthier, A. Black, J. F. Noxon, F. Stuhl, K. H. Welge, S. V Filseth, A. Zia, T. N. Jones, D. Biedenkapp, P. H. Fraser, R. W. Nicholls, J. E. Morgan, E. A. Ogryzlo, A. Arbor, *Chemical Physics* **1970**, *55*, 1093–1097.
- [44] W. Jo, S. Moru, S. Tonda, *ACS Sustainable Chemistry & Engineering* **2019**, *7*, 15373–15384.
- [45] G. Li, Z. Wang, Z. Quan, C. Li, J. Lin, *Crystal Growth & Design* **2007**, *7*, 1797–1802.
- [46] F. Lei, B. Yan, *Journal of Solid State Chemistry* **2008**, *181*, 855–862.
- [47] P. Yang, C. Li, W. Wang, Z. Quan, S. Gai, J. Lin, *Journal of Solid State Chemistry* **2009**, *182*, 2510–2520.
- [48] X. Chen, D.-H. Kuo, D. Lu, *RSC Advances* **2016**, *6*, 66814–66821.
- [49] M. J. Bojdys, J.-O. Müller, M. Antonietti, A. Thomas, *Chemistry - A European Journal* **2008**, *14*, 8177–8182.
- [50] Y. C. Zhao, D. L. Yu, H. W. Zhou, Y. J. Tian, O. Yanagisawa, *Journal of Materials Science* **2005**, *40*, 2645–2647.
- [51] X. Li, J. Zhang, L. Shen, Y. Ma, W. Lei, Q. Cui, G. Zou, *Applied Physics A: Materials Science and Processing* **2009**, *94*, 387–392.
- [52] X. Li, G. Hartley, A. J. Ward, P. A. Young, A. F. Masters, T. Maschmeyer, *The Journal of Physical Chemistry C* **2015**, *119*, 14938–14946.
- [53] S. Tonda, S. Kumar, Y. Gawli, M. Bhardwaj, S. Ogale, *International Journal of Hydrogen Energy* **2017**, *42*, 5971–5984.
- [54] Y. Wang, X. Wang, M. Antonietti, *Angewandte Chemie International Edition* **2012**, *51*, 68–89.
- [55] J. Zhang, R. Li, L. Liu, L. Li, L. Zou, S. Gan, G. Ji, *Ultrasonics Sonochemistry* **2014**, *21*, 1736–1744.
- [56] N. Niu, P. Yang, W. Wang, F. He, S. Gai, D. Wang, J. Lin, *Materials Research Bulletin* **2011**, *46*, 333–339.

[57] S. Manchala, A. Gandomalla, N. R. Vempuluru, S. Muthukonda Venkatakrishnan, V. Shanker, *Journal of Colloid and Interface Science* **2021**, 583, 255–266.

[58] P. Jiménez-Calvo, C. Marchal, T. Cottineau, V. Caps, V. Keller, *Journal of Materials Chemistry A* **2019**, 7, 14849–14863.

[59] S. Manchala, L. R. Nagappagari, S. M. Venkatakrishnan, V. Shanker, *ACS Applied Nano Materials* **2019**, 2, 4782–4792.

[60] S. Manchala, L. R. Nagappagari, S. Muthukonda Venkatakrishnan, V. Shanker, *International Journal of Hydrogen Energy* **2018**, 43, 13145–13157.

[61] P. Raizada, P. Singh, A. Kumar, G. Sharma, B. Pare, S. B. Jonnalagadda, P. Thakur, *Applied Catalysis A: General* **2014**, 486, 159–169.

[62] S. Kumar, S. Karthikeyan, A. Lee, *Catalysts* **2018**, 8, 74.

[63] X. Wang, K. Maeda, A. Thomas, K. Takanabe, G. Xin, J. M. Carlsson, K. Domen, M. Antonietti, *Nature Materials* **2009**, 8, 76–80.

[64] D. Masih, Y. Ma, S. Rohani, *Applied Catalysis B: Environmental* **2017**, 206, 556–588.

[65] Z.-F. Yao, Z.-X. Dai, Z.-J. Zhang, G.-H. Zheng, X. Xu, *Applied Organometallic Chemistry* **2019**, 33, e4648.

[66] Y. Wang, H. Xu, C. Shao, J. Cao, *Applied Surface Science* **2017**, 392, 649–657.

[67] Z. Yao, G. Zheng, Z. Zhang, Z. Dai, L. Zhang, Y. Ma, *Journal of Electronic Materials* **2018**, 47, 5359–5369.

[68] A. M. Huerta-Flores, I. Juárez-Ramírez, L. M. Torres-Martínez, J. E. Carrera-Crespo, T. Gómez-Bustamante, O. Sarabia-Ramos, *Journal of Photochemistry and Photobiology A: Chemistry* **2018**, 356, 29–37.

[69] S. M. Hosseinpour-mashkani, A. Sobhani-Nasab, M. Mehrzad, *Journal of Materials Science: Materials in Electronics* **2016**, 27, 5758–5763.

[70] S. Tonda, S. Kumar, S. Kandula, V. Shanker, *Journal of Materials Chemistry A* **2014**, 2, 6772.

[71] S. C. Yan, Z. S. Li, Z. G. Zou, *Langmuir* **2010**, 26, 3894–3901.

[72] B. Cheng, Y. Le, J. Yu, *Journal of Hazardous Materials* **2010**, 177, 971–977.

[73] R. Geng, J. Yin, J. Zhou, T. Jiao, Y. Feng, L. Zhang, Y. Chen, Z. Bai, Q. Peng, *Nanomaterials* **2019**, 10, 1.

[74] T. Surendar, S. Kumar, V. Shanker, *Phys. Chem. Chem. Phys.* **2014**, 16, 728–735.

- [75] M. Amiri, K. Dashtian, M. Ghaedi, S. Mosleh, R. Jannesar, *New Journal of Chemistry* **2019**, *43*, 1275–1284.
- [76] C. Li, S. Yu, H. Che, X. Zhang, J. Han, Y. Mao, Y. Wang, C. Liu, H. Dong, *ACS Sustainable Chemistry & Engineering* **2018**, *6*, 16437–16447.

◆-----◆

## Chapter V

# Microwave-assisted synthesis of ZnAl-LDH/g-C<sub>3</sub>N<sub>4</sub> composite for degradation of antibiotic ciprofloxacin under visible light illumination

◆-----◆

## Chapter V

# Microwave-assisted synthesis of ZnAl-LDH/g-C<sub>3</sub>N<sub>4</sub> composite for degradation of antibiotic ciprofloxacin under visible-light illumination

### 5.1 Introduction

The most recent environmental issues are antibiotic pollutants, due to its excessive use in the form of drugs it become hotspot research topic for current scientists to address these issues. In this regard, design and development of highly efficient semiconductor photocatalysts for removal of antibiotic pollutants are in great demand. Ciprofloxacin (CIP) is a fluoroquinolone family antibiotic known as one of the most hazardous and colorless emerging pollutants released into drinking water, surface, and groundwater to pollute thousands of waterbodies globally.<sup>[1-5]</sup> The complete and successful removal of antibiotic CIP from the water bodies has become a primary concern, as CIP has more chemical stability and non-biodegradable antibiotics than most other pharmaceutical chemicals. As a result, the removal of CIP using various techniques has become a hotspot of research in the field of wastewater treatment.<sup>[6-8]</sup> To date, several methods have been reported for the removal of wastewater containing antibiotics, such as biological methods, physical methods, advanced oxidation processes, photo-degradation, ozonation, and heterogeneous photocatalysis.<sup>[9-16]</sup> Owing to its high mineralization and degradation capability, low cost, low toxicity, and strong oxidizing power, recently, heterogeneous photocatalysis has emerged to be an effective process to remove the antibiotic organic pollutants. There is no secondary product formed under visible light conditions in heterogeneous photocatalysis.<sup>[17,18]</sup>

Graphitic carbon nitride (CN) has attracted great consideration in recent years as a “sustainable” photocatalyst. Because it can be synthesized by a very simple thermal condensation method, with inexpensive melamine as a precursor having most earth abundant elements (carbon and nitrogen). Besides, having moderate bandgap energy which is suitable for the more visible light absorption, and tunable electronic structure, high thermal, chemical stability, and 2D planar conjugation structure.<sup>[19-23]</sup> Although, CN photocatalytic activity is limited in practical applications as a result of its low surface area, low quantum efficiency, and high photogenerated excitons recombination.<sup>[24,25]</sup> Numerous methods have been reported to overcome aforementioned drawbacks of CN. Coupling CN with other suitable semiconductors to form a composite is an

effective method to enhance photocatalytic activity.<sup>[26]</sup> The formation of composite between two varied semiconductors does not only improve the photocatalytic performance but also improves the visible light absorption ability and reduce the excitons recombination by transferring electrons from one semiconductor to another semiconductor through interface.<sup>[27,28]</sup> Till now several types of g-C<sub>3</sub>N<sub>4</sub> based composites have been reported.<sup>[29-34]</sup>

Layered double hydroxides (LDHs) are a branch of synthetic 2D nanostructured anionic clays with hydrotalcite-like materials in which divalent cations are arranged octahedrally with hydroxyl groups and trivalent cations have been exchanged isomorphously. Some hydrogen bonded water molecules may occupy any residual free space in the interlayer section.<sup>[35,36]</sup> LDHs are encouraging materials for a greater number of practical applications such as photochemistry, electrochemistry, catalysis, adsorption, and pharmaceuticals. These vast variety of applications are because of their high flexibility, cost-effective, and easily tailored properties which make it potential to produce materials considered to achieve specific necessities.<sup>[37-39]</sup> Nevertheless, pristine LDHs generally showed deprived photocatalytic efficiency in most cases because of it's low response to visible light, wide bandgap, less charge carrier mobility, and having high probability of photogenerated excitons recombination rate.<sup>[40-42]</sup> To get the better of above concerns, several attempts have been made to improve the photocatalytic performance of LDHs. Amongst the developed strategies, construction of composite with other semiconductors have been considered as efficient route to enhance the photocatalytic activity of LDHs.<sup>[43,44]</sup> Microwave-assisted synthesis of nanomaterials has gained special consideration owing to low cost, easy and rapid synthesis, more yields with less reaction time. In present investigation we used microwave-assisted method for synthesis of nanomaterials.<sup>[45-47]</sup>

In the present study, for the first time we demonstrate a simple microwave-assisted synthesis of ZALDH/CN composites and its application towards the highly efficient photocatalytic antibiotic pollutant ciprofloxacin degradation under visible-light illumination. The fabricated ZALDH/CN composite photocatalysts have shown enriched photocatalytic activity compared to bare ZALDH and CN. Moreover, the degradation reaction pathway was also studied. Finally, plausible photodegradation reaction mechanism is also proposed. The results confirmed that as-synthesized ZALDH/CN composites could be used for not only ciprofloxacin degradation but also useful for other environmental remediation applications.

## 5.2 Experimental section

### 5.2.1 Materials and method

All aqua solutions were preparation using double distilled (DD) water and all chemicals used in this study are analytical grade and no need for further purification. Zink nitrate hexahydrate (Finar, 99 %), aluminum nitrate (Finar, 98 %), sodium hydroxide (Finar, 97 %), sodium carbonate (Loba Chemie, 99.5 %), ciprofloxacin (TCI, 98 %), melamine (Ottokemi, 98 %), isopropanol (Choneye extra pure, 99.9 %), EDTA-2Na (Panreac, 90.0 %), silver nitrate (Aencore, 99.8 %).

### 5.2.2 Synthesis of g-C<sub>3</sub>N<sub>4</sub>

By the use of thermal condensation method, CN was synthesized. Briefly, 5 g of melamine was ground well, transferred to an aluminum boat, kept in a tubular furnace, and maintained temperature 550 °C for 2 h with a ramp rate of 5 °C per minute. After cooling naturally to the room temperature (R.T.), light yellow color powder was obtained and ground well for further use.

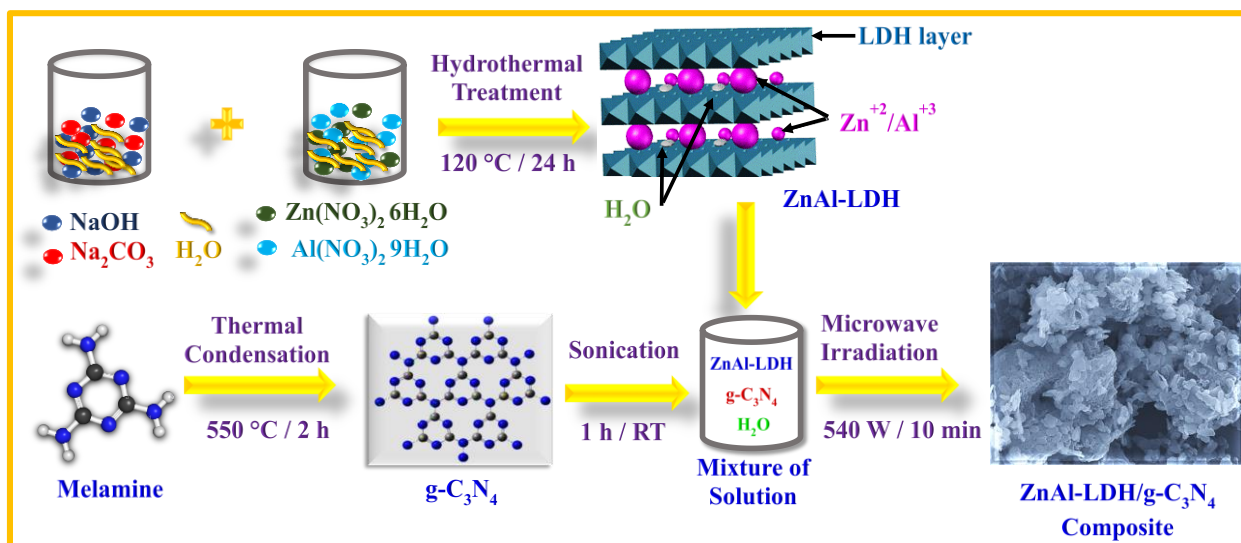
### 5.2.3 Synthesis of ZnAl-LDH

ZALDH was synthesized by a simple hydrothermal method. Concisely, 4.689 g (0.0125 moles) of aluminum nitrate (Al (NO<sub>3</sub>)<sub>3</sub>) and 7.437 g (0.0250 moles) of zinc nitrate (Zn (NO<sub>3</sub>)<sub>2</sub>) was added (molar ratio of Zn:Al = 2:1) into the 100 mL DD water in a beaker and stirred for 1h at R.T. and marked as (Solution A). Simultaneously, another solution was prepared, having 100 mL DD water with 3.375 g of NaOH and 2.645 g of Na<sub>2</sub>CO<sub>3</sub> was stirred well up to homogeneous mixture was formed and marked as (Solution B). Afterwards, solution B was transferred gently to the (solution A) while stirring, a white color solution was formed and the solution was kept stirring for 2 more hours at R.T. Afterwards, whole mixture (mixture of solution A and solution B) was transferred in to a 250 mL hydrothermal bomb and kept in a programmable muffle furnace and operated at 120 °C for 24 hours at a heating rate of 3 °C. After completion, the reaction was allowed to cool naturally to R.T and the obtained products was washed four times with DD water and with the help of hot air oven the obtained ZALDH was dried overnight.

### 5.2.4 Synthesis of ZnAl-LDH/CN composite photocatalysts

For the synthesis of ZALDH/CN composites a facile and simple one-step microwave irradiation method was adopted. Briefly, appropriate amount of pre-synthesized CN was taken into a beaker with 50 mL of DD water and sonicated for 1h at R.T. To the above mixture, calculated amount of already synthesized ZALDH was added and stirred for another 1h at R.T. The resulted

mixture was subjected to 540 W microwave irradiation for 10 min using a microwave oven. After the microwave treatment, a white color semisolid product was formed and washed several times with DD water to remove un-reacted particles. Finally, white color product was collected for further use. Same as the above method, series of materials were synthesized with varying the concentration, 5%, 10%, 15% of CN to ZALDH and labelled as ZALDH/CN-5, ZALDH-CN-10, and ZALDH-CN-15 respectively. A complete synthesis procedure of CN, ZALDH, and ZALDH/CN composites was represented as shown below in Scheme 5.1.



**Scheme 5.1:** Schematic representation of synthesis of ZALDH, CN, and ZALDH/CN composites.

### 5.2.5 LC-MS studies

LC-MS studies were performed with the help of MaXis ESI-QTOF tandem MS system (Bruker Daltonics, Breman, Germany). To identify the CIP photodegradation intermediate products for the optimized ZALDH/CN-10 composite. This instrument was used in the positive mode under the control of a microOTOFcontrol program. Agilent 1100 series capillary pump (Agilent, Palo Alto, CA) equipped with a home-made converse phase C18 column (300 Å, 5 µm, 320 µm × 150 mm) were used for Chromatographic separation with a flow rate of 15 µL/min. DD water having 0.1 % formic acid and acetonitrile having 0.1 % formic acid were used as mobile phase A and mobile phase B in the present analysis.

### 5.2.6 Photocatalytic activity

To know the photocatalytic activity of the synthesized pure CN, pure ZALDH, and ZALDH/CN composites. The CIP photocatalytic degradation investigations were carried out with

the help of 35 W Xe arc lamp. The initial (pH = 6.5) for the CIP solution, initial concentration of CIP solution was 20 ppm (20 mg/lit), and 30 mg of the synthesized photocatalyst was added in 50 mL of as prepared CIP aqua solution in a jacketed beaker and sonicated for 10 min. The jacketed beaker was connected with water circulation system to maintain a constant temperature of 30 °C with the help of a chiller. For 30 minutes, the CIP solution with catalyst was stirred in the dark to determine adsorption and desorption equilibrium between the photocatalyst and CIP. After 30 min solution was exposed to visible-light illumination, and at every predetermined 20 min time interval, reaction mixture sample was collected and centrifuged to isolate the catalyst from the CIP solution for the analysis of the percentage of CIP photo-degradation with the help of UV-Vis spectrophotometer. To explain the effect of different experimental aspects, controlled experiments were performed in the absence of light and catalyst which tells that there is no photo-degradation of CIP, indicating that, for the photo-degradation, light and catalyst are the primary elements. Trapping experiments were carried out in the same experimental conditions as described above, but with the addition of altered quenchers to the reaction system to investigate the role of photogenerated reactive species. Moreover, the recyclability of photocatalysts were also carried out by collecting the catalyst after every run with the help of centrifugation and washing thoroughly with DD water, and dry it before use.

### 5.3. Results and discussions

#### 5.3.1. PXRD, FT-IR, and TRFL studies

The crystallinity and phase structure of the fabricated CN, ZALDH, ZALDH/CN composites was examined by PXRD studies, and the PXRD results are depicted in Figure 5.1(a). For pure CN, two distinctive diffraction peaks were observed. The sharp and high intense peak at  $2\theta = 27.59^\circ$  is responsible for interplanar stacking of (002) lattice plane and the minor peak at  $2\theta = 13.16^\circ$  resulting from in-plane structural repeating unit corresponds to (100) lattice planes, respectively.<sup>[20,48,49]</sup> For pure ZALDH, the sharp and high intense diffraction peaks found at  $2\theta = 11.74^\circ, 23.55^\circ, 34.66^\circ, 39.25^\circ, 46.80^\circ, 60.22^\circ$ , and  $61.59^\circ$  are attributed to the (003), (006), (012), (015), (018), (110), and (113) lattice planes, which can be indexed to the hexagonal phase of ZALDH and well-coordinated with standard diffraction data of (JCPDS No. 38–0486).<sup>[50,51]</sup> In the case of ZALDH/CN composites, combined XRD patterns of ZALDH and CN were observed, but the intensity of CN was very low in composites. Since the amount of CN in the composite is too low at around 5, 10, and 15%, peaks belonging to CN were overshadowed by excessive amount of

ZALDH in the final composite material and therefore no CN peaks could be identified in composite. With the increasing CN amount on the ZALDH/CN composites, the diffraction peak at 27.59° intensity was increased as shown in Figure 5.1(b), with reflecting their respective amount of CN in the ZALDH/CN composites. This indicates the coupling between the CN and ZALDH in ZALDH/CN composites.

To know the composition and structural vibrations of the synthesized photocatalysts FT-IR analysis was carried out. Figure 5.1(c) shows the spectrum of FT-IR for pure CN, pure ZALDH and ZALDH/CN composites. The spectrum of pure CN contains a sharp peak at  $810\text{ cm}^{-1}$  which is mainly because of the stretching vibrations of S-triazine ring, between the wavenumber values of 1200 and  $1650\text{ cm}^{-1}$  it contains a broad band which is a consequence of stretching vibrations generated by aromatic heterocycles, precisely C–N and C=N heterocycles. Furthermore, the broadband appears at  $3208\text{ cm}^{-1}$  corresponds to the stretching vibrations of residual N-H groups which are linked with undiminished amino groups.<sup>[52]</sup> The broad band appeared at  $3424\text{ cm}^{-1}$  and  $1627\text{ cm}^{-1}$  for the ZALDH are because of the stretching vibrations generated by -OH group. The ZALDH spectrum also consists peaks at wavenumber values of  $448\text{ cm}^{-1}$ ,  $553\text{ cm}^{-1}$ ,  $613\text{ cm}^{-1}$ , these peaks are ascribed to the translational vibrations generated by the metal-oxygen and metal-oxygen-metal (Zn–O, Al–O and Zn–O–Al) bonds present in the ZALDH compound. We have also observed peaks at  $1364\text{ cm}^{-1}$  and  $1495\text{ cm}^{-1}$ , the former peak was intense one compared to the later one, these peaks are formed because of the symmetric and asymmetric stretching vibrations generated by (O–C–O) present in  $\text{Na}_2\text{CO}_3$  precursor used in the synthesis.<sup>[53,54]</sup> It can be noted that the FT-IR spectra of ZALDH/CN composites have coexistence of all the characteristic bands of CN and ZALDH. The appearance of these characteristic peaks demonstrates the successful formation of ZALDH/CN composites.

The photogenerated excitons lifetime and their separation efficiency at the interface of the ZALDH with CN can be efficiently studied by using time-resolved fluorescence lifetime (TRFL) analysis. The TRFL spectra were obtained for pure ZALDH, CN, and ZALDH/CN-10 composite with the excitation and emission wavelength are 380 and 466 nm respectively. As represented in Figure 5.1(d), the ZALDH/CN composite curve is less steep than bare CN and steeper than bare ZALDH. As shown in the below (equation 5.1). These average lifetime decay curves were perfectly fitted when bi-exponential functional equation was used.

$$Fit = B + A_1 \exp\left(\frac{-x}{t_1}\right) + A_2 \exp\left(\frac{-x}{t_2}\right) \quad (5.1)$$

In this 'A' constitutes  $n^{\text{th}}$  decay weighing parameter and 'B' represents constant. Whereas, the average lifetime was calculated from (equation 5.2) mentioned below,

$$t_{av} = \left( \frac{A_1 t_1 + A_2 t_2}{A_1 + A_2} \right) \quad (5.2)$$

As shown in Table 5.1, after the formation of composites, ZALDH/CN, the longer and shorter lifetimes of components  $t_2$  and  $t_1$  were reduced as compared with pure ZALDH and CN. In the case of ZALDH/CN-10 composite,  $t_1$  is contributed by non-radiative process which has a larger contribution percentage of  $A_1$  and another component  $t_2$ , that is related to second lifetime of recombination process, has a lower contribution percentage of  $A_2$ . These findings suggesting the enhanced charge carrier migration from CN to ZALDH. Moreover, the average lifetime of ZALDH/CN-10 (3.23 ns) is less than pure CN (4.89 ns) and more than pure ZALDH (1.60 ns). The decrease in the lifetime of ZALDH/CN-10 composite points out the existence of charge transfer through different non-radiative pathway by means of newly formed channels induced by the presence of ZALDH. The charge carriers which are generated by the incident photons are rapidly captured by ZALDH. This expeditious electron transfer from CN to ZALDH confirms the formation of ZALDH/CN-10 composite. Because of this speedy process the electron and hole pairs are separated effectively and assist the enhancement of photocatalytic activity of the ZALDH/CN-10 composite compared to constituents of CN and ZALDH. Similar explanations have been reported in earlier literature as well.<sup>[55,56]</sup>

**Table 5.1:** Shorter and longer lifetime components  $t_1$ ,  $t_2$ , and average life time of CN, ZALDH, and ZALDH/CN-10.

Photocatalysts	$A_1$ (rel. %)	$t_1$ (ns)	$A_2$ (rel. %)	$t_2$ (ns)	$t_{av}$ (ns)
CN	0.097	19.918	0.965	3.388	4.896
ZALDH	0.599	1.600	0.599	1.600	1.600
ZALDH/CN-10	0.841	2.111	0.182	8.400	3.230

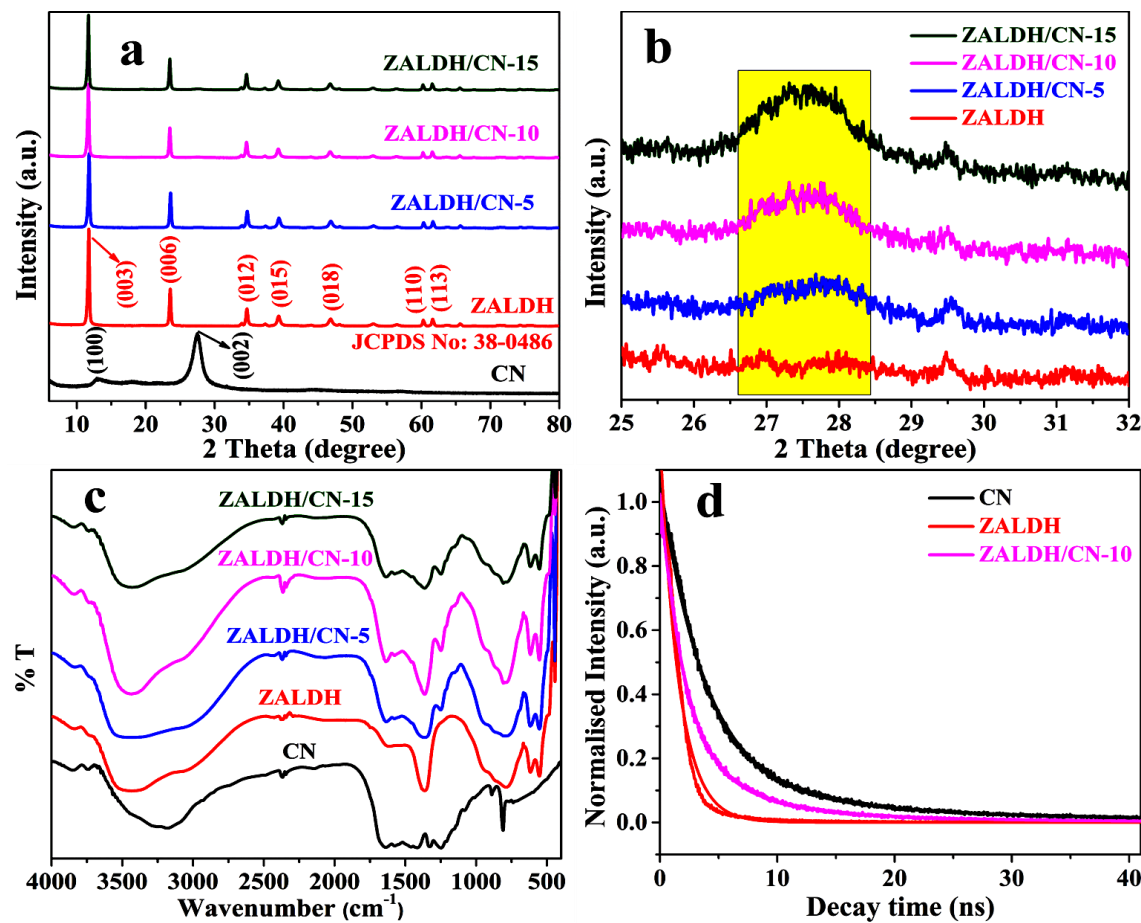


**Figure 5.1:** (a) PXRD patterns of synthesized pure CN, pure ZALDH, and ZALDH/CN composites, (b) respective expanded patterns of XRD, (c) FT-IR spectra of synthesized pure CN, pure ZALDH, and ZALDH/CN composites, and (d) Lifetime PL studies of pure CN, pure ZALDH and ZALDH-10 composite.

### 5.3.2 FE-SEM, TEM, and EDS studies

FE-SEM and EDS studies were performed to investigate the surface morphology and elements present in the synthesized pure CN, pure ZALDH, and ZALDH/CN-10 composite. As shown in Figure 5.2(a), FE-SEM images of pure CN show sheet like morphology, whereas in Figure 5.2(b), pure ZALDH displays a small plate like morphology. Figure 5.2(c-e), shows the ZALDH/CN-10 composite indicating the presence of both pure CN and pure ZALDH morphologies. Furthermore, there is no breakdown in the basic skeleton of CN and ZALDH after the formation of the ZALDH/CN composite. To know the composite formation and interaction between the CN and ZALDH in ZALDH/CN-10 composite. The atomic and weight percentages of the synthesized ZALDH/CN-10 composite was shown in Figure 5.2(f). TEM analysis was

carried out at different magnifications and results are shown in Figure 5.2(g-i). As showed in image the circle with yellow color indicates the presence of dual material morphology and formation of a composite hybrid which can yield a better interaction between CN and ZALDH. These results further conclude the successful formation of composite ZALDH/CN.

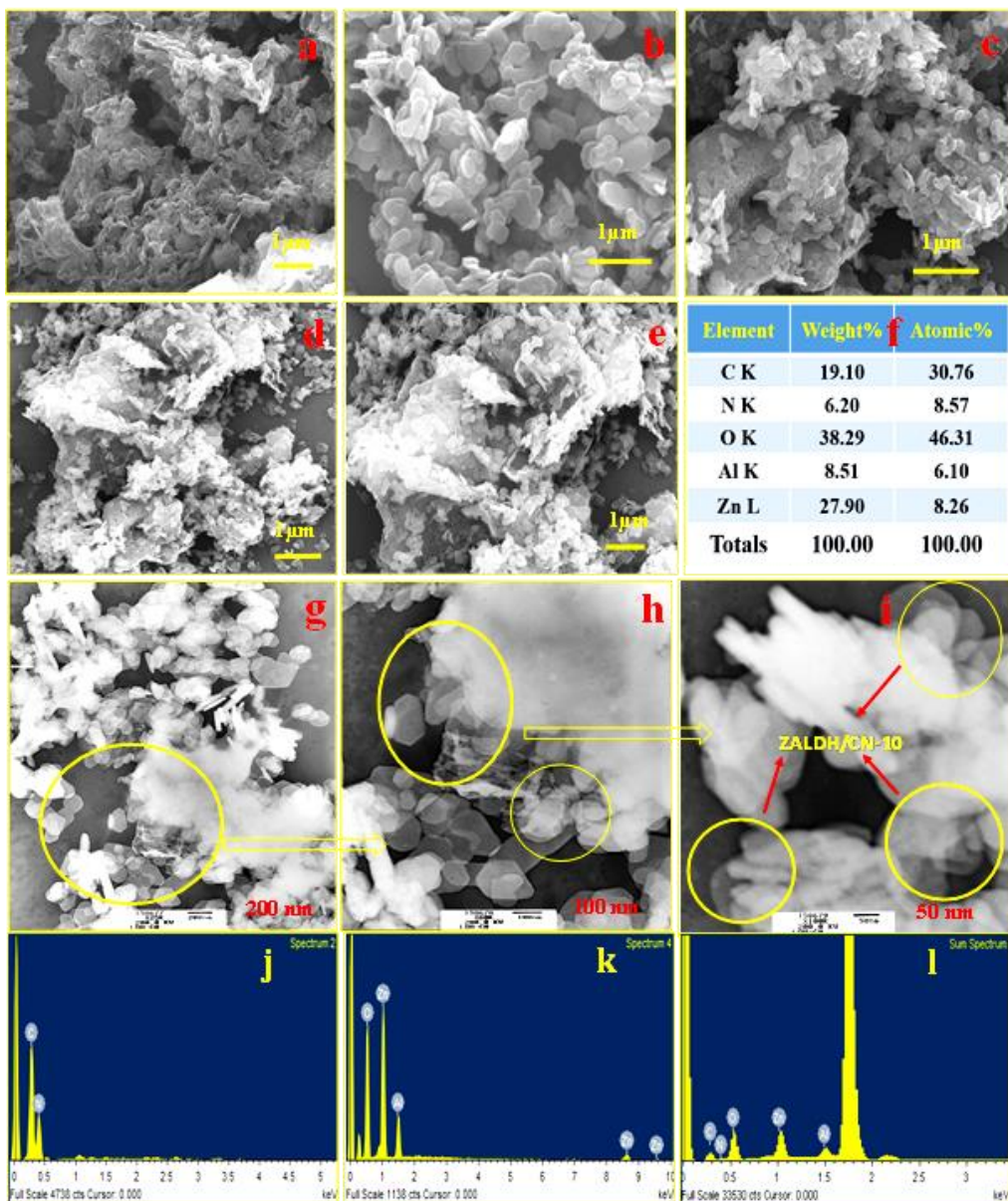


**Figure 5.2:** (a) FE-SEM images of pure CN, (b) pure ZALDH, (c-e) ZALDH/CN-10 composite, (f) weight and atomic percentages of ZALDH/CN-10 composite, (g-i) TEM images of ZALDH/CN-10 with different magnifications, and (j) EDS elemental analysis of CN, (k) ZALDH, (l) ZALDH/CN-10 composite.

The EDS elemental analysis of the ZALDH/CN-10 composite is shown in Figure 5.2(j-l) tells about the presence of Zn, Al, C, and N elements with varying weight ratios. To study the distribution of elements in the ZALDH/CN-10 composite selected area EDS elemental mapping studies were carried out and shown in Figure 5.3(a-f), which indicates the uniform dissemination of Zn, Al, C, N, and O elements respectively. Above results confirm the construction of ZALDH/CN-10 composite.

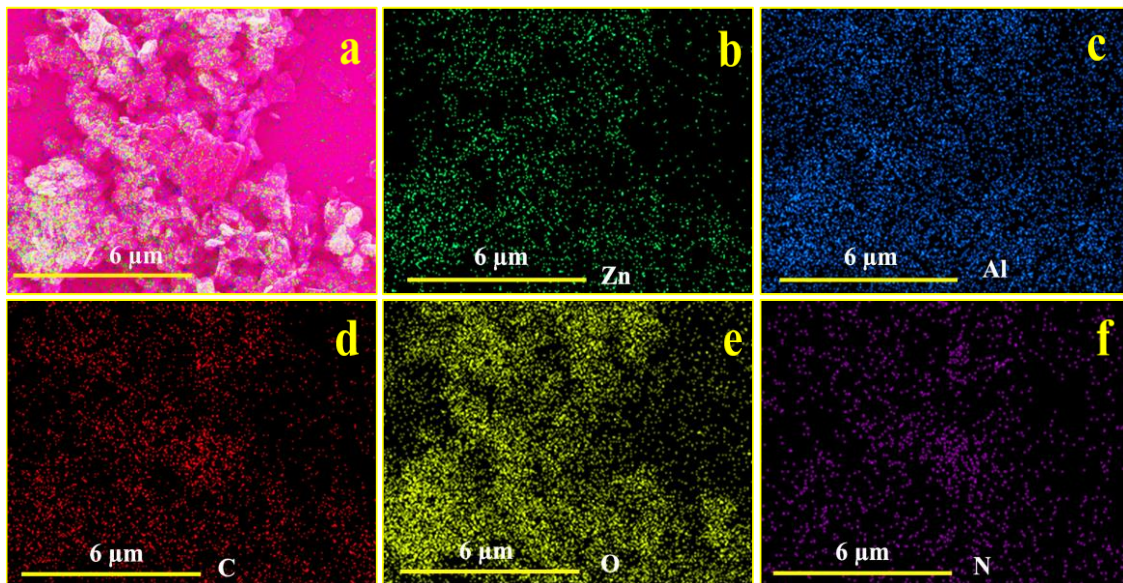


**Figure 5.3:** (a-f) EDS elemental mapping images of ZALDH/CN-10 composite with respective elements.

### 5.3.3 UV-Vis DRS and BET studies

Figures 5.4(a-b) depicts the UV-Vis DRS studies, which are used to determine the synthesized photocatalyst's light harvesting properties, since optical absorption characteristics are more important for better understanding of the photocatalytic activity. Pure CN displays a strong absorption edge near to 467 nm indicating that CN can be excited under visible region of the solar spectrum.<sup>[57,58]</sup> Pure ZALDH exhibits a weak absorption band in the UV-light range 200-400 nm, which corresponds to electronic transitions of O 2p state to metal ns or np levels ( $n = 3$  for Al and  $n = 4$  for Zn) in ZALDH.<sup>[51,59,60]</sup> As shown in Figure 5.4(a), the composites of ZALDH/CN displays a slight blue shift, and as the CN content increased, the absorption edge shifted towards the lower wavelength field, which is accountable for the more visible light absorption in composite ZALDH/CN. The absorption regions of all the composites are observed in between the pure CN and ZLDH. ZALDH/CN-15 has a higher absorption in the region 200-450 nm (absorbance region

of CN) due to the excess amount of CN i.e; 15%. However, it should be noted that, in the region of 450-600 nm, absorbance of ZALDH/CN-10 exceeds that of ZALDH/CN-15. Bandgap energies of CN, ZALDH, and ZALDH/CN composites were determined according to Tauc plots  $(\alpha h\nu)^{1/2} = A(h\nu - E_g)$  as depicted in Figure 5.4(b). The calculated bandgap of CN, ZALDH, are 2.73 eV and 3.07 eV.<sup>[54,61]</sup> The improved visible-light absorption capacity in ZALDH/CN composites can enhance the photocatalytic activity compared to those of bare CN and ZALDH materials.

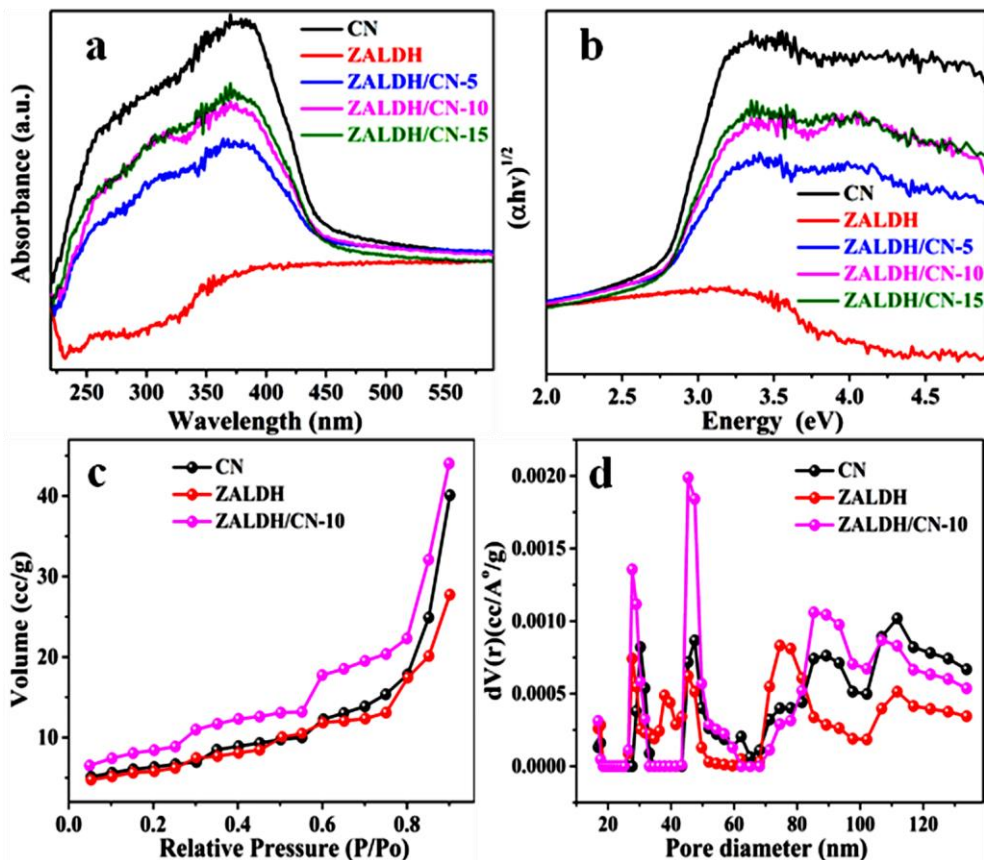


**Figure 5.4:** (a) Ultra Violet –Visible DRS spectra of CN, ZALDH, and composites of ZALDH/CN, (b) Tauc plots of the respective photocatalysts, (c) nitrogen adsorption isotherms of pure CN, pure ZALDH, ZALDH/CN-10 composite, and (d) respective pore size distribution plots.

To investigate the BET surface area and pore size distribution of fabricated pure CN, pure ZALDH, and ZALDH/CN-10 composite, BET adsorption measurements were carried out under room temperature, and prior to analysis, sample was degassed at 150 °C. The obtained BET results are depicted in Figure 5.4. As shown in Figure 5.4(c), nitrogen adsorption isotherms of CN, ZALDH, and ZALDH/CN-10 composite, in comparison with bare CN and ZALDH materials, ZALDH/CN-10 composite possess more specific surface area. The calculated surface area of pure

CN, ZALDH, and ZALDH/CN-10 composite is as follows; 17.60 m<sup>2</sup>/g, 16.17 m<sup>2</sup>/g, and 23.60 m<sup>2</sup>/g respectively. The high specific surface area of ZALDH/CN-10 composite can provide additional visible light absorption capacity of reactant molecules due to the exposed surface area resulting in effective photocatalytic degradation of pollutants. The corresponding pore size distribution curves are shown in Figure 5.4(d). The calculated pore volumes of the CN, ZALDH, and ZALDH/CN-10 Composite as follows 0.056 cc/g, 0.039 cc/g, and 0.063 cc/g respectively.

### 5.3.4 XPS Analysis

To determine the surface chemical composition and detailed oxidation states of the elements present in ZALDH/CN-10 composite XPS measurements were carried out. Figure 5.5(a) displays the survey spectrum of ZALDH/CN-10 composite, which indicates the presence of Zn, Al, C, N, and O, elements with the respective binding energies of 1022.32 eV, 75.23eV, 286.6 9 eV, 397.90 eV, and 532.28 eV respectively. This confirms the successful formation of composite between CN and ZALDH which is also consistent with XRD and TEM results. The high resolution Zn 2p spectrum is shown in Figure 5.5(b). Two major peaks appear at binding energies of 1022.13 and 1045.38 eV corresponding to Zn 2p<sub>3/2</sub> and Zn 2p<sub>1/2</sub> indicates the presence of Zn binding with the oxygen molecule (M-O bond). The additional satellite peaks appearing at binding energies of 1026.58 eV and 1049.73 eV are responsible for the high spin divalent state of Zn<sup>2+</sup> in ZALDH/CN-10 composite.<sup>[62]</sup>

Figure 5.5(c) shows the high resolution XPS spectrum of Al 2p, which can be deconvoluted into two peaks located at binding energies of 74.18 and 76.98 eV which confirms the existence of the Al<sup>3+</sup> and Al(OH)<sub>3</sub> respectively, in the composite of ZALDH/CN-10.<sup>[63]</sup> The deconvolution spectrum of C1s is depicted in figure 5.5(d). The spectrum consists of five peaks which indicates the five different carbon environments in the system. The peak at 285.18 eV raised due to the contaminant carbon present in the vacuum oil during the measurement. The peak at 286.93 eV is assigned to the carbon bound to the nitrogen inside triazine ring and the peak at 288.43 eV formed due to the carbon bound to the nitrogen in CN. Peaks at 289.53, and 290.60 eV are formed due to the carbon present in (O=C=O) group intercalated between the ZALDH layers. The XPS deconvolution spectrum of N1s is shown in figure 5.5(e). The spectrum shows three different peaks precisely at 397.68 eV, 399.93 eV and 402.38 eV. The lower binding energy value peak at 397.68 eV is formed because of nitrogen present in (C=N=C) group, the second peak located at 399.93 eV is may be because of the nitrogen bound to three different carbons precisely ternary Nitrogen

(N–(C)<sub>3</sub> groups). The higher binding energy value peak situated at 402.38 eV is may be because of the Nitrogen present in the amino functional groups (C–N–H). Apart from these three peaks, there is also a small peak positioned at 404.58 eV. This peak may be a consequence of  $\pi$ -excitations in the CN group.<sup>[51,64–66]</sup> Figure 5.5(f), illustrates the deconvolution spectrum of O1s. In this spectrum we can identify two peaks found at 531.83 eV and 535.83 eV respectively. The former peak located at lower binding energy which might be formed because of the lattice oxygen species (O<sup>2–</sup>) which is bound to metals present in ZALDH. The later peak positioned at higher binding energy value has formed because of the oxygen present in the hydroxide group (–OH).<sup>[60]</sup> Compared with reported binding energies of bare ZALDHs 1022.2 eV, 74.3 eV, and 531.8 eV for Zn2p, Al2p, and O1s. It is noted that the binding energies of ZALDH/CN-10 shifts to the higher value 1022.3 eV, 75.23 eV and 532.28 eV for Zn2p, Al2p, and O1s respectively. Such high positive binding energy shifts of metal and oxygen elements are similar to those reported in the case of ZnAl-LDH/CNTs composite.<sup>[64]</sup> Therefore, the shift towards higher binding energy for ZALDH/CN-10 as compared with bare ZALDHs, confirms the efficient interaction between ZALDH nanoparticles and CN can possibly be ascribed to the formation of ZALDH/CN-10 composite photocatalyst effectively.

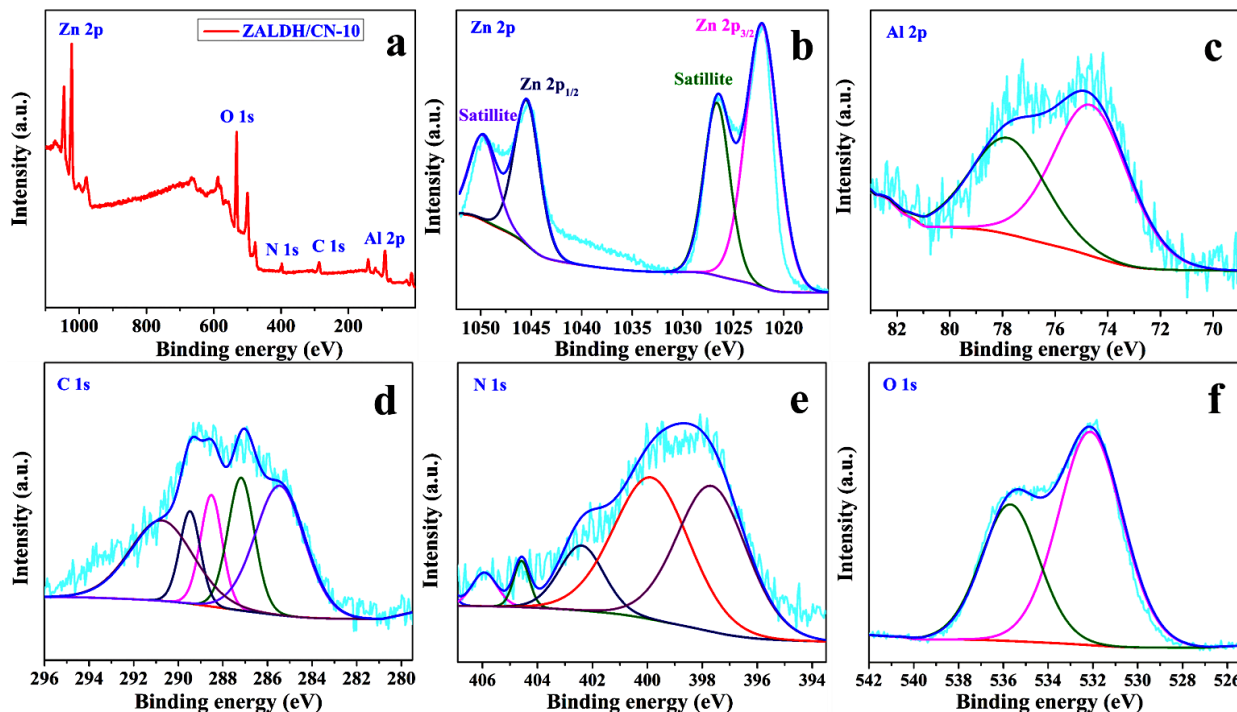


**Figure 5.5:** (a) XPS survey spectrum of ZALDH/CN-10 composite, (b) Zn 2p, (c) Al 2p, (d) C1s, (e) N 1s, and (f) O 1s.

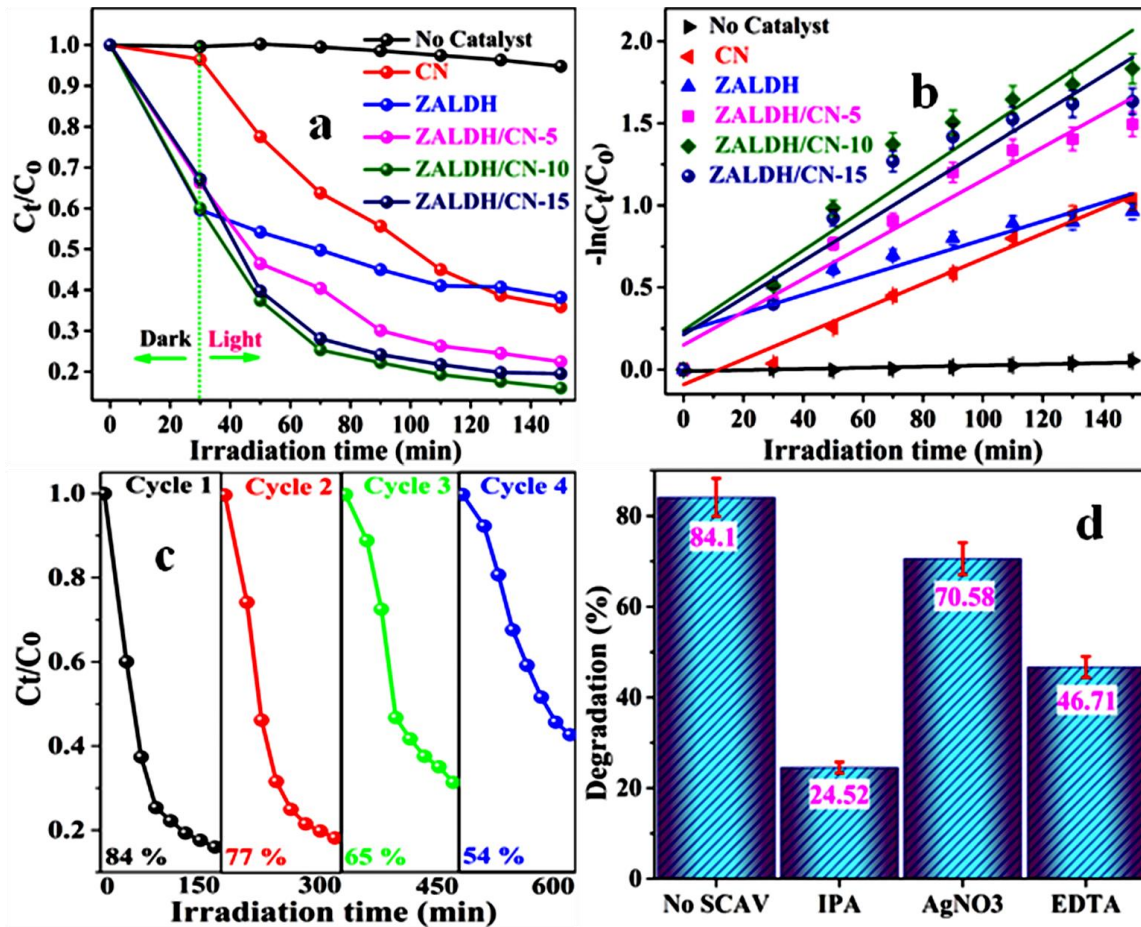
### 5.3.5 Photocatalytic activity studies

Figure 5.6(a) depicts the complete CIP degradation comparison curves between irradiation time vs  $C_t/C_0$  (concentration of CIP at a particular time/initial concentration of CIP). For pure CN the photodegradation was 64.2 % whereas for pure ZALDH it was 61.9 %. As for composites ZALDH/CN-5, ZALDH/CN-10, and ZALDH/CN-15 the photodegradation was 77.6 %, 84.1%, and 80.5 % respectively. Amongst all analyzed samples, ZALDH/CN-10 shows the highest photocatalytic activity with 84.1 % degradation of CIP within 150 min. The improved photocatalytic activity could be contributed by the formation of the composite between two semiconductor materials with negatively charged CN and positively charged metal ions of ZALDH. In the ZALDH/CN composites, the photodegradation percentage was found to be elevated with increasing the CN weight ratio up to 10 % which later on decreased when CN was 15 %. This may be caused by excessive amounts of CN blocking the photoactive sites on LDH and with increasing amount of CN, there is a high probability of agglomeration among the composites which could be directly responsible for low catalyst-light interaction leading to lower efficiency.

We conducted experiment, without catalyst and light and concluded that there is no effect on degradation indicating the highly stable nature of ciprofloxacin. Figure 5.6(b) shows the plots between  $-\ln (C_t/C_0)$  vs irradiation time which gives linear plots. From these linear plots, we calculated error with the relative standard deviation of duplicate runs, included error bars in the Figure 5.6(b). From the slope of these linear plots, we calculated the rate constant of the reaction, and found that the degradation process followed a pseudo first order kinetics model as  $(-\ln (C_t/C_0) = kt)$ . The rate constant (k) for the CN, ZALDH, ZALDH/CN-5, ZALDH/CN-10, and ZALDH/CN-15 was determined as  $6.8 \times 10^{-3} \text{ min}^{-1}$ ,  $6.4 \times 10^{-3} \text{ min}^{-1}$ ,  $1.0 \times 10^{-2} \text{ min}^{-1}$ ,  $1.2 \times 10^{-2} \text{ min}^{-1}$  and  $1.1 \times 10^{-2} \text{ min}^{-1}$  respectively.

Table 5.2 shows the rate constant and percentage of degradation. Moreover, we conducted a stability test for ZALDH/CN-10 composite. In This process photocatalyst was extracted from the aqueous solution by centrifugation after 150 minutes of irradiation in each cycle, rinsed thoroughly with DD water, and dried overnight. As shown in Figure 5.6(c), ZALDH/CN-10 exhibited a considerable loss of degradation efficiency after four successive cycles of ZALDH/CN-10 composite for photocatalytic degradation of CIP. The reasons for the loss in the degradation could be as follow. The process for reused catalysts were rinsed with DI water,

which was unable to properly remove the excessive CIP adsorbed onto the catalyst material during degradation cycles. Under the studied parameters, the composite had good photo-chemical stability.



**Figure 5.6:** (a) Photocatalytic dye degradation activity comparison curves of synthesized pure CN, ZALDH, and ZALDH/CN composites, (b) first order kinetics of pure CN, ZALDH, and ZALDH/CN composites. Error bars represent the standard deviations of duplicate runs, (c) photocatalyst stability studies of ZALDH/CN-10 composite, and (d) scavengers trapping studies of ZALDH/CN-10 composite. Error bars represent the standard deviations of duplicate runs.

Figure 5.6(d) shows the active species trapping experiments, which gives information about photogenerated excitons which are responsible for the photocatalytic CIP degradation process. Disodium ethylene diamine tetraacetate (EDTA 2Na), silver nitrate (AgNO<sub>3</sub>), and Isopropanol (IPA) were used as quenchers for the holes (h<sup>+</sup>), electrons (e<sup>-</sup>), and hydroxide radicals (·OH) respectively. CIP degradation efficiency was dramatically suppressed by the addition of IPA, which indicates that, ·OH is a major reactive species for the degradation of CIP, whereas with

the addition of EDTA 2Na and  $\text{AgNO}_3$  to the reaction system the degradation capacity was inhibited moderately indicating that  $\text{h}^+$  and  $\text{e}^-$  were also responsible in minor portions. A similar type of discussion has been reported in previous works.<sup>[67]</sup> The increased absorption ability in the visible-light field, as well as the improved charge separation efficiency at the well-formed interface between CN and ZALDH, it might be responsible the increased photocatalytic activity.

**Table 5.2:** Rate constant and percentage of degradation of CN, ZALDH, and ZALDH/CN-10 composites.

Photocatalysts	Rate ( $\text{min}^{-1}$ )	Degradation (%)
CN	$6.8 \times 10^{-3}$	64.1
ZALDH	$6.4 \times 10^{-3}$	61.8
ZALDH/CN-5	$1.0 \times 10^{-2}$	77.6
ZALDH/CN-10	$1.2 \times 10^{-2}$	84.1
ZALDH/CN-15	$1.1 \times 10^{-2}$	80.5

To examine the effect of temperature on the efficiency of CIP antibiotic pollutant photocatalytic degradation, we performed photocatalytic degradation experiments by using a water circulation system with a jacketed beaker to reach higher temperatures (40 °C and 50 °C). The temperature-dependent photo-degradation curves of CIP over ZALDH/CN-10 have been shown in Figure 5.7(a). The efficiency of degradation has improved at higher temperatures. Photo-degradation efficiency from 30 to 50 °C with an increment of 10 °C was calculated and found to be 84.1% at 30 °C, 89.5 % at 40 °C and 90.5% at 50 °C. Figure 5.7(b) was plotted with  $-\ln(C_t/C_0)$  on Y-axis and irradiation time on X-axis. A linear fit was obtained with their respective slope values at various temperatures are calculated errors with the relative standard deviation of duplicate runs, included error bars in the Figure 5.7(b). Slope of the linear fit was the rate constant at that particular temperature according to the equation  $-\ln(C_t/C_0) = kT$ . From the linear plots it can be emphasized that CIP degradation under visible light irradiation using ZALDH/CN-10 catalyst followed a pseudo first order kinetics. The calculated rate constant value at 30 °C was  $2.22 \times 10^{-2} \text{ min}^{-1}$ , when the temperature was increased to 40 °C, the rate constant was found to be  $2.27 \times 10^{-2} \text{ min}^{-1}$ . Finally when the temperature was further increased to 50 °C, the rate constant was calculated as  $2.38 \times 10^{-2} \text{ min}^{-1}$ . By observing the calculated rate constant values at different temperatures, it can be said there is a definite increase in rate constant with an increase in the

temperature. This increase in CIP degradation rate can be explained as follows. When the temperature is raised, the molecules are more likely to be agitated due to the absorbed energy which will lead to their high likelihood of collision, subsequently leading to higher rate of reaction which is otherwise lower at low temperatures leading to a lesser rate of reaction.

**Table 5.3:** Complete thermodynamic parameters of ZALDH/CN-10

Temperature (°C)	E <sub>a</sub> (KJ Mole <sup>-1</sup> )	ΔH (KJ Mole <sup>-1</sup> )	ΔS (KJ Mole <sup>-1</sup> K <sup>-1</sup> )	ΔG (KJ Mole <sup>-1</sup> )
30	9.700	7.097	-0.038	18.611
40				18.991
50				19.371

For a reaction to occur the particles must collide to lower the activation energy of the overall reaction. Arrhenius equation was taken into consideration to calculate the activation energy of the system using rate constant values obtained at different temperatures.<sup>[68]</sup> Figure 5.7(c) was plotted between  $\ln k$  and  $1/T$ . we have observed linear sloped lines at all the temperatures, these slope values have been substituted in the Arrhenius equation and we have calculated the activation energy values. The used equations are listed below.

$$\ln k = \ln A - E_a/RT \quad (5.3)$$

$$\ln \left( \frac{k}{T} \right) = \ln \left( \frac{A}{h} \right) - \frac{\Delta H}{RT} + \frac{\Delta S}{R} \quad (5.4)$$

'R'- universal gas constant, 'A'- Arrhenius factor, 'k'- Rate constant , 'h'- Planks constant, 'E<sub>a</sub>'- activation energy of the system, 'K'- Boltzmann constant, 'T'- Temperature (in Kelvin). ΔH is enthalpy and ΔS is entropy respectively. Figure 5.7(d) shows a plot between  $\ln (k/T)$  on Y-axis and  $1/T$  on X-axis. We have observed a straight line with a slope and intercept. The slope of this plot gives the enthalpy of the reaction (Slope =  $-\Delta H/R$ ) and the intercept of this plot gives the entropy of the reaction (Intercept =  $\ln(k/h) + \Delta S/R$ ). Gibbs free energy equation was used to calculate the Gibbs free energy of activation, since we have already calculated the enthalpy of the reaction and entropy of the reaction. The equation is given below.

$$\Delta G = \Delta H - T\Delta S \quad (5.5)$$

The calculated thermodynamic parameters for instance Gibbs free energy of activation ( $\Delta G$ ) was found to be a positive value and enthalpy of the reaction ( $\Delta H$ ) was also found to be a positive value whereas, entropy of the reaction ( $\Delta S$ ) was found to be a negative value. By taking

all these into consideration, it can be emphasized that the overall degradation process of CIP was endothermic, non-spontaneous reaction. It can also be said that the reaction process is endergonic in nature. All the calculated parameters are listed in Table 5.3.

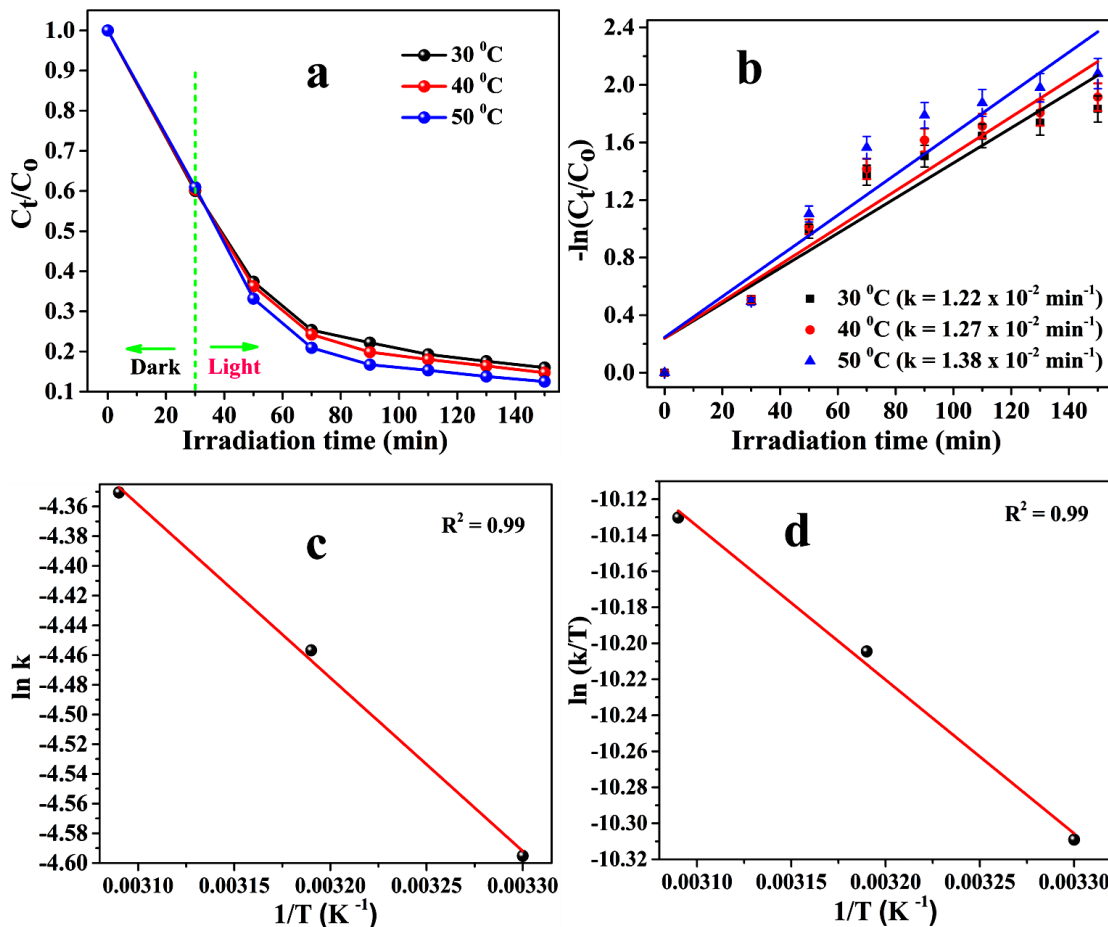


**Figure 5.7:** (a) Plots of  $C_t/C_0$  vs degradation time, (b) curves of  $-\ln(C_t/C_0)$  vs degradation time. Error bars represent the standard deviations of duplicate runs, (c) at different temperatures, time as a function the graph between  $\ln(k)$  vs  $1/T$ , and (d)  $\ln(k/T)$  vs  $1/T$ .

### 5.3.6 Proposed reaction mechanism

The remarkable results reported as above, a synergistic effect amongst the ZALDH and CN was observed, which indicates the improved photocatalytic degradation of antibiotic pollutant CIP with ZALDH/CN-10 composite and we proposed a suitable mechanism as demonstrated in Figure 5.8. According to the following empirical equations (5.6 and 5.7), the edge potentials of VB and CB ( $E_{VB}$  and  $E_{CB}$ ) are calculated.

$$E_{CB} = X - E_e + 0.5 E_g \quad (5.6)$$

$$E_{VB} = E_g - E_{CB} \quad (5.7)$$

The calculated valence band edge potentials ( $E_{VB}$ ) and conduction band edge potentials ( $E_{CB}$ ) of CN are +1.43 eV and -1.30 eV and of ZALDH's VB and CB are +3.62 eV and +0.55 eV, respectively.<sup>[54,61,69]</sup>

' $X$ ' is the Mulliken's electronegativity that is the geometric mean of the electronegativity of the constituent atoms of the semiconductor (6.59 eV for ZnAl-LDH and 4.73 eV for g-C<sub>3</sub>N<sub>4</sub>); ' $E_e$ ' is the energy of free electrons on the hydrogen scale (~4.50 eV); ' $E_g$ ' is the band gap energies of the ZnAl-LDH and g-C<sub>3</sub>N<sub>4</sub> are 3.07 eV and 2.73 eV in our experiment.

When we supply energy to the semiconductor more than their respective bandgap energy the electrons are excited from the VB to CB of the semiconductor. Since pure ZALDH is ultra violet light active, therefore it cannot excite electrons from VB to CB under visible-light, however in case of CN, have more visible light harvesting capacity. Because of this property, when CN was exposed to visible light irradiation it can absorbed light energy more than band gap of CN, subsequently the electrons are excited from VB to CB. Resulting, the holes are present in VB of CN and electrons are accumulated in the CB of the CN. Consequently, the photogenerated electrons on the CB of CN could readily migrates towards the CB of ZALDH since the CB of CN is (-1.30 eV) was more negative than that of ZALDH (+0.55 eV) while the holes remains in the VB of CN. The movement of electrons from CB of CN to CB of ZALDH supports the suppression of electron-hole pair recombination of CN and increase the effective charge separation of photogenerated excitons. Resulting enhanced photocatalytic activity of ZALDH/CN-10 composite compared to bare CN and ZALDH. Since more electron density is located at the CB of ZALDH, it could participate photo-reduction reaction to reduce dissolved oxygen O<sub>2</sub> to O<sub>2</sub><sup>•-</sup>. These formed superoxide anions at CB of ZALDH can react with dissolved H<sub>2</sub>O to generate 'OH, these formed 'OH are responsible for the degradation of CIP under visible-light illumination.

Though, as compared with the standard redox potential ('OH/OH<sup>-</sup> = +1.99 eV), the VB position of CN (+1.43 eV) is less positive, which reveals that, remaining holes in the VB of CN could not oxidize from OH<sup>-</sup> or H<sub>2</sub>O to form 'OH, it might be directly react with the CIP to form degradation products. Meanwhile electron density remains at the CB of CN, after transferring to CB of ZALDH. It could participate photo-reduction reaction to reduce dissolved oxygen O<sub>2</sub> to O<sub>2</sub><sup>•-</sup>. These formed superoxide anions at CB of CN can react with dissolved H<sub>2</sub>O to generate 'OH,

these formed  $\cdot\text{OH}$  are responsible for the degradation of CIP under visible-light illumination. Thus, photogenerated  $\cdot\text{OH}$  and  $\text{h}^+$  are the main active species for the CIP photo degradation under visible-light over the ZALDH/CN-10 composite. These occurrences were supported by the trapping experiment results. Similar discussions have been reported with previous works.<sup>[51,70]</sup> It has been worth to note that, there is availability of  $\pi$ -electron cloud density on the surface of  $\text{g-C}_3\text{N}_4$  sheets, along with having positive ions and more number of hydroxyl groups on the surface of layered double hydroxides (LDHs). These surface hydroxide groups of LDHs are interact with  $\text{g-C}_3\text{N}_4$  to get structure stability as well as to formation of heterojunction among the ZALDH and CN, because of these strong structural stability and interactions in ZALDH/CN-10 composite has shown enhanced photocatalytic CIP degradation performance under visible-light illumination. As depicted in Table 5.4, our work was compared with recently reported literature for the photocatalytic degradation of antibiotic CIP, and our synthesized composite ZALDH/CN-10 shows good competitiveness. It reveals that, it can be used application point of view in photocatalytic antibiotic degradation of CIP.

**Table 5.4:** Comparison of our work with recently reported literature for CIP photocatalytic degradation.

Photocatalyst	Amount of Catalyst	CIP Concentration	Light source	Time (min)	Degradation (%)	Reference
$\text{FeTiO}_3/\text{ZnO}$	1000 mg	10 ppm	80W UV lamp	180	100	[71]
Nano-ZnO	N.A	5 ppm	8 W Hg fluorescent	30	93	[72]
$\text{CeO}_2/\text{Ag/AgBr}$	50 mg	10 ppm	300W Xe lamp	120	93	[73]
$\text{WO}_3/\text{RGO}$	50 mg	20 ppm	300 W	150	94	[74]
$\text{CS@Au/ZnO}$	1000 mg	5 ppm	visible light	180	61	[75]
Fe-doped ZnO	100 mg	10 ppm	Sun light	210	66	[76]
ZnAl-LDH/ $\text{g-C}_3\text{N}_4$	30 mg	20 ppm	35W Xe lamp	150	84	Present work

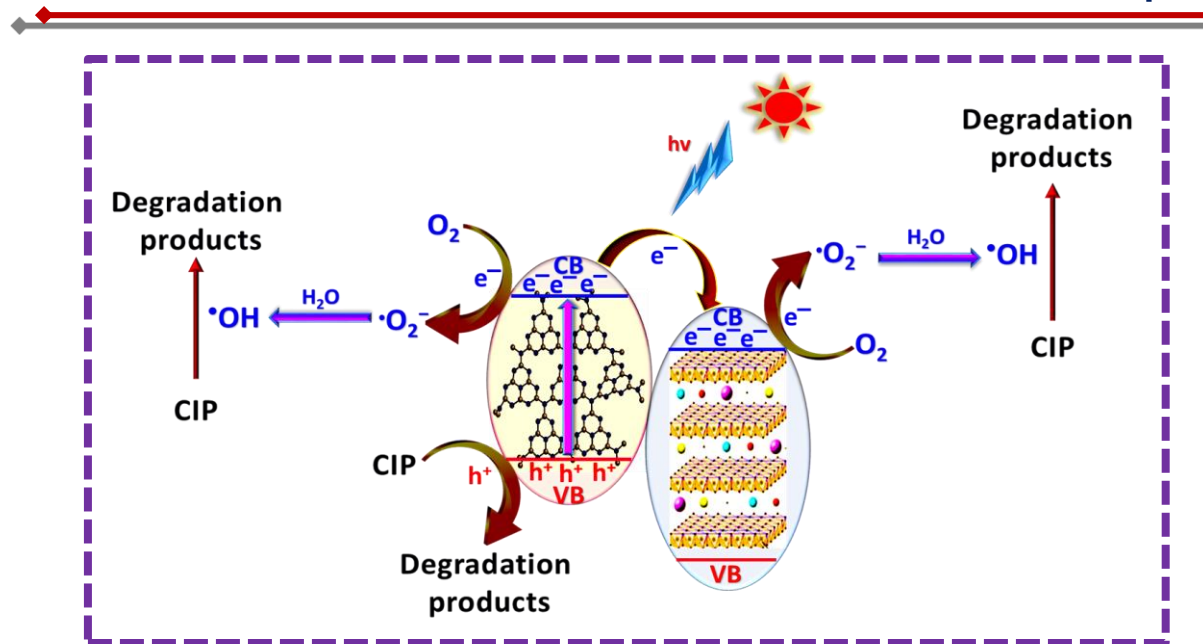


**Figure 5.8:** Suggested mechanism for CIP photocatalytic degradation over the composite ZALDH/CN-10 under visible-light.

### 5.3.7 Photocatalytic CIP degradation pathway

Major intermediate products are formed during the photocatalytic degradation process of CIP identified by LC-MS analysis and results are depicted in Table 5.5.

**Table 5.5:** Intermediate products formed during the photocatalytic degradation CIP under visible-light for ZALDH/CN-10 composite photocatalyst.

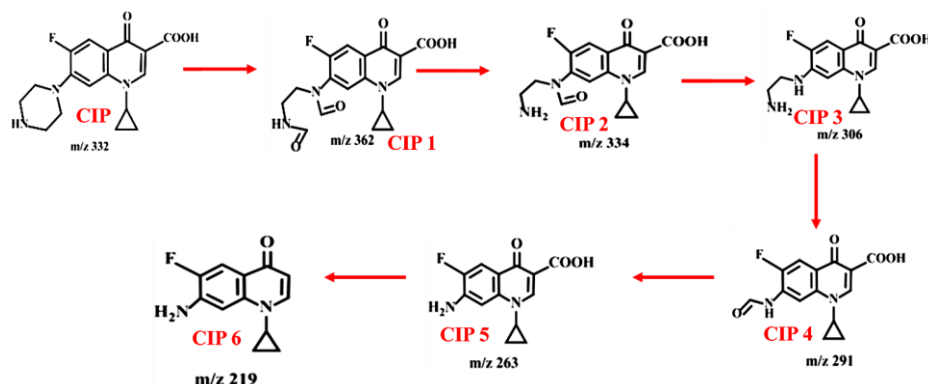
S.No	Intermediate	Mass(m/z)	Molecular formula	Proposed chemical structure
1	CIP	332	C <sub>17</sub> H <sub>18</sub> FN <sub>3</sub> O <sub>3</sub>	
2	CIP-1	362	C <sub>17</sub> H <sub>16</sub> FN <sub>3</sub> O <sub>5</sub>	



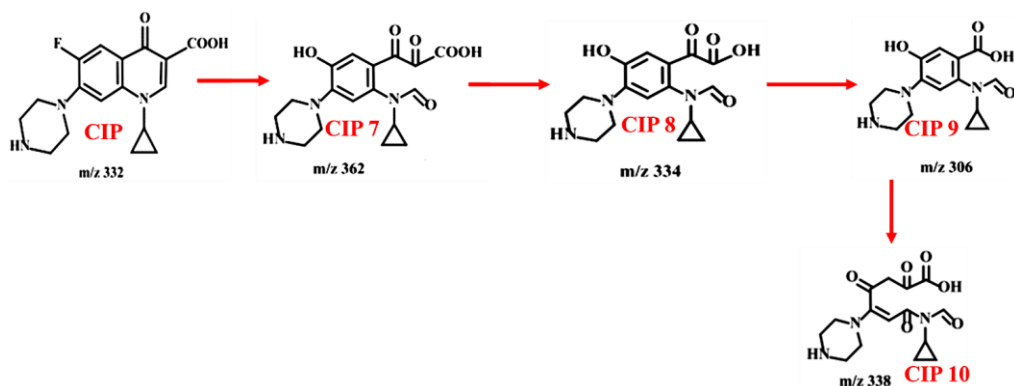
Three possible photocatalytic degradation routes of CIP have been proposed and shown in Scheme 5.2. (i) Pathway-1 is the primarily emphasis on the piperazinyl ring moiety breaking. According to previous studies, CIP-1 was formed when the piperazine ring in CIP is opened.<sup>[77,78]</sup> Consequently, with the elimination of one ( $\text{C}=\text{O}$ ) moiety from CIP-1 can be changed to CIP-2. Further removal of one more ( $\text{C}=\text{O}$ ) group from CIP-2 to form CIP-3. The transformation of CIP-3 from CIP-2 was observed by previous researchers also, means this transformation is consistent. Further, CIP-3 can undergo deamination to form CIP-4. Then CIP-4 would have participated in decarbonylation and decarboxylation to formation of CIP-6 via CIP-5. By undergoing all these processes, the piperazinyl moiety of CIP was completely fragmented or in other words, degraded. (ii) Pathway-2, mainly three types of cleavages can be observed, in which first one is defluorination, second one is the destruction of quinolone moieties, and lastly the breakage of benzene rings. As reported in previous works.<sup>[67,73]</sup> Hence, CIP-7 can be generated from defluorination and cleavage of quinolone moieties on the ( $\text{C}=\text{C}$ ) bond adjacent to the carboxylic acid of CIP simultaneously. From the CIP-7, with the loss of two carboxylic acid groups, CIP-8, CIP-9 were formed. Subsequently, CIP-10 was formed by the cleavage of benzene

ring from the CIP-9. (iii) Pathway-3 primarily describes hydroxylation of CIP. It was hydrolyzed to various degrees, resulting in formation of CIP-11, CIP-12, and CIP-13. Earlier research reports suggested a similar route.<sup>[79-81]</sup> Furthermore, CIP-6, CIP-10, and CIP-13 also may undergo a series of cleavage reactions such as quinolone ring and piperazine rings, decarboxylation and, hydroxylation, and all these products are finally converted into  $\text{CO}_2$ ,  $\text{NO}_3^-$ ,  $\text{H}_2\text{O}$ , and  $\text{F}^-$ . Since various radicals can be involved, we are unable to depict this aspect of the degradation pathway here.

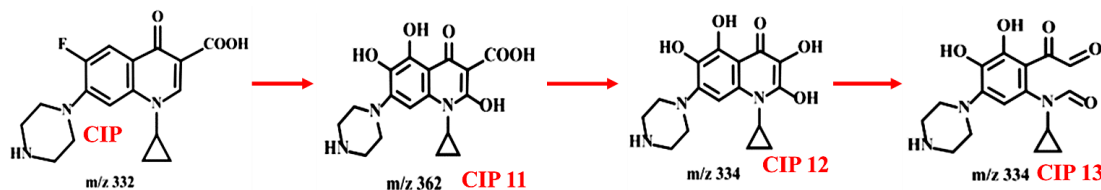
**(i) Pathway-1**



**(ii) Pathway-2**



**(iii) Pathway-3**



**Scheme 5.2:** Proposed pathways for photocatalytic degradation of CIP under visible light.

## 5.4 Conclusions

In summary, ZALDH/CN composites were successfully synthesized by a simple microwave irradiation method, which established a strong interface system due to the positively charged metal ions of  $Zn^{2+}$  and  $Al^{3+}$  in ZALDH sheets and negatively charged ions in the CN nanosheets. The results concluded that the optimized ZALDH/CN-10 composite showed a better photocatalytic performance compared to pure materials and remaining composites for the photocatalytic degradation of CIP under visible light irradiation. Photo generated active species trapping studies confirm that, hydroxyl radicals, holes and electrons were responsible for the degradation process, and also we conducted recyclability test for the ZALDH/CN-10 composite which revealed the stability of the composite. Moreover, we proposed three major degradation pathways based on LC-MS results for the photocatalytic degradation of CIP under visible light. As a result, the findings of this study offer useful information for improving photocatalytic activity for wastewater treatment and long-term energy generation applications.

## 5.5 References

- [1] A. Habibi-Yangjeh, S. Asadzadeh-Khaneghah, S. Feizpoor, A. Rouhi, *Journal of Colloid and Interface Science* **2020**, 580, 503–514.
- [2] J. Fick, H. Söderström, R. H. Lindberg, C. Phan, M. Tysklind, D. G. J. Larsson, *Environmental Toxicology and Chemistry* **2009**, 28, 2522.
- [3] C. Bojer, J. Schöbel, T. Martin, M. Ertl, H. Schmalz, J. Breu, *Applied Catalysis B: Environmental* **2017**, 204, 561–565.
- [4] M.-C. Danner, A. Robertson, V. Behrends, J. Reiss, *Science of The Total Environment* **2019**, 664, 793–804.
- [5] S. Manchala, A. Gandomalla, N. R. Vempuluru, S. Muthukonda Venkatakrishnan, V. Shanker, *Journal of Colloid and Interface Science* **2021**, 583, 255–266.
- [6] A. Cuprys, P. Thomson, Y. Ouarda, G. Suresh, T. Rouissi, S. Kaur Brar, P. Drogui, R. Y. Surampalli, *Journal of Hazardous Materials* **2020**, 389, 121890.
- [7] C. Zheng, H. Zheng, C. Hu, Y. Wang, Y. Wang, C. Zhao, W. Ding, Q. Sun, *Bioresource Technology* **2020**, 296, 122288.
- [8] D. Avisar, Y. Lester, H. Mamane, *Journal of Hazardous Materials* **2010**, 175, 1068–1074.
- [9] S. Asadzadeh-Khaneghah, A. Habibi-Yangjeh, M. Shahedi Asl, Z. Ahmadi, S. Ghosh,

*Journal of Photochemistry and Photobiology A: Chemistry* **2020**, *392*, 112431.

- [10] S. Siliveri, S. Chirra, C. Tyagi, A. Gandamalla, A. K. Adepu, S. Goskula, S. R. Gujjula, N. Venkatathri, *ChemistrySelect* **2019**, *4*, 9135–9142.
- [11] S. Álvarez-Torrellas, J. A. Peres, V. Gil-Álvarez, G. Ovejero, J. García, *Chemical Engineering Journal* **2017**, *320*, 319–329.
- [12] N. Dorival-García, A. Zafra-Gómez, A. Navalón, J. González, J. L. Vílchez, *Science of The Total Environment* **2013**, *442*, 317–328.
- [13] J. Lyu, J. Shao, Y. Wang, Y. Qiu, J. Li, T. Li, Y. Peng, F. Liu, *Chemical Engineering Journal* **2019**, *358*, 614–620.
- [14] N. Wang, L. Zhu, Y. Huang, Y. She, Y. Yu, H. Tang, *Journal of Catalysis* **2009**, *266*, 199–206.
- [15] J. Nawrocki, B. Kasprzyk-Hordern, *Applied Catalysis B: Environmental* **2010**, *99*, 27–42.
- [16] H. Safardoust-Hojaghan, M. Salavati-Niasari, *Journal of Cleaner Production* **2017**, *148*, 31–36.
- [17] K. Wetchakun, N. Wetchakun, S. Sakulsermsuk, *Journal of Industrial and Engineering Chemistry* **2019**, *71*, 19–49.
- [18] A. Gandamalla, S. Manchala, P. Anand, Y.-P. Fu, V. Shanker, *Materials Today Chemistry* **2021**, *19*, 100392.
- [19] E. Vesali-Kermani, A. Habibi-Yangjeh, S. Ghosh, *Journal of Industrial and Engineering Chemistry* **2020**, *84*, 185–195.
- [20] S. C. Yan, Z. S. Li, Z. G. Zou, *Langmuir* **2009**, *25*, 10397–10401.
- [21] Y. Gong, M. Li, Y. Wang, *ChemSusChem* **2015**, *8*, 931–946.
- [22] X. Wang, S. Blechert, M. Antonietti, *ACS Catalysis* **2012**, *2*, 1596–1606.
- [23] Z. Zhao, Y. Sun, F. Dong, *Nanoscale* **2015**, *7*, 15–37.
- [24] L. Ge, F. Zuo, J. Liu, Q. Ma, C. Wang, D. Sun, L. Bartels, P. Feng, *The Journal of Physical Chemistry C* **2012**, *116*, 13708–13714.
- [25] H. Li, J. Liu, W. Hou, N. Du, R. Zhang, X. Tao, *Applied Catalysis B: Environmental* **2014**, *160–161*, 89–97.
- [26] A. Akhundi, A. Habibi-Yangjeh, M. Abitorabi, S. Rahim Pouran, *Catalysis Reviews* **2019**, *61*, 595–628.
- [27] J. Zhang, X. Chen, K. Takanabe, K. Maeda, K. Domen, J. D. Epping, X. Fu, M. Antonietti,

X. Wang, *Angewandte Chemie International Edition* **2010**, *49*, 441–444.

[28] Y. Zhu, Y. Zhang, L. Cheng, M. Ismael, Z. Feng, Y. Wu, *Advanced Powder Technology* **2020**, *31*, 1148–1159.

[29] S. He, W. Li, X. Wang, Q. Ma, M. Li, W. Xu, X. Wang, C. Zhao, *Applied Surface Science* **2020**, *506*, 144948.

[30] Y. Li, M. Zhou, B. Cheng, Y. Shao, *Journal of Materials Science & Technology* **2020**, *56*, 1–17.

[31] X. Dang, Z. Song, H. Zhao, *Sensors and Actuators B: Chemical* **2020**, *310*, 127888.

[32] A. Akhundi, A. Badiei, G. M. Ziarani, A. Habibi-Yangjeh, M. J. Muñoz-Batista, R. Luque, *Molecular Catalysis* **2020**, *488*, 110902.

[33] S. Asadzadeh-Khaneghah, A. Habibi-Yangjeh, *Journal of Cleaner Production* **2020**, *276*, 124319.

[34] E. Vesali-Kermani, A. Habibi-Yangjeh, H. Diarmand-Khalilabad, S. Ghosh, *Journal of Colloid and Interface Science* **2020**, *563*, 81–91.

[35] F. Cavani, F. Trifirò, A. Vaccari, *Catalysis Today* **1991**, *11*, 173–301.

[36] K. Hosni, E. Srasra, *Materials Sciences and Applications* **2011**, *02*, 684–691.

[37] B. König, *Angewandte Chemie* **1997**, *109*, 1055–1056.

[38] V. Rives, M. Angeles Ulibarri, *Coordination Chemistry Reviews* **1999**, *181*, 61–120.

[39] W. Kagunya, Z. Hassan, W. Jones, *Inorganic Chemistry* **1996**, *35*, 5970–5974.

[40] L. Mohapatra, K. Parida, *Journal of Materials Chemistry A* **2016**, *4*, 10744–10766.

[41] Y. Zhao, X. Jia, G. I. N. Waterhouse, L.-Z. Wu, C.-H. Tung, D. O'Hare, T. Zhang, *Advanced Energy Materials* **2016**, *6*, 1501974.

[42] S. Kumar, M. A. Isaacs, R. Trofimovaite, L. Durndell, C. M. A. Parlett, R. E. Douthwaite, B. Coulson, M. C. R. Cockett, K. Wilson, A. F. Lee, *Applied Catalysis B: Environmental* **2017**, *209*, 394–404.

[43] H. Zhang, L. Nengzi, Z. Wang, X. Zhang, B. Li, X. Cheng, *Journal of Hazardous Materials* **2020**, *383*, 121236.

[44] B. Li, Y. Zhao, S. Zhang, W. Gao, M. Wei, *ACS Applied Materials & Interfaces* **2013**, *5*, 10233–10239.

[45] H. Li, L. Luo, P. Kunal, C. S. Bonifacio, Z. Duan, J. C. Yang, S. M. Humphrey, R. M. Crooks, G. Henkelman, *The Journal of Physical Chemistry C* **2018**, *122*, 2712–2716.

[46] H. Guo, H. Li, K. Jarvis, H. Wan, P. Kunal, S. G. Dunning, Y. Liu, G. Henkelman, S. M. Humphrey, *ACS Catalysis* **2018**, *8*, 11386–11397.

[47] G. W. Piburn, H. Li, P. Kunal, G. Henkelman, S. M. Humphrey, *ChemCatChem* **2018**, *10*, 329–333.

[48] Z. Chen, P. Sun, B. Fan, Z. Zhang, X. Fang, *The Journal of Physical Chemistry C* **2014**, *118*, 7801–7807.

[49] F. Fina, S. K. Callear, G. M. Carins, J. T. S. Irvine, *Chemistry of Materials* **2015**, *27*, 2612–2618.

[50] X. Zhao, L. Wang, X. Xu, X. Lei, S. Xu, F. Zhang, *AIChE Journal* **2012**, *58*, 573–582.

[51] X. Yuan, W. Li, *Applied Clay Science* **2017**, *138*, 107–113.

[52] S. Manchala, V. S. R. K. Tandava, L. R. Nagappagari, S. Muthukonda Venkatakrishnan, D. Jampaiah, Y. M. Sabri, S. K. Bhargava, V. Shanker, *Photochemical & Photobiological Sciences* **2019**, *18*, 2952–2964.

[53] A. A. Khassin, T. M. Yurieva, G. N. Kustova, I. S. Itenberg, M. P. Demeshkina, T. A. Krieger, L. M. Plyasova, G. K. Chermashentseva, V. N. Parmon, *Journal of Molecular Catalysis A: Chemical* **2001**, *168*, 193–207.

[54] H. Li, Q. Deng, J. Liu, W. Hou, N. Du, R. Zhang, X. Tao, *Catal. Sci. Technol.* **2014**, *4*, 1028–1037.

[55] L. Lin, C. Hou, X. Zhang, Y. Wang, Y. Chen, T. He, *Applied Catalysis B: Environmental* **2018**, *221*, 312–319.

[56] A. Verma, D. P. Jaihindh, Y.-P. Fu, *Dalton Transactions* **2019**, *48*, 8594–8610.

[57] L. Ge, *Materials Letters* **2011**, *65*, 2652–2654.

[58] D. B. Hernández-Uresti, A. Vázquez, D. Sanchez-Martinez, S. Obregón, *Journal of Photochemistry and Photobiology A: Chemistry* **2016**, *324*, 47–52.

[59] C.-W. Jeon, S.-S. Lee, I.-K. Park, *ACS Applied Materials & Interfaces* **2019**, *11*, 35138–35145.

[60] G. Mendoza-Damián, F. Tzompantzi, A. Mantilla, R. Pérez-Hernández, A. Hernández-Gordillo, *Applied Clay Science* **2016**, *121–122*, 127–136.

[61] S. Manchala, V. S. R. K. Tandava, L. R. Nagappagari, S. Muthukonda Venkatakrishnan, D. Jampaiah, Y. M. Sabri, S. K. Bhargava, V. Shanker, *Photochemical & Photobiological Sciences* **2019**, *18*, 2952–2964.

[62] R. Tholkappiyan, K. Vishista, *Solar Energy* **2014**, *106*, 118–128.

[63] Y. Wang, X. Hao, G. Wang, Z. Jin, *Catalysis Letters* **2020**, DOI 10.1007/s10562-020-03346-1.

[64] H. Wang, X. Xiang, F. Li, *AIChE Journal* **2009**, *59*, NA-NA.

[65] Z. Zhao, Y. Sun, Q. Luo, F. Dong, H. Li, W.-K. Ho, *Scientific Reports* **2015**, *5*, 14643.

[66] X. Du, G. Zou, Z. Wang, X. Wang, *Nanoscale* **2015**, *7*, 8701–8706.

[67] D. Ding, C. Liu, Y. Ji, Q. Yang, L. Chen, C. Jiang, T. Cai, *Chemical Engineering Journal* **2017**, *308*, 330–339.

[68] M. Peleg, M. D. Normand, M. G. Corradini, *Critical Reviews in Food Science and Nutrition* **2012**, *52*, 830–851.

[69] M. J. Wu, J. Z. Wu, J. Zhang, H. Chen, J. Z. Zhou, G. R. Qian, Z. P. Xu, Z. Du, Q. L. Rao, *Catalysis Science & Technology* **2018**, *8*, 1207–1228.

[70] F. Cavani, F. Trifirò, A. Vaccari, C. R. Chen, H. Y. Zeng, M. Y. Yi, G. F. Xiao, R. L. Zhu, X. J. Cao, S. G. Shen, J. W. Peng, *Ecotoxicology and Environmental Safety* **2019**, *11*, 423–431.

[71] R. E. Núñez-Salas, A. Hernández-Ramírez, V. Santos-Lozano, L. Hinojosa-Reyes, J. L. Guzmán-Mar, M. Á. Gracia-Pinilla, M. de L. Maya-Treviño, *Journal of Photochemistry and Photobiology A: Chemistry* **2021**, *411*, 113186.

[72] A. Ulyankina, T. Molodtsova, M. Gorshenkov, I. Leontyev, D. Zhigunov, E. Konstantinova, T. Lastovina, J. Tolasz, J. Henych, N. Licciardello, G. Cuniberti, N. Smirnova, *Journal of Water Process Engineering* **2020**, 101809.

[73] X.-J. Wen, C.-G. Niu, L. Zhang, C. Liang, H. Guo, G.-M. Zeng, *Journal of Catalysis* **2018**, *358*, 141–154.

[74] T. Govindaraj, C. Mahendran, V. S. Manikandan, J. Archana, M. Shkir, J. Chandrasekaran, *Journal of Alloys and Compounds* **2021**, *868*, 159091.

[75] Z. Qin, H. Sun, Y. Tang, Z. Chang, S. Yin, Z. Liu, H. Sun, Y. Tang, Z. Chang, S. Yin, Z. Liu, **2020**.

[76] S. Das, S. Ghosh, A. Misra, A. Tamhankar, A. Mishra, C. Lundborg, S. Tripathy, *International Journal of Environmental Research and Public Health* **2018**, *15*, 2440.

[77] X. Zhang, R. Li, M. Jia, S. Wang, Y. Huang, C. Chen, *Chemical Engineering Journal* **2015**, *274*, 290–297.

- [78] S. Babić, M. Periša, I. Škorić, *Chemosphere* **2013**, *91*, 1635–1642.
- [79] H. Ou, J. Ye, S. Ma, C. Wei, N. Gao, J. He, *Chemical Engineering Journal* **2016**, *289*, 391–401.
- [80] X.-J. Wen, C.-G. Niu, D.-W. Huang, L. Zhang, C. Liang, G.-M. Zeng, *Journal of Catalysis* **2017**, *355*, 73–86.
- [81] C. Liu, V. Nanaboina, G. V. Korshin, W. Jiang, *Water Research* **2012**, *46*, 5235–5246.



## Chapter VI

# Photo-thermal studies of stable and potential $\text{Ce}(\text{MoO}_4)_2/\text{g-C}_3\text{N}_4$ binary composite towards degradation of ciprofloxacin and methylene blue under visible light



## **Chapter VI**

### **Photo-thermal studies of stable and potential Ce(MoO<sub>4</sub>)<sub>2</sub>/g-C<sub>3</sub>N<sub>4</sub> binary composite towards degradation of ciprofloxacin and methylene blue under visible light**

#### **6.1 Introduction**

The utilization of renewable energy resources is an urgent bustle in the rapid industrial growth, urbanization, and social economy. It is essential for achieving long-term change in the face of rapidly depleting fossil fuels and worsening environmental issues. Toxic constituents such as dyes, antibiotics, heavy metals, and pesticides are entering the aquatic environment to produce harmful effects and eventually threaten human health.<sup>[1,2]</sup> Therefore, it is of great practical importance to eliminate diverse pollutants from wastewater using various water treatment methods include membrane separation, adsorption, advanced oxidation, biological processes, and photocatalytic degradation.<sup>[3-8]</sup> Particularly, the materials or photocatalysts, which are being used for waste- water treatment plays a key role and the development of prominent materials for wastewater treatment method become the hotspot research interest for researchers.

Among the various photocatalytic materials, non-metal graphitic carbon nitride (g-CN) is an n-type semiconductor, which is prepared by thermal condensation of polymerizing monomers like urea, thiourea, melamine and dicyandiamide. The structure of g-CN is analogous to 2D conjugated lamellar assembly of graphene which contains heptazine rings bonded with hydrogen bonding and Van Der Waal forces.<sup>[9-11]</sup> Because of its unique characteristics, including excellent stability, bandgap energy (2.7 eV) for the more visible light absorption capacity, adequate water oxidation and reduction band levels, and conveniently altered molecular structure.<sup>[12-18]</sup> g-CN has gathered particular interest is an effective non-metal photocatalyst for CO<sub>2</sub> reduction, degradation of organic pollutants, and water splitting, etc. Even though the practical applications of the bare g-CN as photocatalyst faces numerous obstacles, such as weak redox ability, fast recombination of photogenerated excitons and minimal surface to volume ratio.<sup>[19,20]</sup> To overcome disadvantages as mentioned earlier of g-CN, various approaches have been developed, such as doping metal/nonmetal ions, changing morphology, and making binary composites with other semiconductors.<sup>[21-23]</sup> The development of heterojunction between g-CN and other semiconductor is an effective approach to boost the photocatalytic-degradation efficiency of environmental pollutants by g-CN.

Recently, transitional metal molybdates gained particular interest due to their various properties. And they were significantly used in various applications like photocatalysis, sensors, supercapacitors, Li-ion storage batteries, and optical fibers.<sup>[24-28]</sup> Among the transitional metal molybdates, cerium molybdates  $\text{Ce}(\text{MoO}_4)_2$  is a significant in-organic semiconductor photocatalyst material and gained an excellent attraction to the researchers due to its distinctive properties such as good catalytic convertor, corrosion inhibitor, and high photo-stability. Owing to these features,  $\text{Ce}(\text{MoO}_4)_2$  is extensively used in a variety of industrial applications, such as paints, plastics and ceramics. It is also broadly used in catalysis including the corrosion industry for the corrosion suppression of aluminium alloys.<sup>[29-31]</sup> More significantly, recent studies reveal that cerium molybdates have sufficient valance band edge position to oxidize the organic pollutants and provide superior visible light active photocatalytic performance.<sup>[32,33]</sup> The main objective of the synthesis of the binary nanocomposites, in this we can effectively separate the photogenerated excitons and inhibits the recombination rate of photogenerated excitons by the transfer of one semiconductor to another vice versa.

In the present study, we have successfully fabricated  $\text{CeM/g-CN}$  binary composites via a facile hydrothermal method. We have investigated the effect of  $\text{CeM}$  loading on the photodegradation of dye pollutants. The optimized  $\text{CeM/g-CN-20}$  composite was exhibited enhanced photocatalytic degradation for different pollutants CIP and MB under visible light, compared with bare  $\text{g-CN}$  and  $\text{CeM}$ . Furthermore, we have proposed suitable photocatalytic pollutants degradation mechanism based on the experimental results, and the role of photoactive species that are responsible for the degradation processes were analyzed by using scavenger experiments. As far as we are aware, it was the first study on  $\text{CeM/g-CN}$  binary composites for the effective photocatalytic pollutants degradation of CIP and MB under visible light.

## 6.2 Experimental Section

### 6.2.1 Materials

All the chemicals were of analytical grade used in this study without any further purification. Cerium nitrate tetra hydrate (Hmedia, 99 %), ammonium molybdate (Finar, extra pure), ethylene glycol (Finar, 99%), ciprofloxacin (TCI 98 %), isopropyl alcohol (Choneye, 99.9 %), silver nitrate (Aencore, 99.9 %), benzoquinone (Aencore, 99.8 %), and EDTA-2Na (Panreac 90.0 %).

### 6.2.2 Synthesis of pure g-C<sub>3</sub>N<sub>4</sub>

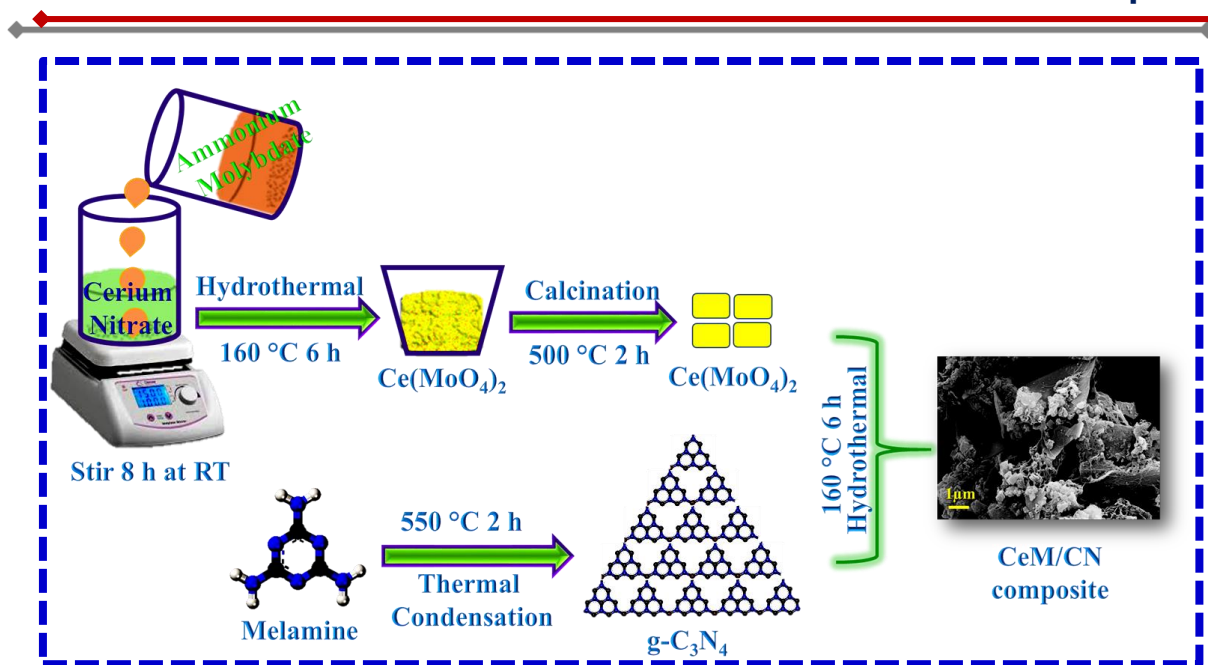
The pristine g-CN was fabricated by a well-known thermal condensation routine with melamine used as Nitrogen (N) and Carbon (C) source. Briefly, 5 gr of melamine was ground well with a motor pestle and transferred to an aluminium boat and kept in a programmable tubular furnace maintained at 550 °C for 2 h with keeping heating rate of 5 °C/min. After cooling naturally, the light yellow colored powder was stored for further use.

### 6.2.3 Synthesis of Ce(MoO<sub>4</sub>)<sub>2</sub>

Ce(MoO<sub>4</sub>)<sub>2</sub> was fabricated by a simple one-step hydrothermal route. Concisely, 2 mmol cerium nitrate hexahydrate was dispersed in 30 mL of ethylene glycol via stirring for 1 h marked as solution A. Meanwhile in another beaker, with 30 mL ethylene glycol having 2 mmol of ammonium molybdate was dissolved and marked as solution B and continue stirring for another 1 h. Afterwards, solution B was mixed with solution A while stirring. The stirring was continued for 6 h at room temperature (R.T). The total solution mixture was transferred to a hydrothermal bomb and placed in a microprocessor programmable controlled oven and maintained at temperature of 160 °C for 6 h. We have applied heating rate of 4 °C per minute. After successfully completion of the reaction, the obtained products are washed with DD water several times to eliminate any unreacted precursors. The achieved product was calcined at 500 °C for 2 h and finally a white color product was obtained.

### 6.2.4 Synthesis of Ce(MoO<sub>4</sub>)<sub>2</sub>/g-C<sub>3</sub>N<sub>4</sub> binary composites

The CeM/g-CN binary composites were fabricated by a simple hydrothermal method. Concisely, 30 mL of DD water was taken in a beaker and an appropriate amount of already synthesized g-CN and sonicated for 1 h at R.T. Subsequently add suitable amount of CeM and sonicated for 10 min and continuously stirred for another 2 h at R.T. and the total mixture of the solution was shifted into a pre-cleaned hydrothermal bomb and maintained at a temperature of 160 °C for 6 h with ramp rate 3 °C per minute. After naturally cooling to R.T., the obtained product was thoroughly washed several times with water and kept in oven for overnight to dry the obtained products. As mentioned above, we have fabricated a series of materials with different CeM to g-CN ratio and denoted as CeM/g-CN-10 (CeM 10%), CeM/g-CN-20 (CeM 20%), and CeM/g-CN-30 (CeM 30%) respectively. The detailed synthesis methods of all materials are shown in scheme 6.1.



**Scheme 6.1:** Pictorial illustration of the fabrication of CeM/g-C<sub>3</sub>N<sub>4</sub> binary composites.

### 6.2.5 Photocatalytic experiments

The photocatalytic performance of the fabricated materials was studied by photodegradation of CIP and MB. For the photocatalytic study, 50 mL of 20 ppm of CIP, and in the case of MB, 50 mL of 10 ppm solution was taken separately in a 100 mL water-jacketed beaker and constant temperature (30 °C) was maintained with the help of a water circulation system as described in our previous work <sup>[34]</sup>. Subsequently, 30 mg of the photocatalyst was suspended to the above dye solution, and allowed it for sonicate i.e; 10 minutes followed by stirring under dark environments for 30 minutes to achieve adsorption and desorption equilibrium between photocatalyst and pollutant. Afterward, a visible light source (35 W Xe arc lamp) used with color temperature of 6000 K was used for the photodegradation process. Every 20 minutes, ~5 mL of reactant solution was taken from the total reaction mixture, and it was centrifuged to isolate the photocatalyst and degraded solution for further analysis of absorption measurements by using UV-Vis spectrophotometer. The stability of the photocatalysts were studied in the same manner as mentioned above, and 4 successive cycles were performed. Before starting each experiment, the photocatalyst was separated via centrifugation with ethanol and DD water and drying at 70 °C overnight in a hot air oven. Scavenger experiments were also completed under the same experimental conditions as mentioned above but with the addition of respective scavenger (10 mmol) to each experiment before the light illumination. The degradation percentage of dye was

calculated by reducing the absorption intensities of the remaining dye. The degradation efficiency of any dye pollutants was calculated using the (equation 6.1).<sup>[35]</sup>

$$\text{Degradation efficiency} = \left(1 - \frac{C_t}{C_0}\right) \times 100 \quad (6.1)$$

Where  $C_t$  - concentration of dye solution after light irradiation,  $C_0$  - initial concentration of the dye solution.

### 6.3 Results and discussions

#### 6.3.1 PXRD, FT-IR, and UV-Vis DRS studies

From the PXRD studies, crystal structure and lattice parameters of synthesized pristine g-CN, CeM, and CeM/g-CN materials were revealed, and the respective results are depicted in Figure 6.1. As depicted in Figure 6.1(a), PXRD patterns of pure CeM, the sharp and highly intense peaks appear at the  $2\theta = 28.05^\circ, 30.21^\circ, 33.57^\circ, 45.77^\circ, 48.22^\circ, 52.31^\circ, 56.69^\circ, 57.95^\circ$ , and  $73.82^\circ$  which belong to the crystal planes of (112), (004), (200), (220), (204), (116), (303), (312), and (316) respectively, corresponding to tetragonal phase of pure  $\text{Ce}(\text{MoO}_4)_2$  and good agreed with the standard JCPDS card number 33-0330.<sup>[36-38]</sup> From the diffraction data it could be concluded that, there are no additional impurity peaks noticed, indicating that the pure tetragonal phase of CeM has formed. For pure g-CN, the prominent diffraction peak appears at two theta =  $27.5^\circ$ , which corresponds to the (002) plane assigned to the interplanar staking of g-CN, and the small peak appears at 2 theta =  $13.4^\circ$ , which corresponds to the (001) plane's in-plane motif.<sup>[34]</sup> After formation of binary composites, the combination diffraction peaks of both g-CN and CeM are observed, which confirms the construction of CeM/g-CN binary composites. More importantly, with the increasing CeM amount in the composite, the prominent diffraction peak of CeM becomes broaden and intense. These results conclude that there is formation of a strong composite between the g-CN and CeM. The formation of binary composite was further confirmed with FE-SEM and XPS results.

Functional groups present in the synthesized materials were analyzed with the help of FT-IR analysis and the results are depicted in Figure 6.1(b). The FT-IR analysis were done in the range of  $400\text{--}4000\text{ cm}^{-1}$  for the synthesized pure g-CN, CeM, and CeM/g-CN binary composites. For the pure CeM the broad bands appear in the range of  $3250\text{ cm}^{-1}$  and  $3530\text{ cm}^{-1}$  corresponding to the O–H stretching mode, and the band found at  $1650\text{ cm}^{-1}$  is assigned to O–H bending vibrations due to the physically adsorbed moisture. The band which appears at  $1100\text{ cm}^{-1}$  corresponds to M–

O–H bending vibration consequently confirming the existence of Ce–O–H. Peaks that appear at 715 and 829 cm<sup>-1</sup> assigned to the overlapping vibration of molybdate ions and Ce(OH)<sub>2</sub>. The peak that appears at 413 cm<sup>-1</sup> is responsible for the terminal–oxygen bonds in the MoO<sub>4</sub><sup>-2</sup> ions.<sup>[32,39]</sup> Therefore, the FT-IR analysis is endorsed to the existence of H<sub>2</sub>O, –OH, MoO<sub>4</sub><sup>-2</sup> ions, and Ce–O–H groups. For pure g-CN the FT-IR absorption spectra, the prominent distinguishing peak appears at 808 cm<sup>-1</sup> assigned to s-triazine stretching vibrations of. The peaks appearing at the range of 1250 cm<sup>-1</sup> to 1575 cm<sup>-1</sup> corresponds to the aromatic C–N stretching. Besides, at 3100-3340 cm<sup>-1</sup> can be ascribed to stretching vibrations of amino N–H groups.<sup>[40,41]</sup> In the CeM/g-CN binary composite FT-IR spectra, the main distinctive band of g-CN at 808 cm<sup>-1</sup> was appeared in all the binary composites. Besides, CeM bands were also seen in the binary composites. The FT-IR studies further indorse the formation of CeM/g-CN binary composite.

To know the optical absorption properties of pristine g-CN, CeM, and CeM/g-CN binary composites, UV-Visible DRS analysis was carried out, and the results are depicted in Figure 6.1(c, d). As shown in Figure 6.1(c), the absorption edge of pristine g-CN is observed at 460 nm.<sup>[42]</sup> In contrast, the optical absorption for pristine CeM is 556 nm,<sup>[43]</sup> which confirms that both the bare materials g-CN and CeM belong to visible light active photocatalysts. While for the binary composites, the absorption values lie between those of both g-CN and CeM. Figure 6.1(d) shows the Tauc plots of synthesized materials. According to tauc equation, the estimated bandgap energies are 2.69 and 2.23 eV for pure g-CN and CeM, respectively.<sup>[44]</sup> Table 6.1 depicts the band gap energies of CeM/g-CN-10, CeM/g-CN-20, and CeM/g-CN-30 binary binary composites. Interestingly, after the formation of the binary composites, the bandgap energies show a redshift in UV-Vis absorption spectra, which further supporting the formation of strong heterojunction between g-CN and CeM.

**Table 6.1:** Calculated bandgap of synthesized CeM, CN, and CeM/CN binary composites.

Photocatalyst	Bandgap (eV)
CN	2.69
CeM	2.23
CeM/CN-10	2.64
CeM/CN-20	2.63
CeM/CN-30	2.59

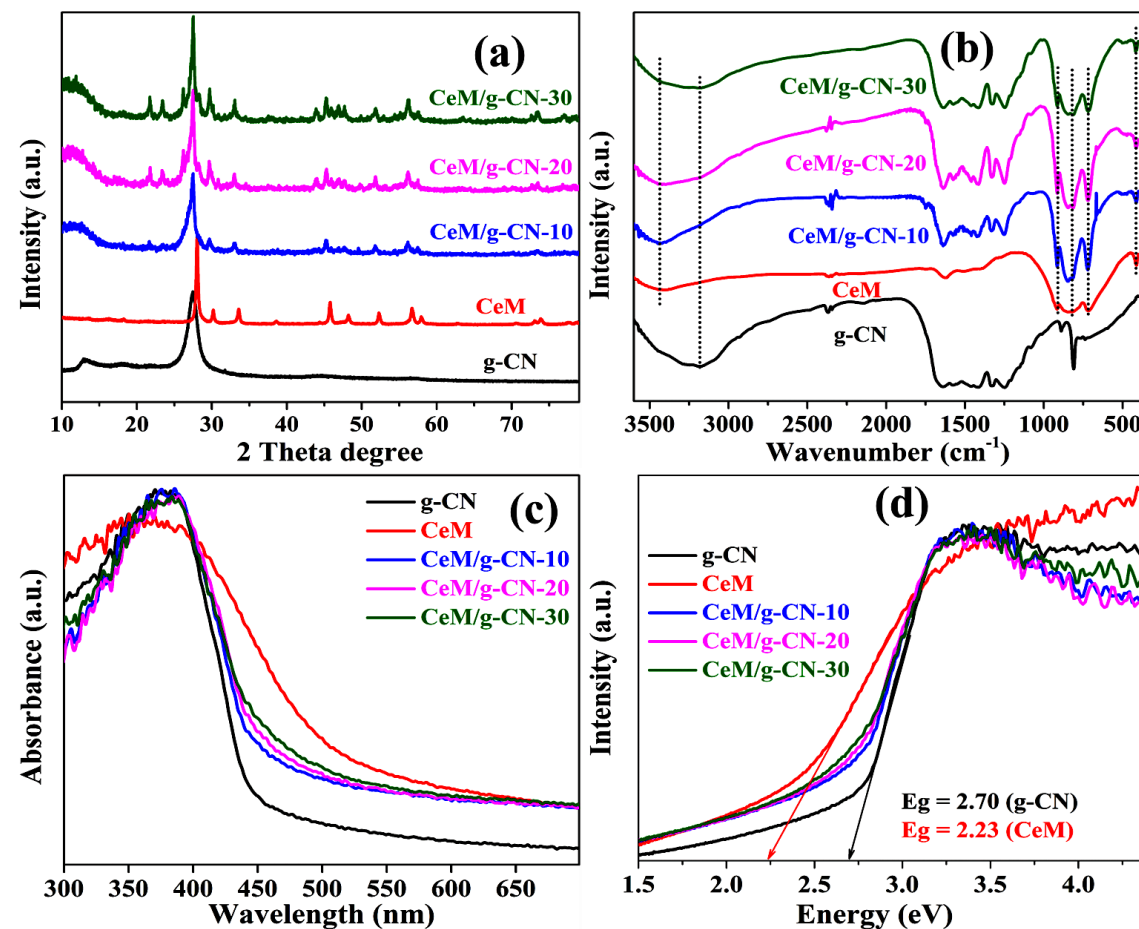


**Figure 6.1:** (a) PXRD studies of fabricated g-CN, CeM, and CeM/g-CN materials, (b) FT-IR studies of fabricated g-CN, CeM, and CeM/g-CN materials, (c) UV-Vis DRS studies of fabricated g-CN, CeM, and CeM/g-CN materials, and (d) respective Tauc plot calculations of bandgap.

### 6.3.2 FE-SEM, TEM, EDS, and elemental mapping analysis

To know the surface morphology and elemental composition of the synthesized binary composites, FE- SEM and TEM analysis were performed and the results are depicted in Figure 6.2. As shown in Figure 6.2(a-c), in the FE-SEM images of CeM/g-CN-20 composite at different magnifications. One could observe the yellow circles which denotes the pure CeM showcasing nanosheets-like morphology as reported earlier researchers.<sup>[38]</sup> Moreover, the rest of the part belongs to g-CN sheet-like morphology.

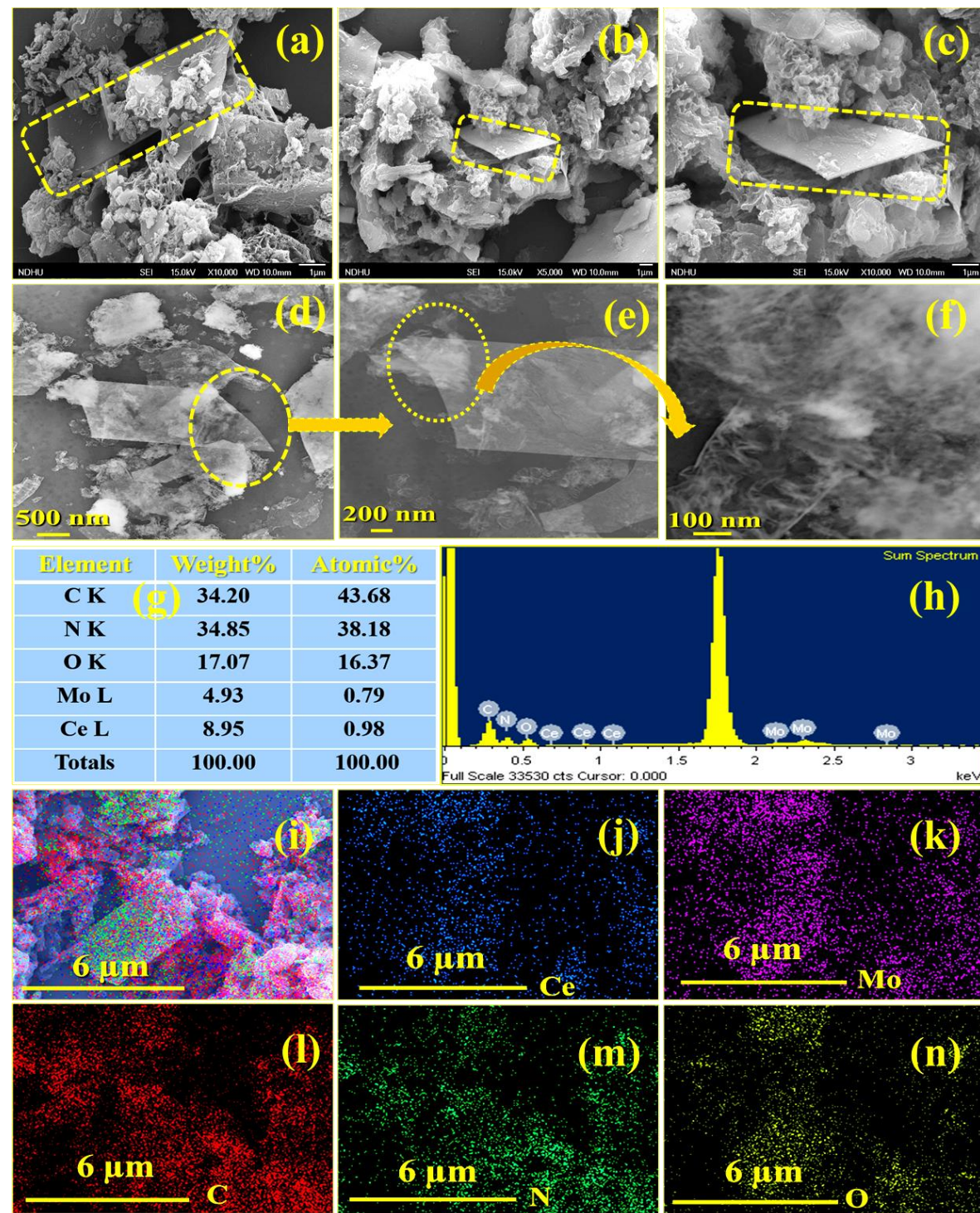


**Figure 6.2:** (a-c) FE-SEM images of CeM/g-CN-20 binary composite at different magnifications, (d-f) TEM images of CeM/g-CN-20 binary composite with different magnifications, (g) elemental percentages, (h) EDS elemental analysis of CeM/g-CN-20 binary composite, and (i-n) EDS elemental mapping images of CeM/g-CN-20 binary composite photocatalyst.

From these images, we can identify both the morphologies of g-CN and CeM which further endorses the formation of CeM/g-CN composite. Figure 6.2(d-f) shows the TEM images of CeM/g-CN-20 binary composite at diverse magnifications, which is depicting the existence of both the materials in the binary composites and further confirming the formation of CeM/g-CN-20 binary composite. Figure 6.2(g-h) shows the elemental percentages and the EDS elemental analysis of respective elements in the CeM/g-CN -20 binary composite, which confirms the presence of respective elements, i.e., Ce, Mo, C, N, and O. Figure 6.2(i-n) depicts the elemental mapping analysis of CeM/g-CN-20 binary composite, which further confirms the existence of all corresponding elements in the CeM/g-CN-20 binary composite.

### 6.3.3 XPS Studies

In order to analyze the synthesized materials with respect to the chemical states and their chemical composition, XPS analysis was employed and the data were depicted in Figure 6.3. As depicted in Figure 6.3(a), photoemission spectra can be observed for the CeM/g-CN-20 binary composite (survey spectrum), which denotes the presence of all respective elements. The peaks representing binding energies at 232.11 eV (Mo 3d), 287.80 eV (C 1s), 398.52 eV (N 1s), 530.83 eV (O 1s), and 884.74 eV (Ce 3d) confirms the formation of CeM/g-CN-20 binary composite, and the results are well matched with EDS elemental analysis which is defined in the above section. As presented in Figure 6.3(b), the two peaks which appear at a binding energy of 885.73 eV and 905.33 eV in the high-resolution XPS spectra of Ce 3d, correspond to Ce 3d<sub>5/2</sub> and Ce 3d<sub>3/2</sub>, demonstrating that Ce in the Ce<sup>4+</sup> state.<sup>[45]</sup> Figure 6.3(c) shows the expanded mode of Mo 3d core level XPS spectrum, the peaks appearing at the binding energies of 232.68 eV (Mo 3d<sub>5/2</sub>) and 235.73 eV (Mo 3d<sub>3/2</sub>) confirms the Mo ion in Mo<sup>6+</sup> state.<sup>[46]</sup>

The high-resolution XPS spectra of C 1s, as illustrated in Figure 6.3(d) can be deconvoluted into three peaks, which appear at corresponding binding energies of 284.38 eV of sp<sup>2</sup> hybridized (C=C) carbon, 286.28 eV of carbonyl carbon (C=O) and 287.98 eV of N=C-N coordination endorses the presence of g-CN in the binary composite. The high-resolution XPS spectra of N 1s showed in Figure 6.3(e) was deconvoluted into further three peaks with binding energies of 398.35, 400.02, and 403.88 eV which are corresponding to triazine rings with sp<sup>2</sup> hybridized C-N-C groups, ternary nitrogen banded to C (N-(C)<sub>3</sub> groups and amino C-N-H groups, respectively.<sup>[34,41]</sup> The high-resolution XPS spectra representing O 1s as shown in Figure 6.3(f) appear at a binding energy of 530.73 eV, which corresponds to the metal-oxygen bond present in the binary composite

CeM/g-CN-20, Hence, the XPS results concludes the harmony of g-CN and CeM in the CeM/g-CN-20 binary composite material. Furthermore these findings directly supports with XRD and TEM results.

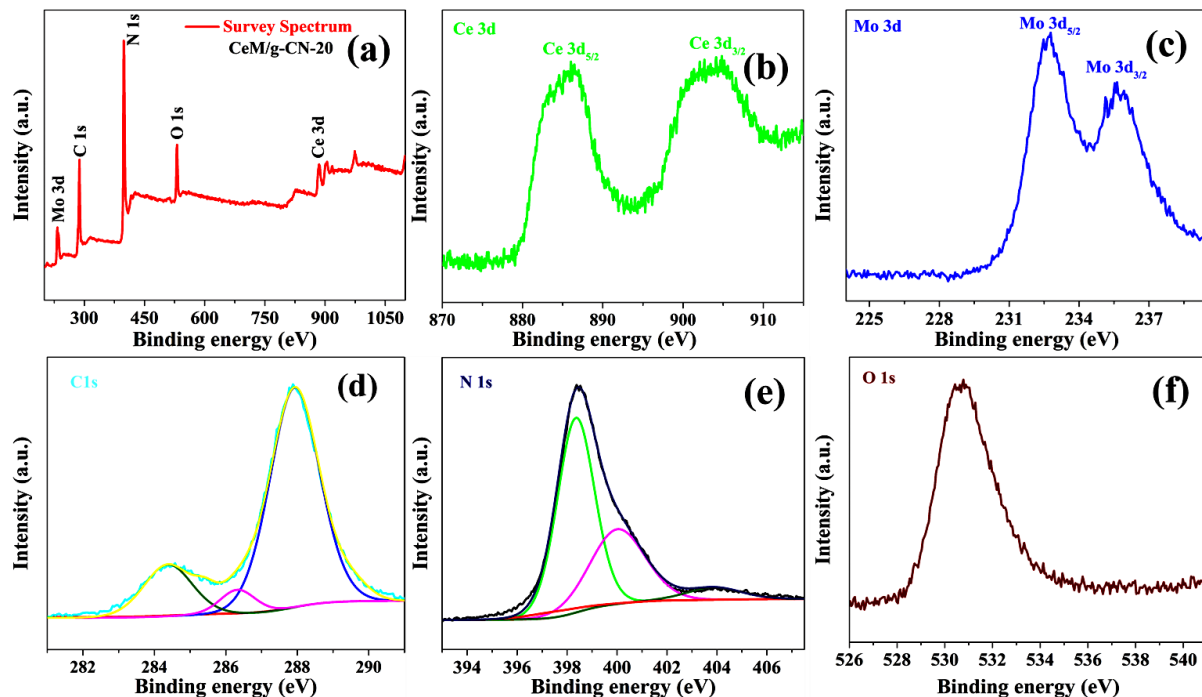


**Figure 6.3:** XPS Analysis of CeM/g-CN-20 binary composite (a) survey spectrum, (b) Ce 3d, (c) Mo 3d, (d) C 1s, (e) N 1s, and (f) O 1s.

### 6.3.4 PL, TRFL, and BET studies

To determine the photo-generated electron hole pair recombination capacity and average lifetime for the synthesized pristine g-CN, CeM, CeM/g-CN binary composites PL and TRFL, studies were carried out and shown in Figure 4(a-b). As we know that, less PL peak intensity represents lower recombination of photo-generated excitons and more PL intensity represents higher recombination of photo-generated excitons. As depicted in Figure 6.4(a), the excitation and emission values for synthesized pristine g-CN are 365 nm, and 465 nm.<sup>[47]</sup> Further, pure CeM excited at 320 nm and it shows a weak emission band observed at 465 nm, due to localized states in bandgap,<sup>[48,49]</sup> and the PL excitation values could be well correlated with the UV-Vis absorbance spectra values. In the CeM/g-CN binary binary composites, position of emission peak is identical to g-CN, but the intensity was relatively low compared to pure g-CN, suggesting that after the formation of CeM/g-CN binary composites the electron-hole pair recombination was suppressed when a suitable amount of CeM addition to the g-CN. Here CeM/g-CN-20 binary composite

displays a less PL intense peak responsible for the enhancement in the photocatalytic degradation of pollutants. Furthermore, as displayed in Figure 6.4(b), the effect of the interface dynamics on the photogenerated excitons has been investigated using TRFL techniques. The lifetime PL decay curves of g-CN, CeM, and CeM/g-CN-20 binary composite are fit with the 'bi-exponential' function as shown in the equation below.<sup>[50]</sup>

$$\text{Fit} = B + A_1 \exp\left(\frac{-x}{t_1}\right) + A_2 \exp\left(\frac{-x}{t_2}\right) \quad (6.2)$$

Where 'B' exponential constant, 't<sub>1</sub>' is the shorter decay lifetime for non-radiative, and 't<sub>2</sub>' the longer decay lifetime of the radiative process. 'A<sub>1</sub>' constants correspond to non-radiative, and 'A<sub>2</sub>' constant belongs to the radiative process. With the help of the following equation (6.3) average life time of the photo-generated excitons was calculated<sup>[51]</sup>. A list of all values obtained from the fitted parameters was shown in Table 6.2.

$$t_{av} = \frac{A_1 t_1 + A_2 t_2}{A_1 + A_2} \quad (6.3)$$

**Table 6.2:** All fitted parameters and average lifetime of synthesized CeM, CN, and CeM/CN-20 binary composite.

Photocatalysts	A <sub>1</sub> (rel. %)	t <sub>1</sub> (ns)	A <sub>2</sub> (rel. %)	t <sub>2</sub> (ns)	t <sub>av</sub> (ns)
CN	2.90	3.88	0.12	19.91	4.52
CeM	3.68	1.67	3.68	1.67	1.67
CeM/CN-20	1.81	2.69	1.81	2.69	2.69

The average lifetime of pure CeM and g-CN was calculated as 1.67 ns and 4.52 ns, whereas for the composite, the average lifetime is calculated as 2.69 ns. It shows that the average lifetime of the binary composite CeM/g-CN-20 is less compared to pure CeM and g-CN. This is due to the formation of the non-radiative pathway through newly formed channels in the composite. Therefore, photo-generated charge carriers are rapidly generated and transferred in the CeM/g-CN-20 binary composite. This indication of fast electron transfer from g-CN to CeM endorses the formation of CeM/g-CN binary composites. Which strangely brings about effective separation of photogenerated electrons and holes. Subsequently, the improvement in the photocatalytic activity of CeM/g-CN-20 binary composite achieved as reported previous researchers.<sup>[52-54]</sup>

The BET surface area, pore size, and pore diameter of the fabricated CeM, g-CN, and CeM/g-CN-20 binary composites were calculated by nitrogen adsorption-desorption

measurements, and the results are depicted in Figure 6.4(c-d). The BET surface area of pure CeM, g-CN, and CeM/g-CN-20 binary composite was  $17.50\text{ m}^2/\text{g}$ ,  $9.20\text{ m}^2/\text{g}$ , and  $10.71\text{ m}^2/\text{g}$ , respectively, and the corresponding pore volumes are calculated to be  $0.720\text{ cc/g}$ ,  $0.107\text{ cc/g}$ ,  $0.153\text{ cc/g}$ , respectively. However, the CeM/g-CN-20 binary composite surface area was less compared to pure CeM and more when compared with g-CN. Because, CeM is mainly accountable for surface area improvement and g-CN is accountable for the reduction in surface area. Even though the photocatalytic activity of CeM/g-CN-20 binary composite was more when compared to pure CeM because many other factors contribute to the increase in photocatalytic activity. More importantly, suppressing the recombination of photo-generated excitons in the CeM/g-CN-20 binary composite plays an significant role in photocatalytic activity enhancement. Previous researchers have reported similar findings.<sup>[55]</sup>

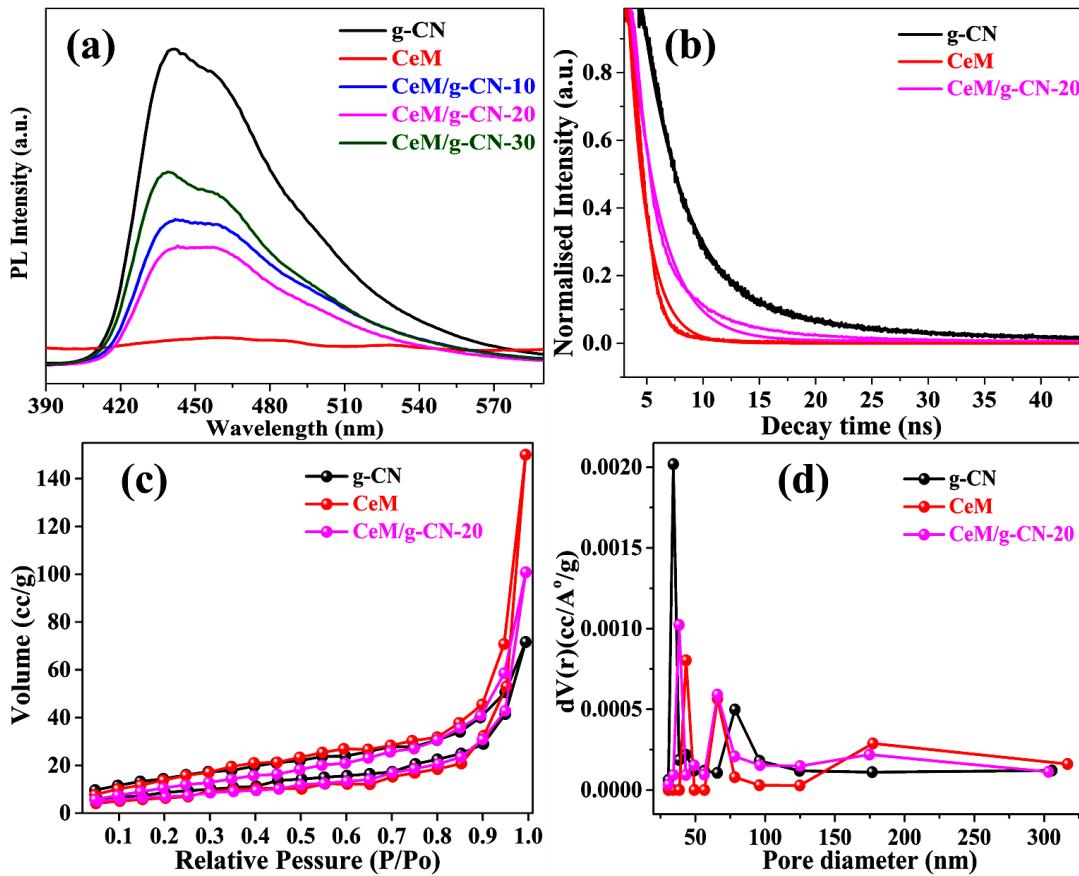


**Figure 6.4:** (a) PL spectra, (b) TRFL, (c) nitrogen adsorption and desorption isotherms and (d) pore volume curves of as-synthesized g-CN, CeM, and CeM/g-CN-20 binary composite.

### 6.3.5 Photocatalytic activity studies

The photocatalytic dye degradation studies of the as-prepared g-CN, CeM, and CeM/g-CN binary composite were tested against the antibiotic and organic pollutants of CIP and MB aqueous solutions under visible-light illumination. The blank test (without catalyst and light source), results demonstrate that there is no degradation. It concludes, for the efficient photocatalytic dye degradation experiment, catalyst and light should be needed. CeM/g-CN-20 binary composite demonstrated the highest photocatalytic performance for the degradation of MB and CIP among all tested samples. Figure 6.5, depicts the corresponding results. As depicted in Figure 6.5(a-c), the comparison of photo-degradation curves of pure g-CN, CeM, and CeM/g-CN binary composites for MB dye and CIP after 150 min of visible-light irradiation. As depicted in Figure 6.5(b-d), the photocatalytic degradation of both the dyes MB and CIP has followed the pseudo-first-order kinetics model equation (6.4).

$$kt = -\ln\left(\frac{C_t}{C_0}\right) \quad (6.4)$$

Where 'k' - degradation rate constant, 't' - reaction time,  $C_t$  - concentration of dye solution at time 't' and  $C_0$  - initial concentration.<sup>[56]</sup> The rate constants were investigated from the slope of the linear plots of  $-\ln(C_t/C_0)$  vs degradation time. For the CeM/g-CN-20 binary composite, the degradation rate constants were calculated as  $15.1 \times 10^{-3} \text{ min}^{-1}$  and  $14.5 \times 10^{-3} \text{ min}^{-1}$  for MB and CIP. Whereas for the pure g-CN and CeM the degradation rate constants are  $10.6 \times 10^{-3} \text{ min}^{-1}$ , and  $2.4 \times 10^{-3} \text{ min}^{-1}$  against MB dye and  $7.8 \times 10^{-3} \text{ min}^{-1}$ , and  $3.2 \times 10^{-3} \text{ min}^{-1}$  for CIP, respectively. As CeM/g-CN-20, binary composite shows enhanced photocatalytic activity for complete degradation of MB and CIP within 150 min, when compared to pure g-CN and CeM and the corresponding degradation percentages for MB dye were 79.80 % and 39.22 %, whereas for CIP the degradation percentages were 66.14% and 45.38%. The degradation percentages and rate constants for MB and CIP were displayed in Figure 6.6(a-b).

The photocatalytic dye degradation percentages and rate constant trends of MB and CIP for all synthesized materials as follow CeM/g-CN-20 > CeM/g-CN-10 > CN > CeM/g-CN-30 > CeM. Furthermore, while increasing the CeM percentage in the CeM/g-CN binary composites the degradation capacity increases up to CeM/g-CN-20, then decreases steadily. The following cause may describe this. The photoactive sites of g-CN may be blocked as the amount of CeM in the CeM/g-CN binary composites (CeM/g-CN-30) increases, and self-agglomeration may occur in the

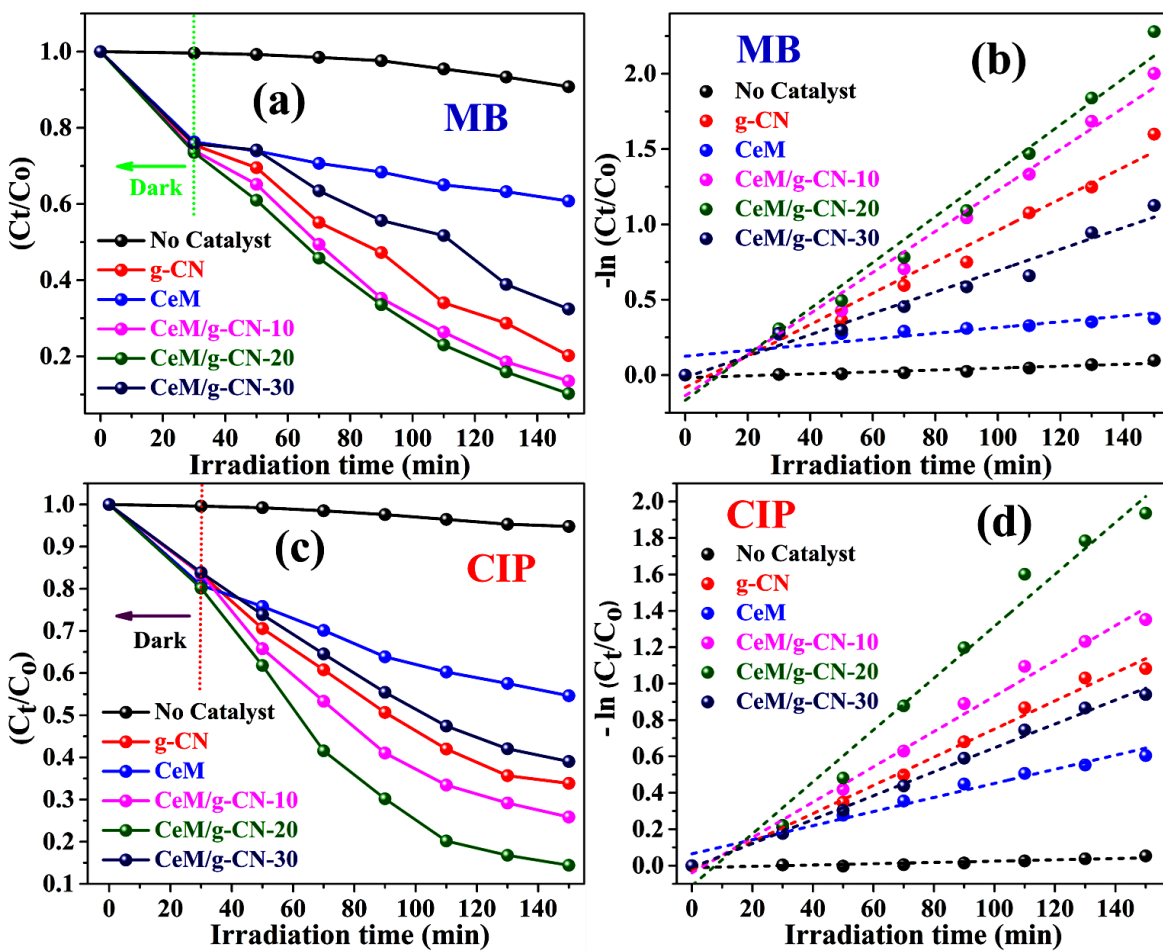
binary composites. These findings support the existence of strong interactions between g-CN and CeM in CeM/g-CN binary composites.

Figure 6.6(c) shows the scavenger test results, which describes the photoactive species which are accountable for the degradation of antibiotic pollutant (CIP) in the CeM/g-CN-20 binary composite. Here we used different quenchers like benzoquinone for superoxide radicals ( $O_2^{\bullet-}$ ),  $AgNO_3$  for electrons ( $e^-$ ), isopropyl alcohol for hydroxyl radicals ( $^{\bullet}OH$ ), and EDTA-2Na for the holes ( $h^+$ ), respectively. As shown in Figure 6.6(c), after adding benzoquinone and  $AgNO_3$  as a quenchers to the reaction system, there is no effect on the photocatalytic dye degradation process, which confirms the photo-generated superoxide radicals ( $O_2^{\bullet-}$ ) and electrons ( $e^-$ ) play a minor role for the degradation of pollutants. With the addition of isopropyl alcohol as a quencher, the photo-degradation rate was suppressed at a certain level, which confirms the hydroxyl radicals ( $^{\bullet}OH$ ) are the minor reactive species for the pollutants degradation. Finally, after the addition of EDTA-2Na to the reaction system, negligible amount of photocatalytic degradation of pollutants was observed, which tells that holes ( $h^+$ ) plays major role in the photocatalytic degradation of pollutants and the order of photo-generated ions as follows ( $h^+ > ^{\bullet}OH > e^- > O_2^{\bullet-}$ ).

**Table 6.3:** Comparison of obtained results with recently reported literature for the photocatalytic MB and CIP degradation.

Photocatalyst	Amount (mg)	Pollutant and Concentration	Light Source	Degradation (%), Time (min.)	Rate Constant (min <sup>-1</sup> )	Ref.
$Ce(MoO_4)_2$	10	Methyl Orange 5 ppm	'UV' lamp	89 %, 300 min	N.A.	[36]
$NaCe(MoO_4)_2$	20	Rhodamine-B/Methylene Blue 100 ppm	80W 'Hg' lamp	75% (RB) and 95% (MB) 60 min	$2.19 \times 10^{-2}$ (RB) $6.6 \times 10^{-2}$ (MB)	[43]
$Ce_2(MoO_4)_3$	100	Methyl Orange 20 ppm	500 W 'Xe' lamp	82% (MO) 24 h	N.A.	[32]
$Ce(MoO_4)_2@TiO_2$	100	Methyl Orange / Rhodamine- B 5 ppm	500 W 'Xe' lamp	95% MO and 93% RhB 50 min	N.A.	[38]
$Ce(MoO_4)_2/GO$	50	Chloramphenicol 20 ppm	500 W 'W' lamp	99%, 50 min	N.A.	[37]
$Ce(MoO_4)_2/g-C_3N_4$	30	Methylene Blue 10 ppm Ciprofloxacin 20 ppm	35 W 'Xe' lamp	89.7%, 150 min for MB 85.5%, 150 min for CIP	$1.5 \times 10^{-2}$ for MB $1.4 \times 10^{-2}$ for CIP	This Work

More excitingly, the as-fabricated composite photocatalyst CeM/g-CN-20 was found to be stable for photocatalytic degradation of antibiotic pollutant (CIP) under visible-light illumination, as depicted in Figure 6.6(d). The CeM/g-CN-20 binary composite was subjected to four sequential cycles to determine its degradation stability. The same photocatalyst was thoroughly washed with water and ethanol several times after each cycle before being dried overnight in a hot air oven at 60 °C. From the first to the fourth cycle, the following is the deterioration percentage: 85.6% > 64.9% > 54.8% > 41.6%. As shown in Table 6.3. We compared our work with recently reported literature for the photocatalytic degradation of MB and CIP under visible-light. The most important thing in our work is we have used the light irradiation of extremely low power compared to other researchers.



**Figure 6.5:** (a) Photocatalytic performance of fabricated  $g\text{-CN}$ ,  $CeM$ , and  $CeM/g\text{-CN}$  binary binary composites in the terms of degradation curves for MB, and (c) CIP, (b) first-order kinetics plots of  $g\text{-CN}$ ,  $CeM$ , and  $CeM/g\text{-CN}$  binary binary composites MB, and (d) CIP.

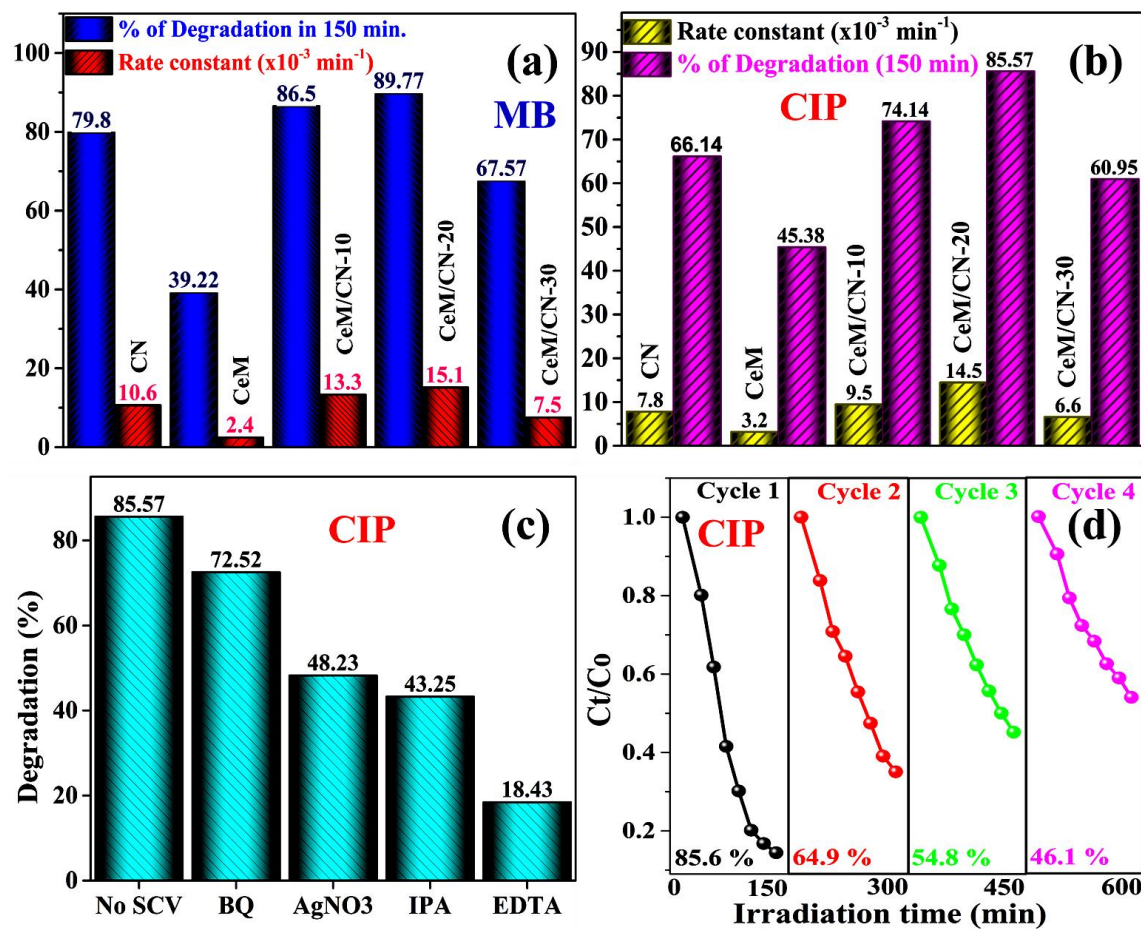


**Figure 6.6:** (a) The rate constant and percentage of degradation of  $\text{g-CN}$ ,  $\text{CeM}$ , and  $\text{CeM/g-CN}$  binary composites for  $\text{MB}$ , (b)  $\text{CIP}$ , (c) scavenger activity of  $\text{CeM/g-CN-20}$  binary composite for  $\text{CIP}$ , and (d) stability of the  $\text{CeM/g-CN-20}$  binary composite up to 4 cycles for  $\text{CIP}$ .

### 6.3.6 Effect of temperature on degradation studies

In order to estimate the effect of temperature on photo degradation efficiency of  $\text{CIP}$  using  $\text{CeM/CN-20}$  binary composite photocatalyst, we have performed degradation experiments at various temperatures. The experiment was conducted using 35W Xe arc lamp as light source and jacketed beaker connected with chiller for the maintenance of temperatures ( $40^\circ\text{C}$  and  $50^\circ\text{C}$ ). Figure 6.7(a) displays significant increase in the efficiency of photo degradation with temperature viz. 85.6 %, 88.0 %, and 90.8 % at  $30^\circ\text{C}$ ,  $40^\circ\text{C}$  and  $50^\circ\text{C}$  respectively. The rate constants for the degradation were calculated at various temperatures from the plot of  $-\ln(\text{C}_t/\text{C}_0)$  vs irradiation time and found to be increased from  $1.4 \times 10^{-2} \text{ min}^{-1}$  at  $30^\circ\text{C}$ ,  $1.5 \times 10^{-2} \text{ min}^{-1}$  at  $40^\circ\text{C}$  to  $1.7 \times 10^{-2} \text{ min}^{-1}$  at  $50^\circ\text{C}$ . The obtained plots agree with pseudo first order kinetics equation model as depicted in Figure 6.7(b). This increase in the rate can be attributed to the rise in thermal energy, which causes

higher number of molecules to have energy more than the activation energy consequently enhancing the effective collisions. Increase in temperature may also increase the active sites on the surface of the catalyst which may lead to increase in adsorption of CIP and thereby increase in the rate of degradation. The activation energy was calculated by the Arrhenius plot of  $\ln k$  vs  $(1/T)$  as depicted in Figure 6.7(c) by using equation (6.5) and (6.6)

$$\ln k = \ln A - E_a/RT \quad (6.5)$$

$$\ln \left( \frac{k}{T} \right) = \ln \left( \frac{K}{h} \right) - \frac{\Delta H}{RT} + \frac{\Delta S}{R} \quad (6.6)$$

where 'k' - rate constant of degradation, ' $E_a$ ' - activation energy, 'A' - pre-exponential factor, 'R' - gas constant, 'T' - temperature of degradation in Kelvin, 'h' - Planck's constant, 'K' - Boltzmann constant,  $\Delta H$  - enthalpy and  $\Delta S$  - entropy of the system.  $\Delta H$  and  $\Delta S$  are calculated from the slope and intercept of  $\ln (k/T)$  vs  $(1/T)$  and the results are represented in Figure 6.7(d). The calculation of Gibbs free energy was done by using equation (6.7)

$$\Delta G = \Delta H - T\Delta S \quad (6.7)$$

The value of  $\Delta S$  was found to be negative which implicates the degradation to be non-spontaneous besides that of  $\Delta H$  and  $\Delta G$  were found to be positive which renders the degradation process to be endothermic and endergonic respectively. A complete list of thermodynamic parameters are tabulated in Table 6.4.

**Table 6.4:** A complete list of thermodynamic parameters at different temperatures.

Temperature (°C)	$E_a$ (KJ mole <sup>-1</sup> )	$\Delta H$ (KJ mole <sup>-1</sup> )	$\Delta S$ (KJ mole <sup>-1</sup> K <sup>-1</sup> )	$\Delta G$ (KJ mole <sup>-1</sup> )
30				17.807
40	9.198	6.596	-0.037	18.177
50				18.547

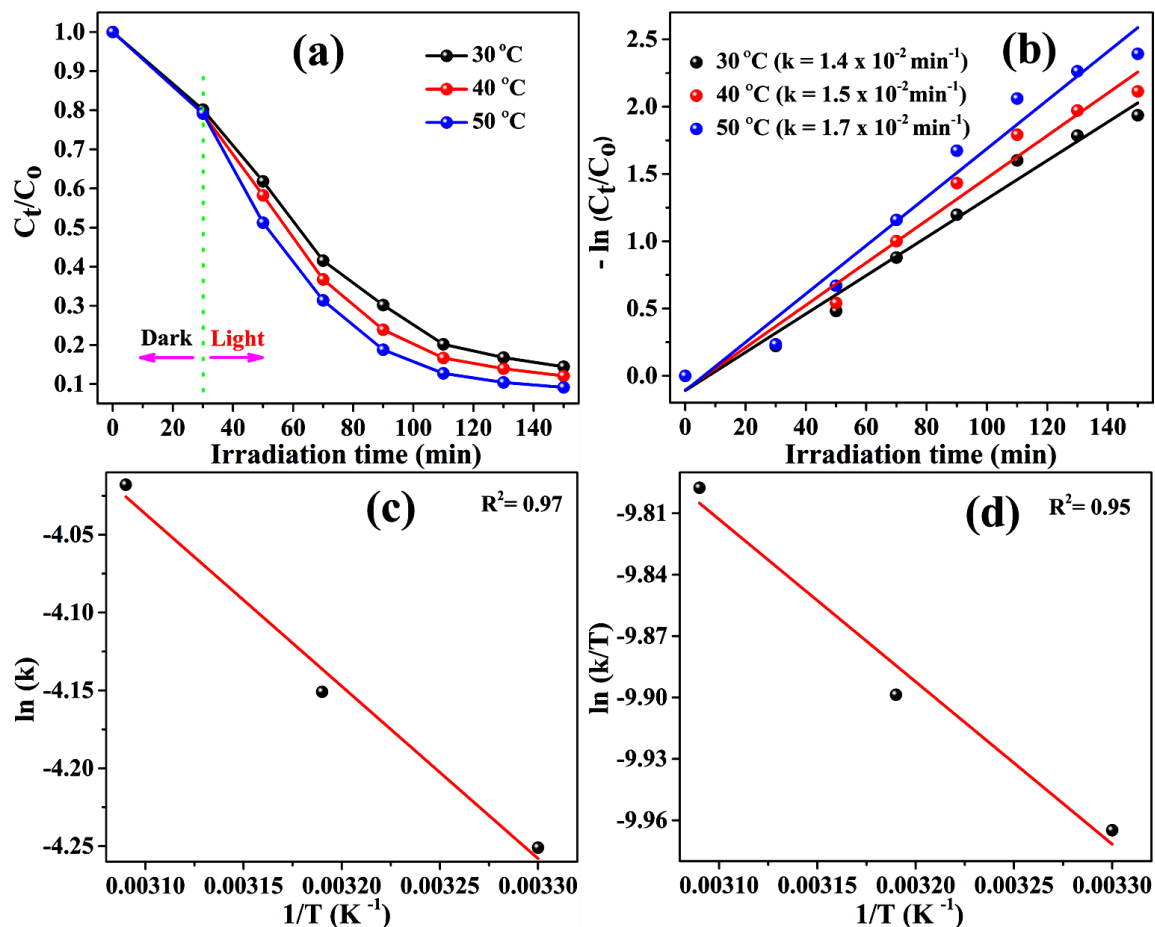


**Figure 6.7:** (a) Curves of  $C_t/C_0$  vs degradation time at altered temperatures, (b)  $-\ln(C_t/C_0)$  vs degradation time at different temperatures, (c)  $\ln(k)$  vs  $1/T$  plot, and (d)  $\ln(k/T)$  vs  $1/T$  plot.

### 6.3.7 Photocatalytic mechanism for CeM/g-CN-20 binary composite photocatalyst

Our experimental results reveals that, the fabricated CeM/g-CN-20 binary composite photocatalyst shows the enhanced photocatalytic efficiency under visible-light illumination. To know the photodegradation pathway for the MB and CIP, we suggested a possible degradation reaction mechanism for the CeM/g-CN-20 binary composite photocatalyst under visible-light illumination, as depicted in Figure 6.9. The conduction band (CB) and valance band (VB) edge potentials of the synthesized pure CeM and g-CN can be identified with the use of VB spectra of XPS and the respective results are depicted in Figure 6.8. From the VB edge potential and bandgap of the semiconductor, we can calculate the CB edge potential as following equations (6.8 and 6.9).

$$E_g = (E_{VB} - E_{CB}) \quad (6.8)$$

$$E_{CB} = (E_{VB} - E_g) \quad (6.9)$$

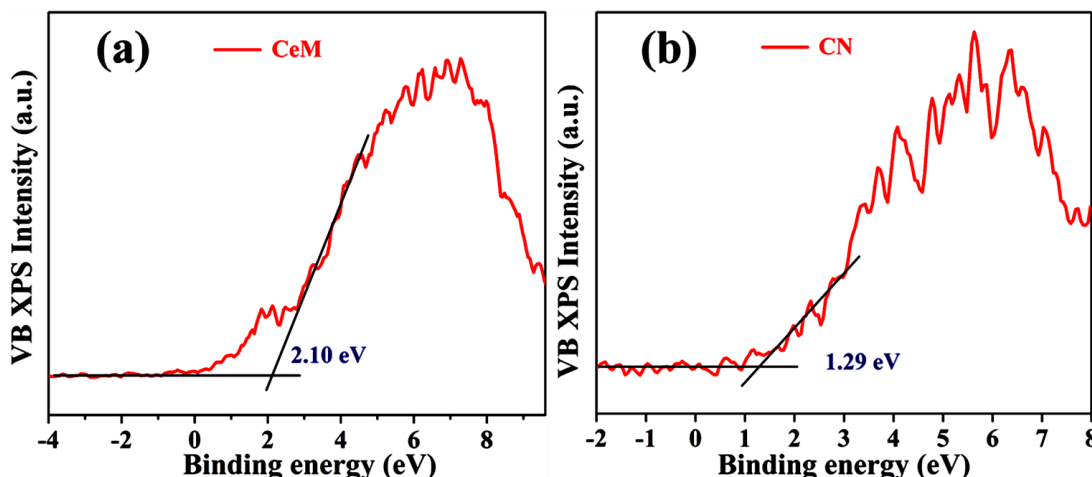


**Figure 6.8:** VB XPS plots of pure (a) CeM, and (b) CN.

Where  $E_{VB}$  and  $E_{CB}$  are edge potentials of the corresponding VB and CB,  $E_g$  is bandgap of the respective semiconductor. The calculated VB and CB edge potentials of the pure CeM (+2.10 eV and -0.13 eV vs. NHE),<sup>[32]</sup> and while for g-CN, the VB and CB edge potentials are calculated as (+1.29 eV and -1.41 eV vs. NHE).<sup>[57]</sup> However, VB and CB redox potentials of the CeM are less negative than those of g-CN. Since redox potentials of the CeM and g-CN lie in visible range, as depicted in Figure 6.9, under the visible-light irradiation, both the CeM and g-CN can absorb photons of energy greater than respective bandgap energy, then photo-generated electrons are excited from VB to CB and leaves holes in the VB. The photo-generated electrons in the CB of g-CN sheets could be easily moved to the CB of CeM. Subsequently, more negative charge was accumulated on the CB of CeM which is close to composite interface. Similarly, photo-generated holes that are present in VB of CeM can transfer to the VB of g-CN.

Consequently, the photo-generated excitons can be effectively separated and recombination of these excitons inhibited between the CeM and g-CN interface, results in the enrichment of the photocatalytic activity of CeM/g-CN-20 binary composite. Besides, more electron density on CB of CeM can efficiently participate in photo- superoxide anion radicals reduction reactions with dissolved oxygen molecules to form  $(O_2^{\cdot-})$ . These superoxide anion radicals ( $O_2^{\cdot-}$ ) do not directly participate in the photo-degradation reaction.<sup>[58]</sup> These may react with water molecules and generates hydroxyl radicals ( $\cdot OH$ ). This phenomenon is supported by trapping experiment results when we added benzoquinone to the reaction mixture as a scavenger, and no degradation was observed, as shown in Figure 6.6(c). Furthermore, the accumulated holes on the VB of g-CN can participate in the photo-oxidation reactions to forms the hydroxyl radicals

(·OH) from water, and some of the holes may directly participate in the degradation reaction. This process is also supported by the scavenger experiment results, after the addition of EDTA 2Na to the reaction system, it do not effectively suppress the degradation of dye, as shown in Figure 6.6(c). This means that under visible light, holes are the dominant reactive species for photocatalytic degradation of MB and CIP.

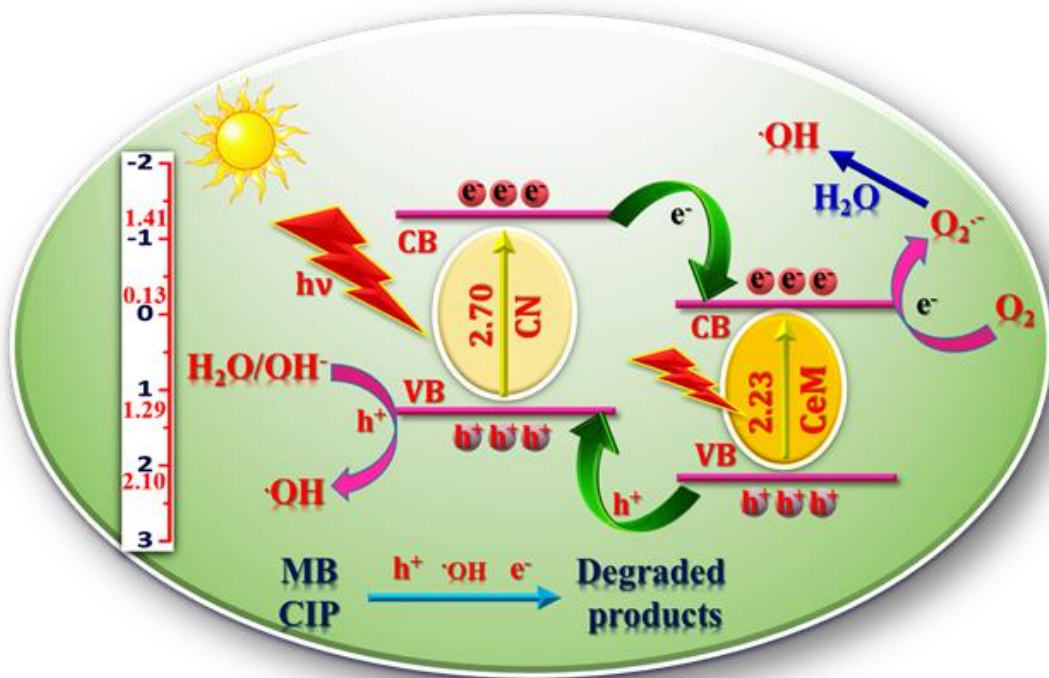


**Figure 6.9:** The proposed mechanism for the enhancement in the photocatalytic activity of CeM/g-CN-20 binary composite for degradation of CIP/ MB pollutants under visible irradiation.

#### 6.4 Conclusions

In brief, g-CN, CeM, and CeM/g-CN binary composite photocatalysts have been successfully synthesized using a simple hydrothermal method. The optimized CeM/g-CN-20 binary composite demonstrates improved photocatalytic pollutants degradation under visible-light for MB and CIP. Because of the existence of close interaction between the materials in the composite of CeM/g-CN, which allows the effective charge transfer between two semiconductors and further inhibit the recombination of photo-generated excitons, and it also enhances the visible-light harvesting capacity. Importantly, CeM/g-CN binary composites demonstrated more stability during the four successive recycle experiments. The scavenger experiment results demonstrated that  $h^+$  and  $\cdot OH$  played a significant role, while  $e^-$  and  $O_2^-$  played the minor roles in the

photocatalytic degradation of pollutants like MB and CIP. As a result, the results of this study can be applied to the production of new materials for environmental remediation and renewable energy generation.

## 6.5 References

- [1] V. K. Gupta, D. Mohan, S. Sharma, *Separation Science and Technology* **1998**, 33, 1331–1343.
- [2] S. Manchala, L. R. Nagappagari, S. M. Venkatakrishnan, V. Shanker, *ACS Applied Nano Materials* **2019**, 2, 4782–4792.
- [3] M. Zeng, I. Echols, P. Wang, S. Lei, J. Luo, B. Peng, L. He, L. Zhang, D. Huang, C. Mejia, L. Wang, M. S. Mannan, Z. Cheng, *ACS Sustainable Chemistry & Engineering* **2018**, 6, 3879–3887.
- [4] M. Ahmaruzzaman, V. K. Gupta, *Industrial & Engineering Chemistry Research* **2011**, 50, 13589–13613.
- [5] Z. Wu, Y. Wang, Z. Xiong, Z. Ao, S. Pu, G. Yao, B. Lai, *Applied Catalysis B: Environmental* **2020**, 277, 119136.
- [6] J. Kim, K. Kim, H. Ye, E. Lee, C. Shin, P. L. McCarty, J. Bae, *Environmental Science & Technology* **2011**, 45, 576–581.
- [7] R. Saravanan, E. Sacari, F. Gracia, M. M. Khan, E. Mosquera, V. K. Gupta, *Journal of Molecular Liquids* **2016**, 221, 1029–1033.
- [8] S. Manchala, A. Gandomalla, N. R. Vempuluru, S. Muthukonda Venkatakrishnan, V. Shanker, *Journal of Colloid and Interface Science* **2021**, 583, 255–266.
- [9] X. Wang, X. Chen, A. Thomas, X. Fu, M. Antonietti, *Advanced Materials* **2009**, 21, 1609–1612.
- [10] H. L. Lee, Z. Sofer, V. Mazánek, J. Luxa, C. K. Chua, M. Pumera, *Applied Materials Today* **2017**, 8, 150–162.
- [11] S. Cao, J. Low, J. Yu, M. Jaroniec, *Advanced Materials* **2015**, 27, 2150–2176.
- [12] X. Wang, K. Maeda, A. Thomas, K. Takanabe, G. Xin, J. M. Carlsson, K. Domen, M. Antonietti, *Nature Materials* **2009**, 8, 76–80.
- [13] J. Liu, Y. Liu, N. Liu, Y. Han, X. Zhang, H. Huang, Y. Lifshitz, S.-T. Lee, J. Zhong, Z. Kang, *Science* **2015**, 347, 970–974.
- [14] Y. Hong, E. Liu, J. Shi, X. Lin, L. Sheng, M. Zhang, L. Wang, J. Chen, *International*

*Journal of Hydrogen Energy* **2019**, *44*, 7194–7204.

- [15] G. Mamba, A. K. Mishra, *Applied Catalysis B: Environmental* **2016**, *198*, 347–377.
- [16] J. Fu, J. Yu, C. Jiang, B. Cheng, *Advanced Energy Materials* **2018**, *8*, 1701503.
- [17] H. Dong, X. Guo, C. Yang, Z. Ouyang, *Applied Catalysis B: Environmental* **2018**, *230*, 65–76.
- [18] J. Barrio, L. Lin, X. Wang, M. Shalom, *ACS Sustainable Chemistry & Engineering* **2018**, *6*, 519–530.
- [19] Q. Han, B. Wang, J. Gao, Z. Cheng, Y. Zhao, Z. Zhang, L. Qu, *ACS Nano* **2016**, *10*, 2745–2751.
- [20] Y. Zhang, J. Liu, G. Wu, W. Chen, *Nanoscale* **2012**, *4*, 5300.
- [21] S. Tonda, S. Kumar, S. Kandula, V. Shanker, *Journal of Materials Chemistry A* **2014**, *2*, 6772.
- [22] J. Xu, L. Zhang, R. Shi, Y. Zhu, *Journal of Materials Chemistry A* **2013**, *1*, 14766.
- [23] M. Xu, L. Han, S. Dong, *ACS Applied Materials & Interfaces* **2013**, *5*, 12533–12540.
- [24] A. Sobhani-Nasab, M. Maddahfar, S. M. Hosseinpour-Mashkani, *Journal of Molecular Liquids* **2016**, *216*, 1–5.
- [25] J. G. Rushbrooke, R. E. Ansorge, *Nuclear Instruments and Methods in Physics Research Section A: Accelerators, Spectrometers, Detectors and Associated Equipment* **1989**, *280*, 83–90.
- [26] R. Sundaram, K. S. Nagaraja, *Sensors and Actuators B: Chemical* **2004**, *101*, 353–360.
- [27] W. Kuang, Y. Fan, Y. Chen, *Catalysis Letters* **1998**, *50*, 31–35.
- [28] Z. Zhang, Y. Liu, Z. Huang, L. Ren, X. Qi, X. Wei, J. Zhong, *Physical Chemistry Chemical Physics* **2015**, *17*, 20795–20804.
- [29] J. N. Cross, P. M. Duncan, E. M. Villa, M. J. Polinski, J.-M. Babo, E. V. Alekseev, C. H. Booth, T. E. Albrecht-Schmitt, *Journal of the American Chemical Society* **2013**, *135*, 2769–2775.
- [30] I. A. Kartsonakis, A. C. Balaskas, G. C. Kordas, *Corrosion Science* **2011**, *53*, 3771–3779.
- [31] K. J. Sreeram, R. Srinivasan, J. Meena Devi, B. Unni Nair, T. Ramasami, *Dyes and Pigments* **2007**, *75*, 687–692.
- [32] G. Xing, H. Guo, Z. Yang, C. Yu, Y. Li, Z. Wu, C. Zhao, *Materials Research Innovations* **2016**, *20*, 272–279.

[33] M. Dong, Q. Lin, H. Sun, D. Chen, T. Zhang, Q. Wu, S. Li, *Crystal Growth & Design* **2011**, *11*, 5002–5009.

[34] A. Gandamalla, S. Manchala, P. Anand, Y.-P. Fu, V. Shanker, *Materials Today Chemistry* **2021**, *19*, 100392.

[35] P. Nandi, D. Das, *Applied Surface Science* **2019**, *465*, 546–556.

[36] A. Sobhani-Nasab, M. Maddahfar, S. M. Hosseinpour-Mashkani, *Journal of Molecular Liquids* **2016**, *216*, 1–5.

[37] R. Karthik, J. Vinoth Kumar, S.-M. Chen, C. Karuppiah, Y.-H. Cheng, V. Muthuraj, *ACS Applied Materials & Interfaces* **2017**, *9*, 6547–6559.

[38] Z. Aghajani, S. M. Hosseinpour-Mashkani, *Journal of Materials Science: Materials in Electronics* **2020**, *31*, 6593–6606.

[39] W. Maisang, A. Phuruangrat, S. Thongtem, T. Thongtem, *Rare Metals* **2018**, *37*, 868–874.

[40] S. Tonda, S. Kumar, M. Bhardwaj, P. Yadav, S. Ogale, *ACS Applied Materials & Interfaces* **2018**, *10*, 2667–2678.

[41] S. Manchala, V. S. R. K. Tandava, L. R. Nagappagari, S. Muthukonda Venkatakrishnan, D. Jampaiah, Y. M. Sabri, S. K. Bhargava, V. Shanker, *Photochemical & Photobiological Sciences* **2019**, *18*, 2952–2964.

[42] S. Tonda, S. Kumar, V. Shanker, *Journal of Environmental Chemical Engineering* **2015**, *3*, 852–861.

[43] J. V. B. Moura, G. S. Pinheiro, J. V. Silveira, P. T. C. Freire, B. C. Viana, C. Luz-Lima, *Journal of Physics and Chemistry of Solids* **2017**, *111*, 258–265.

[44] J. Tauc, R. Grigorovici, A. Vancu, *physica status solidi (b)* **1966**, *15*, 627–637.

[45] N. S. Arul, D. Mangalaraj, R. Ramachandran, A. N. Grace, J. I. Han, *Journal of Materials Chemistry A* **2015**, *3*, 15248–15258.

[46] Z. Xu, Z. Li, X. Tan, C. M. B. Holt, L. Zhang, B. S. Amirkhiz, D. Mitlin, *RSC Advances* **2012**, *2*, 2753.

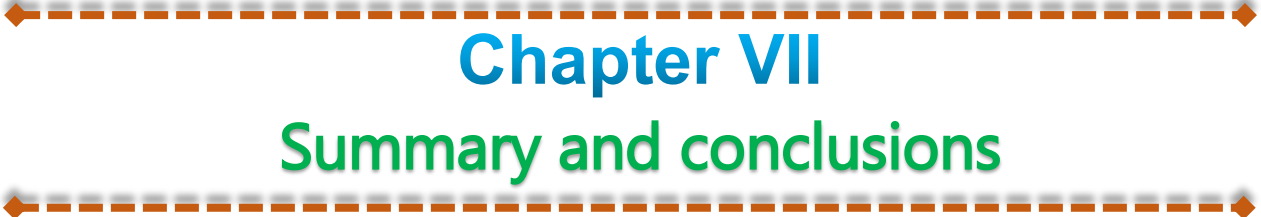
[47] S. C. Yan, Z. S. Li, Z. G. Zou, *Langmuir* **2010**, *26*, 3894–3901.

[48] Y. Li, G. Wang, K. Pan, W. Zhou, C. Wang, N. Fan, Y. Chen, Q. Feng, B. Zhao, *CrystEngComm* **2012**, *14*, 5015.

[49] L. Xu, X. Yang, Z. Zhai, D. Gu, H. Pang, W. Hou, *CrystEngComm* **2012**, *14*, 7330.

[50] A. Verma, S. Kumar, W.-K. Chang, Y.-P. Fu, *Dalton Transactions* **2020**, *49*, 625–637.

- [51] L. Lin, C. Hou, X. Zhang, Y. Wang, Y. Chen, T. He, *Applied Catalysis B: Environmental* **2018**, *221*, 312–319.
- [52] Y. Li, H. Xu, S. Ouyang, D. Lu, X. Wang, D. Wang, J. Ye, *Journal of Materials Chemistry A* **2016**, *4*, 2943–2950.
- [53] S. Cao, N. Zhou, F. Gao, H. Chen, F. Jiang, *Applied Catalysis B: Environmental* **2017**, *218*, 600–610.
- [54] A. Verma, D. P. Jaihindh, Y.-P. Fu, *Dalton Transactions* **2019**, *48*, 8594–8610.
- [55] D. Li, S. Zuo, H. Xu, J. Zan, L. Sun, D. Han, W. Liao, B. Zhang, D. Xia, *Journal of Colloid and Interface Science* **2018**, *531*, 28–36.
- [56] P. Makal, D. Das, *Applied Surface Science* **2018**, *455*, 1106–1115.
- [57] H.-J. Li, B.-W. Sun, L. Sui, D.-J. Qian, M. Chen, *Physical Chemistry Chemical Physics* **2015**, *17*, 3309–3315.
- [58] S. Tonda, S. Kumar, O. Anjaneyulu, V. Shanker, *Phys. Chem. Chem. Phys.* **2014**, *16*, 23819–23828.



## Chapter VII

### Summary and conclusions

## **Chapter VII**

### **Summary and Conclusions**

This chapter summarizes and concludes the present work and has the outlook for future work.

#### **7.1 Present thesis**

This thesis consists of seven chapters. Chapter I describes the general introduction and background, objectives and scope of the present research work. Chapter II displays the synthesis and analytical methods employed for the characterization of materials, and chapter III, IV, V, and VI presents original research work on the systematic study of highly efficient g-C<sub>3</sub>N<sub>4</sub> based metal oxide nanocomposite photocatalysts for environmental applications. Finally, Chapter VII (present chapter) focuses on summary and conclusions.

#### **7.2 Conclusions**

During the course of this research work, a number of conclusions have been reached, regarding the synthesis, characterization and utilization of visible light based photocatalysts for the degradation of organic and antibiotic pollutants.

**Chapter I:** This chapter describes the general background of photocatalysis, state of the problem, objective and scope of the present work. It also describes the literature review on present work, visible light active photocatalysis and nanomaterials, especially advantages of g-C<sub>3</sub>N<sub>4</sub> based photocatalysts.

**Chapter II:** This chapter deals with the synthesis methods and characterization techniques used for the synthesis and analysis of materials. Particularly, the principle of characterization techniques including PXRD, FT-IR, XPS, SEM, FE-SEM, TEM, EDS, UV-Visible DRS, Fluorescence spectroscopy, TGA, and BET surface area studies. Further, the photocatalytic experiment details are also explained.

**Chapter III:** In this work, we have successfully synthesized a versatile hybrid photocatalysts i.e.; CdMoO<sub>4</sub>/g-C<sub>3</sub>N<sub>4</sub> (CMO/CN) by a facile and simple one-pot *in-situ* hydrothermal method. Here CdMoO<sub>4</sub> (CMO) microspheres were deposited on the g-C<sub>3</sub>N<sub>4</sub> (CN) sheets. Fabricated CN, CMO, and CMO/CN composite photocatalysts were analyzed with various characterization techniques like UV-Vis DRS, PL, TRFL, EIS, PXRD, FT-IR, SEM-EDS, TGA,

XPS and BET. The results reveal that the formation of a strong heterojunction between two semiconductors leads to the formation of active photocatalyst. Furthermore, as-synthesized materials were tested for the photoelectrocatalytic oxygen evolution reactions (OER) in acidic medium and photocatalytic degradation of methylene blue (MB) under light irradiation. Among all tested samples, CMO/CN-10 has shown the highest current density  $52.74 \text{ mA cm}^{-2}$  at  $1.93 \text{ V}$  with lowest over potential of  $0.70 \text{ mV}$  on glassy carbon electrode for OER in acidic medium. The photocatalytic degradation rate constant of CMO/CN-10 composite in MB solution is  $k = 2.0 \times 10^{-2} \text{ min}^{-1}$  whereas for the pure CMO and CN degradation rate constant is  $k = 5.7 \times 10^{-3} \text{ min}^{-1}$  and  $k = 1.2 \times 10^{-2} \text{ min}^{-1}$  respectively. This enhancement in photoelectrocatalytic and photocatalytic properties is due to the fast migration of photo-induced electrons in the case of CMO/CN-10 nanocomposite. Trapping experiment results reveal the major reactive species for photocatalytic degradation of MB is  $\cdot\text{OH}$  and  $\text{h}^+$  respectively.

**Chapter IV:** This chapter shows the successful synthesis of pristine  $\text{SrMoO}_4$ ,  $\text{g-C}_3\text{N}_4$  and  $\text{SrMoO}_4/\text{g-C}_3\text{N}_4$  hybrid composite for the first time by a facile mixing and heating methodology and is characterized by various techniques. Phase analysis carried out by PXRD study, morphology and elemental analysis were investigated by FE-SEM, EDS and XPS, thermal stability of synthesized materials were done by TGA, UV-Vis DRS, and PL studies confirm optical properties. The optimized  $\text{SrMoO}_4/\text{g-C}_3\text{N}_4$ -10 composite photocatalyst exhibited superior performance for the photocatalytic degradation of Rhodamine B (RhB) dye under direct sunlight irradiation. The rate of photocatalytic efficiency of  $\text{SrMoO}_4/\text{g-C}_3\text{N}_4$ -10 ( $0.0976 \text{ min}^{-1}$ ) is 4 and 40 times higher than those of pure  $\text{g-C}_3\text{N}_4$  ( $0.0245 \text{ min}^{-1}$ ) and  $\text{SrMoO}_4$  ( $0.0024 \text{ min}^{-1}$ ) respectively. The developed good interfacial interactions among the  $\text{g-C}_3\text{N}_4$  and  $\text{SrMoO}_4$  in  $\text{SrMoO}_4/\text{g-C}_3\text{N}_4$ -10 composite which help in the separation and transfer efficiency of photo-induced excitons by inhibiting the recombination of excitons. The trapping experiment results reveal that  $(\text{O}_2^{\cdot-})$  are the major reactive species. More importantly, our composite  $\text{SrMoO}_4/\text{g-C}_3\text{N}_4$ -10 shows good stability even after four successive runs.

**Chapter V:** This chapter deals with the synthesis highly efficient  $\text{ZnAl-LDH/g-C}_3\text{N}_4$  composites via a simple microwave irradiation method first time for the degradation of ciprofloxacin (CIP), an antibiotic pollutant under visible light. Synthesized materials were analyzed using different characterization techniques like UV-Vis DRS, TRFL, XRD, FT-IR, BET,

FE-SEM, TEM, and XPS for optical, crystal structure, morphological, and elemental analysis. The main reactive intermediates which are formed during the photocatalytic degradation process were analyzed by LC-MS analysis. More importantly, the optimized ZnAl-LDH/g-C<sub>3</sub>N<sub>4</sub>-10 composite showed the highest photodegradation rate constant of  $1.22 \times 10^{-2}$  with 84.10 % degradation which is more than bare g-C<sub>3</sub>N<sub>4</sub> and ZnAl-LDH photocatalysts. ZnAl-LDH/g-C<sub>3</sub>N<sub>4</sub> composite materials showed a high synergy effect with the more specific surface area which helps enhanced visible light adsorption capacity and also increased number of catalytically active sites. Moreover, compared to pure materials for composites of ZnAl-LDH/g-C<sub>3</sub>N<sub>4</sub> are having low electron-hole pair recombination.

**Chapter VI:** This chapter describes the fabrication of a new binary Ce(MoO<sub>4</sub>)<sub>2</sub>/g-C<sub>3</sub>N<sub>4</sub> composite using a simple hydrothermal method. The synthesized Ce(MoO<sub>4</sub>)<sub>2</sub>/g-C<sub>3</sub>N<sub>4</sub> composite has displayed enhanced photocatalytic degradation performance towards the organic pollutants of ciprofloxacin (CIP) and methylene blue (MB) under visible-light. The structure, composition, morphology, and optical absorption properties of synthesized materials were characterized by different techniques like PXRD, FE-SEM, EDS, TEM, XPS, FT-IR, PL, TRFL, BET, and UV-Vis DRS, respectively. Our results conclude that, among the series of synthesized compounds, Ce(MoO<sub>4</sub>)<sub>2</sub>/g-C<sub>3</sub>N<sub>4</sub>-20 composite has shown significant photocatalytic degradation efficiency for two different organic pollutants, those are CIP and MB. The degradation percentage and rate constant of CIP and MB for optimized Ce(MoO<sub>4</sub>)<sub>2</sub>/g-C<sub>3</sub>N<sub>4</sub>-20 composite were 85.57% and  $14.5 \times 10^{-3} \text{ min}^{-1}$ , 89.77%, and  $15.1 \times 10^{-3} \text{ min}^{-1}$  in 150 min under visible-light irradiation. The degradation percentage and rate constant were very high compared to pristine CeM, CN, and other composites. The enhancement in the degradation ability of Ce(MoO<sub>4</sub>)<sub>2</sub>/g-C<sub>3</sub>N<sub>4</sub>-20 may be ascribed to photogenerated charge carriers separation and transferability were more, and recycle test confirms it has good stability.

### 7.3 Summary

The obtained results show that the efficiency of a pollutant degradation process largely depends on the physico-chemical characteristics of the photocatalyst. More importantly, the photocatalytic activity at nanoscale showed a remarkable enhancement when compared to its bulk counterpart. Our results also demonstrate that the semiconductor/semiconductor composite is an alternative strategy to improve the visible light efficiency. The g-C<sub>3</sub>N<sub>4</sub> nanosheet is a promising

visible light active photocatalyst due to its unique electronic structure with a narrow band gap and appropriate CB and VB positions, as well as high surface area. Furthermore, composite with a transition metal oxides and forming a type-II heterostructure of g-C<sub>3</sub>N<sub>4</sub> benefits to improve the charge transfer and separation efficiency. Therefore, metal oxide based materials (CdMoO<sub>4</sub> and SrMoO<sub>4</sub>) and g-C<sub>3</sub>N<sub>4</sub>–based nanostructured photocatalysts appear to be very promising materials for the pollutant degradation.

#### **7.4 Recommendations for future work**

Visible light driven photocatalytic degradation of organic pollutant, using above nanostructured photocatalysts was described in detail as a possible initiator for future work.

- The g-C<sub>3</sub>N<sub>4</sub>-based metal oxide nanostructured photocatalysts could be used in the photocatalytic degradation of other priority pollutants such as dyes, antibiotics, pesticides and pharmaceuticals as well as clean energy H<sub>2</sub> production and CO<sub>2</sub> reduction.
- Furthermore, it would be interesting to explore g-C<sub>3</sub>N<sub>4</sub> based on the formation of particularly type-II heterostructures with unique Nano-architecture in order to fulfill the needs of practical application.
- More importantly, cost–effective g-C<sub>3</sub>N<sub>4</sub> nanosheet based photocatalyst facilitates its utilization and also opens the possibility of working in a continuous regime as the preparation of g-C<sub>3</sub>N<sub>4</sub> can be simply accomplished by thermal condensation of low-cost nitrogen rich precursors. Therefore, it is more economic and environmentally friendly.
- *In situ* observations based on advanced material characterization and fundamental studies based on computer simulations over g-C<sub>3</sub>N<sub>4</sub> are highly desirable to advance further developments in this exciting area of research which help in developing a low-cost photocatalytic system with high efficiency.
- Finally, a cost effective synthesis of g-C<sub>3</sub>N<sub>4</sub> nanosheet based photocatalysts and a possibility of using natural sunlight as irradiation source can result in both environmental and economic advantages.

◆-----◆

## **List of Publications, Conferences, Seminars, Workshops, Courses, and Curriculum Vitae**

◆-----◆

## List of Publications

1. **Ambedkar Gandamalla**, Saikumar Manchala, Pandiyarajan Anand, Yen-Pei Fu, Vishnu Shanker, Development of versatile CdMoO<sub>4</sub>/g-C<sub>3</sub>N<sub>4</sub> nanocomposite for enhanced photoelectrochemical oxygen evolution reaction and photocatalytic dye degradation applications, *Materials Today Chemistry*, 2021, 19, 100392.
2. **Ambedkar Gandamalla**, Saikumar Manchala, Atul Verma, Yen-Pei Fu, Vishnu Shanker, Microwave-assisted synthesis of ZnAl-LDH/g-C<sub>3</sub>N<sub>4</sub> composite for degradation of antibiotic ciprofloxacin under visible-light Illumination, *Chemosphere*, 2021, 283, 131182.
3. **Ambedkar Gandamalla**, Saikumar Manchala, Vishnu Shanker, Facile fabrication of novel SrMoO<sub>4</sub>/g-C<sub>3</sub>N<sub>4</sub> hybrid composite for high-performance photocatalytic degradation of dye pollutant under sunlight, *ChemistrySelect*, 2021, 6, 1-12.
4. Saikumar Manchala, **Ambedkar Gandamalla**, Vempuluru Navakoteswara Rao, Shankar Muthukonda Venkatakrishnan, Vishnu Shanker, High potential and robust ternary LaFeO<sub>3</sub>/CdS/carbon quantum dots nanocomposite for photocatalytic H<sub>2</sub> evolution under sunlight illumination, *Journal of Colloid and Interface Science*, 2021, 583, 255-266.
5. Saikumar Manchala, **Ambedkar Gandamalla**, Vempuluru Navakoteswara Rao, Shankar Muthukonda Venkatakrishnan, Vishnu Shanker, Step-by-step improvement in solar-light responsive H<sub>2</sub> evolution using SrTiO<sub>3</sub> and CdS by encapsulating carbon nanospheres and constructing a novel ternary hierarchical photocatalytic system, *Journal of Nanostructure in Chemistry*, 2021. (doi.org/10.1007/s40097-021-00411-y).
6. Suresh Siliveri, Suman Chirra, Chinkit Tyagi, **Ambedkar Gandamalla**, Ajay Kumar Adepu, Srinath Goskula, Sripal Reddy Gujjula, and Narayanan Venkatathri, New Porous High Surface Area, TiO<sub>2</sub> Anatase/SAPO-35 Mild Brønsted Acidic Nanocomposite: Synthesis, Characterization and Studies on it's Enhanced Photocatalytic Activity, *ChemistrySelect*, 2019, 4, 9135-9142.

### **Papers under communication**

1. **Ambedkar Gandamalla**, Saikumar Manchala, Atul Verma, Yen-Pei Fu, Vishnu Shanker, Development of highly efficient  $\text{Ce}(\text{MoO}_4)_2/\text{g-C}_3\text{N}_4$  composite for the photocatalytic degradation of methylene blue and ciprofloxacin under visible light. **Environmental technology and innovation (under review)**.

### **Papers under preparation**

1. **Ambedkar Gandamalla**, Saikumar Manchala, Priyanka Yadav, and Vishnu Shanker, Synthesis and Characterization of  $\text{BaBiO}_3/\text{g-C}_3\text{N}_4$  composite photocatalysts for Methylene blue degradation under sunlight irradiation.
2. **Ambedkar Gandamalla**, Saikumar Manchala, Vishnu Shanker Effect of Solvents on morphology and optical properties of  $\text{SrMoO}_4$  microcrystals and their photocatalytic studies
3. Saikumar Manchala, **Ambedkar Gandamalla**, Vishnu Shanker, 2D/2D interface Mg, Al-LDH/g-C<sub>3</sub>N<sub>4</sub> Nanocomposites: synthesis, characterization, and their application in photocatalytic dye degradation of Rhodamine-B under sunlight illumination.
4. Saikumar Manchala, **Ambedkar Gandamalla**, Vishnu Shanker, Highly efficient 2D/2D/2D interface Mg, Al-LDH/g-C<sub>3</sub>N<sub>4</sub>/MoS<sub>2</sub> ternary nanocomposites for photocatalytic applications under sunlight illumination.
5. Saikumar Manchala, **Ambedkar Gandamalla**, Vishnu Shanker, Solvent effect on surface properties of g-C<sub>3</sub>N<sub>4</sub> nanosheets and their in turn effect on photocatalytic dye degradation of Rhodamine-B under sunlight illumination.

### **Book chapter under preparation**

➤ Saikumar Manchala, **Ambedkar Gandamalla**, Nanocelluloses for removal of Hazardous Organic Pollutants from Wastewater.

### Conferences and Seminars

- Participated in National Conference on “Frontiers in Chemical sciences and technologies (**FCST-2016**)” organized by Department of Chemistry at NIT-Warangal, during 28<sup>th</sup> -29<sup>th</sup>, January, 2016.
- Participated in National Seminar on “Recent Advances in Organic Synthesis (**RAOS**)” organized by Department of Chemistry, NIT-Warangal, on 29<sup>th</sup> June, 2016.
- Participated in National Symposium on “Recent Advances in Chemical & Material Sciences (**RACMS- 2016**)” organized at RGUKT-Basar, during 20<sup>th</sup> -21<sup>st</sup> , August, 2016.
- Participated and volunteered in One day seminar on “Hindi Divas-2016” organized at NIT-Warangal, on 19<sup>th</sup> September, 2016.
- Participated in “Fourth International Conference on Advanced Oxidation Processes (**AOP-2016**)” organized by Department of Chemistry BITS Pilani K K Birla Goa Campus, during 17<sup>th</sup> to 20<sup>th</sup> , December, 2016.
- Presented a Poster “**Research Conclave-2017**” Organized by NIT Warangal during 18<sup>th</sup> to 19<sup>th</sup> March, 2017
- Presented a Poster in National Conference on “Recent developments in chemical sciences and allied technologies (**RDCST-2017**)” organized by Department of Chemistry, NIT Warangal, during 29<sup>th</sup> to 30<sup>th</sup> June, 2017.
- Presented a Poster in National Conference on “New Perspective to Advanced Functional Materials (**NPAFM-2017**)” organized by Department of Chemistry, Ravenshaw University, Cuttack, Odisha during 15<sup>th</sup> to 17<sup>th</sup> December, 2017.
- Presented a Poster in “International Conference on Advanced Functional Materials (**ICAFM-2017**)” organized by Department of Chemistry, IIIT Basar during 18<sup>th</sup> to 20<sup>th</sup> December 2017.
- Presented a Poster in “Conference on Advances in Catalysis for Energy and Environment (**CACEE-2018**)” organized by Department of Chemical Sciences (TIFR) Homi bhabha Road, Colaba, Mumbai, during 10<sup>th</sup> to 12<sup>th</sup> January-2018.
- Presented a Poster in “National Conference on Advanced Materials for Energy and Environmental Applications (**AMEEA-2018**)” organized by Department of Chemistry, NIT Rourkela, Odisha during 12<sup>th</sup> to 14<sup>th</sup> December, 2018

- Presented a Poster in “Telangana State Science Congress (**TSSC-2018**)” organized by Telangana Academy of Sciences in Association with NIT Warangal, during 22<sup>nd</sup> to 24<sup>th</sup> December, 2018.
- Oral Presentation in “International Conference on Advanced Functional Materials and Devices (**ICAFMD-2019**)” organized by Department of Physics, NIT Warangal, during 26<sup>th</sup> to 28<sup>th</sup> February, 2019.
- Presented a Poster in “International Conference on Materials for the Millennium (**MATCON-2019**)” organized by Department of Applied Chemistry, CUSAT, Kerala, during 14<sup>th</sup> to 16<sup>th</sup> March, 2019.
- Organized and presented a Poster in International Conference on Advances in Chemical Sciences and technologies (**ACST-2019**) organized by Department of Chemistry, NIT Warangal, during 23<sup>rd</sup> to 25<sup>th</sup> September, 2019.
- Presented a Poster in 6<sup>th</sup> International Conference (Virtual) on Nanoscience and Nanotechnology (**ICONN-2021**) organized by Department of Physics and Nanotechnology, SRMIST, SRM Nagar, Chennai, Tamil Nadu, during 1<sup>st</sup> to 3<sup>rd</sup> February 2021.

## PERSONAL INFORMATION



## Mr. Ambedkar Gandamalla

Doctoral Researcher

C/o: Dr. Vishnu Shanker

Associate Professor and Head

Department of Chemistry

National Institute of Technology Warangal (NITW)

Warangal-506004, Telangana

+91 - 9951952358

[ambedkar90@student.nitw.ac.in](mailto:ambedkar90@student.nitw.ac.in); [ambedkarnitw@gmail.com](mailto:ambedkarnitw@gmail.com)

Gender: Male | Date of Birth: 10-01-1990 | Nationality: Indian | Marital status: Single

## GOOGLE SCHOLAR

<https://scholar.google.co.in/citations?hl=en&user=gkfEz7EAAAAJ>

## RESEARCH GATE

<https://www.researchgate.net/profile/Gandamalla-Ambedkar>**OBJECTIVE:**

To enhance my knowledge by being an integral part of a result oriented research team which will utilize my managerial and technical potentials, thereby proving to be a productive and trust worthy professional in the advancements of the organization.

**Education:****January 2016 – Present:****Doctoral Research Scholar (PhD Student)**

Department of Chemistry,

National Institute of Technology, Warangal, Telangana, India.

<http://www.nitw.ac.in/nitw/>Under the Supervision of **Dr. Vishnu Shanker**, Associate Professor and Head.<https://www.nitw.ac.in/faculty/id/16382><https://scholar.google.co.in/citations?user=3Nxi8AwAAAAJ&hl=en>

**Research Topic:** "Development of highly efficient g-C<sub>3</sub>N<sub>4</sub> based metal oxide nanocomposites for photocatalytic applications".

**Status:** To be awarded (Thesis submitted).

**Course Work:**

As a part of PhD programme, Course works have been carried out on the following relevant subjects for one semester.

1. Advanced Analytical Techniques (CY 804).
2. Surface Analytical Techniques (CY 805).
3. Supra molecular chemistry & Nanomaterials (CY 822).
4. Solid state Chemistry (CY 824).
5. English for Scientific Communication.

July 2011 – June 2013:

**Master of Science (Organic Chemistry)**  
Telangana University, Telangana, India  
(<http://www.telanganauniversity.ac.in/>)  
Percentage of Marks: **70.90 (Distinction)**

June 2007 – April 2010:

**Bachelor of Science (Microbiology, Zoology, and Chemistry)**  
Osmania University, Hyderabad, Telangana, India  
(<https://www.osmania.ac.in>)  
Percentage of Marks: **60.00 (First Division)**

June 2005 – March 2007:

**Intermediate (Botany, Zoology, Physics, and Chemistry)**  
Board of Intermediate Education, Andhra Pradesh, India  
(<http://bieap.gov.in/>)  
Percentage of Marks: **70.04 (First Division)**

June 2004 – March 2005:

**Secondary School Certificate (High School)**  
Board of Secondary Education, Andhra Pradesh, India  
(<http://bseaps.org.in/>)  
Percentage of Marks: **65.00 (First Division)**

**RESEARCH INTERESTS**

- Nanostructured Materials synthesis and characterization.
- g-C<sub>3</sub>N<sub>4</sub>-based metal oxide nanocomposites.
- Graphene and Carbon base nanomaterials.
- Photocatalytic and electrocatalytic watersplitting and CO<sub>2</sub> reduction.
- Photocatalytic water purification.
- Energy and environmental related applications.

**JOB-RELATED SKILLS**

I am actively involved in innovative and quality research in the field of design and development of novel and efficient g-C<sub>3</sub>N<sub>4</sub> based metal oxide nanocomposites, Photocatalytic dye degradation and organic transformations during my doctoral and post-graduation studies; I acquired the following instrumental and computational expertise.

- Powder X-Ray Diffractometer, PANalytical.
- FTIR Spectrophotometer, PerkinElmer.
- UV-Visible-NIR Spectrophotometers, Perkin Elmer, Analytik Jena Specord 205.
- Fluorescence Spectrophotometer, TCS Solutions.
- TG-DT Analyser, Netzshu.
- High Temperature Furnace, Hindfur.
- Scanning Electron Microscope, VEGA3, Tescon, USA
- Other small instruments relevant for materials characterization and analysis.
- MS Office, X'Pert HighScore.
- Origin, ChemDraw Ultra 12.0 etc.
- MENDELEY Reference Manager.

**OTHER SKILLS**

- Assisted to my Research Supervisor and worked in several committees in various conferences and workshops organized by Department of Chemistry, Teaching Learning Centre, and Centre for Advanced Materials (NITW).
- Very good interpersonal and communication skills along with management skills.
- Good experience in writing technical papers, presentations and reports.
- Guided many post-graduate students for their projects.

**HONOURS AND AWARDS**

- I have been awarded for Six months (October 1<sup>st</sup> 2019 to March 23<sup>rd</sup> 2020) **TEEP@AsiaPlus, Short-Term Research Internship (STRI) program** under the guidance of Prof. Yen-Pei Fu, Department of Material Science & Engineering, **National Dong Hwa University (NDHU), Taiwan.**
- Receiving scholarship from Ministry of **Human Resource development (MHRD), Government of India**, for pursuing Ph.D. in the **Department of Chemistry, NIT-Warangal**.
- Qualified in **All India Graduate Aptitude Test in Engineering (GATE-2015)** in Chemistry, India.
- Qualified in **State Eligibility Test for Telangana and Andhra Pradesh States for Assistant professor/Lectureship (SET-TS & AP-2014)** in Chemical Sciences.
- Got best poster presentation award at **Research Conclave-2017**, organized by NIT-Warangal 18th to 19th March 2017.